UNIVERSITÀ DEGLI STUDI DELL'INSUBRIA

Facoltà di Scienze Matematiche, Fisiche e Naturali - Como

Anno Accademico 2009-2010

Laurea Specialistica in Fisica


# *THE ELECTRON MUON RANGER FOR THE MICE EXPERIMENT*



Laureanda: Daniela Lietti
Matricola 617710

Tutor: Dr.ssa Michela Prest
Università degli Studi dell'Insubria
Co-Tutor: Dr. Davide Bolognini
Università degli Studi dell'Insubria
Co-Tutor: Dr. Erik Vallazza
INFN Sezione di Trieste

*a Valentina,*
*...il tuo sorriso non smetterà mai*
*di brillare nel mio cuore.*

# Contents

# Riassunto della Tesi

La fisica dei neutrini riveste un ruolo fondamentale nella fisica moderna e, in particolare, rappresenta la prima evidenza sperimentale di nuova fisica oltre il Modello Standard.
Tradizionalmente la nascita della fisica del neutrino è fissata al 4 Dicembre 1930 quando Wolfgang Pauli diede per la prima volta una spiegazione all'anomalia osservata nello spettro del decadimento $\beta$. In tale decadimento, infatti, si ipotizzava che fossero coinvolte solo due particelle e quindi dal punto di vista sperimentale ci si aspettava uno spettro a righe discrete. Tuttavia, nel 1911, in un esperimento condotto da Lise Meitner e Otto Hahn presso l'Università di Berlino, lo spettro energetico misurato risultava essere continuo e ciò era in contraddizione con le leggi di conservazione di momento ed energia; inoltre, anche il valore dello spin dell'atomo di $^{14}$N utilizzato nell'esperimento risultava in disaccordo con la precedente previsione fatta da Rutherford.
L'idea di Pauli fu quella di postulare l'esistenza di un'ulteriore particella (fino ad allora non osservata e molto complicata da rivelare) coinvolta nel decadimento $\beta$; in questo modo l'energia disponibile nel processo veniva suddivisa tra il nucleo, l'elettrone e la nuova particella rispettando le leggi di conservazione e dando origine ad un cosiddetto *three-body final state* il cui spettro risulta effettivamente essere continuo.
Ci vollero però quasi trent'anni (1956) perché l'esistenza di tale particella (denominata da Enrico Fermi *neutrino* per distinguerla dal neutrone di James Chadwick) venisse effettivamente provata: furono Clyde L. Cowan e Frederick Reines i primi ad osservare, presso il reattore di Savannah River, un evento di neutrini attraverso il processo di decadimento $\beta$ inverso ($\overline{\nu} + p \rightarrow e^+ + n$). Il rivelatore utilizzato era costituito da taniche riempite da centinaia di litri di scintillatore liquido (acqua + $CdCl_2$) e circondate da un centinaio di fotomoltiplicatori per la lettura del segnale. Questo storico risultato confermò l'ipotesi di Pauli e aprì la strada dell'inesplorato mondo dei neutrini dando inizio alla cosiddetta *discovery era*.
I neutrini sono però molto difficili da osservare; essi interagiscono solo attraverso l'interazione debole e con sezioni d'urto molto piccole ($< 10^{-37}$ cm$^2$). Per questi motivi la loro osservazione ha richiesto (e richiede tuttora) la costruzione di de-

tector enormi posti in laboratori sotterranei per limitare il fondo di raggi cosmici. Le principali tecniche su cui si basarono e si basano ancora oggi gli esperimenti di neutrini sono:

- il **metodo radiochimico** basato sulla trasmutazione del materiale del detector in un altro elemento chimico (tipicamente $^{37}Cl \rightarrow ^{37}Ar$ o $^{71}Ga \rightarrow ^{71}Ge$) e utilizzato fino alle fine degli anni '90 dai cosiddetti *esperimenti di vecchia generazione* (Homestake, GALLEX, GNO, SAGE);

- la **misura in tempo reale dello spettro di neutrini** che sfrutta il processo di emissione di luce Cherenkov degli elettroni prodotti in seguito all'interazione dei neutrini col materiale del rivelatore (tipicamente $H_2O$ o $D_2O$); questo e altri metodi simili sono la base dei cosiddetti *esperimenti di nuova generazione* (Kamiokande, SuperKamiokande, SNO);

- l'osservazione di **correnti cariche** in seguito all'interazione dei neutrini con il materiale del detector;

- lo studio del **decadimento $\beta$ inverso** (come nell'esperimento di Cowan e Reines) e della **riduzione** del flusso di neutrini prodotti artificialmente (*disappearance experiments*).

In particolare le prime due tecniche vengono utilizzate principalmente negli esperimenti sui neutrini solari mentre gli altri due metodi sono rispettivamente utilizzati per l'osservazione di neutrini atmosferici e di neutrini prodotti artificialmente (da reattori o da acceleratori).
Nonostante i molti risultati ottenuti dagli anni '60 ad oggi (quali la misura dell'elicità, la prova dell'esistenza di diverse generazioni e del fenomeno delle oscillazioni), la fisica del neutrino rimane ancora un campo aperto: il fatto che questa particella abbia una massa così piccola, la corretta gerarchia delle masse, il ruolo dei neutrini in cosmologia, il numero esatto di generazioni rimangono questioni irrisolte che non trovano una completa spiegazione all'interno del Modello Standard. Per questo motivo risulta fondamentale la realizzazione di nuovi complessi (*Neutrino Factory*) e l'impiego di nuove tecniche (*ionization cooling*) grazie alle quali sarà possibile produrre fasci di neutrini sufficientemente intensi, ben collimati e con una limitata contaminazione da parte di altre particelle. Il lavoro di questa tesi si inserisce in questo filone.
La tesi si apre con una panoramica dei principali aspetti della fisica dei neutrini e dei risultati ottenuti finora dal punto di vista sia sperimentale che fenomenologico, dal meccanismo che dà origine a masse così piccole al fenomeno delle oscillazioni sia nel vuoto che nella materia. Il Capitolo 1 contiene inoltre la descrizione di una Neutrino Factory, dei principali elementi necessari per la sua realizzazione e le

motivazioni che ne giustificano la costruzione.
Questo lavoro di tesi, in particolare, è stato svolto nell'ambito dell'esperimento MICE (Muon Ionization Cooling Experiment) il cui principale obiettivo è la dimostrazione sperimentale della tecnica di ionization cooling applicata ad un fascio di muoni (dal cui decadimento vengono prodotti i $\nu$).
La tecnica di ionization cooling (presentata nel Capitolo 2) è stata proposta negli anni '70 ma non è mai stata dimostrata sperimentalmente: l'idea di base è quella di sfruttare la perdita di energia per ionizzazione in un assorbitore leggero (tipicamente idrogeno o elio liquidi) e successivamente riaccelerare le particelle utilizzando cavità a radio frequenza. In particolare, questa tecnica risulta fondamentale nel caso in cui il fascio di neutrini venga prodotto da un fascio di muoni (come nella maggior parte delle soluzioni proposte per una Neutrino Factory); la vita media di soli 2.2 $\mu$s dei muoni rende infatti impossibile l'impiego di altre tecniche di cooling (quali l'electron cooling o lo stochastic cooling).
La sezione di cooling di MICE è in fase di costruzione presso il Rutherford Appleton Laboratory (RAL) in Inghilterra e necessita di rivelatori ad alta precisione per la misura dell'efficienza di cooling in termini di emittanza (definita come il volume occupato dal fascio di particelle nello spazio delle fasi), con una precisione dello 0.1%, e di un sistema in grado di distinguere i muoni dal fondo, che in MICE è rappresentato da pioni (da cui i muoni vengono prodotti) ed elettroni (derivanti dal decadimento dei muoni stessi). Rivelatori basati su sistemi di Time Of Flight e luce Cherenkov permettono l'identificazione dei pioni all'inizio della sezione di cooling mentre la distinzione degli elettroni alla fine del canale è fornita da un apposito calorimetro costituito da un preshower di piombo e fibre scintillanti seguito da un rivelatore realizzato con materiale scintillante, l'Electron Muon Ranger (EMR). Lo sviluppo, la costruzione e i test di EMR rappresentano il fulcro di questo lavoro di tesi.
EMR (Capitolo 3) è costituito da 48 piani di barre estruse di scintillatore plastico; ogni piano è formato da 59 barre di 1.1 m a sezione triangolare lette da una fibra Wave Length Shifter (WLS) connessa da entrambi i lati a sistemi di fotomoltiplicatori, sia a singolo canale (PMT) che multianodo (MAPMT). I segnali dei MAPMT sono amplificati da una scheda di frontend dedicata (*FrontEnd Board - FEB*) basata sull'ASIC MAROC (Laboratoire de L'Acelerateur Lineaire di Orsay), campionati e storati da una *Buffer Board* per essere inviati al sistema di readout VME nell'intervallo tra due bunch di particelle.
Per definire il design finale del detector e studiarne le performance in termini di risoluzione spaziale ed efficienza è stato realizzato un prototipo di piccole dimensioni costituito da barre lunghe 19 cm a sezione rettangolare. Tale prototipo è stato testato sia con fasci estratti di particelle cariche sia con raggi cosmici utilizzando tre diverse catene di lettura: due basate sulla coppia di ASIC VLSI VA64TAP2.1+LS64_2 ed una (quella finale) sul MAROC. In particolare, dal mo-

mento che la struttura temporale del fascio a RAL (un evento ogni 5 $\mu$s in una spill di 1 ms ogni secondo) impone che le schede operino in modalità di lettura digitale, lo studio del comportamento del rumore e l'ottimizzazione dell'elettronica stessa sono stati fondamentali per definire il design del detector finale.
In parallelo all'elettronica, sono state testate diverse configurazioni di lettura delle barre (in termini di numero di fibre WLS per barra e utilizzo o meno della colla) e diverse forme delle barre stesse.
Il Capitolo 4 contiene tutti i risultati ottenuti durante le fasi di test con il prototipo e le diverse barre presso il Proton Synchrotron del CERN e l'Università dell'Insubria.
La risoluzione spaziale misurata per ciascuno dei piani del prototipo di EMR è stata di $\sim 6.5$ mm mentre un valore di quasi il 99% è stato ottenuto per l'efficienza tenendo conto della presenza di zone morte tra barre contigue (escluse nel calcolo dell'efficienza stessa) e perfezionando il metodo di ricostruzione delle tracce. Uno scan in momento (nel range $2-15$ GeV/c) ha permesso di stimare la dimensione di tali zone morte che è risultata pari a $\sim 0.5$ mm (come ci si aspettava dalla forma non perfettamente regolare delle barre stesse).
Nei test sulle varie configurazioni di readout, i risultati migliori (in termini di efficienza e ampiezza del segnale) sono stati ottenuti utilizzando 2 fibre WLS incollate all'interno di ogni barra rettangolare. Tuttavia, nel design finale verrà utilizzata una singola fibra incollata all'interno della barra in modo da limitare contemporaneamente il cross talk tra canali del MAPMT e i costi di produzione. I test sulle barre triangolari hanno infine dimostrato come, grazie alla loro forma, sia possibile ridurre le zone di bassa efficienza tra barre vicine e garantire un'efficienza sufficientemente elevata ($\sim 97\%$) e costante.
EMR è ora in fase di costruzione presso l'Università di Ginevra: test con raggi cosmici di due layer assemblati ed equipaggiati con un prototipo dell'elettronica di readout finale sono stati eseguiti fin dall'inizio dell'anno. I risultati ottenuti in termini di efficienza e risoluzione spaziale sono presentati nel Capitolo 5 insieme ad uno studio dettagliato del noise e dell'effetto di cross talk. L'installazione del detector finale a RAL è prevista per la primavera del 2011.
La Collaborazione MICE (insieme alla Neutrino Factory and Muon Collider Collaboration) si occupa anche della ricerca e sviluppo dei detector per le future Neutrino Factory, sia quelli a corta baseline (*near detector*) sia quelli a lunga baseline (*far detector*). In particolare la costruzione di EMR ha permesso di muovere i primi passi verso la realizzazione dei *Totally Active Scintillator Detectors*, rivelatori di enormi dimensioni costituiti interamente da materiale attivo il cui design (piani x-y di barre triangolari lunghe fino a 15 m) è molto simile a quello di EMR.

# Introduction

The physics of neutrino covers a fundamental role in modern physics and, in particular, it represents the first experimental evidence for new physics beyond the Standard Model.
Since 1930, when Wolfgang Pauli first postulated the existence of a third particle involved in the β-decay process to explain the observed continuous energy spectrum (by Lise Meitner and Otto Hahn at the University of Berlin), neutrino physics has required a worldwide effort both in the development of new techniques and in the construction of dedicated detectors to investigate and study the nature of such a new particle.
The first neutrino events were observed in 1956 at the Savannah River nuclear reactor by Clyde L. Cowan and Frederick Reines exploiting two tanks filled with water and cadmium clorine ($H_2O$ + $CdCl_2$) surrounded by liquid scintillator detectors readout by photomultiplier tubes. This historical result opened the way to the unexplored field of neutrino physics starting the so-called *discovery era*.
Since neutrinos interact very weakly with matter, their observation has required the construction of huge detectors located deep underground to avoid cosmic ray background. From the instrumentation point of view, different techniques took the stage. As far as the solar neutrino observations is concerned, the so-called *old generation experiments* were based on a radiochemical method: the neutrino capture via the electroweak interaction in a target and the subsequent transmutation of the target itself into another chemical element (typically $^{37}Cl \rightarrow ^{37}Ar$ or $^{71}Ga \rightarrow ^{71}Ge$) was the main studied process to observe neutrino events (Homestake, GALLEX, GNO, SAGE). On the other hand, the so-called *new generation experiments* were based on a completely different technique that also provided real time neutrino flux measurements: the interaction of neutrinos with the detector material (typically water or heavy water) causes the emission of electrons and the produced Cherenkov light is subsequently detected by large photomultipliers (Kamiokande, SuperKamiokande, SNO).
The events from atmospheric neutrinos were instead studied observing the charge current events inside the detector while the main techniques used to study the neutrino events from artificial man-made beams are the inverse β-decay process and

the so-called *appearance* and *disappearance* experiments (NOνA, MINOS).
Thanks to these experiments, a lot of details about the neutrino nature and its behavior in the interaction with matter were collected: for example, the oscillation phenomenon, proposed by Bruno Pontecorvo (1957) and subsequently evolved by Ziro Maki, Masami Nakagawa and Shoichi Sakata (1962), has been observed by all these experiments.
Nowadays neutrino physics still remains an open field since the question of such a small mass together with other unsolved aspects (the mass hierarchy, the role of neutrinos in cosmology, the number of generations, etc.) are not yet answered. This motivates a worldwide effort aimed at the development of new facilities (*Neutrino Factory*) and experimental techniques (*ionization cooling*) to produce a larger number of well-known neutrinos from muon decay (simplifying the detector system) to deeply investigate the oscillation phenomenon and its main parameters.
This thesis work has been performed in the framework of the International Muon Ionization Cooling Experiment (MICE) and, in particular, deals with the Electron Muon Ranger detector.
The two main goals of the MICE Collaboration are the demonstration of the ionization cooling technique, developing and building an adequate cooling section for a muon beam, and the measurement of such a cooling channel performances. The MICE cooling channel is under construction at the Rutherford Appleton Laboratory (RAL, UK) and requires several high precision detectors to evaluate the cooling efficiency in terms of emittance reduction. Moreover, an efficient system to reject background (that in MICE means pions and electrons) is needed to obtain an emittance measurement with a 0.1% precision. The pions are rejected at the beginning of the channel by a set of TOF and Cherenkov detectors while a dedicated calorimeter station provides the downstream electron separation. The calorimeter consists of a lead-fiber layer followed by a fully active scintillator detector, the Electron Muon Ranger (EMR).
From the point of view of the thesis organization, a brief historical and theoretical introduction to the main aspects of neutrino physics is presented in Chapter 1: the oscillation phenomenon and the mechanism that generates such a light neutrino mass are described together with the more recent results. Chapter 1 also contains an introduction to the proposed scenario of a Neutrino Factory complex, with its basic elements and physical motivations.
The first part of Chapter 2 is dedicated to the description of the working principle of the ionization cooling technique. The ionization cooling of a muon beam has been proposed in the '70s but has never been demonstrated in practice: it is based on the passage of the particles through a series of light absorbers and the subsequent re-acceleration of the beam through Radio Frequency (RF) cavities. The second part of Chapter 2 describes the MICE cooling channel and the detectors

needed for the tracking and the emittance measurements.
Chapter 3 is devoted to the Electron Muon Ranger, to its small scale prototype and to the components tested to finalize the readout configuration of the detector. EMR consists of 48 layers of extruded scintillator bars; each layer is made of 59 bars with a triangular shape and 1.1 m long, readout by Wave Length Shifter (WLS) fibers and photomultipliers (both single channel and multianode).
To validate the EMR design and the detector performances, a small size prototype with rectangular shape bars has been developed and tested with three different electronics chains with extracted particle beams (at the CERN Proton Synchrotron) and cosmic rays while different setups with long rectangular and triangular bars have been assembled to study different readout configurations and their efficiency.
A detailed description of the EMR prototype and of the setups assembled for the validation tests is presented in Chapter 3.
Chapter 4 and Chapter 5 are the heart of this thesis work. The results obtained with the EMR prototype with the different electronics chains are described in Chapter 4 in terms of noise, spatial resolution and efficiency, together with the component tests.
The final EMR detector is now under construction at the University of Geneva: cosmic ray tests of two layers equipped with a prototype version of the readout electronics have been performed since the beginning of the year. The results in terms of noise, spatial resolution and efficiency, together with a detailed analysis of the cross talk, are presented in Chapter 5. The final electronics has been installed on the two layers at the beginning of May 2010 and the data analysis in ongoing.

# Chapter 1

# Neutrino: why a factory

The first important event in the history of neutrino can be identified with Lise Meitner and Otto Hahn's discovery, in 1911, of the continuous $\beta$ energy spectrum, which was in contradiction with the energy conservation law because it appeared that some energy was lost in the decay process. A few years later, in 1914, James Chadwick confirmed this observation [1, 2] but it was Wolfgang Pauli, in 1930 [3], that postulated the existence of a new particle to solve the dilemma of the $\beta$ decay. He assumed that in such a decay a neutrino is emitted together with an electron and this causes the continuum energy spectrum of the electron while conserving both energy and angular momentum. The experimental observation by Clyde L. Cowan and Frederick Reines (in 1953 [4, 5]) of neutrinos produced at the Savannah River nuclear reactor (by observing the $\overline{\nu} + p \rightarrow e^+ + n$ process) confirmed Pauli's theory and opened the way to an unexplored field of particle physics.
The following decades represented the era of the neutrino research: in 1968 John Bahcall and Ray Davis showed for the first time a deficit in the solar neutrino flux measurement [6]; in 1987 neutrinos coming from the Large Magellanic Cloud were first observed [7]; in 1998 the SuperKamiokande Experiment reported the first evidence of neutrino oscillation [8]; in 2002 the Sudbury Neutrino Observatory finally solved the Solar Neutrino Puzzle [9] while the KAMLAND reactor confirmed the oscillation hypothesis [10]; in May 2010 the observation of the tau lepton by the OPERA experiment [11] represented the first direct measurement of the $\nu_\mu \rightarrow \nu_\tau$ oscillation.
Nowadays there are several neutrino physics puzzles still to be solved both on the theoretical and phenomenological point of view. Massive neutrinos have to be included in the Standard Model, the question of such a small mass and several other unsolved aspects (the mass hierarchy, the role of neutrinos in cosmology, the number of generations) need to be answered. For these reasons, together with the fact that the oscillation phenomenon represents the first evidence of physics

beyond the Standard Model, neutrino physics is still an open field.
The first part of this chapter is dedicated to a brief review of the state of the art of neutrino physics and of its bases. The historical results of the main neutrino experiments will be presented (for a complete review see [12]).
The second part of this chapter contains the description of a Neutrino Factory based on a muon storage ring and of its physics potentials. This concept was first suggested by Dmitrij Koshkarev [13] and subsequently expanded by Davis Neuffer [14] and Robert Palmer [15, 16], whose work led to the formation of the Neutrino Factory and Muon Collider Collaboration (NF-MCC[1]) in 1995. Physics at a Neutrino Factory will be very rich: high precision measurements of all the fundamental parameters of the neutrino mixing and oscillation phenomena will be possible. This facility will also offer the possibility of both QCD and slow muon physics studies [17] and represents the first step towards the construction of high energy Muon Colliders. The basic elements to build such a Neutrino Factory and its main motivations will be discussed.

## 1.1 The state of the art of Neutrino Physics

Neutrinos are 1/2-spin electrically neutral particles with a light mass ($\sim$ 500000 times smaller than the electron mass [18]) and are the most abundant particles in the universe. The three known neutrino types, or *flavors*, ($\nu_e$, $\nu_\mu$ and $\nu_\tau$) interact weakly with matter via the weak bosons. They are originated through different processes, both natural and artificial.
The strongest neutrino source is the Sun: the fusion reaction in which hydrogen is transformed into helium ($^2$H$\rightarrow^4$He) produces $\sim 2\times10^{39}$ electron neutrinos per second that corresponds to a $6\times10^{10}$ $\nu$ cm$^{-2}$s$^{-1}$ flux at the Earth surface [19]. A huge amount of neutrinos (up to $\sim 10^{58}$ neutrinos in a few seconds) are also produced in the Supernovae explosion [7] while relic neutrinos (the so-called *Cosmic neutrino Background - C$\nu$B* [20]) permeate the Universe with a density of $\sim 100$ $\nu$ cm$^{-3}$.
Also the Earth is a source of neutrinos both in the atmosphere and crust. The hadronic showers induced by the interaction of cosmic rays with the high layer of the atmosphere generate a typical flux of $\sim 1$ $\nu$ cm$^{-2}$s$^{-1}$ at the Earth surface [21] while *geoneutrinos* are produced through the $\beta$-decay process of radioactive nuclei (tipically $^{238}$U, $^{232}$Th and $^{40}$K) with a flux of $\sim 10^7$ $\nu$ cm$^{-2}$s$^{-1}$ [22].
Neutrinos can also be produced by artificial man-made sources: electron antineutrinos are generated with a tipical flux of the order of $10^{20}$ $\nu$ per second in nuclear reactors [23] while fluxes up to $10^5$ $\nu$ cm$^{-2}$s$^{-1}$ of $\nu_\mu$ can be achieved with con-

[1] http://www.cap.bnl.gov/mumu

ventional accelerated beams by the interaction of a proton beam with a target and the subsequent decay of the produced mesons.
Traditionally, Wolfgang Pauli's "letter to the group of radioactives at the regional meeting in Tubingen", dated December 4th 1930 [3][2], is considered as the neutrino birthday. But the history of neutrino was effectively born with the continuous β-decay spectrum observation by Lise Meitner and Otto Hahn in 1911 which was really surprising since, by kinematic arguments (the momentum conservation in the centre of mass), this process was expected to be a two-body decay (top left of figure 1.1) in which a discrete energy spectrum should be produced (red line in the bottom of figure 1.1). In 1914, James Chadwick confirmed Meitner and Hahn's hypothesis [1, 2] and this observation resulted in serious difficulties in the interpretation of the β-decay process.

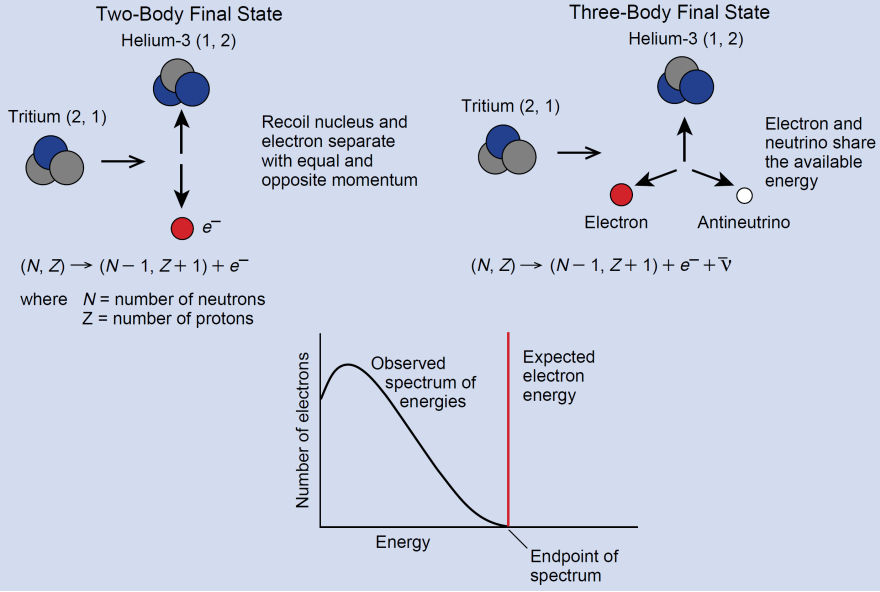


Figure 1.1: Two possible schematic explanations of the β-decay process (top) and the corresponding spectra (bottom). In the *two body final state* process the emerging particles must have the same amount of energy; in particular the conservation of energy and momentum implies that the electron is emitted with a constant energy (red line in the bottom figure). The *three body final state* solution proposed by Pauli foresees that the overall energy is shared between the nucleus, the electron and a new type of particle very difficult to detect: this leads to the continuous spectrum shown with the black line in the bottom figure.

When Pauli, in 1930, realized that the β-decay continuous spectrum (black line in

[2] An english version of Pauli's letter could be found in [24].

the bottom of figure 1.1) could be explained introducing a neutral unobserved 1/2-spin particle (top right of figure 1.1) and two years later Chadwick discovered the neutron [25], the controversy about the β-decay spectrum seemed solved. However, Pauli's particle was also massless, or at least much lighter than the electron, and neutrons could not satisfy this hypothesis. On the other hand, already in 1933, Enrico Fermi published the first account of his theory on β-decay that culminated in his famous weak interaction theory in 1934 [26].

The following two decades have been characterized by a continuous effort to prove the existence of the neutrino and to determine its physical properties. In 1956, Clyde L. Cowans and Frederick Reines saw the first neutrino event by detecting the inverse β-decay process (figure 1.2(a)) at the Savannah River reactor [4, 5] (figure 1.2(b)): Pauli's hypothesis was completely confirmed.

A few years later, Maurice Goldhaber showed that neutrinos involved in the weak interaction are left-handed particles [27], while in 1962 the first evidence of the existence of different neutrino generations came from the $\nu_\mu$ observation at Brookhaven [28]; the third neutrino flavor was discovered later in 2001 at FNAL by the DONuT Experiment [29]. The evidence of different neutrino generations also increased the credibility of neutrino mixing and oscillation, first proposed by Bruno Pontecorvo [30] (for a detailed review see [31]) in 1957 using the same formalism as for kaons, and subsequently evolved by Ziro Maki, Masami Nakagawa and Shoichi Sakata in 1962 [32].

The *discovery era* of neutrino physics begins in 1968 when John Bahcall and Ray Davis first showed a non-negligible deficit in the solar neutrino flux measurement with a detector based on Chlorine in an underground laboratory in the Homestake mine in the USA [6]. The neutrino mixing and oscillation theory was suggested to be a possible solution to the so-called *Solar Neutrino Puzzle - SNP* [12].

The following twenty years were dedicated to the development of detectors and technologies able to study and precisely measure the solar neutrino flux in order to confirm or confute Davis and Bahcall's observation. Since the neutrino cross section is very small ($< 10^{-37}$ cm$^2$ [33]), the detectors were huge, containing several thousands of tons of material, and located deep underground to maximize the cosmic ray rejection: all the main solar neutrino experiments[3] (Homestake [34], SAGE [35] and GALLEX [36]) confirmed the solar neutrino flux deficit observed by Davis and Bahcall. It was only in 2002 that the SNP was solved by the Sudbury Neutrino Observatory (SNO) experiment [9]: it was the first solar model independent test of the solar neutrino oscillations. An innovative method, ever used be-

[3] The so-called *old generation experiments* (Homestake, GALLEX, SAGE and others) were based on a radiochemical method [33]. The signature of the interaction of neutrinos with a target was given by the transmutation process of the target itself into another chemical element (typically $^{37}$Cl$\rightarrow^{37}$Ar or $^{71}$Ga$\rightarrow^{71}$Ge). They were able to explore the first part of the solar spectrum (up to 0.8 MeV) but could not provide a real time measurement.

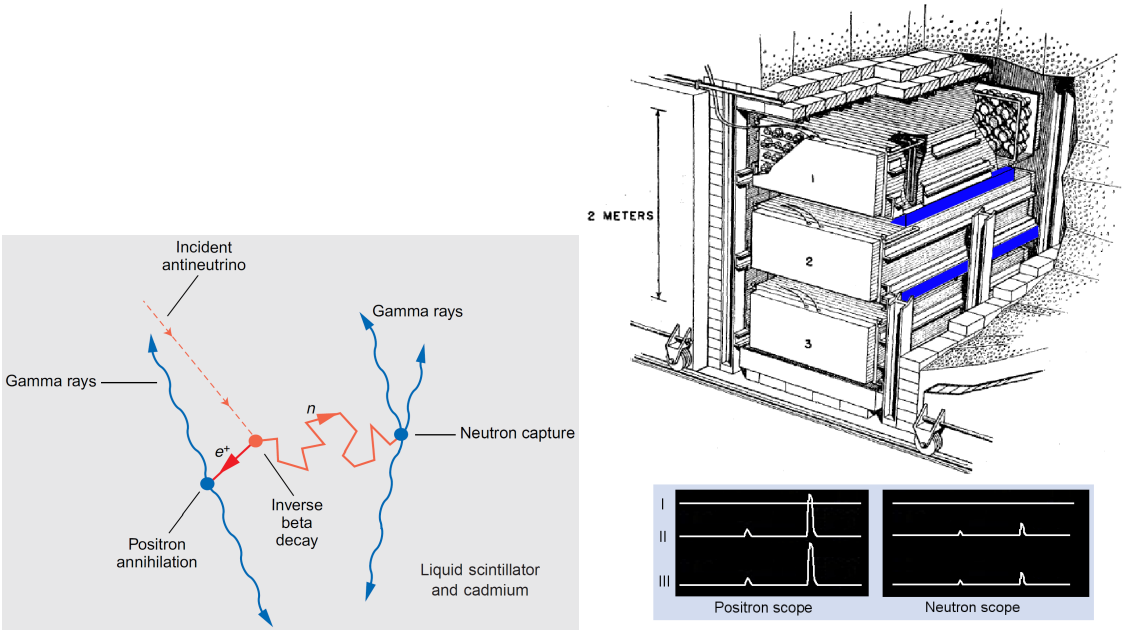


(a) (b)

Figure 1.2: (a) Signature of the inverse β-decay reaction taking place in a liquid scintillator and cadmium based detector: an incident antineutrino (red dashed line) interacts with a proton creating a positron and a neutron. The positron annihilates almost immediately with an electron producing two back to back gamma rays and causing an intense flash of visible light in the scintillator. The neutron instead travels randomly until it is captured by a cadmium nucleus and the subsequent retarded gamma emission causes a second less intense light flash. The two slightly separated signals on the photomultipliers represent the signature of the inverse β-decay process. (b) Schematic layout of the detector used by Cowans and Reines to detect the neutrino at the Savannah River reactor [5] (top): it consisted of two large plastic tanks (in light blue) filled with 200 l of water mixed with $CdCl_2$ and sandwiched between three 1400 l liquid scintillator detectors (named 1, 2 and 3); the light was measured by 110 $5''$ photomultiplier tubes. The first neutrino event was observed with an oscilloscope (bottom): the three lines in each figure represent the three signals of each detector. Two signals separated by $\sim 15.3\ \mu$s gave the signature of the process presented in figure 1.2(a) and confirmed the existence of a new type of particle involved in the β-decay process.

fore, based on a real time Cherenkov detector exploiting $D_2O$ water imaging was able to detect three different processes at the same time (Neutral Current (NC), Charged Current (CC) and Elastic Scattering (ES)) and allowed the measurement of the total flux of the non-electron flavor active neutrinos. The historical result also known as *Bahcall's glory* [9], finally confirmed the mixing hypothesis as the solution of the SNP.
At the same time, the neutrino oscillation has also been observed in the atmospheric neutrino field: an upward-downward $\nu_\mu$ asimmetry was observed without a corresponding deficit in $\nu_e$. This means that the ratio between the $\nu_\mu/\nu_e$ flux ratio observed by SuperKamiokande and the one expected from the Monte Carlo simulation (that is $\frac{(\nu_\mu/\nu_e)_{obs}}{(\nu_\mu/\nu_e)_{MC}}$) was not 1 and the oscillation among the muon neutrinos and the tau ones was proposed as a possible explanation of this deficit [8].
Other experiments dedicated to the determination of the oscillation parameters have been built in the following years, also exploiting nuclear reactor neutrino beams. The KAMLAND experiment provided several confirmations of both the solar and atmospheric neutrino oscillation results [10] and opened the way to the study of the $\nu_\tau \rightarrow \nu_e$ mixing [37] (that nowadays still remains the most unexplored branch of the neutrino oscillation phenomenon).
As it will be discussed in detail in the following sections, for three flavour oscillations the six relevant parameters are three mixing angles ($\theta_{12}$, $\theta_{13}$ and $\theta_{23}$), a CP violating phase $\delta$ and two mass-squared differences $\Delta m^2_{12}$ and $\Delta m^2_{23}$, where $\Delta m^2_{ij} = m^2_i - m^2_j$ (see also figure 1.3). The oscillation parameters obtained from the two most recent global fits to the world neutrino data [38] are summarized in table 1.1.

## 1.2 Theory & Phenomenology

### 1.2.1 Neutrino mass and the See-Saw mechanism

Although in the Standard Model electroweak theory the neutrino is predicted as a left-handed massless particle [27, 39] and, consequently, no associated mixing could take place, experimental evidence for mass and mixing has been accumulated. Moreover, the existing data demonstrate that massive neutrinos are significantly lighter than their charged lepton counterparts ($m_j < 2.5$ eV at 95% C.L. [18]).
In the Standard Model (SM) field theory the masses of heavy leptons and quarks are determined by the Dirac mass term in the Lagrangian that describes the particle interaction:

$$L_D = -f_q < \phi >_0 \bar{q_L} q_R + h.c. \tag{1.1}$$

| parameter | best fit ($\pm1\sigma$) | $3\sigma$ interval | best fit ($\pm1\sigma$) | $3\sigma$ interval |
|---|---|---|---|---|
| $\Delta^2 m_{12}$ [$10^{-5}$ eV$^2$] | $7.65^{+0.23}_{-0.20}$ | 7.05-8.34 | $7.67^{+0.22}_{-0.21}$ | 7.07-8.34 |
| $\Delta^2 m_{31}$ [$10^{-3}$ eV$^2$] | $\pm2.40^{+0.12}_{-0.11}$ | $\pm$(2.07-2.75) | $-2.39\pm0.12$<br>$+2.49\pm0.12$ | $-$(2.02-2.79)<br>+(2.13-2.88) |
| $\sin^2\theta_{12}$ | $0.304^{+0.022}_{-0.016}$ | 0.25-0.37 | $0.321^{+0.023}_{-0.022}$ | 0.26-0.40 |
| $\sin^2\theta_{23}$ | $0.50^{+0.07}_{-0.06}$ | 0.36-0.67 | $0.47^{+0.07}_{-0.06}$ | 0.33-0.64 |
| $\sin^2\theta_{13}$ | $0.010^{+0.016}_{-0.011}$ | $\leq 0.056$ | $0.003\pm0.015$ | $\leq 0.049$ |

Table 1.1: Present values of the oscillation parameters as obtained from the available data [38].

where $f_q < \phi >_0$ represents the effective quark mass and *h.c.* is the hermitian conjugate. A similar mechanism can be used to extend the SM to include non-zero neutrino masses. By adding a right-handed field $\nu_R$ near the left-handed one $\nu_L$ that couples to the $W$ and $Z$ bosons, the neutrino mass term can be defined in the same way as quark masses are accomodated:

$$L_D = -f_\nu < \phi >_0 \bar{\nu}_L \nu_R + h.c. \tag{1.2}$$

where $f_\nu < \phi >_0$ gives the effective neutrino mass.
It can be shown [40] that massive fermions, including neutrinos, can be described by a two component spinor $\psi = \psi_L + \psi_R$. Since, according to the SM, neutrinos are massless fermions, the so-called *Majorana condition*

$$\psi = \psi^C = C\bar{\psi}^T \tag{1.3}$$

(where $C$ is the charge conjugation matrix and $T$ denotes transposition) is valid. In turns, this implies that the right-handed field is not independent from the left-handed component since $\psi_R = \psi_L^C$.

A *Majorana mass term* thus arises both from the $\psi_L$ and $\psi_R$ component:

$$\begin{aligned} L_{M_L} &= -\frac{m_L}{2}\overline{\nu}_L^C \nu_L + h.c. \\ L_{M_R} &= -\frac{m_R}{2}\overline{\nu}_R^C \nu_R + h.c. \end{aligned} \tag{1.4}$$

Supposing that the neutrino has a Dirac mass ($m_D$), like quarks and charged leptons, and also a right-handed Majorana mass (for electrically neutral neutrinos there is nothing in the SM that prohibits the existence of a right-handed mass term), the total mass term[4] is then

$$\begin{aligned} L_{m_\nu} &= -m_D \overline{\nu}_R \nu_L - \frac{m_R}{2}\overline{\nu}_R^C \nu_R + h.c. \\ &= -\frac{1}{2}[\overline{\nu}_L^C, \overline{\nu}_R] \begin{bmatrix} 0 & m_D \\ m_D & m_R \end{bmatrix} \begin{bmatrix} \nu_L \\ \nu_R^C \end{bmatrix} \end{aligned} \tag{1.6}$$

where the second line derives from the Majorana two-component fermion theory and the matrix

$$M_\nu = \begin{bmatrix} 0 & m_D \\ m_D & m_R \end{bmatrix} \tag{1.7}$$

is known as the *neutrino mass matrix*.
The most popular explanation of the observed light neutrino mass is the *See Saw Mechanism* (SSM) [12, 41]. The diagonalization of the $M_\nu$ matrix yields the eigenvalues

$$\begin{aligned} \lambda_\pm &= \frac{m_R}{2} \pm \sqrt{m_R^2 + 4m_D^2} \\ \Rightarrow \quad \lambda_+ &\approx m_R \\ \lambda_- &\approx -\frac{m_D^2}{m_R^2} \end{aligned} \tag{1.8}$$

where the minus sign is not physically important and can be removed by choosing an appropriate phase, while the approximations derive from the fact that $m_R >>$

[4] More rigorously, one has to consider the existence of both left-handed and right-handed Majorana mass terms that lead to the following expression for the total neutrino mass term:

$$\begin{aligned} L_{m_\nu} &= L_D + L_{M_R} + L_{M_L} = -m_D \overline{\nu}_R \nu_L - \frac{m_R}{2}\overline{\nu}_R^C \nu_R - \frac{m_L}{2}\overline{\nu}_L^C \nu_L + h.c. \\ &= -\frac{1}{2}[\overline{\nu}_L^C, \overline{\nu}_R] \begin{bmatrix} m_L & m_D \\ m_D & m_R \end{bmatrix} \begin{bmatrix} \nu_L \\ \nu_R^C \end{bmatrix} \end{aligned} \tag{1.5}$$

Since in the SSM [12, 41] the Majorana mass matrix is not related to the electroweak mass scale $v = 2^{-1/4} G_F^{-1/2} \approx 250$ GeV (where $G_F$ is the Fermi coupling constant), one can choose $m_R$ much larger than this scale that means one eigenstate has a much larger mass than the others; $m_L$ can be chosen equal to 0.

$m_D$. If the Majorana mass is of the order of the Grand Unified Theory (GUT[5]), e.g. $m_R \sim 10^5$ GeV, assuming the Dirac mass $m_D \approx m_{top} = 174$ GeV, the subsequent light neutrino mass is approximately $3\times10^{-2}$ eV that is in the range of the experimentally predicted neutrino masses.
The SSM thus gives a natural explanation of the lightness of neutrino masses although it expects neutrinos to be Majorana particles[6] which is not yet experimentally confirmed. This motivates the large effort to look for direct measurements of the neutrino mass and, in particular, the search for the neutrinoless double beta decay ($0\beta\beta$ decay [43]).

### 1.2.2 Neutrino mixing

The fact that neutrinos have masses implies that there is a spectrum of neutrino mass eigenstates $\nu_i$, $i = 1,2,3$, each with a mass $m_i$. In turn this means that mixing among the three known neutrino flavours is possible [44]. Mixing means that in the $W^{\pm}$ decays to the particular charged lepton $l_\alpha$ (antilepton $\bar{l}_\alpha$), $\alpha = e,\mu,\tau$, the accompanying neutrino mass eigenstate is not always the *same* $\nu_i$, but can be *any* of the different $\nu_i$s.
In particular, the neutrino mixing is described by the $3\times3$ Pontecorvo-Maki-Nakagawa-Sakata unitary matrix $U_{PMNS}$, which is analogous to the CKM matrix in the quark sector [33, 45]:

$$U_{PMNS} = \begin{pmatrix} c_{12}c_{13} & c_{13}s_{12} & s_{13}e^{-i\delta} \\ -c_{23}s_{12} - s_{13}s_{23}c_{12}e^{i\delta} & c_{12}c_{23} - s_{12}s_{13}s_{23}e^{i\delta} & c_{13}s_{23} \\ s_{12}s_{23} - s_{13}c_{12}c_{23}e^{i\delta} & -s_{23}c_{12} - s_{12}c_{23}s_{13}e^{i\delta} & c_{13}c_{23} \end{pmatrix} K' \tag{1.9}$$

where $c_{ij} = \cos\theta_{ij}$, $s_{ij} = \sin\theta_{ij}$ with $i,j = 1,2,3$ and $K'$ is a diagonal matrix with elements $diag(1, e^{i\phi_1}, e^{i\phi_2})$. The phase factors $\phi_1$ and $\phi_2$ are non-zero only if neutrinos are Majorana particles but do not affect neutrino oscillations since they are situated on the diagonal. The phase factor $\delta$ is non-zero only if the neutrino oscillation violates CP symmetry. The $U_{PMNS}$ matrix thus relates the mass eigenstates ($\nu_1$, $\nu_2$, $\nu_3$) to the light-neutrino flavor eigenstates ($\nu_e$, $\nu_\mu$, $\nu_\tau$).
Using the Dirac formalism, a neutrino of flavor $\alpha$ can be expressed as a superposition of the three mass eigenstastes through the following formula:

$$|\nu_\alpha> = \sum_i U^*_{\alpha i} |\nu_i> \tag{1.10}$$

[5]The Grand Unified Theory predicts that the electromagnetic, weak and strong interactions unite at very large energies [42].

[6]A particle that satisfies the Majorana condition (equation 1.3) is called a *Majorana particle*, that is the particle is its own antiparticle.

On the other hand this relation can be inverted to express each mass eigenstate as a superposition of the flavor ones:

$$|\nu_i >= \sum_{\alpha} U_{\alpha i} |\nu_\alpha > \tag{1.11}$$

Here, $U^*_{\alpha i}$ ($U_{\alpha i}$) corresponds to the $U_{PMNS}$ matrix element and denotes the probability amplitude for the $W^+$ decay to produce the specific combination $l_\alpha + \nu_i$; the fraction of the $\alpha$ flavor in $\nu_i$ is $|U_{\alpha i}|^2$.
The relationship between the weak eigenstates and the mass ones and the mixing angles ($\theta_{12}$, $\theta_{13}$, $\theta_{23}$) that arise from equation 1.9 are presented in figure 1.3.

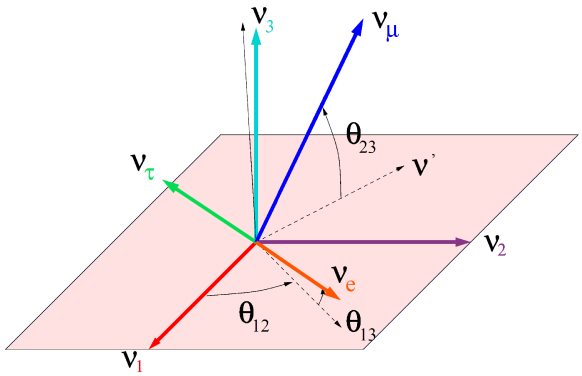


Figure 1.3: Rotation of the neutrino mass eigenstates $\nu_1$, $\nu_2$, $\nu_3$ into the flavour eigenstates $\nu_e$, $\nu_\mu$, $\nu_\tau$ as stated in equation 1.9. The definitions of the Euler angles $\theta_{12}$, $\theta_{13}$, $\theta_{23}$ are also indicated [46].

### 1.2.3 Neutrino oscillation formalism

The following two sections are dedicated to the description of the neutrino oscillation phenomenon both in vacuum and in matter. The neutrino oscillation theory has been first proposed by Pontecorvo [31] (1957) and subsequently evolved by Maki, Nakagawa and Sakata [32] (1962). Although this process is a strictly quantum-mechanical phenomenon, the oscillation probability $P(\nu_\alpha \rightarrow \nu_\beta)$, that indicates the probability of finding a neutrino created in a given flavour state to be in another one, can be derived using an efficient and simple approach that contains all the essential quantum physics (for a complete review see [44]).

#### 1.2.3.1 Neutrino flavor change in vacuum

A typical neutrino flavor change, or *oscillation*, is represented schematically in figure 1.4. A neutrino source produces a neutrino of flavor $\alpha$ together with the

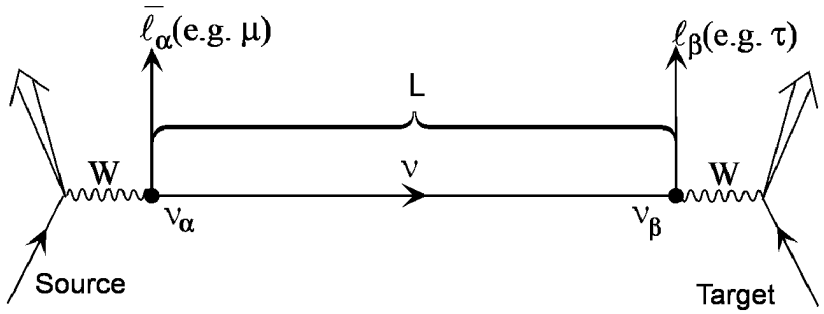


Figure 1.4: Neutrino oscillation scheme: a neutrino of flavor $\alpha$ together with its corresponding charged lepton $\bar{l}_\alpha$ is emitted by a neutrino source and travels for a distance $L$; when it interacts with the detector it produces a second charged lepton $l_\beta$. Hence the $\nu_\alpha$ neutrino has oscillated into the $\nu_\beta$ neutrino while travelling from the source to the detector [44].

corresponding charged antilepton $\bar{l}_\alpha$: thus, at the source level, the neutrino is a $\nu_\alpha$. Let's suppose it travels a distance $L$ to a detector where it interacts with a target and produces a second charged lepton $l_\beta$. Hence, at the time of its interaction in the detector, the neutrino is a $\nu_\beta$. If $\alpha \neq \beta$ (for example, if $l_\alpha$ is a muon and $l_\beta$ is a tau), the neutrino has changed from a $\nu_\alpha$ into a $\nu_\beta$ while travelling from the source to the detector.
Since $\nu_\alpha$ is a coherent superposition of the mass eigenstates $\nu_i$, the contributions of the different $\nu_i$ must be added coherently. The oscillation amplitude of each $\nu_i$ is a product of three factors:

- $U^*_{\alpha i}$, the probability amplitude for the neutrino produced by the source together with a $l_\alpha$ to be a $\nu_i$;

- $Prop(\nu_i)$, the probability amplitude for the produced $\nu_i$ to propagate from the source to the detector;

- $U_{\beta i}$, the probability amplitude for the charged lepton created by the $\nu_i$ interaction in the detector to be a $l_\beta$.

Given the Hamiltonian describing the neutrino-charged lepton-W boson couplings is Hermitian, it follows that if

$$A(W \to \bar{l}_\alpha \nu_i) = U^*_{\alpha i} \tag{1.12}$$

then

$$A(\nu_i \to W l_\beta) = U_{\beta i} \tag{1.13}$$

Thus the final factor in the $\nu_i$ contribution is $U_{\beta i}$ and the transition amplitude connecting states of different flavors after an interval $t$ is

$$A(\nu_\alpha \to \nu_\beta) = < \nu_\beta(t)|\nu_\alpha > = \sum_i U^*_{\alpha i} Prop(\nu_i) U_{\beta i} \tag{1.14}$$

$Prop(\nu_i)$ can be estimated considering the time evolution of the mass eigenstate $\nu_i$ in its rest frame; it obeys the trivial Schrödinger equation:

$$i\frac{\partial}{\partial \tau_i}|\nu_i(\tau_i) > = m_i|\nu_i(\tau_i) > \tag{1.15}$$

where $\tau_i$ is the time and $m_i$ is the mass of the neutrino in the rest frame. The solution of this equation is:

$$|\nu_i(\tau_i) > = \exp[-im_i\tau_i]|\nu_i(0) > \tag{1.16}$$

Thus, the amplitude $< \nu_i(0)|\nu_i(\tau_i) >$ to find the original $\nu_i$ state $|\nu_i(0) >$ in the time evolved state $|\nu_i(\tau_i) >$ corresponds to $Prop(\nu_i)$, with $\tau_i$ the proper time taken by $\nu_i$ to travel from the neutrino source to the detector.
The propagation probability amplitude can be expressed in terms of several variables in the laboratory frame. Two of these are the laboratory frame distance $L$ and the laboratory frame time $t$. The values of $L$ and $t$ are related to the choice of the location of both the source and the detector; thus, $L$ and $t$ are defined by the experiment and are common to all the $\nu_i$ components of the beam. The other two variables are the energy $E_i$ and momentum $p_i$ of the mass eigenstate $\nu_i$ in the laboratory frame. Because of Lorentz invariance, the phase $m_i\tau_i$ in the propagator $Prop(\nu_i)$ is given by:

$$m_i\tau_i = E_i t - p_i L \tag{1.17}$$

Since only the components of a neutrino beam which have the same energy contribute coherently to the neutrino oscillation [47], at the energy $E$ the mass eigenstate $\nu_i$ with a mass $m_i$ has a momentum $p_i$ given by

$$p_i = \sqrt{E^2 - m_i^2} \approx E - \frac{m_i^2}{2E} \tag{1.18}$$

where the last approximation follows from the extreme lightness of neutrinos, meaning $m_i^2 << E^2$ for any relativistic energy. The phase in the propagation amplitude can be rewritten as

$$\begin{aligned} m_i\tau_i &= E(t-L) + \frac{m_i^2}{2E}L \\ m_i\tau_i &\approx \frac{m_i^2}{2E}L \end{aligned} \tag{1.19}$$

where the second expression is given by the fact that the phase $E(t-L)$ is irrelevant since it is common to all the interfering mass eigenstates. The final expression for $Prop(\nu_i)$ is thus:

$$Prop(\nu_i) = \exp[-im_i^2 \frac{L}{2E}] \tag{1.20}$$

Using this result, it follows from equation 1.14 that the probability amplitude for a neutrino of energy $E$ to change from a $\nu_\alpha$ into a $\nu_\beta$ flavour while travelling a distance $L$ in vacuum is given by

$$A(\nu_\alpha \to \nu_\beta) = \sum_i U^*_{\alpha i} \exp[-im_i^2 \frac{L}{2E}] U_{\beta i} \tag{1.21}$$

where the sum runs over all the light mass eigenstates. Squaring it and using the unitarity of the mixing matrix $U_{PMNS}$, it follows that the oscillation probability $P(\nu_\alpha \to \nu_\beta)$ for neutrinos, or equivalently $P(\bar{\nu}_\alpha \to \bar{\nu}_\beta)$ for antineutrinos, assuming that the CPT invariance is valid[7]

$$P(\bar{\nu}_\alpha \to \bar{\nu}_\beta) = P(\nu_\beta \to \nu_\alpha) \tag{1.22}$$

is given by

$$\begin{aligned} P(\overset{(-)}{\nu}_\alpha \to \overset{(-)}{\nu}_\beta) &= |A(\overset{(-)}{\nu}_\alpha \to \overset{(-)}{\nu}_\beta)|^2 \\ &= \delta_{\alpha\beta} - 4 \sum_{i>j=1} \Re(U^*_{\alpha i} U_{\beta i} U_{\alpha j} U^*_{\beta j}) \sin^2 \left( \Delta m^2_{ij} \frac{L}{4E} \right) \\ &\underset{(-)}{+} 2 \sum_{i>j=1} \Im(U^*_{\alpha i} U_{\beta i} U_{\alpha j} U^*_{\beta j}) \sin \left( \Delta m^2_{ij} \frac{L}{2E} \right) \end{aligned} \tag{1.23}$$

where

$$\Delta m^2_{ij} = m^2_i - m^2_j \tag{1.24}$$

This expression is valid for an arbitrary number of neutrino mass eigenstates and holds whether $\beta$ is different from $\alpha$ or not.
Several features of neutrino oscillations arise from the oscillation probability formula:

- if neutrinos are massless, i.e. $\Delta m^2_{ij} = 0$, equation 1.23 becomes $P(\nu_\alpha \to \nu_\beta) = \delta_{\alpha\beta}$. Hence, the observation that neutrinos can change flavor implies neutrino masses to be non-degenerate, and in particular non-zero. Indeed, it was this observation that led to the conclusion that neutrinos have non-zero masses [44];

[7] From equation 1.23 it follows that if the mixing matrix $U_{PMNS}$ is complex, $P(\bar{\nu}_\alpha \to \bar{\nu}_\beta)$ and $P(\nu_\beta \to \nu_\alpha)$ will be typically different. Given $\bar{\nu}_\alpha \to \bar{\nu}_\beta$ is the CP-mirror image of $\nu_\beta \to \nu_\alpha$, $P(\bar{\nu}_\alpha \to \bar{\nu}_\beta) \neq P(\nu_\beta \to \nu_\alpha)$ would indicate a CP violation [44].

- the flavor-change probability depends on the quantity $L/E$. Apart from a constant, it indicates the proper time that elapses in the neutrino rest frame while a neutrino of energy $E$ travels a distance $L$: the flavor change appears as an evolution of the neutrino itself over time [44]. Depending on the choice of $L$ (known as *baseline* [12] and indicating the distance from the neutrino source and the detector, experiments can be classified in Short BaseLine (SBL) and Long BaseLine (LBL); typically in a SBL experiment $L/E$ is of the order of $10^2-10^3$ while this value grows up to $10^4-10^6$ for the LBL ones [12] (see also the values listed in table 1.2);

- neutrino mixing appears as a direct consequence that neutrino flavors can oscillate. Suppose there is no leptonic mixing; this means that in the $W^+$ decay the particular charged antilepton $\bar{l}_\alpha$ is always accompanied by the *same* neutrino mass eigenstate. In this way, if $U^*_{\alpha i} = 0$ then $U^*_{\alpha j}$ vanishes for all $j \neq i$ and $P(\nu_\alpha \to \nu_\beta) = \delta_{\alpha\beta}$;

- there are two main ways to detect neutrino flavor oscillations: *appearance* and *disappearance* experiments [44]. In a beam of neutrinos which are initially all of flavor $\nu_\alpha$, the observation of neutrinos of a new flavor $\nu_\beta$ (*appearance*) or of a $\nu_\alpha$ flux reduction (*disappearance*) are both possible. Two examples of experiments exploiting these two techniques are the NO$\nu$A experiment [48] and the MINOS one [49] both managed by the Fermi National Accelerator Laboratory (FNAL) in the USA. Figure 1.5 shows the oscillation probability as a function of the energy in arbitrary units [50]. The signatures for the value of the mixing angle and of the mass splitting in

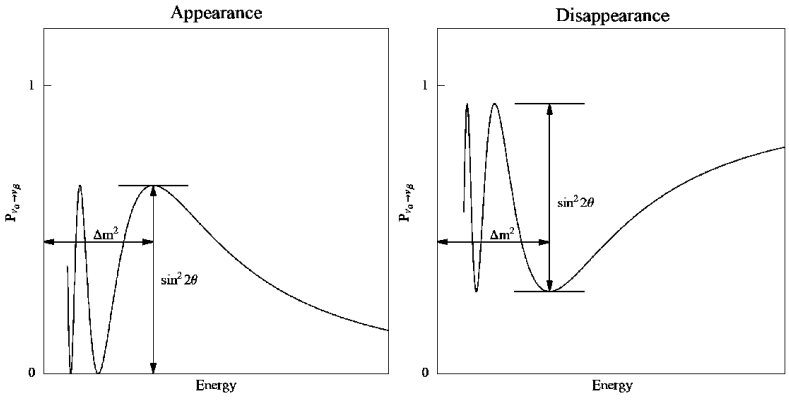


Figure 1.5: The oscillation probability as a function of the energy in arbitrary units for an *appearance* (left) and a *disappearance* (right) experiment [50]. The vertical lines indicate the signature of the mixing angle $\theta$ while the horizontal arrows are the ones for the mass splitting.

an appearance experiment (left) are respectively given by the height and the position of the oscillation peak. The same signatures for a disappearance experiment (right) are identified by the oscillation depth and its position;

- the neutrino oscillation probability depends only on the neutrino squared-mass splittings $\Delta m^2_{ij}$ and not on the individual neutrino masses [44]. Oscillation experiments can thus determine the neutrino squared-mass spectral patterns (figure 1.6), but not how far above zero the entire spectrum lies. Two possibilities for the mass orders are foreseen: the situation where $m_3 > m_2 > m_1$ (left side of figure 1.6) is known as *direct* (or *normal*) *hierarchy* while the *inverse hierarchy* is given by $m_2 > m_1 > m_3$ (right panel in figure 1.6);

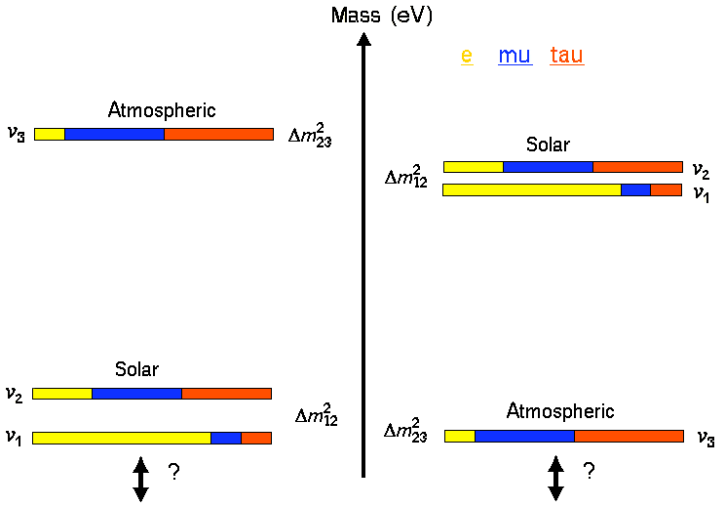


Figure 1.6: Neutrino mass possible spectra allowed by the present data [38]: two different possibilities are foreseen [51]. The one on the left side is known as *direct* (or *normal*) *hierarchy* and the mass ordering is $m_3 > m_2 > m_1$; the one on the right side is known as *inverse hierarchy* and foresees the following mass order: $m_2 > m_1 > m_3$. Moreover, since $m_2 \approx m_1$ leads to $\Delta m^2_{13} \approx \Delta m^2_{23}$, assuming the two-flavor description, the mass-splitting $\Delta m^2_{12}$ well describes the oscillations between the $\nu_1 - \nu_2$ mass eigenstates (and similarly between $\nu_e - \nu_\mu$) while the $\nu_2 - \nu_3$ (and $\nu_\mu - \nu_\tau$) phenomenology is well described by the $\Delta m^2_{23}$ mass splitting. Each mass eigenstate $\nu_i$ in terms of its flavor intensities $\nu_\alpha$ ($\alpha = e, \mu, \tau$) is also shown.

- including the $\hbar$ and $c$ factors, the argument of the sin in equation 1.23 is

given by

$$\Delta m^2_{ij}\frac{L}{4E} \Rightarrow \Delta m^2_{ij}\frac{c^3 L}{4\hbar E} = 1.27\Delta m^2_{ij}[\mathrm{eV}^2]\frac{L[\mathrm{km}]}{E[\mathrm{GeV}]} \tag{1.25}$$

For an experiment with a given $L/E$, the sensitivity to the neutrino mass splittings $\Delta m^2_{ij}$ [eV$^2$] is given by $(L/E)^{-1}$. Thus, an experiment with $L \sim 10^4$ km (approximately the diameter of the Earth) and $E = 1$ GeV is sensitive to $\Delta m^2_{ij}$ down to $\sim 10^{-4}$ eV$^2$ [44]. Table 1.2 gives the values of the baseline and of the corresponding sensitivity for the main types of neutrino oscillation experiments [12];

| source | type | $L$ [m] | $E$ [MeV] | $L/E$ | $\Delta m^2_{ij}$ sensitivity [eV$^2$] |
|---|---|---|---|---|---|
| sun | disapp. | $10^{10}$ | 1 | $10^{10}$ | $10^{-10}$ |
| atmosphere | disapp. | $10^4-10^7$ | $10^2-10^5$ | $10^1-10^4$ | $10^{-1}-10^{-4}$ |
| reactors | disapp. | SBL $10^2-10^3$<br>LBL $10^4-10^5$ | 1<br>1 | $10^2-10^3$<br>$10^4-10^5$ | $10^{-2}-10^{-3}$<br>$10^{-4}-10^{-5}$ |
| accelerators | both | SBL $10^2$<br>LBL $10^5-10^6$ | $10^3-10^4$<br>$10^4$ | $10^1$<br>$10^2-10^3$ | $>0.1$<br>$10^{-2}-10^{-3}$ |

Table 1.2: Typical baseline and sensitivity values for the main neutrino oscillation experiment types [12]: for a given $L/E$ the sensitivity to $\Delta m^2_{ij}$ is given by $(L/E)^{-1}$.

- the neutrino flavor oscillation does not change the total flux in a neutrino beam, but simply redistributes it among the flavors. It follows that

$$\sum_{\beta}(\nu_\alpha \to \nu_\beta) = 1 \tag{1.26}$$

where the sum runs over all the flavors $\beta$ including the original flavor $\alpha$. As a direct consequence, the probability that a neutrino (antineutrino) does not

oscillate into a new flavor is given by

$$P(\overset{(-)}{\nu}_\alpha \rightarrow \overset{(-)}{\nu}_\alpha) = 1 - P(\overset{(-)}{\nu}_\alpha \rightarrow \overset{(-)}{\nu}_\beta) \tag{1.27}$$

Both the results from solar and atmospheric neutrinos have shown that a simplified *two-flavor* approximation can be an accurate description for several sets of data. In this simplest case of two neutrino mixing between $\nu_\alpha$, $\nu_\beta$ and $\nu_1$, $\nu_2$, there is only one squared-mass difference $\Delta m^2 = \Delta m^2_{12} = m^2_2 - m^2_1$ and the mixing matrix can be parametrized in terms of only one mixing angle $\theta$:

$$U = \begin{pmatrix} \cos\theta & \sin\theta \\ -\sin\theta & \cos\theta \end{pmatrix} \tag{1.28}$$

The resulting survival probability of a given flavor can be written as

$$P(\nu_\alpha \rightarrow \nu_\alpha) = 1 - \sin^2 2\theta \sin^2 \left( 1.27 \Delta m^2 [\mathrm{eV}^2] \frac{L[\mathrm{km}]}{E[\mathrm{GeV}]} \right) \tag{1.29}$$

where $\sin^2 2\theta$ is the oscillation amplitude.
This simplified approach also leads to the identification of two separate mass splittings for the solar neutrino field and the atmospheric one. It is possible to find a relationship between $\Delta m^2_{12} = m^2_2 - m^2_1 > 0$ and the solar neutrino oscillations and, in the same way, $\Delta m^2_{23} = m^2_3 - m^2_2 \approx m^2_3 - m^2_1$ dominates for the atmospheric neutrino ones [44].
Given the unitarity, the $U_{PMNS}$ matrix can be parametrized as the product of three rotations between the states connected to three independent mixing angles:

$$U_{PMNS} = \begin{pmatrix} c_{12} & s_{12} & 0 \\ -s_{12} & c_{12} & 0 \\ 0 & 0 & 1 \end{pmatrix} \begin{pmatrix} 1 & 0 & 0 \\ 0 & c_{23} & s_{23} \\ 0 & -s_{23} & c_{23} \end{pmatrix} \times$$

$$\begin{pmatrix} c_{13} & 0 & s_{13} e^{-i\delta} \\ 0 & 1 & 0 \\ -s_{13} e^{-i\delta} & 0 & c_{13} \end{pmatrix} \begin{pmatrix} e^{i\phi_1} & 0 & 0 \\ 0 & e^{i\phi_2} & 0 \\ 0 & 0 & 1 \end{pmatrix} \tag{1.30}$$

Now it becomes clear why the two-flavor approximation is a good description of the available experimental data. The first submatrix describes the solar neutrino oscillations; the second one is related to the atmospheric neutrino phenomenology; the third submatrix is tested by reactors and accelerators neutrino measurements while the last one contains the Majorana phase and is present only if neutrinos are Majorana particles [44].

#### 1.2.3.2 Neutrino flavor change in matter

The formalism for the neutrino oscillation in matter is slightly more complicated. In the following, only the basic ideas to obtain the oscillation probability will be given (a complete discussion of the oscillation phenomenon in matter can be found in [44]).
Considering for simplicity only the two-component approximation, the Hamiltonian in vacuum $H_{vac}$ can be written as:

$$H_{vac} = \frac{\Delta m_V^2}{4E} \begin{pmatrix} -\cos 2\theta_V & \sin 2\theta_V \\ \sin 2\theta_V & \cos 2\theta_V \end{pmatrix} \tag{1.31}$$

where the subscript $_V$ refers to vacuum. The two-flavor oscillation probability is given by

$$P(\nu_e \to \nu_\mu) = \sin^2 2\theta_V \sin^2 \left( \Delta m_V^2 \frac{L}{E} \right) \tag{1.32}$$

When neutrinos cross matter between the source and the target detector, their coherent forward scattering due to particles in matter can significantly modify the oscillation pattern and in particular the mixing angles. This effect is known as the Mikheyev - Smirnov - Wolfenstein (MSW) mechanism [52].
A neutrino can interact with matter in two possible ways. Figure 1.7 shows the Feynman diagrams of a charged (left) and neutral (right) boson exchange of a neutrino interacting with matter. If, and only if, it is a $\nu_e$ it can exchange a $W$ boson with an electron (*charge current*) while, any neutrino flavor in matter can exchange a $Z$ boson with an electron, a proton or a neutron (*neutral current*); the amplitude for this $Z$ exchange is thus flavor independent. Assuming matter is electrically neutral (equal electron and proton densities), the contributions from electrons and protons to the coherent forward scattering via $Z$ exchange can be neglected.

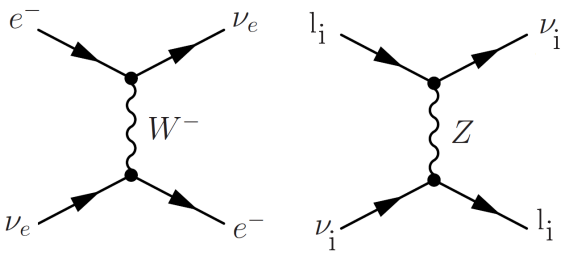


Figure 1.7: Feynman diagrams of charged current (left) and neutral current (right) neutrino interactions with matter.

The $2\times2$ vacuum Hamiltonian $H_{vac}$ is thus replaced by a matrix $H_M$ (where now

the subscript $_M$ refers to matter) in which the contribution to the interaction potential energy caused by the $W$ exchange affects only the electron neutrino element $\nu_e - \nu_e$. On the other side, the same contribution from the $Z$ exchange affects all flavors equally and its contribution to $H_M$ is a multiple of the identity matrix, and consequently can be dropped. Defining

$$\begin{aligned} \Delta m^2_M &= \Delta m^2_V \sqrt{\sin^2 2\theta_V + (\cos 2\theta_V - x)^2} \\ \sin^2 2\theta_M &= \frac{\sin^2 2\theta_V}{\sin^2 2\theta_V + (\cos 2\theta_V - x)^2} \end{aligned} \tag{1.33}$$

where

$$x = \frac{V_W/2}{\Delta m^2_V/4E} = \frac{2\sqrt{2}G_F N_e E}{\Delta m^2_V} \tag{1.34}$$

(here, $V_W$ is the interaction potential energy due to the $W$ exchange, $G_F$ is the Fermi coupling constant and $N_e$ is the number of electrons per unit volume), the mixing matrix for the neutrino in matter is given by

$$H_M = \frac{\Delta m^2_M}{4E} \begin{pmatrix} -\cos 2\theta_M & \sin 2\theta_M \\ \sin 2\theta_M & \cos 2\theta_M \end{pmatrix} \tag{1.35}$$

In other words, the Hamiltonian in matter is identical to its vacuum counterpart and can be obtained from that one by replacing the vacuum parameters $\Delta m^2_V$ and $\theta_V$ with $\Delta m^2_M$ and $\theta_M$ which are respectively defined as the *effective* mass splitting and the *effective* mixing angle in matter [44]. As a result, the oscillation probability is the same given in equation 1.32 but with the mass splitting and the mixing angle replaced by their values in matter. Thanks to the MSW effect, these values can largely differ from those in vacuum [52]: a peculiar example is the one in which $\theta_V$ is very small but since $x = \cos 2\theta_V$, $\sin^2 2\theta_M$ in equation 1.33 is $\sim 1$. Even if in vacuum the mixing angle is very small, the matter effect produces a maximal mixing angle value.

## 1.3 The Neutrino Factory

### 1.3.1 Basic element of the Neutrino Factory design

The overall layouts of a possible Neutrino Factory, as proposed by the International Design Study (IDS [53]) and by the European Centre for Nuclear Research (CERN [54]), are shown in figure 1.8. Such a complex includes both the infrastructures for the production, tuning and acceleration of the muon beams and the near ($\sim$ 4000 km) and far ($\sim$ 7500 km) detectors for the wrong sign muon (*golden*

*channel*) and positive or negative tau (*silver channel*) final states detection[8].
The two proposed facilities share a common basic idea: an intense proton beam, with an energy of hundreds of GeV, impinges on a conversion target where a pion beam is generated. After a strong focusing decay channel, the muons emerge with a large energy spread and occupy a large phase space volume: the ionization cooling of the beam is thus necessary to obtain a sufficiently collimated muon beam. Given that during the cooling the energy loss reduces the muon momentum, a subsequent RF accelerating system is needed to restore the longitudinal momentum and re-accelerate the particles. The acceleration up to the nominal muon energy ($\sim$ 25 GeV in the IDS scheme [53] and about twice in the CERN one [54]) is obtained exploiting a series of Recirculating Linear Accelerators (RLAs [53]). The muons are then injected into a storage ring (a "Race Track" Decay Ring design in the IDS [53] or a triangular shape one in the CERN [54] project) where they circulate until they decay producing two neutrino beams along the straight sections.

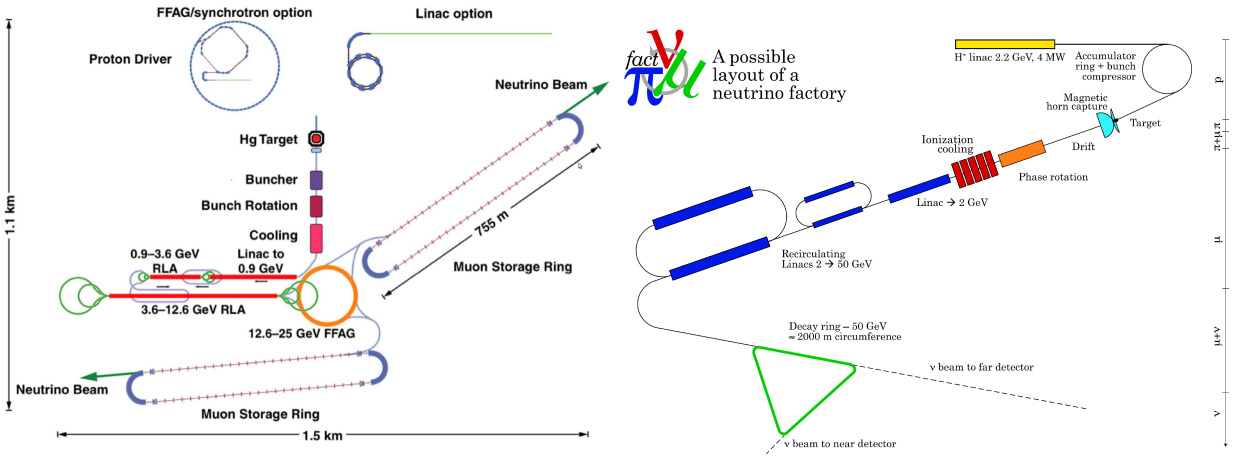


(a) (b)

Figure 1.8: (a) Schematic drawing of the IDS baseline for the Neutrino Factory accelerator complex [53]. (b) Conceptual layout of a possible Neutrino Factory complex at CERN [54]. In both scenarios, a pion beam is produced via the proton conversion in a target and left to decay in a strong focusing channel. The obtained muons then pass through a cooling section to reduce their large emittance while the lost momentum is restored by RF cavities. The final muon beam, well collimated and sufficiently intense, is injected into an accumulator where the neutrinos are produced by the subsequent muons decay.

[8] They denote, respectively, appearance experiments in which $\bar{\nu}_\mu$ are detected as a consequence of the electron and muon flavor oscillation which gives a wrong sign $\mu^+$, and appearance experiments in which $\tau^\pm$ are observed as a consequence of $\bar{\nu}_\mu \to \bar{\nu}_\tau$ or $\nu_e \to \nu_\tau$ oscillation [17, 53].

The main requirements of the proton driver of a Neutrino Factory are to deliver an intensity of $10^{21}$ muon decays/year (and a similar number of muons/year stored in the ring), that means a beam power of the order of 4 MW, and to have a very low particle loss to allow an inexpensive maintenance of the components. Figure 1.9(a) (top) shows the schematic overview of a possible configuration for the pion production as proposed by the NF-MCC [55]. The proton beam impinges on a long transversely thin target, followed by solenoid magnets with RF cavities to compress the bunch energy while increasing the bunch length: in this way the desired phase rotation[9] can be achieved. In such a scheme 0.3 muons per proton with a mean energy of 150 MeV and a 20% energy spread are tipically produced [56].

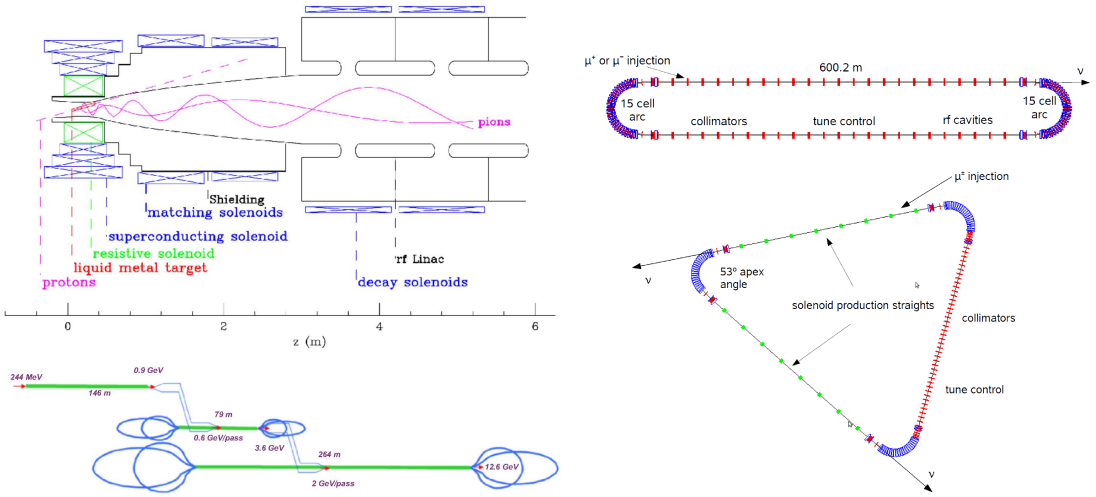


(a) (b)

Figure 1.9: (a) Schematic view of pion production, capture and initial phase rotation as proposed by the NF-MCC [55] (top): a proton beam (dashed violet line) impinges on a target inside a high-field solenoid magnet followed by a decay and phase rotation channel. Sketch of the "Dog Bone" design as proposed by IDS [53] (bottom). (b) A schematic view of two possible muon storage ring designs [57]: "Race Track" design (top) and isosceles triangle (bottom).

Targets of varying composition (C, Al, Cu, Ga, Hg and Pb; $6< Z <82$), radii ($0.2-3$ cm) and thicknesses ($0.5-3$ nuclear interaction lengths) have been tested using a Monte Carlo simulation [55]: high density materials (e.g. Hg, nuclear interaction length $\Lambda = 130$ mm, MERIT experiment at CERN [58]) placed tilted with respect to the field axis allow to maximize the pion production while reduc-

[9]The phase rotation consists in accelerating the lower energy particles and decelerating the higher energy ones to collect as many particles as possible reducing the energy spread [55].

ing the re-absorption in the target[10].
After the cooling (that is discussed in detail in the following chapter), the muons are injected in RLAs to increase the energy: the most popular design is the so-called "Dog Bone" configuration (figure 1.9(a) bottom) in which the muons are accelerated in steps to the nominal energy [53]. The beam is then injected into a storage decay ring (figure 1.9(b)): the three basic elements are straight sections, arcs and matching sections all equipped with both dipole and quadrupole magnets for the beam optics. The rings also house several monitoring detectors for the beam diagnostic.

### 1.3.2 Physics at a Neutrino Factory

The physics program at a Neutrino Factory will be very rich [17]: several measurements in both the neutrino oscillation framework and in the neutrino mixing one (that is the determination of the mixing matrix elements) will be possible with very high precision. The studies of slow muon physics in such a facility will also open the way to lepton collisions at extremely high energies.
The primary goal of a Neutrino Factory is the very high precision measurement of the mixing matrix elements [17]. A muon storage ring providing neutrino beams is the optimal tool for the measurements of the $U_{PMNS}$ elements, basically because it can offer a well defined energy spectrum together with a high purity beam. The flavor composition is in fact well known and the beam is very small and intense. Secondly, the presence of high energy electron neutrinos allows not only the $\nu_e \rightarrow \nu_\mu$ oscillation to be tagged by the so-called *wrong sign muon tag* method, but also to study the $\nu_e \rightarrow \nu_\tau$ channel given the beam energy is above the threshold for the tau lepton production [17].
The second basic goal of a Neutrino Factory is the oscillation parameters measurement with high precision [17, 46]:

- $\Delta m^2_{23}$ and $\theta_{23}$ will be determined with the best precision ever achieved (the present value is shown in table 1.1);
- the small mixing angle $\theta_{13}$ will be measured with a precision better than half a degree;
- the measurement of the sign of the $\Delta m^2_{23}$ mass splitting will be possible thanks to the MSW matter effect on electron neutrinos and to the observation of the resulting asymmetry in the $\bar{\nu}_e \rightarrow \bar{\nu}_\mu / \nu_e \rightarrow \nu_\mu$ ratio.

[10] If the axis of the target coincides with the one of the solenoid field, there is a relatively high probability that pions are lost due to nuclear interactions inside the target. Such a probability can be reduced by tilting the target by 100-150 mrad with respect to the field axis: the overall pion yield is thus increased by 60% [55].

Moreover, since a Neutrino Factory characteristic is to provide very pure $\bar{\nu}_e$ and $\nu_\mu$ beams without $\nu_e$ and $\bar{\nu}_\mu$ contamination [59], the high precision observation of the $\bar{\nu}_e \to \bar{\nu}_\mu / \nu_e \to \nu_\mu$ asymmetry will also allow more precise studies of the leptonic CP violation.
Figure 1.10 shows the predicted ratio $\Re = N(\bar{\nu}_e \to \bar{\nu}_\mu)/N(\nu_e \to \nu_\mu)$ as a function of the baseline [60]. At very short baselines ($L \approx 0$), both CP violation and matter effects are not present: the ratio is 0.5 reflecting the expected symmetry from neutrino and antineutrino cross sections. Increasing the baseline, the ratio $\Re$ becomes larger (smaller) thanks to the matter effect if the sign of the mass splitting is negative (positive). When the baseline is sufficiently long, the matter effect overcomes also the variation of the CP phase $\delta$ (indicated by the light red bands). Thanks to this large separation of the two curves, the high precision measurements of $\Re$ will provide both the sign of $\Delta m^2_{23}$ and the CP phase determination.

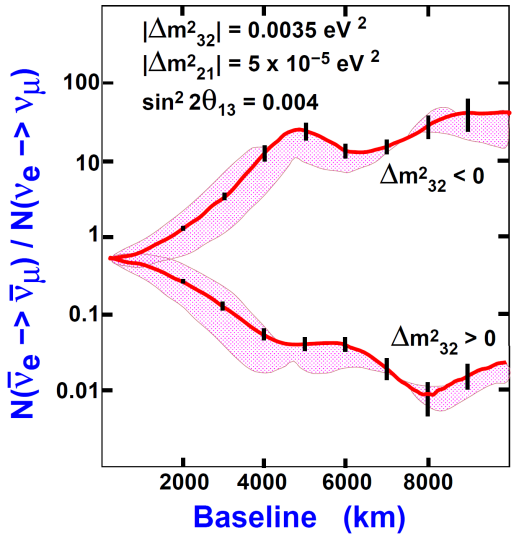


Figure 1.10: Event rate $\Re = N(\bar{\nu}_e \to \bar{\nu}_\mu)/N(\nu_e \to \nu_\mu)$ as a function of the baseline [60]. The two possibilities of positive and negative $\Delta m^2_{23}$ are shown together with the variation of the CP phase (indicated by the light red bands).

The Neutrino Factory physics potential in terms of the $\sin^2 2\theta_{13}$ and $sign(\Delta m^2_{31})$ sensitivities has also been compared with the one of the main future LBL experiments [61]. Table 1.3 summarizes the considered combinations of beams and detectors and their most important parameters. JPARC-SK indicates a combination of the JPARC neutrino beam[11] with the existing SuperKamiokande detector [62], and similarly JPARC-HK with the proposed HyperKamiokande detector [63]; in

[11] Artificial neutrino beam produced at the Japan Proton Accelerator Research Complex (JPARC) from a 50 GeV proton beam accelerator [62].

both cases water Cherenkov detectors are used [61]. NuMI is the proposed combination of the NuMI off-axis beam with a low-Z calorimeter [64]. NuFact-I is an *entry level* Neutrino Factory (without cooling and a modest intensity beam), while NuFact-II is a fully developed facility.

| acronym | detector | baseline [km] | matter density [g·cm$^{-3}$] | $(L/E)_{\text{peak}}$ [km·GeV$^{-1}$] |
|---|---|---|---|---|
| JPARC-SK | water Cherenkov | 295 | 2.8 | 378 |
| NuMI | low-Z calo | 735 | 2.8 | 337 |
| NuFact-I | 10 kt magnetized iron | 3000 | 3.5 | 90 |
| JPARC-HK | water Cherenkov | 735 | 2.8 | 295 |
| NuFact-II | 40 kt magnetized iron | 3000 | 3.5 | 90 |

Table 1.3: The characteristics of the combinations of beams and detectors considered in [61]. See text for details.

The Neutrino Factory superiority in the determination of $\sin^2 2\theta_{13}$ and $sign(\Delta m^2_{31})$ is shown respectively in figure 1.11(a) and 1.11(b). The left end of the bars (blue region) indicates the statistical sensitivity limit; it is reduced if also correlations with other oscillation parameters and degeneracy errors (green and yellow regions) are included. The final achievable sensitivity is given by the mostright edge: in both cases a fully developed Neutrino Factory overcomes the sensitivity of the other experiments up to two orders of magnitude.
Apart from the high precision measurements of the mixing and oscillations parameters, a Neutrino Factory also offers the possibility to study several other physics fields, from the measurements of the QCD parameters to the exploration of the electroweak sector of the Standard Model.
Precise measurements of the Deep Inelastic Scattering (DIS) neutrino physics are very difficult with neutrino beams provided by pion decay, basically because large and dense targets are required causing a not well determined beam spectrum. The narrower and purer beams from a Neutrino Factory will allow to disentangle the different partons structure functions and determine the flavor composition of the nucleon structure; also precise measurements of the strong coupling constant will be possible [17].
The electroweak sector of the Standard Model, in particular the determination of $\sin^2\theta_W$, could be tested from the measurements of both electron and muon neutrino cross sections: the present error[12] of $\sim 0.002$ could be improved by a factor

[12]The most precise present day measurement from neutrinos is the one of the NuTeV Collaboration [65]:

$$\sin^2\theta_W = 0.2309 \pm 0.0019(stat) \pm 0.0024(syst) \tag{1.36}$$

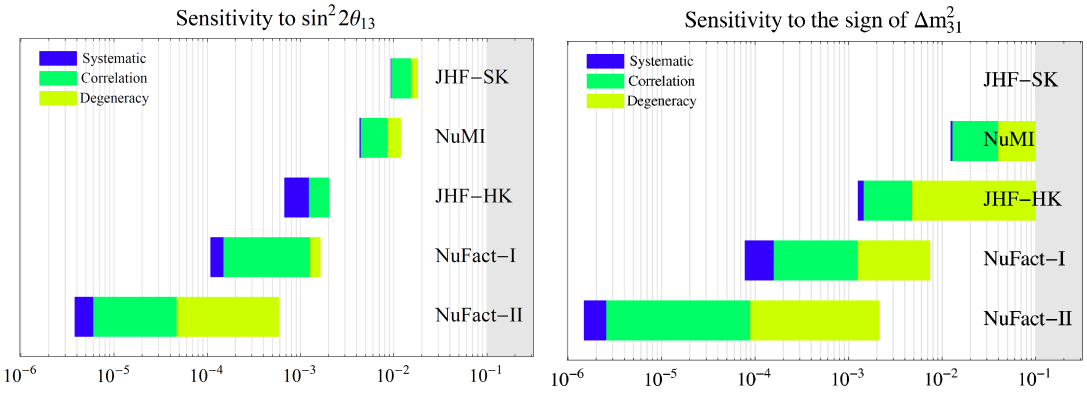


(a) (b)

Figure 1.11: Comparison of the sensitivity to $\sin^2 2\theta_{13}$ (a) and to $sign(\Delta m^2_{31})$ (b) of the main future LBL projects [61]. $10^{19}$ muon decays per year at a muon beam energy of 50 GeV are assumed. In both figures the left edge of the bars is the sensitivity statistical limit. This limit decreases if also systematical, correlational and degeneracy errors are considered. The final achievable sensitivity is given by the mostright edge. The Neutrino Factory performances are about one or two orders of magnitude better than the other projects.

20 at a future Neutrino Factory [17].
Non-neutrino science would also be possible; intense beams of muons with momenta of $\sim$ 100 MeV/c and a variety of time structures can be provided and slow muon physics studies can be performed with sufficiently high statistics. Both muon lifetime high precision measurements and magnetic muon studies will allow many parameters of the SM to be determined with unprecedent precision [17].

# Chapter 2

# The ionization cooling and the MICE experiment

Muon beams of high brilliance and well known flux and purity represent a fundamental milestone towards the construction of a Neutrino Factory based on a muon storage ring [16, 53, 59]. An efficient cooling system is thus necessary to improve the performances of such a Neutrino Factory. However, given the muons are short lived particles (their lifetime is 2.2 $\mu$s at rest [33]), the standard cooling techniques (stochastic, electron and radiation cooling) cannot be implemented, basically because they are too slow. Nevertheless, a thirty year old method, the *ionization cooling technique*, could provide the right phase-space reduction needed for a Neutrino Factory [53].

The principles of ionization cooling are discussed in the first part of this chapter. It has never been demonstrated experimentally and it is based on the passage of particles through a series of absorbers: the muon momentum decreases while the beam size is maintained and the emittance reduced [66]. The energy of the incoming muons is then restored exploiting Radio Frequency (RF) cavities, while the beam focusing is provided with a series of magnetic coils.

The second part of this chapter is dedicated to the description of the Muon Ionization Cooling Experiment (MICE [46]), an international R&D project whose goal is the experimental demonstration of the ionization cooling of muon beams. The engineering, design and construction of a cooling section capable of fulfilling the requirements of a Neutrino Factory and the measurements of such a cooling channel performances are the two main goals of the MICE Collaboration. The second part of the chapter contains also the description of the MICE entire cooling section and of the detectors needed for the tracking and the emittance measurements.

## 2.1 The ionization cooling technique

The cooling of beams of charged particles represents a fundamental step of any particle and nuclear physics experiment [66]. In almost all cases, in fact, it is important to work with monochromatic and well collimated beams. In addition beam cooling allows to accumulate particles, increasing the intensity[1], and suppressing various "warming" diffusion processes such as the Multiple Coulomb scattering. The balance between heating and cooling processes determines the equilibrium "temperatures" and sizes of the beam.
Four main cooling techniques have so far been used (for a detailed description see [66]):

- *radiation cooling*; it is based on the natural process of synchrotron radiation emission of relativistic charged particles moving along a circular trajectory. On average each particle is cooled by a quantity proportional to its own emitted radiation. This method is mostly exploited for cooling and storing of light leptons ($e^{\pm}$) and in electron-positron colliding experiments;

- *electron cooling*; it is typically exploited for the cooling of heavy particle beams. In its simplest form, an intense and well collimated electron beam with the same mean velocity of the heavy particle one is arranged to circulate in parallel with it. The cooling is obtained through the Coulomb collisions between the two beams and continues until the heavy particle beam reaches, in the center of mass system, the same temperature of the electron one;

- *stochastic cooling*; it is based on the use of an active feedback system which interacts with the beam to correct the motion of the particles, e.g. through special plates or magnets that compensate the deviation of each individual particle;

- *ionization cooling*; the passage of charged particles through a series of fairly dense targets causes their energy loss as a result of the interaction of the beam with the electrons of the absorber.

Concerning the cooling of muon beams, in particular, the large mass of this lepton compared to the one of the electron prevents cooling by radiation damping while the short lifetime of the muon doesn't allow the use of both the electron and stochastic cooling methods. On the other side, given the muon interaction length is quite large, the ionization cooling technique can be adopted to cool muon beams.

[1] This is particularly important when very intense secondary beams are required, like in positron and antiproton experiments, and becomes fundamental in colliding beam experiments.

### 2.1.1 The principle of ionization cooling

The energy loss described by the Bethe-Bloch curve [67] is the physical process on which the ionization cooling technique is based. Ionization in the absorbing material decreases the muon momentum (both the transverse and the longitudinal one) not affecting the beam size. Figure 2.1 shows how the angular divergence of the beam can be reduced exploiting the ionization cooling technique.

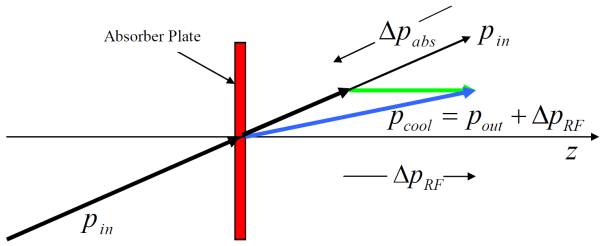


Figure 2.1: Conceptual picture of the principle of ionization cooling [68]. Each particle loses momentum by ionizing an energy absorber and the angular divergence is reduced until limited by the Multiple Coulomb scattering. A low Z target is clearly favoured.

At the same time, the process is complicated by the Multiple Coulomb scattering in the target which increases the beam divergence acting as a source of "heat". The cooling effect thus dominates for low Z materials [66] combined with strong focusing fields. The simplest and most popular solution considered for a Neutrino Factory cooling channel foresees the use of a lithium, beryllium or liquid hydrogen target embedded in a lattice of solenoid magnets [53, 56, 59]: the absorber provides the energy loss while the large aperture solenoids the required focusing. A figure of merit to evaluate the cooling efficiency[2] is represented by the beam *emittance* [46]. It is defined as the volume occupied by the beam in the phase space and, considering a coordinate system where $z$ is directed along the beam axis while $x$ and $y$ are the orthogonal transverse directions, it can be expressed as

$$\varepsilon = \sqrt{D} \tag{2.1}$$

where $D$ is the determinant of the 6-dimensional covariance matrix of the beam particle in the 6D coordinates ($x$, $y$, $t$, $dx/dz$, $dy/dz$ and $cdt/dz$). Taking into account also the natural decrease of the beam size with the acceleration, it is convenient to define the *normalized* emittance by using the coordinates ($x$, $y$, $t$,

[2]The *cooling efficiency* is defined as the number of survived muons exiting the cooling section within the acceptance of the acceleration system with respect to the number of particles entering the cooling channel [16, 46].

$p/mc \cdot dx/dz$, $p/mc \cdot dy/dz$ and $p/m \cdot dt/dz$).
In the two following sections both the transverse and longitudinal emittance behavior is discussed in terms of its dependence on various physical parameters. The transverse emittance is chosen as the one in a 2D plane (e.g. $x$, $dx/dz$) while the longitudinal emittance is defined similarly in the time-energy dimensions ($t$, $cdt/dz$).

### 2.1.2 Transverse emittance cooling

The transverse emittance can be defined statistically as [56]

$$\varepsilon_x^2 = < x^2 >< \theta^2 > - < x\theta >^2 \tag{2.2}$$

where $\theta$ is the angular divergence of the particle trajectory projected onto the $x-z$ plane, and the expectation values are taken over all the particles in the beam. The normalized transverse emittance is thus defined as

$$\varepsilon_{xN} = \beta\gamma\varepsilon_x \tag{2.3}$$

where $\beta$ and $\gamma$ are the usual relativistic particle velocity and energy, respectively[3]. The interesting quantity is the rate of change of the normalized emittance while the beam proceeds through the absorber material. As noted above, a particle experiences both the cooling (due to the decrease of the factor $\beta\gamma$ ) and the heating due to the Multiple Coulomb scattering (that enters as an increase in the factor $\varepsilon_x$). The equation describing the total rate of change of the transverse emittance is a delicate balance of these cooling (first term) and heating (second term) effects:

$$\frac{d\varepsilon_{xN}}{dz} = \varepsilon_x \frac{d(\beta\gamma)}{dz} + \beta\gamma \frac{d\varepsilon_x}{dz} \tag{2.4}$$

It is possible to relate the first term of equation 2.4 to the ionization energy loss described by the Bethe-Bloch formula:

$$\frac{d\varepsilon_{xN}}{dz}(cool) = -\frac{1}{\beta^2}\frac{\varepsilon_{xN}}{E_\mu}\left|\frac{dE_\mu}{dz}\right| \tag{2.5}$$

where $E_\mu$ is the total energy of the muons.
The second term can be instead rewritten in the following way:

$$\begin{aligned}\frac{d\varepsilon_{xN}}{dz}(heat) = &\frac{\beta\gamma}{2\varepsilon_x}\left[< x^2 > \frac{d < \theta_C^2 >}{dz}\right] \\ &+ \frac{\beta\gamma}{2\varepsilon_x}\left[< \theta_C^2 > \frac{d < x^2 >}{dz} - 2 < x\theta_C > \frac{d < x\theta_C >}{dz}\right]\end{aligned} \tag{2.6}$$

[3] More rigorously: $\beta = v/c$ represents the velocity in terms of the speed of light while $\gamma = E/m$ is the so-called *Lorentz factor*.

where $\theta_C$ is the angular spread due to the Multiple Coulomb scattering.
Assuming that the cooling and the focusing are enough, it is possible to neglect both the effects of correlation in the beam parameters and the growth of the beam size in the transverse direction (the second and third terms in equation 2.6) which leads to:

$$\frac{d\varepsilon_{xN}}{dz}(heat) \approx \frac{\beta\gamma}{2\varepsilon_x} < x^2 > \frac{d < \theta_C^2 >}{dz} \tag{2.7}$$

Together with the beam emittance, the betatron function[4] $\beta_\perp$ determines the local size and divergence of the beam. The expectation value $< x^2 >$ can be expressed as a function of $\beta_\perp$ in the magnetic channel[5] and the emittance $\varepsilon_{xN}$ through the following formula:

$$< x^2 >= \beta_\perp \varepsilon_x \tag{2.8}$$

and observing that the simplest expression for the rate of change in $\theta_C^2$ is given by the Moliere scattering theory [67]

$$\theta_C \approx \frac{E_s}{pc\beta}\sqrt{\frac{z}{X_0}} \tag{2.9}$$

where $X_0$ is the radiation length of the absorber material, $p$ is the muon momentum and $c$ is the speed of light, it is possible to rewrite equation 2.7 in the form:

$$\begin{aligned} & \frac{d\varepsilon_{xN}}{dz}(heat) \approx \beta\gamma\frac{\beta_\perp}{2}\frac{d < \theta_C^2 >}{dz} \\ \Rightarrow \quad & \frac{d\varepsilon_{xN}}{dz}(heat) \approx \frac{1}{\beta^3}\frac{\beta_\perp}{2}\frac{E_S^2}{E_\mu m_\mu c^2}\frac{1}{X_0} \end{aligned} \tag{2.10}$$

where $m_\mu$ is the muon mass and $E_S$ has a value of 0.014 GeV [33].
The total rate of change of the normalized transverse emittance is thus given by:

$$\frac{d\varepsilon_{xN}}{dz} \approx -\frac{1}{\beta^2}\frac{\varepsilon_{xN}}{E_\mu}\left|\frac{dE_\mu}{dz}\right| + \frac{1}{\beta^3}\frac{\beta_\perp}{2}\frac{E_S^2}{E_\mu m_\mu c^2}\frac{1}{X_0} \tag{2.11}$$

showing that the rate of cooling decreases as the beam proceeds along the absorber while the rate of heating increases. Moreover, the heating term is minimized if $\beta_\perp$ is small (strong focusing) and $X_0$ is large (a low-$Z$ absorber).
The *minimum achievable* or *equilibrium* emittance, after which the emittance will begin to grow again, for a given absorber in a given focusing field is reached when

[4]The betatron function describes a particle moving in an accelerator and provides an emittance-independent representation of the properties of a beam transport system [69].

[5]This expression is approximated to the cylindrically symmetric case of solenoid focusing where $\beta_x = \beta_y = \beta_\perp$.

the cooling rate equals the heating one in equation 2.11. Its value depends both on the focusing conditions and the material absorbers through the formula:

$$min(\varepsilon_{xN}) \approx \frac{\beta_{\perp} E_S^2}{2\beta m_{\mu} c^2 X_0 \left|\frac{dE_{\mu}}{dz}\right|} \tag{2.12}$$

where $X_0 \left|dE_{\mu}/dz\right|$ is known as the cooling factor $F_{cool}$ (see section 2.1.4.1 for details). For example, in MICE, liquid hydrogen targets are used as absorbers: the estimated equilibrium emittance is about $2.5\pi$ mm·rad [70].

### 2.1.3 Longitudinal emittance cooling

The energy loss rises as the particle momentum decreases once it is below a few hundreds of MeV/c; as a consequence any transverse cooling is necessarily accompanied by some heating of the longitudinal emittance. This is primarily due to the fact that the energy loss is a statistical process and there is a spread of energy loss around the mean value (*energy straggling* [67]). If not controlled, the longitudinal heating leads to beam loss and limits the degree of transverse cooling that is possible to achieve.
The normalized longitudinal emittance is defined as

$$\begin{aligned} \varepsilon_{zN} &= \beta_z \gamma \delta \sigma_z \\ \delta &= \frac{\sigma_{p_z}}{p_z} \end{aligned} \tag{2.13}$$

where $\sigma_z$ is the bunch length, $\sigma_{p_z}$ is the momentum rms spread in the beam and $p_z$ is the momentum along the $z$ direction. Assuming the motion is predominantly along z, the total rate of change of the normalized longitudinal emittance is given by

$$\frac{d\varepsilon_{zN}}{dz} = \beta\gamma\delta\frac{d\sigma_z}{dz} + \beta\gamma\sigma_z\frac{d\delta}{dz} + \delta\sigma_z\frac{d(\beta\gamma)}{dz} \tag{2.14}$$

Using the relations among the relativistic variables and noting that for relativistic beams the change in $\sigma_z$ is negligible, the previous equation can be rewritten as

$$\frac{d\varepsilon_{zN}}{dz} \approx \frac{\beta\gamma\sigma_z}{p_z}\frac{d\sigma_{p_z}}{dz} \tag{2.15}$$

There are two main effects that modify the energy spread in the beam:

- particles with different energies lose different amounts of energy. The fractional loss in energy in a step $dz$ gives

$$\frac{d\sigma_{p_z}}{dz} = \frac{\sigma_E}{\beta c}\frac{d}{dE}\left(\frac{dE}{dz}\right) \tag{2.16}$$

If the particle energy is below the ionization minimum, this term causes an increase of the energy spread (heating) while it results in a decrease (cooling) if the energy is above. However, the rate of cooling is very small since the slope of the $dE/dx$ curve in the region of relativistic rise is small. For example the rate of change of $dE/dx$ over the 600-800 MeV energy range varies from $0.41\times10^{-4}$/cm for a liquid hydrogen absorber to $4.46\times10^{-4}$/cm for an aluminum one, in roughly the reverse order as their efficiency for transverse emittance cooling [56];

- the statistical fluctuations in the energy loss (energy straggling). This effect gives

$$\begin{aligned} \frac{d\sigma_{p_z}}{dz} &= \frac{K_s}{2\beta c\sigma_E}\gamma^2\left(1-\frac{1}{2}\beta^2\right) \\ K_s &= 4\pi(r_e m_e c^2)^2\frac{N_A Z\rho}{A} \end{aligned} \tag{2.17}$$

where $\sigma_E$ is the energy spread of the beam, $r_e$ and $m_e$ are respectively the classical radius and the mass of the electron, $c$ is the speed of light, $N_A$ is the Avogadro's number and $Z$, $\rho$ and $A$ are the atomic number, the density and the atomic weight of the material. Note that the growth in energy spread is proportional to $\gamma^2$, so cooling at low energy is preferred.

The longitudinal ionization cooling is thus possible in principle but appears to be impractical since, as shown above, the resulting cooling effect is weak and quickly exceeded by the energy-loss straggling.
A possible solution is represented by the *emittance exchange* between the longitudinal and the transverse degrees of freedom [68]. Since the longitudinal cooling of a moving beam is always associated with a transverse heating and viceversa, the longitudinal emittance reduction requires an increase in the transverse one. Conceptually, such emittance exchange can be accomplished by placing a transverse variation in the absorber density or thickness in a region of non-zero dispersion. In practice, it is obtained introducing a change of the beam profile through shaped edges (*wedge absorber*): the beam is dispersed across the absorbing material such that higher momentum particles passing through the thicker part of the absorber lose more energy. After the absorber the muons become more monoenergetic and thus the longitudinal emittance is reduced. A conceptual picture of the emittance exchange approach is given in figure 2.2.

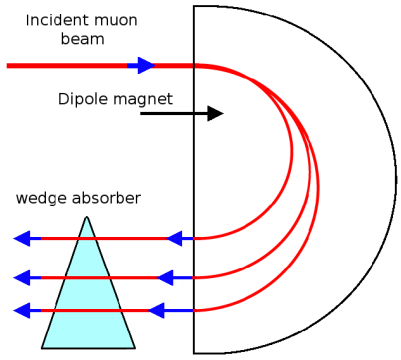


Figure 2.2: Basic principle of the longitudinal cooling exploiting a wedge absorber [68]. After passing through a dipole magnet the particles meet a wedge absorber that cools higher momentum particles more than the lower momentum ones.

The fractional change in momentum spread can be written as

$$\begin{aligned} \frac{d\sigma_{p_z}}{dz} &\approx \frac{1}{\beta c}\frac{dE}{dz}\frac{\eta\delta}{\alpha L_0} \\ \eta &= \frac{dx}{d\delta} \\ \alpha &= \frac{dx}{dz} \end{aligned} \tag{2.18}$$

where $\eta$ is the dispersion, $\alpha$ is the wedge angle and $L_0$ is the thickness of the wedge at $x = 0$. The longitudinal cooling is thus associated with the heating in the transverse space due to the Multiple Coulomb scattering in the absorber.

### 2.1.4 Cooling channel design

An engineering sketch of a ionization cooling channel design is shown in figure 2.3: the three basic elements are a low-Z absorber, providing energy loss, high-gradient RF cavities, to restore the longitudinal momentum, and a focusing system to squeeze the beam.
A few important characteristics can be defined for such a cooling channel [46, 71]:

- the overall *cooling factor*. The 6D emittance reduction by cooling is at best a factor $\Delta\varepsilon/\varepsilon = \Delta E/E$, where $\Delta E$ is the average energy loss in the absorbers (which is restored in the RF cavities) and $E$ is the average particle kinetic energy. Considering a typical muon energy of 200 MeV/c, a *10% cooling*

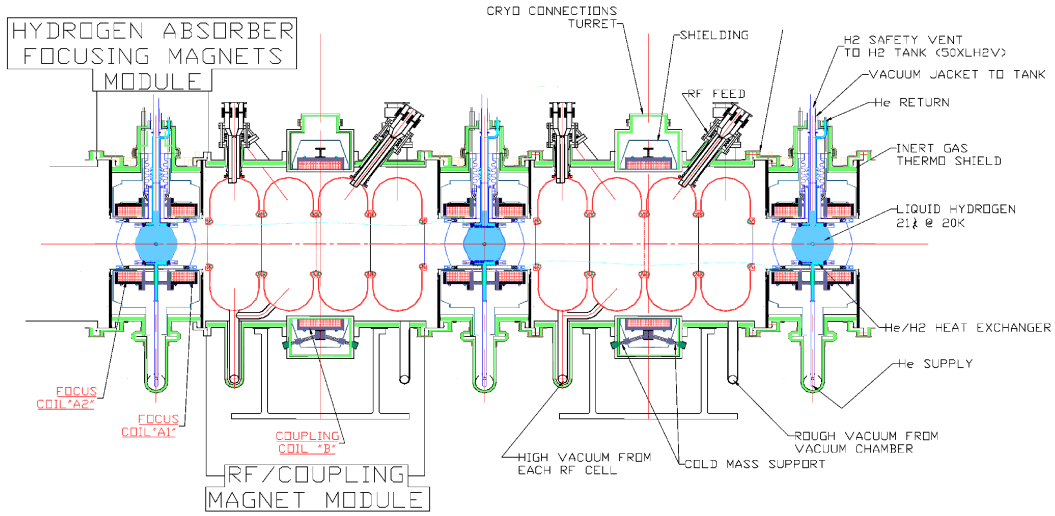


Figure 2.3: A 3D schematic view of the cooling channel design of the Muon Ionization Cooling Experiment [46]. Three liquid-hydrogen targets, each embedded within a pair of focusing solenoids, act as absorbers. A couple of 4 201 MHz RF cavities, each surrounded by a coupling solenoid, provide the muon re-acceleration.

*experiment* requires an energy loss of about 20 MeV and a similar gain in the RF system[6];

- the *frequency* of the RF cavities. There are several existing scenarios: in the US Feasibility Study-II [59], cooling is performed with 201 MHz cavities while the scheme developed at CERN [54] has proposed 88 MHz RF cavities. This has been basically motivated by the different preparation of the beam before the cooling section. Another crucial parameter is the gradient that can be achieved with such RF systems;

- the *beam properties*. The beam is characterized by its average energy, energy spread, size and angular divergence. In particular, these features vary along the cooling channel. A typical scenario could be:

  · energy: 200 MeV (momentum 280 MeV/c)

  · momentum spread: $\pm 10\%$

[6]Equation 2.11 shows that the percentage of decrease in the normalized emittance is proportional to the percentage of energy loss; hence cooling in one transverse dimension by a factor $1/e$ requires $\sim 100\%$ momentum loss and replacement. A low beam momentum is favored thanks to the increase of $dE/dx$ for momenta below the ionization minimum and because it requires a lower accelerating voltage.

· beam size: 5 cm rms in both projections

· beam angular divergence: 150 mrad rms in both projections

- the *magnetic field* and *diameter* of the magnetic channel, typically a 4−6 T field with an aperture radius of 15 cm.

The study of the cooling process with different beam conditions and by varying these relevant parameters is fundamental for the experimental demonstration of the feasibility of the ionization cooling technique. It also opens the way to different cooling channel designs, for example the one in which circular cooling sections are foreseen [72, 73]. Figure 2.4 shows some of the proposed projects.

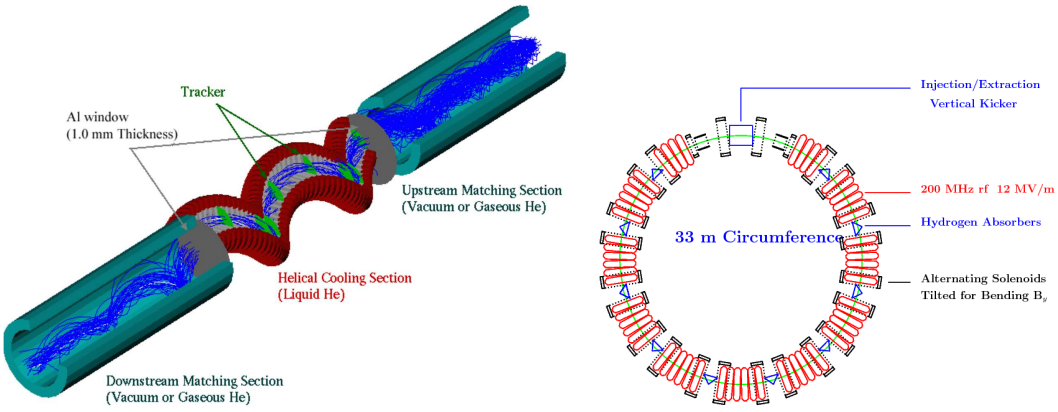


(a) (b)

Figure 2.4: Two different approaches to six-dimensional muon cooling: (a) simulation of a possible Helical Cooling Channel (HCC) as proposed by the MANX experiment [72]; (b) the ring cooling design based on RFOFO solenoids [73].

#### 2.1.4.1 Absorbing materials

Liquid or gaseous hydrogen is the best candidate as absorbing material for the ionization cooling technique. Other materials, including helium, lithium, lithium hybrid, beryllium and aluminum, have been investigated but show a worse cooling performance. A possible figure of merit is the cooling factor[7] $F_{cool} = X_0 \left| dE_\mu/dz \right|$. The main properties of the most popular absorbing materials that might be useful for ionization cooling [56, 74, 75] are listed in table 2.1. The second, third and

[7] For a fixed $\beta_\perp$, it can be uniquely defined for each material and, observing that the cooling takes place for both the transverse planes, the figure of merit is $F_{cool}^2$. For a given material, $F_{cool}$ does not depend on its density $\rho$, since the energy loss $dE_\mu/dz$ is proportional to it while the radiation length $X_0$ goes as the inverse of $\rho$ [68].

fourth column give respectively the density, the energy loss for a ionizing particle and the radiation length of the different materials. The fifth column shows the coefficient of $\beta_\perp$ in equation 2.12 for a relativistic particle ($\beta = 1$). For a relativistic muon ($\beta \approx 0.87$) in liquid hydrogen with a beta function $\beta_\perp = 8$ cm (which corresponds roughly to the confinement in a 15 T solenoidal field), the minimum achievable emittance is about 340 mm·mrad [59]. The last column gives $F^2_{cool}$ normalized to the one of liquid hydrogen. Hydrogen is best by a factor $\sim 2$ or more over any of the other materials although its advantage could be limited by the presence of containing windows[8].

| material | $\rho$ [g/cm$^3$] | *dE/dz* [MeV/g·cm$^2$] | $X_0$ [g/cm$^{-2}$] | coeff. $\beta_\perp$ [mm·mrad/cm] | $F^2_{cool}$ [A.U.] |
|---|---|---|---|---|---|
| liquid $H_2$ | 71 | 4.034 | 61.28 | 42 | 1.000 |
| liquid $He_2$ | 125 | 1.937 | 94.32 | 59 | 0.524 |
| LiH | 0.780 | 1.94 | 79.30 | 78 | 0.352 |
| Li | 0.534 | 1.639 | 82.76 | 79 | 0.268 |
| Be | 1.848 | 1.594 | 85.19 | 103 | 0.172 |
| Al | 2.700 | 1.614 | 24.30 | 275 | $\sim 0.05$ |

Table 2.1: Most relevant properties of some of the materials tested for ionization cooling absorbers [56, 74, 75].

#### 2.1.4.2 Radio Frequency cavities and focusing methods

Between absorbers, high-gradient acceleration of the muons must be provided to restore the lost longitudinal momentum: in this way the ionization cooling process can be repeated many times. The RF cavities dominate the length of the cooling channel (as shown in figure 2.3) and the achievable RF gradient determines how much cooling is practical before an appreciable fraction of the muons has decayed. Different possible designs have been proposed or are still under investigation [56]: the most popular scenario foresees the use of both normal-conducting and superconducting RF elements.
The ionization cooling technique also needs some form of focusing to limit the emittance growth due to an increase of the beam size itself. Three main possible focusing elements have been studied for a linear cooling section (for a detailed description see [56]):

[8]The thickness of the absorber windows is a critical parameter: it must be large enough to sustain the pressure e.g. of the liquid $H_2$, and at the same time as small as possible to reduce the Multiple Coulomb scattering [16, 59].

- **quadrupole FODO cell**; it consists of equal strength, horizontally and vertically focusing quadrupoles separated by a drift distance and is optimal for high momentum muon beam focusing;

- **solenoid**; a particle travelling parallel to the axis of a solenoid at a radius $a$ experiences an azimuthal momentum kick

$$p_\phi = \frac{eB_z a}{2} \tag{2.19}$$

  while crossing the fringe field region at the end of the solenoid. This produces a radial force in the central part of the solenoid, causing the particle to follow a helicoidal trajectory (figure 2.5). Thus the radius of a single particle oscillates between $a$ and the axis of the solenoid;

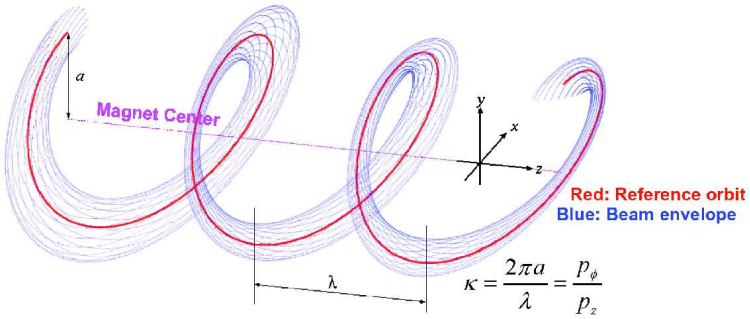


Figure 2.5: Helicoidal motion of the beam moving inside a solenoid along the $z$ axis (violet), which corresponds to the solenoid center [72]. For a given momentum, muons (blue) oscillate around the periodic equilibrium orbit (red). $\lambda$ is the transverse field period (the helical orbit period), $a$ is the helix orbit radius and $\kappa$ is $a$ in terms of $\lambda/2\pi$.

- **solenoid FOFO cell**; it consists in a series of short solenoids separated by a distance $d$. The system focuses both the transverse planes simultaneously.

## 2.2 The MICE experiment

The International Muon Ionization Cooling Experiment (MICE [46]) is a R&D project whose main goals are the study of the feasibility of a Neutrino Factory based on a muon storage ring and the experimental demonstration of the ionization cooling technique.
In other words, MICE goals are [46]:

- the design, engineering and building of a cooling section capable of giving the desired performances for a Neutrino Factory;

- its characterization in a muon beam.

MICE intends to reduce the transverse emittance of the muon beam by 10%: this corresponds to an absolute precision of 0.1% in the upstream and downstream emittance measurements [46].
The experiment is under construction at the Rutherford Appleton Laboratory (RAL) (figure 2.6(a)) in Didcot (UK), and works in a parasitic mode to the normal operation of the ISIS ring[9] (figure 2.6(b)). The muon beam for MICE comes from a pion beam that in turn derives from the interaction of the 800 MeV ISIS proton beam with a titanium target[10]. The pions are then captured by a triplet of quadrupoles (Q1−3), as shown in figure 2.7(a), and left to decay in a 5 m long decay solenoid (DS) provided by the Paul Scherrer Institute (PSI, Switzerland). The muons are then identified by a scintillating fiber monitor (GVA1) and pass through a series of dipole and quadrupole magnets (D2+Q4−6) for the beam focusing before entering the cooling channel. A photo of the MICE experimental area is given in figure 2.7(b) with the beam entering from the left. MICE will typically work with a muon beam with a momentum in the range[11] 140−240 MeV/c, $\beta = 42$ cm at the centre of the absorber and normalized emittance[12] between $1-10\pi$ mm·rad [46].
The cooling section design follows the guidelines of the US Feasibility Study-II [59]. A 3D engineering layout of the MICE cooling channel is shown in figure 2.8(a) while figure 2.8(b) gives a schematic layout (not in scale) of the detectors and cooling section elements position.
The cooling is performed exploiting three liquid hydrogen absorbers and two RF accelerating structures. The tracking and particle identification is accomplished by two scintillating fiber detectors and Time Of Flight+Cherenkov systems. The upstream PID detectors provide the background reduction from pions and electrons while the downstream ones, together with a dedicated calorimetry station, give the electron rejection at the end of the channel. The overall length of the MICE experiment is $\sim$ 11.5 m [46].

[9] ISIS is a synchrotron which primarily produces intense proton, neutron and muon beams [76]. http://www.stfc.ac.uk

[10] The target can be remotely controlled and is inserted into the ISIS beam at a rate of 0.3 Hz: a flux of $2.5\times10^{13}$ protons per bunch is assumed [76, 77].

[11] In addition, in this momentum range also the pion production cross section is enhanced. This motivates the typical choice of the 140−400 MeV/c range by all the main muon cooling project designs [74].

[12] The incoming emittance can be tuned through a set of adjustable diffusers placed at the beginning of the cooling channel [78].

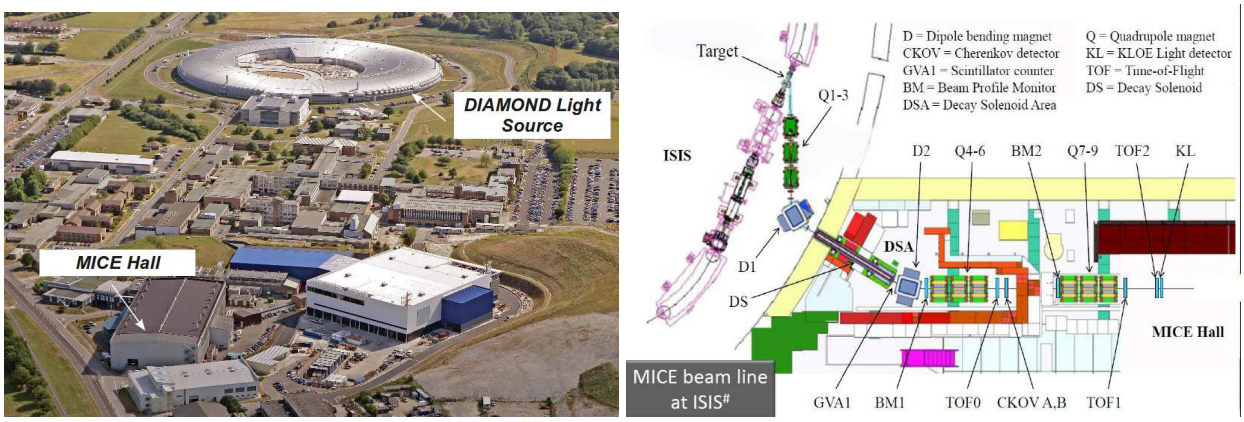


(a) (b)

Figure 2.6: (a) A top view of the RAL complex in Didcot: the MICE experiment is under construction in building R5.2. (b) MICE layout in the experimental hall: the main components needed for the muon transport are shown.


(a)


(b)

Figure 2.7: (a) A photo of the triplet of quadrupole magnets that capture and select in momentum the pions produced by the interaction of the ISIS proton beam with a titanium target. (b) A photo of the MICE experimental area: the muon beam comes from the left. It covers 560 $m^2$ of floor space and occupies $\sim$ 4500 $m^3$ of volume [46].

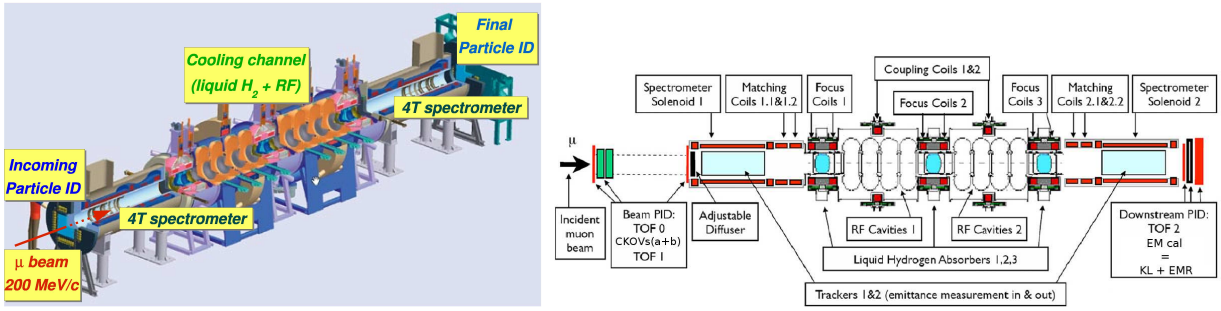


(a) (b)

Figure 2.8: A 3D view (a) and a schematic layout (b) of MICE (with the beam entering from the left) [46]. The muon beam derives from the interaction of the ISIS proton beam with a titanium blade and the subsequent decay of the produced pions. Three liquid hydrogen absorbers interspersed by two RF accelerating structures provide the muon cooling. The tracking system consists of two scintillating fiber spectrometers, both embedded in a 4 T solenoid. A pair of Time Of Flight and Cherenkov detectors (TOF0 + CKOVa+b + TOF1) provide the upstream particle identification and the incoming emittance measurements. A final hodoscope (TOF2) and a calorimeter system (EMcal) are placed at the end of the channel for the muon-electron rejection and the downstream emittance measurement.

### 2.2.1 The cooling channel

The basic elements of the MICE cooling channel are three Absorber and Focusing Coil (AFC) modules and two RF cavity and Coupling Coil (RFCC) stations [79]. The overall length of the channel is $\sim$ 5.5 m. Each AFC module (figure 2.9(a)) contains a liquid hydrogen absorber at a cryogenic temperature that provides the energy loss of muons, and a pair of focusing coils to reduce the beta function that ensures a small equilibrium emittance. Each RFCC station consists of four 201 MHz normal-conducting RF cavities and one super-conducting solenoid as shown in figure 2.9(b).

### 2.2.2 The Particle Identification detectors

High precision timing measurements of the particles passing through the cooling channel are needed both to relate the time of the incoming beam to the phase of the accelerating field in each RF cavity (with a 5° precision [46]) and for the particle identification. In particular, the PID is provided by two systems based on Time Of Flight (TOF) and Cherenkov detectors.
Three TOF stations [80] are positioned along the cooling section to provide the time coordinate ($t$) measurement for the emittance estimation. TOF0 is placed at

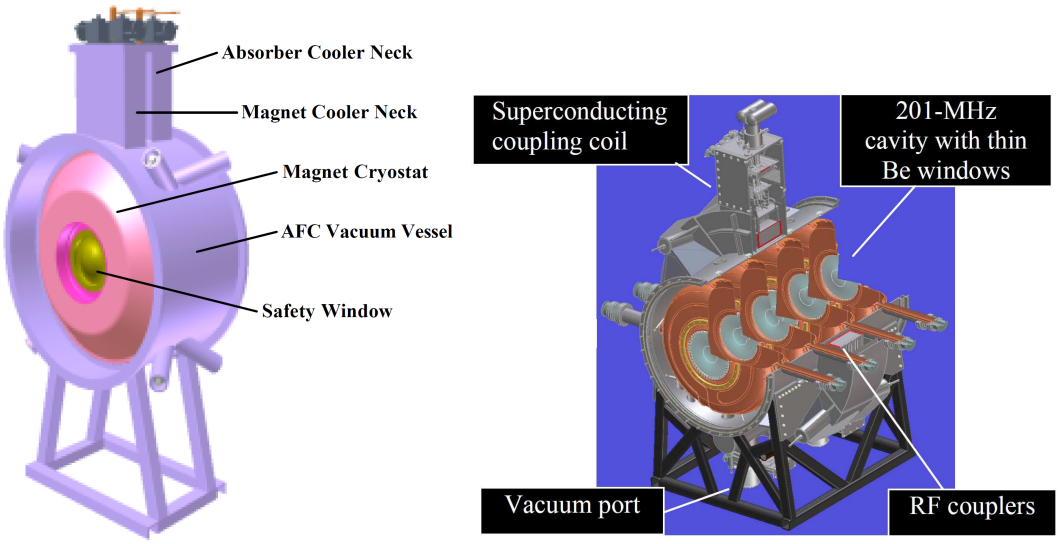


(a) (b)

Figure 2.9: (a) A 3D schematic view of the MICE AFC station [79]: liquid hydrogen absorbers and focusing coils are used to provide the muon energy loss and beta function reduction. (b) A 3D engineering view of the MICE RFCC module: it contains four 201 MHz normal-conducting RF cavities and one super-conducting solenoid.

the beginning of the channel, $\sim$ 10 m from the first solenoid, while TOF1 and TOF2 are positioned respectively at the entrance and at the exit. The main task of the upstream TOFs is the pion background separation at low momenta (below $\sim 210$ MeV/c); they also supply the trigger for the experiment in coincidence with the ISIS clock [46]. TOF2 at the end of the section selects the particles passing through it for the downstream emittance measurement and the cooling efficiency estimation.
The TOF stations have a common design (figure 2.10(a)): two planes of fast scintillator counters have been organized in a x$-$y way and are readout from both sides by the R4998 photomultipliers (Hamamatsu[13]).

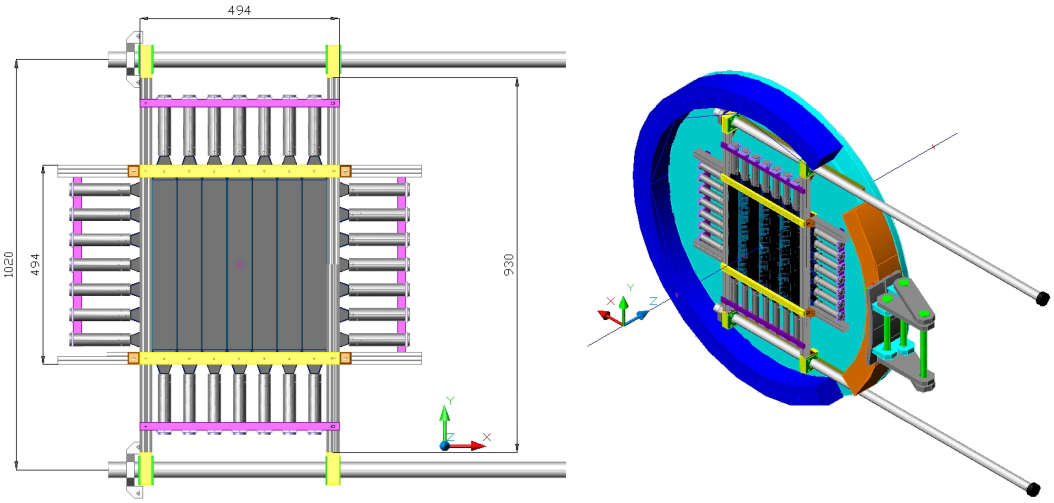


(a) (b)

Figure 2.10: (a) Schematic view of the TOFs design: two planes of scintillator counters per station have been organized in a x-y way and readout with high gain photomultipliers. (b) 3D engineering view of the magnetic shielding for the TOF1 and TOF2 stations.

Given the working conditions[14] of the TOFs, all the photomultipliers are equipped with mumetal shielding. In addition, TOF1 and TOF2 are placed inside a dedicated magnetic shielding cage (figure 2.10(b)). The readout electronics is based on the V1724 Flash Analog to Digital Converter (FADC, CAEN[15]), for the charge measurement and the time walk correction [81], and on the fast CAEN V1290

[13] http://www.hamamatsu.com

[14] High residual magnetic field due to the spectrometer solenoids is present at the TOF positions: the maximum value is 1200 Gauss for the orthogonal component and 400 Gauss for the longitudinal one [80] requiring an adequate protection for the photomultipliers.

[15] http://www.caen.it

Time to Digital Converter (TDC) that provides timing measurements. A $\sim 50-60$ ps intrinsic time resolution has been measured during a commissioning phase at RAL (see [80] for details).
Given that for a momentum range between 220 and 360 MeV/c the time of flight difference between muons and pions is $\sim 2$ ns over a distance of $\sim 10$ m [82], two Cherenkov counters are used to provide a sufficiently good pion/muon separation. A 3D engineering view of the Cherenkov detectors [83, 84] is presented in figure 2.11(a): the active radiator is a high density silica aerogel plate while the produced light is readout by four $8''$ EMI 9356 KA photomultipliers, provided by the HARP experiment [85]. A conical shape for the internal mirrors has been chosen to enhance the light collection of the photomultipliers [84]. A photo of the first Cherenkov detector during the installation at RAL is shown in figure 2.11(b): a beam purity up to 99.98% has been obtained (see [86] for details).

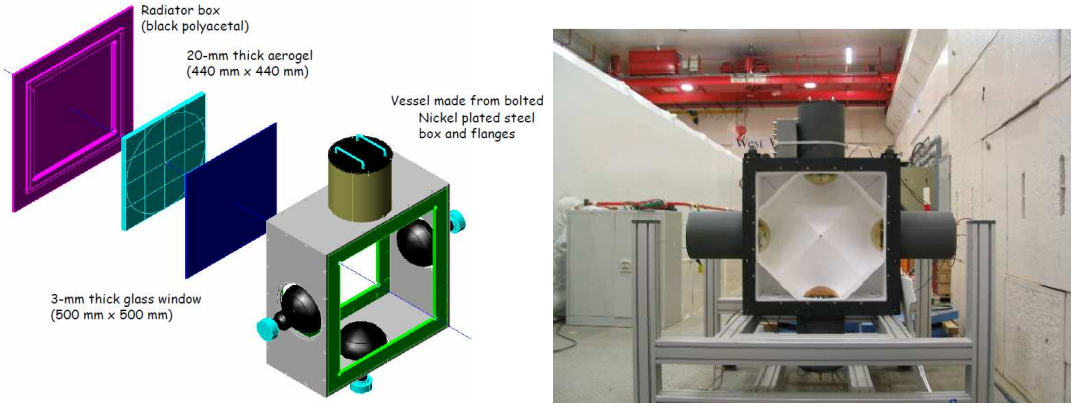


(a) (b)

Figure 2.11: (a) A schematic view of the Cherenkov detectors: a high density silica aerogel plate is used as a radiator while the light collection is performed by four $8''$ EMI 9356 KA photomultipliers. (b) A front view photo of the first Cherenkov counter during its installation at RAL: the conical shape of the internal mirror is visible.

### 2.2.3 The scintillating fiber trackers

Charged-particle tracking in MICE is provided by two solenoidal spectrometers [87] that are required to determine the expected relative change in transverse emittance of approximately 10% with a precision of $\sim 1\%$ (i.e. a 0.1% precision on the absolute emittance [46]). Given that MICE is a single particle experiment [46, 71],

in a reference system with the beam aligned with the $z$ axis, four of the six coordinates used in the emittance definition ($x$, $y$, $dx/dz$ and $dy/dz$) together with the transverse momenta ($p_z$ and $p_t$)[16] are here measured for each particle [82].
Each spectrometer consists of a 4 T superconducting solenoid instrumented with a 1.1 m long tracker, composed of five planar scintillating fiber stations: a schematic view of the tracker is given in figure 2.12(a).

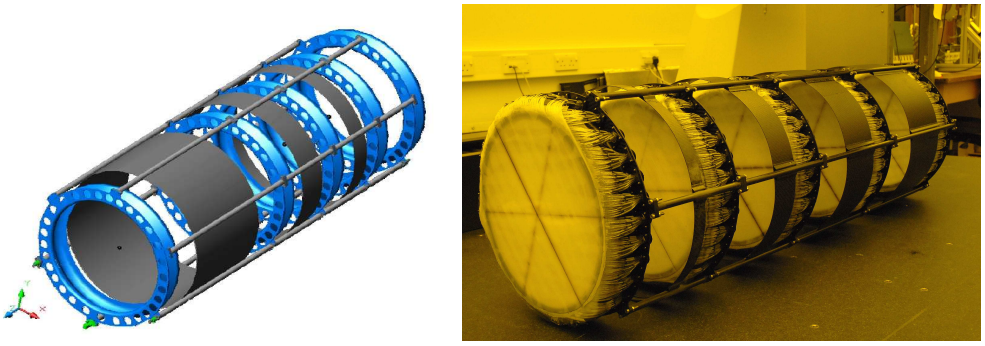

(a) (b)

Figure 2.12: (a) Schematic view of the solenoid spectrometers: each detector houses 5 stations of 3 doublet-layers scintillating fibers arranged in a stereo geometry and readout with VLPCs [87]. (b) A photo of the upstream scintillating fiber tracker.

Each station is composed of three 120° tilted doublet-layers of scintillating fibers with a 350 $\mu$m diameter, providing an accurate identification of the point in space and an acceptable level of Multiple Coulomb scattering. The light yield is also enhanced by grouping seven neighboring fibers together and feeding them into a single clear waveguide. Each of them is readout with cryogenic Visible Light Photon Counters (VLPCs), light-electrical signal converters with a quantum efficiency of $\sim$ 80%, high gain and high rate tolerance [88]. A photo of the assembled upstream spectrometer is shown in figure 2.12(b).
The tracker readout is based on the DØ Central Fiber Tracker (CFT) optical readout and electronics system [88]: the VLPCs signals are digitized using the Analogue Front End with Timing (AFE IIt) board developed by the DØ collaboration. One of the trackers has been tested at RAL with cosmic rays: a spatial resolution of 682$\pm$1 $\mu$m (including the Multiple Coulomb scattering contribution) and an efficiency of 99.82$\pm$0.1% have been found (see [87] for details).

[16] The muon trajectories are circles in the $x-y$ plane thanks to the presence of the solenoid field: the radius of the circle gives the transverse momentum $p_t$ while the number of orbits combined with the time measurement by the TOF stations determines $p_z$ [82].

### 2.2.4 The calorimetry station

The electron background rejection at the end of the cooling channel is based on the Electron Muon calorimeter (EMcal) station: the electron shower starts in an electromagnetic preshower calorimeter (KLOE-Light) while the penetrating muons are detected afterwards in a fully active scintillating bar tracker-calorimeter (Electron Muon Ranger, see next chapter for a detailed description).
The KL (KLOE-Light lead-scintillating fiber calorimeter) design is based on the electromagnetic calorimeter of the KLOE experiment [89] at the DAΦNE Factory in Frascati[17]. It consists of a $80\times80$ cm$^2$ grooved lead layer transversally segmented with 1 mm diameter blue scintillating fibers inserted and glued in the lead holes: figure 2.13(a) shows a schematic front view of its *spaghetti* design. The thickness is $\sim$ 4 cm corresponding to less than 2.5 radiation lengths. The light is readout at both edges with R1335 photomultipliers from Hamamatsu provided by the HARP experiment [85].

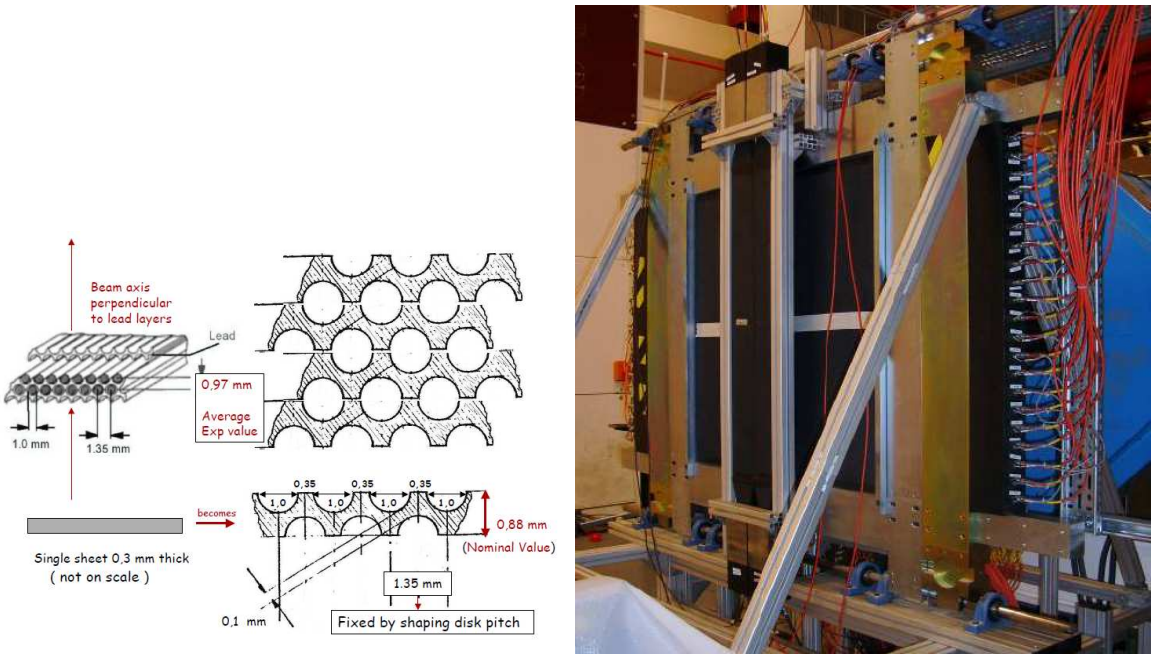


(a) (b)

Figure 2.13: (a) A schematic view of the *spaghetti* design implemented for the KL calorimeter [24]: the module is composed of grooved lead foils in which 1 mm diameter scintillating fibers are embedded. (b) A photo of the calorimeter installed at RAL for the commissioning tests (the beam enters from the right).

[17] Laboratori Nazionali di Frascati (LNF); http://www.lnf.infn.it/acceleratori

The KL energy resolution has been found to be $\sigma_E/E = 7\%/\sqrt{E(\mathrm{GeV})}$ while the time resolution is $\sigma_t = 70\ \mathrm{ps}/\sqrt{E(\mathrm{GeV})}$ [82]. Figure 2.13(b) shows the complete calorimeter installed at RAL together with the KL Tag Counter, consisting of 2 scintillator slabs with a cross section of $10\times80\ \mathrm{cm}^2$ and 2.5 cm thick.

# Chapter 3

# The Electron Muon Ranger

The upstream particle identification and tracking in MICE [46] are provided by a system based on TOF and Cherenkov detectors [80, 83] and two superconducting spectrometers [87]. However, simulation studies on the behavior of the particles at the end of the cooling channel [24] have shown that a detector able to distinguish the muons from the electrons (that in turn derive from the muons decay) is needed together with the TOF2 station in order to achieve a high precision measurement of the beam downstream emittance [24, 46].
In other words, a tracker-calorimeter is necessary for the particle identification at the end of the MICE channel. This detector is a lead-scintillator calorimeter (KL, see section 2.2.4 for details) followed by a fully active scintillator detector called *Electron Muon Ranger - EMR* which is the main topic of this thesis work.
This chapter is dedicated to the description of EMR and its readout electronics: the detector is based on scintillating triangular shape bars for a total of more than 1 ton of plastic scintillator while the electronics chain is based on a dedicated *FrontEnd Board (FEB)* and standard VME boards. Several characterization tests have been performed on the prototype of the FEB and are presented in Appendix A.
The detector construction and commissioning is under the responsibility of the University of Geneva (UNIGE) while the Como (Insubria)/Trieste (INFN) group has developed the FEB electronics and tested the performances of the different prototypes. In fact, the construction of a detector such as EMR has required the development of a small size prototype [90] and several component tests to study both the mechanical and electrical aspects. A complete description of the prototype and its readout electronics will also be presented here.

## 3.1 The Electron Muon Ranger design

### 3.1.1 Motivations

Particle identification upstream and downstream the MICE cooling channel is a fundamental task to obtain a precise enough beam emittance measurement. Since MICE works with muon beams of tunable emittance and energy, everything which is not muon is considered background. There are three main sources of background:

- some of the pions, from which the muons are produced, that remain in the beam (the beam transport line before the cooling section ensures a muon purity better than 99.9% [77]);
- the dark current originating from the RF cavities operating in high electric and magnetic fields: the electrons may be ripped off the surface of the cavities and accelerated along the cooling channel causing bremsstrahlung photon emission. In turn this corresponds to a source of background in the trackers [24];
- muons decay inside the cooling section or in one of the spectrometers in a small fraction of events ($\sim$ 1% [46]). The number of muons and electrons arriving at the end of the cooling channel as a function of the muon initial momentum [46] is shown in figure 3.1(a): decreasing the energy the great part of the muons in the beam decays into electrons and some of the background is due to muons decaying at rest.

The pion/muon separation and the RF electron background rejection at the beginning of the MICE cooling section are provided by the upstream TOF and Cherenkov stations and the spectrometer trackers [24]. The main problem for the emittance high precision measurement is thus represented by the downstream particle identification. Kinematics cuts can reject about 80% of decay electrons [46], but this is not enough to avoid a bias in the emittance measurement. Dedicated detectors are thus necessary to separate electrons from muons; different solutions based on a calorimeter system have been proposed and their performances in terms of electron/muon separation efficiency have been studied with G4MICE simulations [24]. Figure 3.1(b) shows the results for three alternative designs. The red line indicates the configuration in which four KL-like layers are present; the black one shows a design that foresees the use of a front KL layer followed by a fully active plastic scintillator detector (KL+SW[1]) while the purple line represents a solution with only the TOF2: the best choice is the second one [24].

[1]The original proposed design of EMR, called SandWich (SW), was exploiting a KL-like front layer followed by 10 modules of plastic scintillator with different thicknesses [24]. The detector

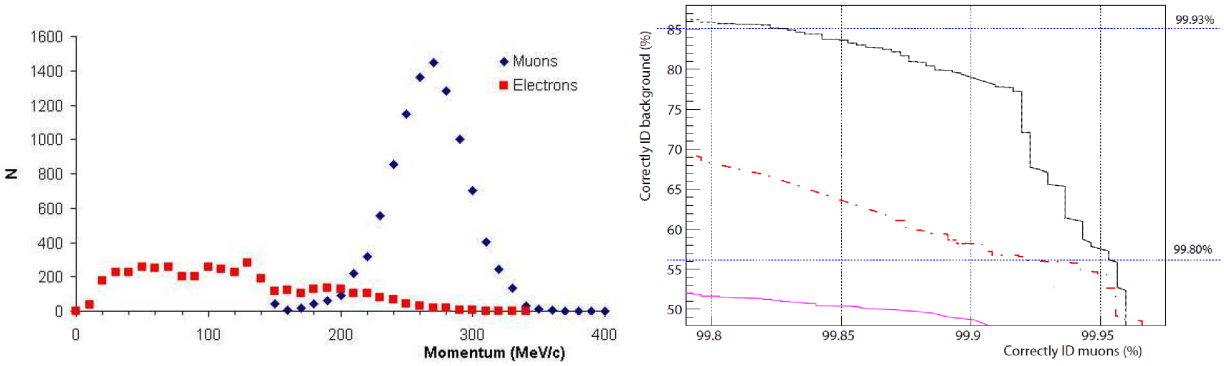


(a) (b)

Figure 3.1: (a) Momentum distributions of muons and electrons arriving downstream of the second spectrometer [46]. The lower the energy, the larger is the fraction of muons that decay along the cooling channel. (b) Simulation of the PID detectors performance with different detector configurations [24]: the black line indicates the complete KL+SW configuration (see text for details), the red line represents a design in which only 4 KL-like layers are present and the purple line shows the situation without the calorimeter (only TOF2).

The basic idea for the downstream background rejection is to distinguish electrons from muons using the longitudinal profile of the electromagnetic shower at the end of the cooling section [24]. A high Z material (e.g. a lead preshower) combined with a low Z one (e.g. scintillating plastic) is the ideal choice: the electrons lose most of their energy in the preshower generating an electromagnetic cascade in the following layer while the muons penetrate the high Z material without interacting. This means muon events can be distinguished from the background ones thanks to their different topology [24].

### 3.1.2 The detector

Figure 3.2(a) shows a 3D engineering rendering of the Electron Muon Ranger (EMR) placed after the KL calorimeter. EMR consists of 48 layers, organized in a x−y geometry (24 modules, being one module made of 1x+1y layer), of extruded scintillator bars [91] made of blue-emitting DOW Styron 663 W polystyrene + 1% PPO + 0.03% POPOP dopants. The bars have been provided by the Fermi National Accelerator Laboratory (FNAL) and their main properties are listed in table 3.1. The layers are positioned one after the other and are supported by a

design has been subsequently changed basically because of cost reduction and simplification in the manufacturing.

metallic frame; the whole detector is enclosed in an aluminum box (EMR Outer Box, EOB) to protect it from light.

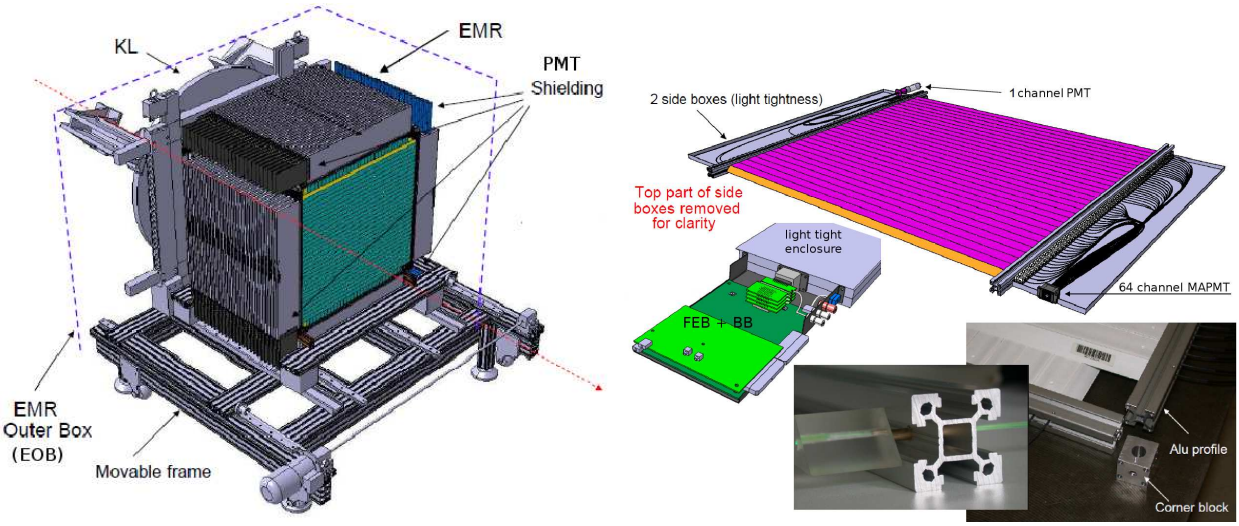


(a) (b)

Figure 3.2: (a) A 3D engineering view of the EMR detector and its mechanical support; also the KL calorimeter is shown. The red arrow indicates the muon beam direction. (b) Schematic view of one of the EMR layers: it consists of 59 triangular shape bars readout with one 1.2 mm diameter WLS fiber per bar connected on both sides to a photomultiplier readout system. The schematic view for the mechanical support for the FrontEnd Board (dark green) and the Buffer Board (light green) for the MAPMT readout is also shown (bottom). [Courtesy of the UNIGE group]

Each layer (figure 3.2(b)) consists of 59 bars with a triangular shape (base=3.3 cm and height=1.7 cm) and 1.1 m long, for a total of 2832 bars for the whole detector. In total each EMR layer covers an active region of $\sim 1$ m$^2$. The total weight per layer is $\sim 28$ kg that means $\sim 1.5$ ton for the whole calorimeter.

| material | DOW Styron 663 W polystyrene |
|---|---|
| dopant 1 | 1% PPO |
| dopant 2 | 0.03% POPOP |
| emission color | blue |
| absorption cut-off | 400 nm |
| emission peak | 420 nm |

Table 3.1: Main properties of the blue-emitting extruded scintillator bars.

The light produced in each bar is carried out by one 1.2 mm BFC-91A Wave Length Shifter (WLS) fiber[2] whose main properties are summarized in table 3.2. All the fibers have the same length ($\sim$ 1.2 m from the exit of each side of the bar for a total of $\sim$ 3.5 m) even if the photomultipliers are located on one end of the layer; in this way the efficiency is the same for all the bars independently from their position (and each bar is mechanically equivalent to the others). The fibers are connected on both sides but using two different photomultiplier systems (described in detail in section 3.1.3). A total of about 11 km of WLS fibers will be used to assemble the entire EMR detector. To protect the fibers and support the photomultipliers and their electronics (figure 3.2(b) bottom), each layer is equipped with an aluminum box at each side that also provides light tightness. Each box is connected to the metalic frame that holds the bars.

| | |
|---|---|
| core material | polystyrene |
| cladding material | acrylic |
| core refractive index | 1.6 |
| cladding refractive index | 1.49 |
| emission color | green |
| emission peak | 494 nm |
| decay time | 12 ns |
| 1/e length | $>$3.5 m |

Table 3.2: Main properties of the BFC-91A Wave Length Shifter fibers.

The detector is under construction at the Département de Physique Nucléaire et Corpusculaire (DPNC) of the University of Geneva: figures 3.3(a) and 3.3(b) present some photos of the assembly phases of the final detector. The assembly procedure has been defined during the construction of the prototype (see section 3.2 for details) and is the following:

- the raw bars, $\sim$ 3.5 m long, have been first cut at the right length (figure 3.3(a) top) grouping 4 bars together to simplify and getting the procedure faster;
- both ends of each bar are then polished and fine milled (figure 3.3(a) bottom);
- a WLS fiber per bar has been inserted and glued[3] in the bar hole (figure 3.3(b) top); each bar is then equipped with a threaded cylinder per side to allow the passage of the fibers through the mechanical support;

[2]Saint Gobain crystals, http://www.detectors.saint-gobain.com

[3]The glue is the epoxy resin E-30 from Prochima; http://www.prochima.it

- finally the fibers are covered with dark plastic to avoid cross talk and to protect the fibers themselves (figure 3.3(b) bottom);
- 59 bars are then grouped together to form a layer (figure 3.4(a)) and the fibers are aligned with the MultiAnode Photomultiplier Tubes (MAPMT) mask (figure 3.4(b)); once inserted in the mask, they are glued, cut and polished.

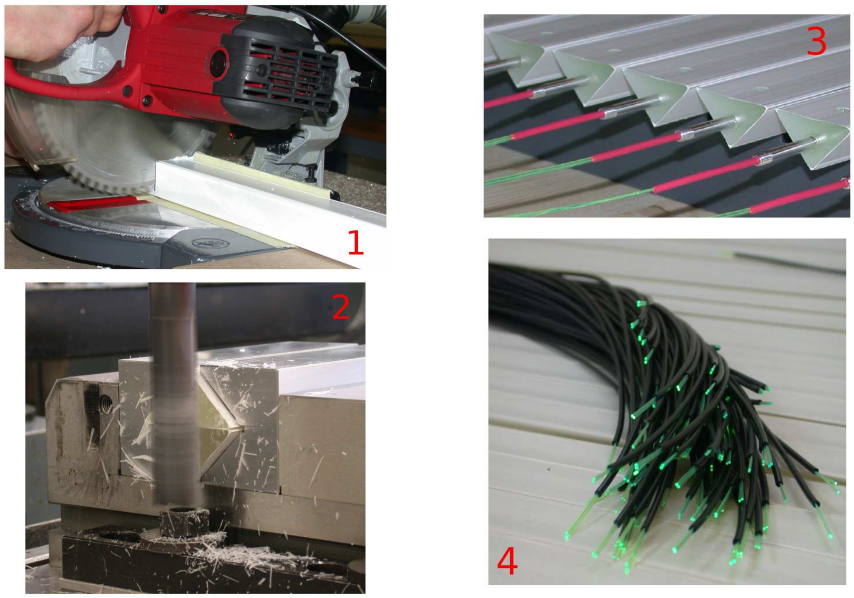


(a) (b)

Figure 3.3: Photos of the EMR assembly phases. (a) The bars are first cut at the right length (top), polished and fine milled (bottom). (b) One 1.2 mm diameter WLS fiber per bar is inserted and glued in the bar hole (top); the bar surfaces from which the fiber exits are then white painted. The fibers part outside the bars is covered with black plastic (bottom) to avoid cross talk. [Courtesy of the UNIGE group]

### 3.1.3 The photomultipliers and their mechanics

On one side, the fibers exiting from each bar are grouped together and are connected, through a dedicated mask (figure 3.5(b) top), to the single channel XP2972 (PHOTONIS[4]) PMT[5] whose main characteristics are listed in table 3.3.

[4] http://www.photonis.com

[5] In this way it is possible to measure the particle energy from the total charge deposit in each layer.

(a)

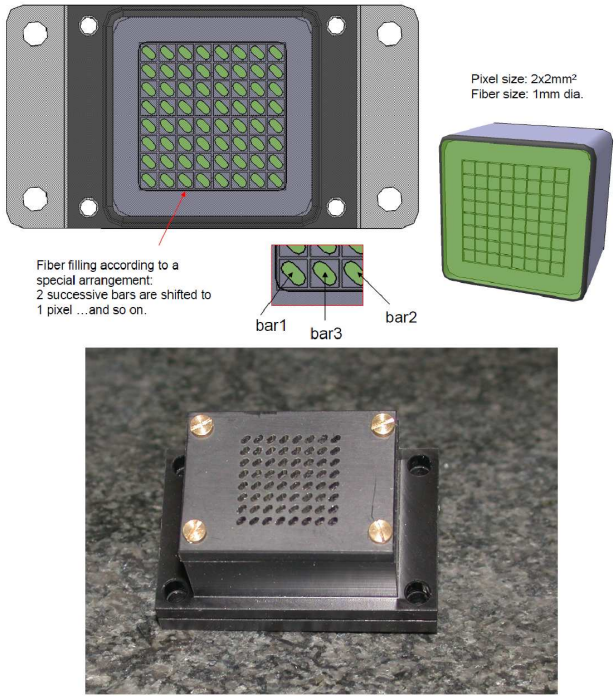


(b)

Figure 3.4: (a) Photo of one of the final EMR layers. (b) Schematic view of the 64 channel MAPMT mask (top) and a photo of the interface mask (bottom). [Courtesy of the UNIGE group]

| | |
|---|---|
| effective area | 415 $mm^2$ |
| spectral range | 290-650 nm |
| peak wavelength | 420 nm |
| photocathode material | bi-alkali |
| window material | lime glass |
| maximum HV | -1300 V |
| gain | $9.3 \times 10^5$ |

Table 3.3: Main properties of the XP2972 PHOTONIS single channel photomultiplier.

The frontend electronics of the PMT (figure 3.5(a)) has been adapted to put it directly inside the metallic support that provides the shielding against the magnetic field. Its assembly phases are described in figure 3.5(b).

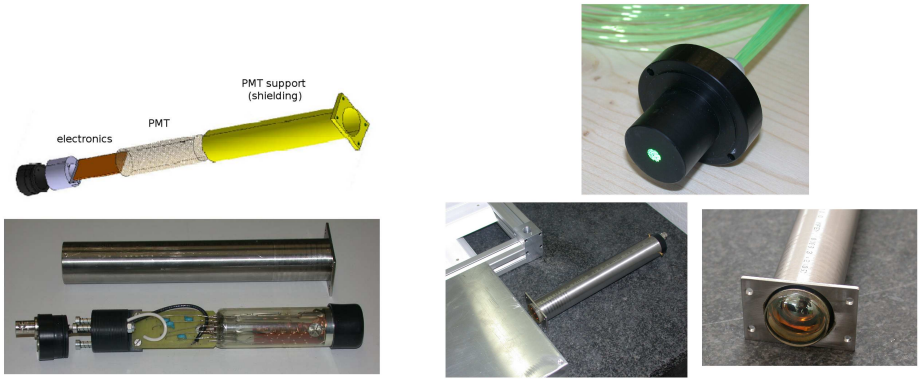


(a) (b)

Figure 3.5: (a) Schematic view of the single channel PMT support shielding (top) and a photo of the PMT and its holding mechanics (bottom). (b) Some photos of the single channel PMT during the assembly phase: the interface mask is also shown, on the top. [Courtesy of the UNIGE group]

On the other side, the fiber of each bar is connected, through a dedicated mask (figure 3.4(b)), to a channel of a multianode green enhanced photomultiplier R7600-00-M64 (H7546B assembly, Hamamatsu) whose main properties are summarized in table 3.4.
The connection of the MAPMT with the frontend electronics has been studied in detail given both the mechanical constraints and the possibility of introducing a noise source [92]. A schematic view of the connection is given in figure 3.6(a): the rear of the MAPMT is soldered to a 4 layer rigid-flex (kapton) circuit (shown

| | |
|---|---|
| anode size | $2\times2$ mm$^2$ |
| effective area | $1.81\times1.81$ mm$^2$ |
| spectral range | 300-650 nm |
| peak wavelength | 420 nm |
| quantum efficiency at 390 nm | 21% |
| photocathode material | bi-alkali |
| window material | borosilicate glass |
| maximum HV | -1000 V |
| gain | $3\times10^5$ |
| anode gain uniformity | 1:3 |
| cross talk | 2% |

Table 3.4: Main properties of the green enhanced R7600-00-M64 Hamamatsu 64 channel photomultiplier.

in detail in figure 3.6(b)) that allows the needed mechanical flexibility. The study of the noise will be presented in Chapter 5.

### 3.1.4 The electronics chain

The EMR electronics chain has to cope with the MICE experimental duty cycle: the beam time structure foresees one 1 ms spill every second; up to one good event every 5 $\mu$s is expected within the spill. During this time interval the EMR electronics chain has to sample and discriminate the signals of each MAPMT, assign a time stamp to every bar over threshold, store data in a digital form and make them available for the readout at the end of the spill.
The EMR electronics is divided in 3 main blocks:

- the *FrontEnd Boards (FEBs)*, which are located near the fibers exit; they provide the connection for the MAPMT, the ASIC for the MAPMT signals conditioning and the interface with the second block of the electronics;

- the *Buffer Boards (BBs)*, which are being developed as piggy back boards of the FEBs; they are the boards that sample the digital outputs of the ASIC with a 400 MHz clock and, in presence of the trigger of the experiment, store the above threshold bar numbers with a timestamp (to send them to the DAQ in the interspill period). The digital outputs are the ASIC discriminator outputs; the choice to use only the digital information (thus with no information on the energy deposit in each bar) has been dictated by the time structure of the MICE beam. The sampled data are stored with a timestamp and the trigger number in the spill for the offline reconstruction of the event;

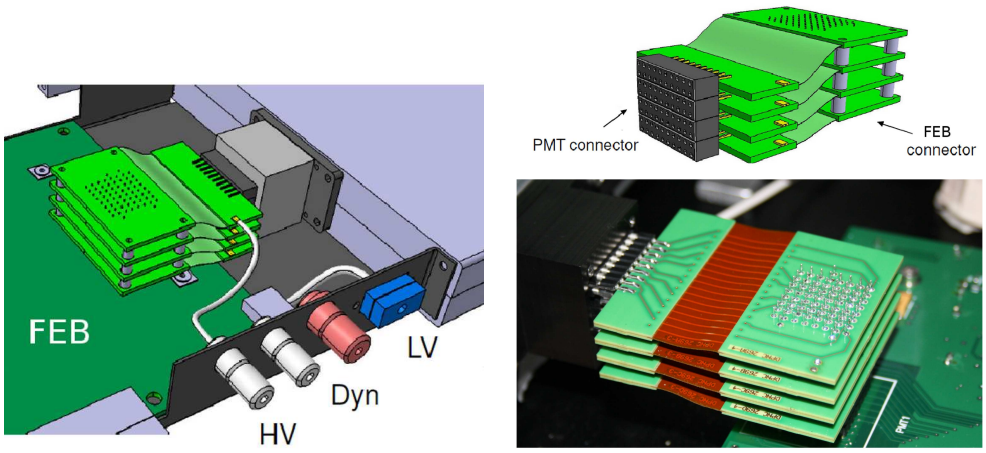


(a) (b)

Figure 3.6: (a) Schematic view of the connection between the MAPMT and the frontend electronics. (b) Schematic view and photo of the flexible kapton connectors. [Courtesy of the UNIGE group]

- the *Data AcQuisition system (DAQ)*, consisting in a VME crate hosting the configuration, the trigger and the readout boards. The Configuration Board main task is the configuration of the FEBs that is the setting of the ASIC mask (including the preamplifier gain, the shaper parameters, the discriminators threshold). The configuration of the BBs (in terms of clock rate, data format, etc.) will also be managed by this board. The boards will be configured at the beginning of each run. A dedicated trigger board is foreseen to send the experiment trigger and the spill gate to the BBs. The clock synchronization between the boards will be performed using the trigger signal.

The communication between the BBs and the readout boards will be based on the TLK1501 (Texas Instrument[6]) Gigabit link; 6 BBs will be daisy chained with twisted cables while the Gigabit link will use a coaxial cable, thus 8 readout boards are foreseen.
A scheme of the complete EMR electronics chain is given in figure 3.7. The analog signal of each single channel PMT is sampled and digitized by a V1731 Wave Form Digitizer (WFD, CAEN) housed in the VME crate.

#### 3.1.4.1 The prototype FEB

As it will be described in section 3.2, the design of EMR has required the production and test of several prototypes of the frontend electronics, in order to optimize

[6] http://www.ti.com

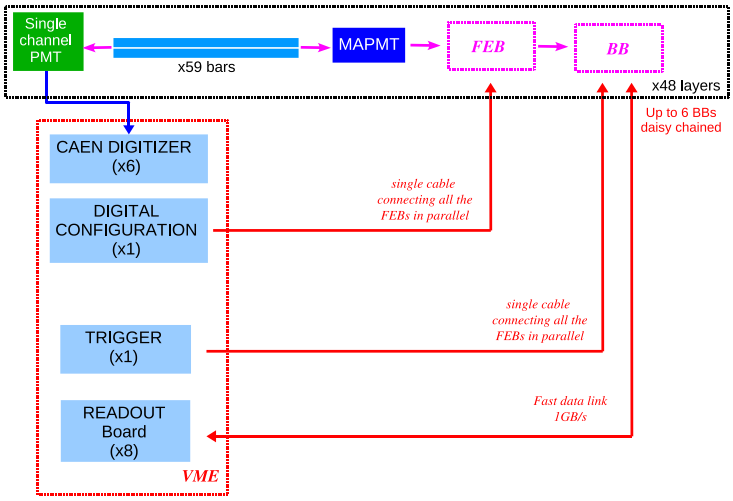


Figure 3.7: Scheme of the electronics chain for the readout and setting of the EMR detector. The single channel PMT output is directly connected to a CAEN WFD housed in the VME crate. The MAPMTs signals are sampled and digitized by the FrontEnd Board (FEB) and the Buffer Board (BB). The connection between the BBs and the VME system is made through a Gigabit link.

the readout choices and the cost. The prototype presented in figure 3.8 is the last one; the final board will have the same features and will be smaller from the dimension point of view.
The board hosts a socket for the 64 channel photomultiplier, the MAROC-II ASIC and two Altera Cyclone II FPGAs[7], 2 FLEX connectors for the configuration and analog readout and 2 high density ERNI[8] connectors to provide the digital signals to the Buffer Board.
The ASIC chosen for EMR is the MAROC-II (Multi-Anode ReadOut Chip II) ASIC[9] (Laboratoire del'Acélérateur Linéaire, LAL Orsay) which has been designed for the readout of the Hamamatsu photomultipliers used by the ATLAS Luminometer [93]: it has an area of 16 $mm^2$ and it is manufactured with the AMS[10] Si-Ge 0.35 $\mu$m technology (figure 3.9(a)). The ASIC is packaged in a CQFP240 package so no bonding for the connections is needed and the FEB does not require a fine pitch (reducing considerably the costs).
The block diagram of the MAROC-II ASIC is shown in figure 3.9(b): it has 64

[7] model EP2C8Q208C7; Altera Corporation, http://www.altera.com
[8] ERNI Electronics Inc., http://www.erni.com
[9] MAROC-II datasheet, http://omega.in2p3.fr/V1/data/Maroc/docs/datasheet_maroc2.pdf
[10] Austria Mikro Systeme International AG; http://www.austriamicrosystems.com

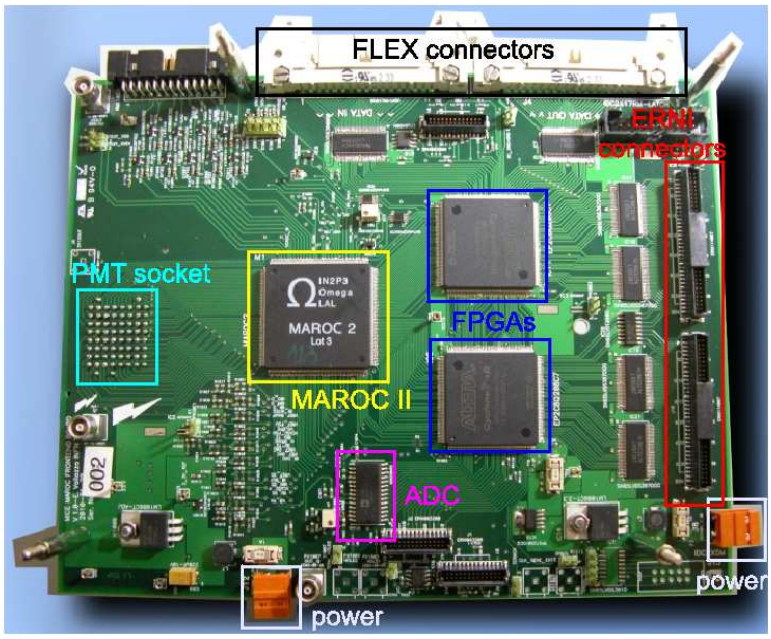


Figure 3.8: A photo of the FrontEnd Board (FEB) with all its components.

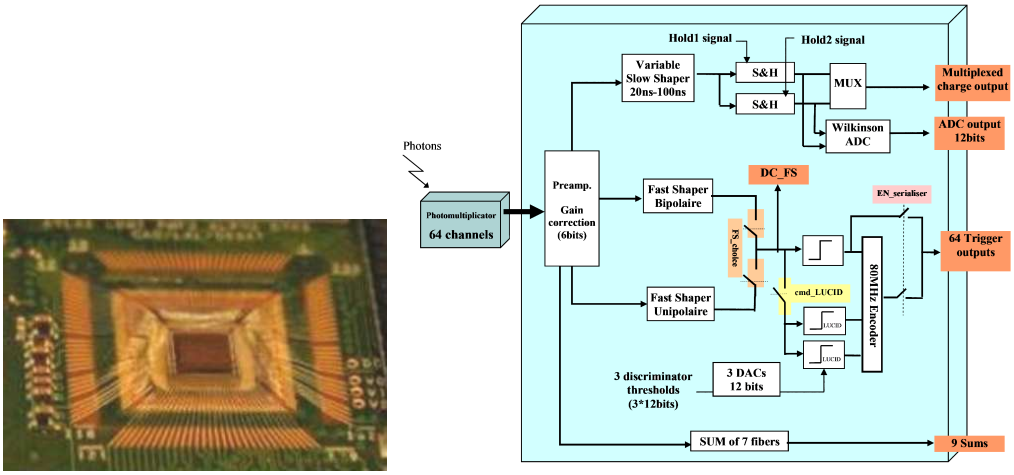


(a) (b)

Figure 3.9: (a) A photo of the MAROC-II ASIC. (b) Schematics of the MAROC-II architecture.

identical channels consisting of a preamplifier, 2 shapers (a fast and a slow one), a Sample&Hold circuit and a discriminator; a 12 bit Wilkinson ADC is integrated in the ASIC (but it does not work in the MAROC-II version which is the one tested in this thesis).
For each of the 64 channels, the MAPMT signals are first amplified by a variable gain preamplifier which has low noise and low input impedance. The amplified current then feeds a slow shaper, with three switchable capacitances to allow tuning the peaking time, combined with two Sample&Hold buffers. The multiplexed analog data are sent out to be digitized by the AD9220 (Analog Devices[11] ADC integrated in the board[12].
In parallel, 64 trigger outputs are produced through the fast channels consisting of a fast ($\approx 20-50$ ns) shaper followed by three identical discriminators (two of them are not used in the EMR readout): the thresholds are set by an internal effective 12 bit DAC (4 bits for the coarse tuning and 8 for the fine one).
The sum of up to seven preamplifier outputs has also been implemented for a total of 9 sum outputs. For example, SUM8 corresponds to the sum over the first 7 channels.
Several characterization tests have been performed on the FEB to study the analog output as a function of the different tunable parameters: the obtained results are summarized in Appendix A.
Two of these boards are presently used for the test of the planes during the construction at UNIGE.

## 3.2 The Electron Muon Ranger prototypes

The design of EMR has been finalized in steps optimizing materials, cost and performance. A first small scale prototype (called *EMR small prototype* [90]) has been developed to define the assembly procedure, the time schedule of the construction and to be used as a test bench for the electronics development; this prototype has allowed to measure the performance in terms of spatial resolution and efficiency of the complete system.
Together with the prototype, different bar configurations have been tested:

- four long rectangular shape bars with the same length as in the final detector and readout with different configurations (one or two WLS fibers, glued or not in the bar hole);

[11] http://www.analog.com

[12] A multiplexed readout is the one in which the sampled signals are sent out one after the other on the differential output buffer thanks to a clock signal.

- five long triangular shape bars with the same length as in the final detector readout with two 0.8 mm diameter WLS fibers glued in the bar hole.

These two setups have allowed to determine in a conclusive way the need of glue inside the bar hole[13] and the increased efficiency with the triangular bars.

### 3.2.1 The EMR small prototype

A schematic view of the EMR small prototype is shown in figure 3.10(a): it has been produced by INFN Sezione di Trieste (INFN TS) in Spring 2007. It consists of 8 modules organized in 2 blocks, with 2x and 2y layers each, separated by a 3 cm air gap (figure 3.10(b)). Each layer is composed of 10 19 cm long extruded scintillator bars with a rectangular cross section ($1.9 \times 1.5$ cm$^2$). The light produced in the scintillators is brought out by four 0.8 mm diameter WLS fibers to a 64 channel multianode photomultiplier (R7600-00-M64, H7546B assembly - Hamamatsu). One MAPMT is used for each layer type, thus only 40 anodes per MAPMT are connected. The fibers have been aligned with the cathode through a double mask: one to direct them and one in front of the MAPMT itself. The whole detector is housed in an aluminum box that provides both the light tightness and the MAPMTs and their electronics support.

#### 3.2.1.1 The electronics

Three different versions of the frontend electronics have been tested with the EMR small prototype during these two years to study their performances as a readout system for the scintillator bars:

- the first version is exactly the same used in the ASACUSA experiment for the readout of the FAST detector (a scintillating fiber tracker [96, 97]). Given the mechanical constraints of FAST, the frontend electronics was divided on two different boards, one with the VLSI ASICs for the conditioning of the MAPMT signals and one (repeater) for the interface with the VME DAQ;

- the second version consisted of a single board, called *MUSTAP board* (MUSashi vaTAP board), that included both the frontend and repeater features to reduce the noise due to cabling and to limit the number of connections;

[13] The different values of the refraction index of the bar, of the WLS fiber and of the air inside the bar hole cause, in fact, reflections between the different interfaces and consequently a reduction of the light transmission. Nevertheless, this can be improved by filling the bar hole using a medium with a refraction index much closer to that of the scintillator and fiber coating, like the epoxy glue. In this way the light collection can be larger by a factor $1.9-2.0$ [94, 95].

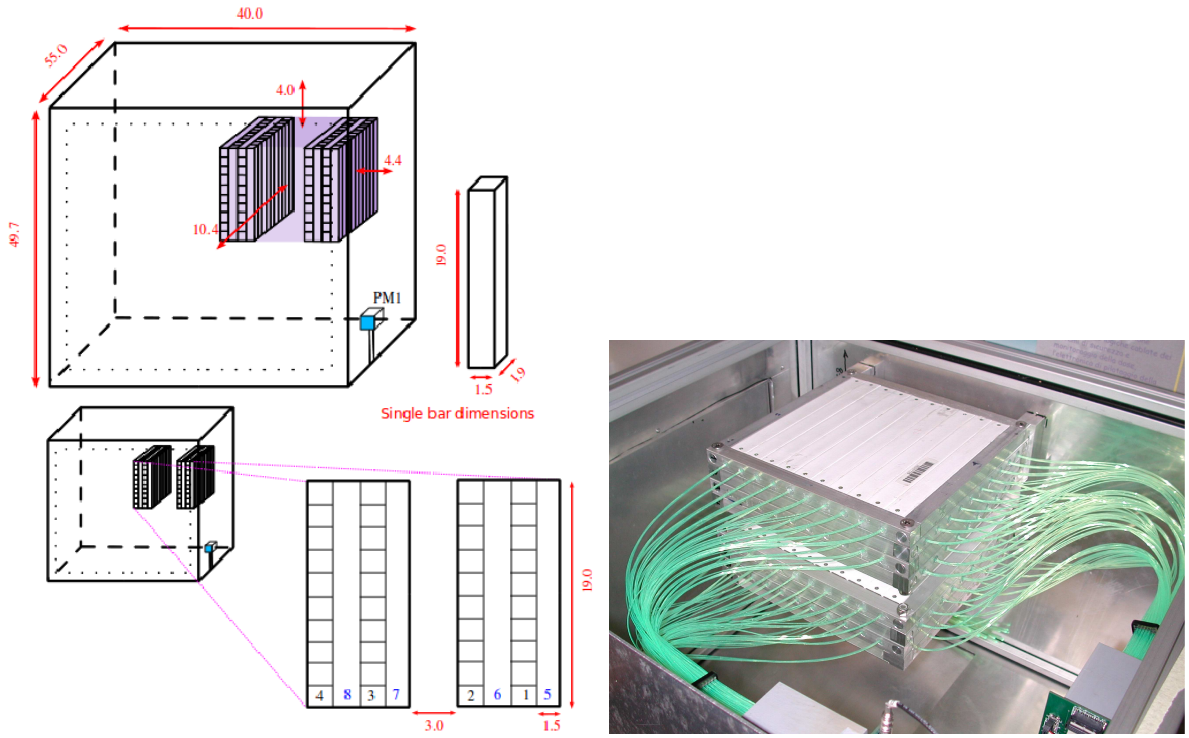


(a) (b)

Figure 3.10: (a) Schematic view of the EMR small prototype (the dimensions are in cm): it consists of 8 layers of rectangular shape scintillator bars in a x−y geometry arranged in 2 blocks separated by a 3 cm air gap. (b) A photo of the EMR small prototype inside its aluminum box.

- the last one, based on the MAROC-II ASIC, is the same used in the final detector (see section 3.1.4 for the details).

The readout electronics was the same for all the three studied frontend configurations and was based on a standard VME system with custom boards for the readout sequence generation, the configuration of the frontend and the data storage.
A schematic view of the first version of the EMR small prototype electronics chain is given in figure 3.11(a).

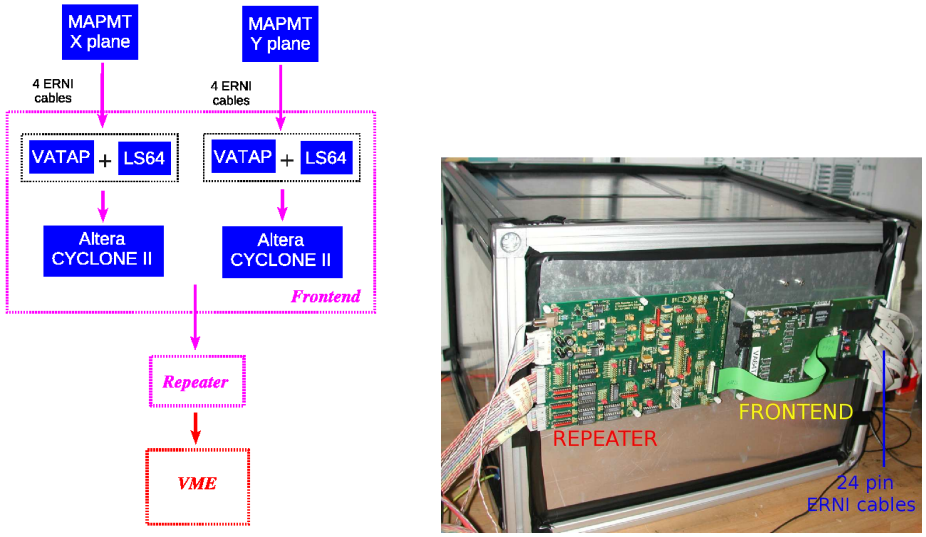


(a) (b)

Figure 3.11: (a) Scheme of the first version of the readout electronics for the EMR small prototype. The frontend board is based on a couple of ASICs (VA64TAP2.1 and LS64_2) and an Altera Cyclone II. The repeater board is the interface between the frontend one and the VME system. (b) A photo of the electronics chain connected to the EMR small prototype.

The frontend board (figure 3.11(b)) consisted of a Printed Circuit Board (PCB) of $125 \times 230$ mm$^2$ with two complete readout chains. The 64 signals of each MAPMT are brought to the board with 4 26 pin ERNI short cables and are amplified, shaped, discriminated and sampled by the VA64TAP2.1 ASIC (Gamma Medica - IDEAS[14]). This ASIC is built in 0.35 $\mu$m N-well CMOS double-poly triple metal technology. The architecture of a single channel of the ASIC is shown in figure 3.12(a). It consists of a preamplifier with pole zero cancellation to minimize pile-up effects, a CR-RC fast shaper ($50-75$ ns of peaking time) and a

[14] http://www.gm-ideas.com

discriminator with a global threshold for all the channels and a 4 bit trim DAC per channel to minimize the offset spread. It can work both in analog and digital mode. The analog readout is a multiplexed one with a maximum readout clock of 10 MHz.
When the digital outputs are enabled, the discriminators generate a fixed width square pulse whenever the shaper output overcomes the threshold. The discriminated signal duration is set by a monostable, hence there is no correlation between its value and the pulse height of the shaper output. The parallel trigger outputs are open drain and are terminated with a low impedance to prevent pile-up effects. To feed a FPGA they are level-shifted to low voltage TTL (LV-TTL) by a second ASIC, the LS64_2 (Gamma Medica - IDEAS) (see [98] for a complete description of the readout electronics). Figure 3.12(b) shows a photo of the couple of ASICs.

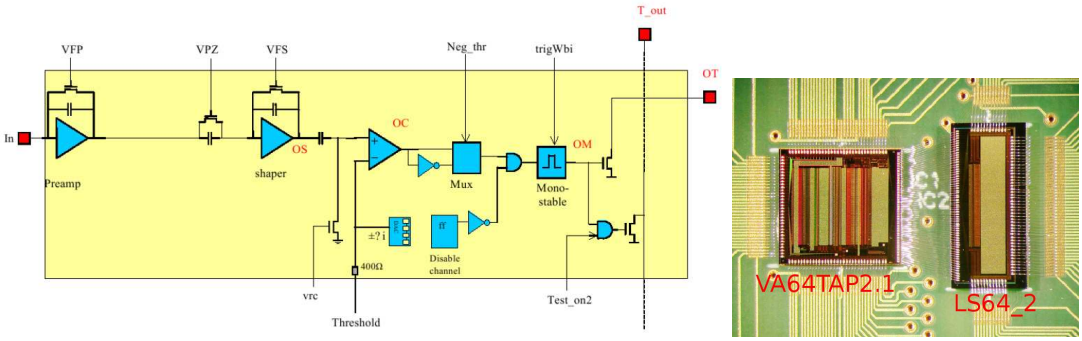


(a) (b)

Figure 3.12: (a) Schematic of one channel of the VA64TAP2.1 ASIC. (b) A photo of the two ASICs used in the frontend board.

The repeater board has the following tasks:

- it provides the biases and control signals of the ASICs and sets the discriminators threshold;
- it performs a further amplification of the analog output with a NE592 (Texas Instrument);
- it handles the communication between the control FPGAs and the VME DAQ system.

Even if this version of the electronics would allow to perform both the analog and digital (as in FAST) readout, the prototype has always been tested using the analog option.
Figure 3.13 presents a schematic view and a photo of the second version of the

EMR small prototype electronics that is the *MUSTAP board*. This board has been designed for the ASACUSA CUSP-TRAP (MUSASHI) experiment [92, 99] for the readout of a scintillating bar tracker made of 4 (x+y) modules of the same squared bars tested in this thesis work (see section 3.2.2). The MUSTAP board is based on the same couple of ASICs of the FAST electronics and the functions of both the frontend and repeater boards have been integrated in it. Moreover it includes a dedicated socket to directly connect the MAPMTs limiting the electromagnetic noise induced on the ERNI cables [92]. As in the previous case, the prototype has been tested using the analog option. In the MUSTAP board however, the ADC (AD9220 by Analog Devices) is directly located on the board thus the trasmission concerns only digital signals which are then zero-suppressed on the VME readout board (INFN TS).

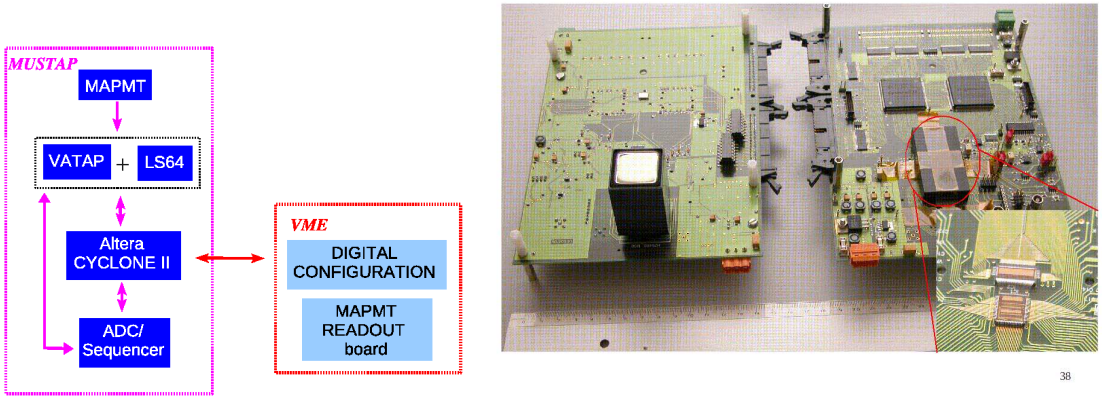


(a) (b)

Figure 3.13: (a) Scheme of the second version of the readout electronics for the EMR small prototype: it is based on the *MUSTAP board*. (b) A photo of the MUSTAP board: the MAPMTs are directly plugged into the board through a dedicated socket to avoid electromagnetic noise.

The EMR small prototype has also been tested with the prototype of the FEB described in detail in section 3.1.4.1.

### 3.2.1.2 Design and construction

The construction of the EMR small prototype has allowed to define the assembly procedure and time schedule of the final EMR detector; the following items have been considered:

- *bar preparation*; the cutting speed of the scintillator bars has been chosen carefully to prevent bars from breaking: a too high speed means melting

them, a too small one resulted in creating cracks that could decrease the light collection efficiency;

- *gluing procedure*; before inserting the fibers, two holes have been manufactured on the two ends of the bar top face. The fiber is then inserted and blocked at the two ends closing the main holes with silicone glue. A syringe with the glue is inserted in one of these holes and the glue insertion goes on until the glue itself comes out from the other hole (figure 3.14(a)); particular care has been taken not to leave air inside;

- *final assembly*; 10 bars are grouped together to assemble each layer: an aluminum frame, including an extension to protect the fibers (figure 3.14(b)), has been designed to support each layer.

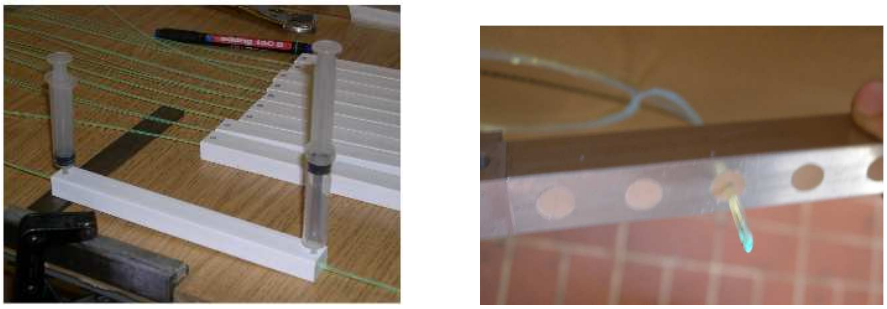

(a) (b)

Figure 3.14: EMR small prototype assembly phases. (a) The WLS fibers have been inserted and glued in the bar hole paying attention not to leave air inside the bar hole. (b) In order to protect and support the fibers exiting from each bar, an aluminum frame has been designed: the fibers pass through the o-ring of the frame and are then fixed with silicone glue. [Courtesy of INFN Sezione di Trieste]

### 3.2.2 The long bars

While the small scale prototype has been used to test the electronics versions and the overall detector performance in terms of spatial resolution, efficiency and stability in long term data takings, dedicated setups had to be assembled for the validation and test of the scintillating bars and of the best readout configuration (number of fibers per bar and use of the glue).
Two different setups have been developed for the test of:

- four rectangular shape bars with the same cross section of the small size prototype ones and a length of 96 cm provided by FNAL. Their response in terms of efficiency and pulse height has been studied with four different readout configurations [90]. One or two 0.8 mm diameter WLS fibers have been inserted and glued or not in the bar hole (figure 3.15(a)); also a configuration consisting of a 1 mm diameter WLS fiber without glue has been studied. The fibers have been interfaced to a 16 channel H8711-100 MAPMT from Hamamatsu (figure 3.15(b)) and the signal was integrated by a QDC (V792 from CAEN); no amplification was provided;

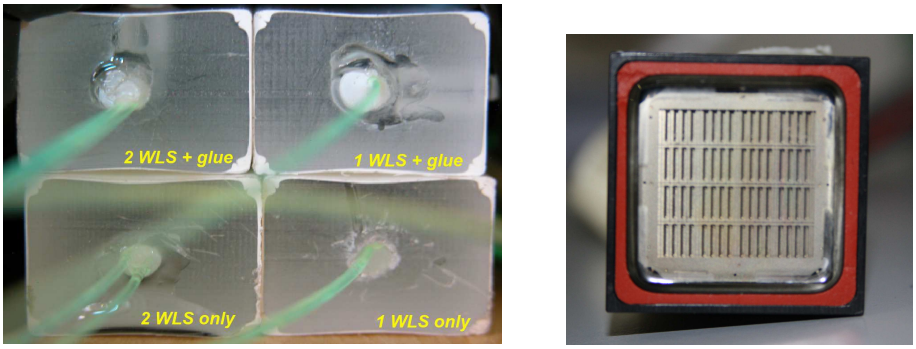


(a) (b)

Figure 3.15: (a) A front view photo of the four rectangular shape bars: the readout configuration is indicated on the photo. (b) A front view photo of the 16 channel H8711-100 MAPMT.

- five triangular shape bars (base=3.3 cm, height=1.7 cm and length=1.1 m, figure 3.16) connected to the MUSTAP board [100]. The light was brought out by two 0.8 mm diameter WLS fibers with the same length of the final ones and glued[15] in the bar hole. The fibers were connected on both sides to the same 64 channel H7546B.

Both the four rectangular shape bars and the five triangular shape ones have been tested at the CERN Proton Synchrotron (PS) T9 beam line (summer 2008 and 2009) with electron, muon and pion beams in a momentum range between 0.5 and 15.0 GeV/c [90, 100]. The complete setup and the results are presented in the next chapter (section 4.4.1 and 4.4.2).

[15] In one of the bars there wasn't the glue.

Figure 3.16: A photo of the five triangular long bars connected to the MAPMT + FEB prototype: each bar is 1.1 m long and is readout by two 0.8 mm diameter WLS fibers connected on both sides to the 64 channel MAPMT.

# Chapter 4

# The EMR design qualification tests

The design of the Electron Muon Ranger (Chapter 3) of the MICE experiment has required several tests, both with cosmic rays (at the Insubria University in Como) and extracted particle beams (at the CERN Proton Synchrotron beamlines), of its prototype and components to study the detector performances with different readout configurations and identify the best solution for the final readout electronics.
As already described in Chapter 3, a small scale prototype has been developed both to understand the performance of the overall system (scintillator + WLS fibers + MAPMT) and to use it as a test bench for the electronics chain. On the other hand, the final shape of the bars and the number of fibers to use per bar (together with the presence of the glue) have been studied using the same procedure as for the prototype.
The first part of this chapter is dedicated to the description of the CERN experimental areas, of the test procedure and of the instrumentation (tracking and trigger systems) used in the test setups.
The second part of the chapter contains the results obtained both with the small scale prototype and the components.
The stripping procedure for the analysis of the raw data is presented in Appendix B.

## 4.1 The CERN PS T9 and T10 beamlines

The T9 and T10 beamlines [101] are located in the East Hall Area (building 157) of the CERN complex (figure 4.1(a)). These two experimental areas provide secondary beams of charged particles (typically $\mu, \pi$ and $e$) in a momentum range from 0.5 to 15 GeV/c (T10 only up to 7 GeV/c) deriving from the interaction of a primary 24 GeV/c proton beam with a target[1]. The beam structure foresees typical

[1] Different types of targets are available and allow to vary the percentage of electrons, muons and pions in the secondary beams.

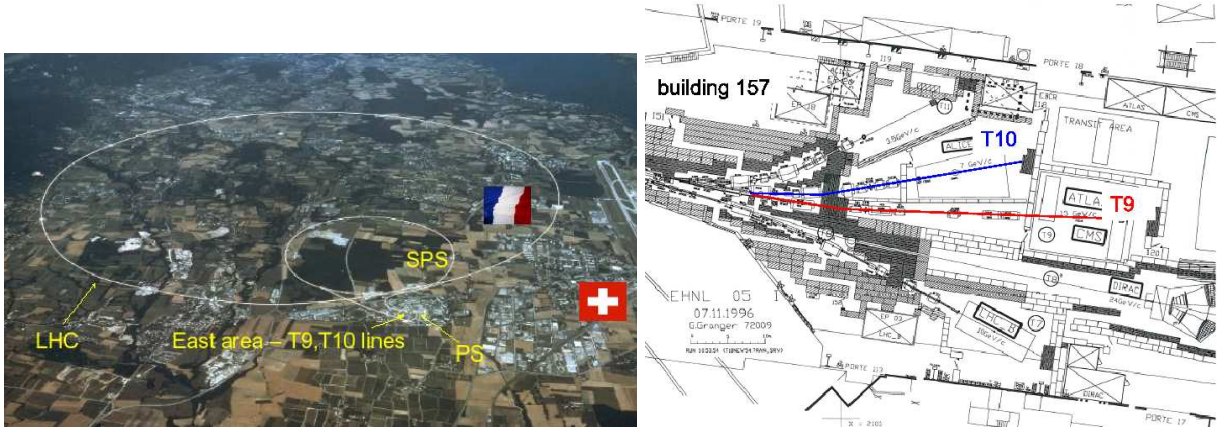


(a) (b)

Figure 4.1: (a) An aerial view of the CERN complex: the T9 and T10 beamlines are located in the East Hall of the PS complex. (b) Schematic layout of the East Hall: T10 is indicated with the blue line while T9 with the red one.

intensities of the order of $10^4-10^5$ particles per bunch (the so-called *spill*) for a bunch duration of $\sim 300$ ms with a repetition period of 45 s. The secondary beams are selected by a horizontal collimator at the beginning of the line (not shown in figure 4.1(b)) while the focusing and tuning of the beam can be performed with a set of dipole and quadrupole magnets and both vertical and horizontal collimators. Both the lines are also equipped with threshold Cherenkov counters and beam chamber monitors.
Figure 4.2(a) presents an example of the T9 beam profile (both in the horizontal and vertical directions) as measured by the Silicon Beam Chambers (SiBCs, see section 4.2.2): the shape of the beam is due to the setting of the collimators. Figure 4.2(b) presents the beam divergence (that is the rms of the angular distribution of the beam particles) reconstructed with the SiBCs; this value includes the Multiple Coulomb scattering contribution due to the material along the beamline. No particular care has been dedicated to the divergence reduction ($\sigma_x = 4.52 \pm 0.01$ mrad and $\sigma_y = 2.91 \pm 0.05$ mrad) given there was no particular requirement for these tests.
Similar results have been obtained for the T10 beam.

## 4.2 Experimental setup

The typical setup is basically the same for the two tests (cosmic rays and extracted beamtests) and is shown in figure 4.3. It consists of a trigger system (TRIG), a

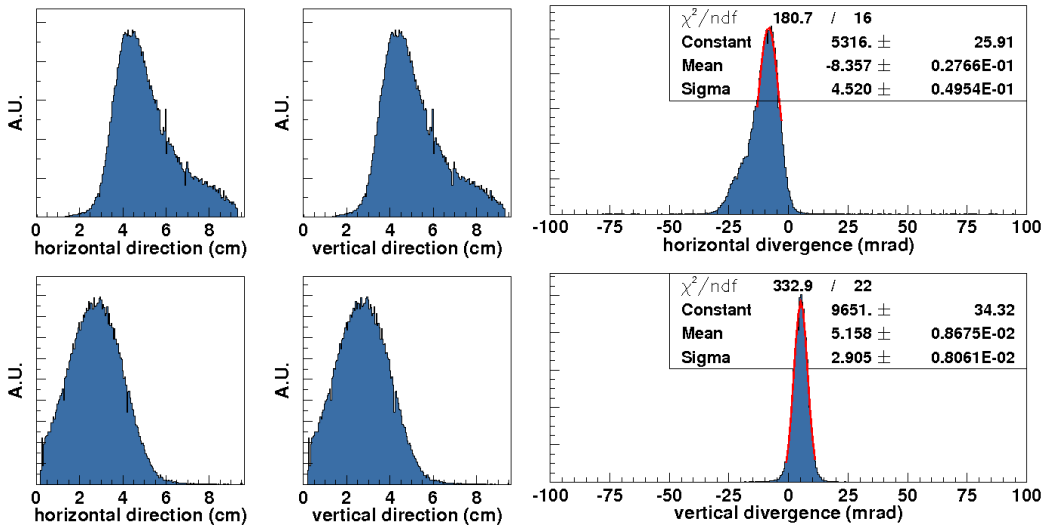


(a) (b)

Figure 4.2: Beam profile (a) and beam divergence (b), in both directions, of the T9 beamline as measured by the SiBCs.

tracking system (TRACKING) for the particle position and direction reconstruction and the detector under test (TEST).
For the trigger, several types of scintillator counters (section 4.2.1) have been used trying to maximize the covered solid angle. In the case of a data taking with an extracted beam (such as on the PS beamlines), the trigger was generated by the coincidence of the scintillator signals and the machine slow extraction one (spill). For the tracking, a set of two silicon microstrip detectors has been used (section 4.2.2).

### 4.2.1 Plastic scintillator counters

Three types of plastic scintillator counters have been used both during the data taking at the CERN PS and in the cosmic ray tests:

- *type I*: a set of two polystyrene tiles with an active area of $3\times10$ cm$^2$ and a thickness of 1 cm (figure 4.4(a)); they are directly connected to two photomultiplier tubes for the readout of the light produced by the particles;

- *type II*: a counter with a larger sensitive area of $10\times10$ cm$^2$ (figure 4.4(b)); also in this case the light produced by the interacting particles is readout with a photomultiplier tube directly connected to the scintillator tile;

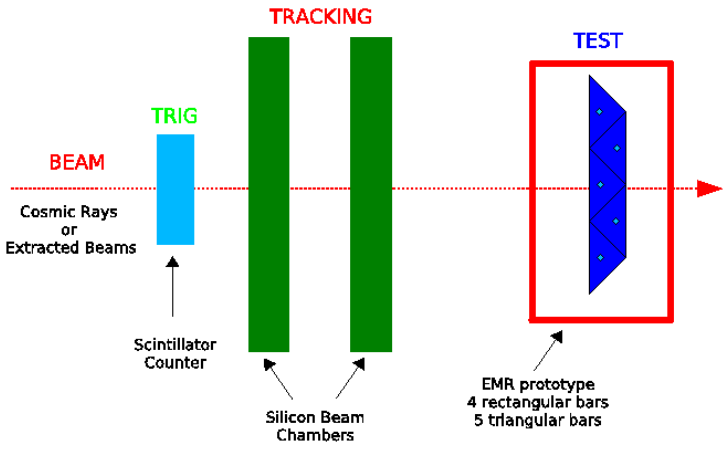


Figure 4.3: A schematic view of the typical setup used for the tests at the CERN PS lines and with cosmic rays. TRIG indicates the triggering device, TRACKING the detector used to reconstruct the particle position and TEST the detector or component under test.

(a)

(b)

Figure 4.4: (a) Photo of the $3\times10$ cm$^2$ scintillator counters (*type I*). (b) Photo of the $10\times10$ cm$^2$ scintillator counter (*type II*).

- *type III*: a set [102] of two $1\times20\times30$ cm$^3$ NE120 (Nuclear Enterprises) scintillator tiles (figure 4.5(a) top) readout by 2 P30CW5 photomultipliers (Electron Tubes[2], figure 4.5(a) bottom) directly coupled to the scintillator (figure 4.5(b) top) and housed in a PVC box (figure 4.5(b) bottom).

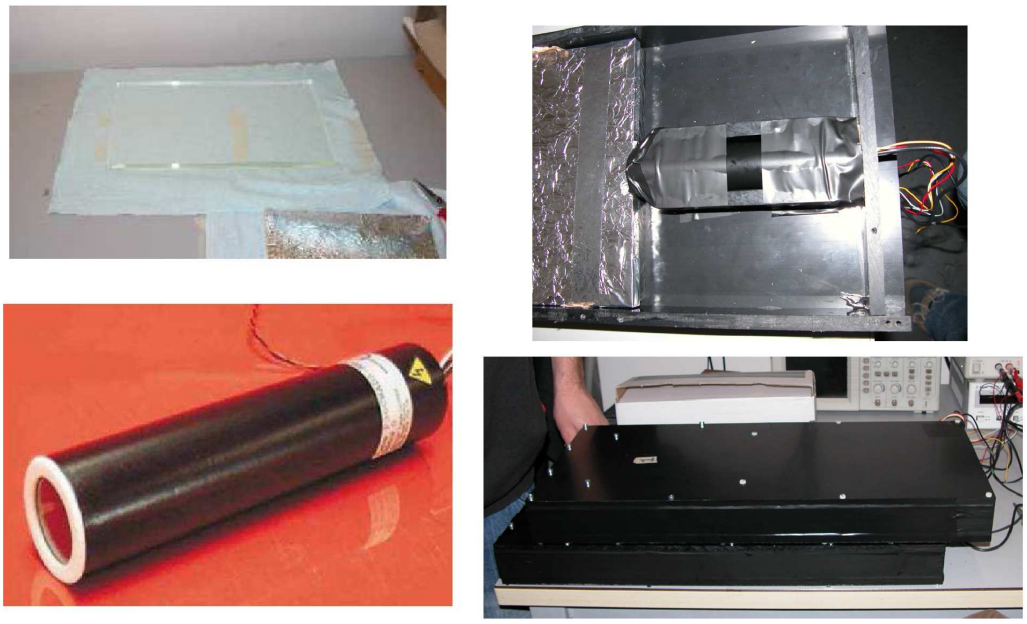

(a) (b)

Figure 4.5: Photos of the third trigger system [102] (*type III*). (a) It is based on two $1\times20\times30$ cm$^3$ NE120 plastic scintillators readout by 2 P30CW5 photomultiplier tubes. (b) A PVC box houses both the scintillator tiles and the PMT.

### 4.2.2 Silicon detectors

The particle tracking system was based on the silicon detectors (called *Silicon Beam Chambers - SiBCs*) developed for the AGILE satellite [103].
Each chamber consists of two single side silicon microstrip detectors (Hamamatsu), arranged in a x$-$y geometry and glued on an epoxy fiberglass support (figure 4.6(a) top). Each silicon tile is 410 $\mu$m thick and has a dimension of $9.5\times9.5$ cm$^2$ for a total of 768 strips. The physical pitch is 121 $\mu$m while the readout one is 242 $\mu$m: a one floating strip scheme has been adopted providing a $\sim$ 40 $\mu$m spatial resolution [103].

[2]http://www.electrontubes.com, now www.senstech.com

Each silicon layer is readout by three 128 channel self-triggering[3] TA1 ASICs (Gamma Medica - IDEAS). The readout is a multiplexed one with a maximum clock frequency of 10 MHz.
The detectors are housed in an aluminum box (figure 4.6(a) bottom) together with a part of the frontend electronics consisting of the PCB with the ASICs and of a repeater board that generates the bias voltages for the ASICs, transforms the digital input signals from RS422 to single ended and amplifies the multiplexed analog output with a NE592 (Texas Instrument).
The readout sequence is generated by a VME Sequencer (INFN TS) while an *ADC Board* (that can be directly located near the SiBCs, figure 4.6(b)) provides the analog output digitization (with a 12 bit AD9220, Analog Devices). The digitized data are sent to a VME Input/Output register that hosts a FPGA responsible of the zero suppression[4] allowing a data taking rate of $\sim$ 1 kHz.

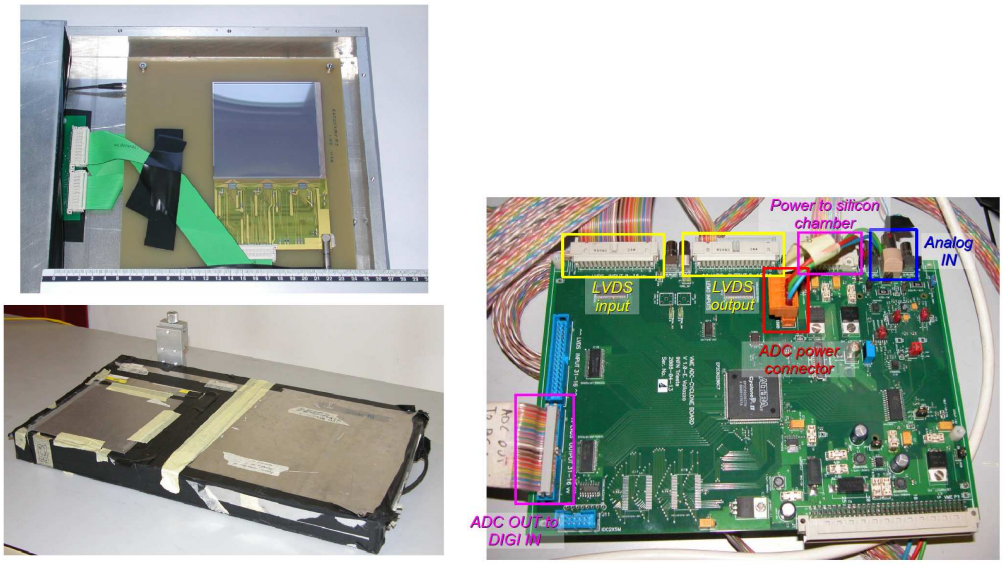


(a) (b)

Figure 4.6: (a) A photo of the single side silicon microstrip detector used for the tracking system (top); the silicon layers are housed in an aluminum box together with a part of the readout electronics (bottom). (b) A photo of the ADC board for the readout of the Silicon Beam Chambers.

[3]The self-triggering feature of this ASIC has not been used since both at the CERN data taking and during the cosmic ray tests the trigger was provided by the set of scintillator counters presented in the previous section.

[4]Only the strips with a signal over a given threshold are stored; the threshold is set considering the noise rms (see Appendix B).

### 4.2.3 The DAQ system

A schematic view of the DAQ chain is shown in figure 4.7(a): the blue lines represent the input signals while the pink ones the output signals from each detector.

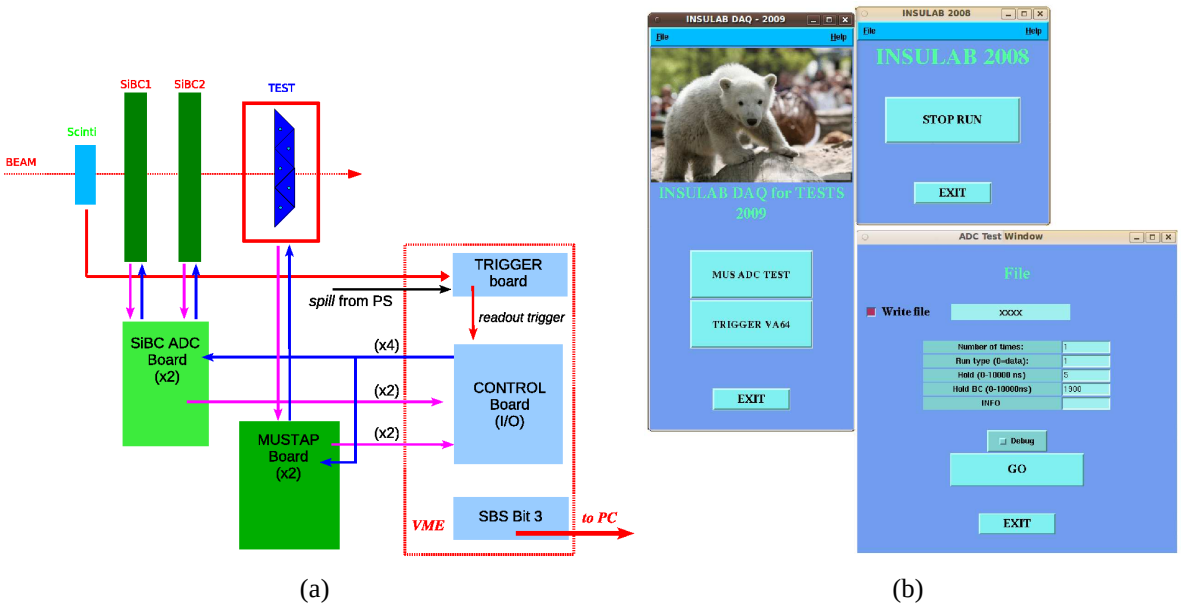


(a) (b)

Figure 4.7: (a) The DAQ chain: it is based on a standard VME system with custom boards. (b) The DAQ user interface.

It is a standard VME system controlled by a SBS Bit3 model 620 bridge[5] optically linked to a PC running the Linux operating system. As mentioned above, the trigger signal is generated by the set of scintillator counters (and the coincidence with the spill signal in the CERN data taking). The conditioning of the trigger signal is provided by a custom VME board (the *trigger board*) and the signals are then sent to a VME *Control Board* (INFN TS) to generate the DAQ trigger and the readout sequence; the board is also responsible of the ASICs configuration before the start of the run. The signals of the SiBCs and of the detector under test are digitized by two dedicated boards (the ADC board and the MUSTAP one, respectively) and sent to the Control Board that is also responsible of the zero suppression of the SiBCs data.
The DAQ software is written in C with Tcl/Tk[6] for the graphic user interface (fig-

[5]SBS Technologies Inc., US, http://www.ge-ip.com

[6]Tcl (Tool Command Language) is a dynamic programming language and Tk is its graphical user interface toolkit, http://www.tcl.tk.

ure 4.7(b)); the output data are stored in binary files (PAW ntuples) and processed offline to obtain ASCII DST (Data Summary Tape) output files with all the relevant information (see Appendix B for details); the analysis software is written in FORTRAN.

### 4.2.4 Test procedure

Although the electronics chain (both for the small scale prototype and the long bars) can work both in analog and digital mode (see section 3.2 for details), the data have been acquired only in analog mode.
The data taking procedure is the following:

- a *pedestal* run is acquired using a random trigger in order to evaluate the baseline and noise distributions of each detector (see section B.1 for details);

- a *data* run is acquired when there are particles. Once an event is triggered by the scintillator counter, a *hold* signal[7], to sample the analog output of the ASICs shapers, is generated by the VME Control Board and starts the readout sequence; the analog outputs are sampled and multiplexed with a maximum readout clock of 10 MHz, sent to the VME Control Board and transferred to the PC; the hold value (which should be set in order to sample the peak of the signal) has been chosen differently for the SiBCs and the EMR prototypes;

- once offline, the pedestal value is subtracted from the raw data in order to evaluate the channel response in units of ADC and to define an event as good (*stripping* procedure, see section B.2 for details);

- the set of good events is stored (see section B.3 for details) and the data analysis to characterize the detectors behaviour is performed.

The performances of both the small scale EMR prototype and of the long rectangular and triangular bars have been tested considering the following figures of merit:

- the *noise*: it has been studied with the pedestal run; its reduction is fundamental, especially for the readout of the final detector at RAL where electromagnetic noise sources are present;

- the *spatial resolution*: the precision with which the detector is able to reconstruct the hit position has been evaluated by means of the SiBCs;

[7] It corresponds to the time interval between the readout trigger generation and the signal sampling.

- the detector *efficiency*: the number of incoming particles computed by the SiBCs and the one measured with the bars have been compared in order to estimate the efficiency and study the different readout configurations to find the best one for the final detector design.

## 4.3 EMR small prototype results

In the following sections the results obtained with the EMR small prototype at the CERN PS T9 beamline are presented. This data taking has allowed to test the overall system (scintillator bars + WLS fibers + MAPMTs) and to validate the FAST electronics.
The setup consisted of the EMR small prototype, two SiBCs placed before it and the *type I* scintillator counter. Only the sets of good events (that means events in which all the 4 SiBC planes have only one cluster) obtained with the stripping procedure shown in Appendix B have been considered in the following analysis.

### 4.3.1 Pedestal and noise

The EMR pedestal distributions are presented in figure 4.8(a) separately for the horizontal and vertical layers. The pedestal distribution represents the baseline of the electronics chain that is the signal digitized by the ADC when there are no particles (see Appendix B for details). This value is affected by the so-called common mode noise which corresponds to a variation of the baseline common to all channels and is due to the noise on the bias line of the detectors. This contribution has been subtracted with the method presented in Appendix B and the obtained distributions of the global noise (black) and of the common mode subtracted one (red) are presented in figure 4.8(b): an average value in the range $1-3$ ADC has been obtained for both the directions. The noisier channels (# 32 in the top and # 48 in the bottom of figure 4.8(b)) can be associated to the fact that these are the channels travelling on the external lines of the ERNI cables connecting the MAPMT and the repeater boards which behave as antennas.

### 4.3.2 Particle position identification

To reconstruct the particle position, i.e. the bar number in which the particle releases its energy, the same method used for the SiBCs has been applied (Appendix B).
The *pull* distribution, that is the ratio between the signal of each bar of each layer and the noise rms of the bar itself, has been considered and a threshold in terms

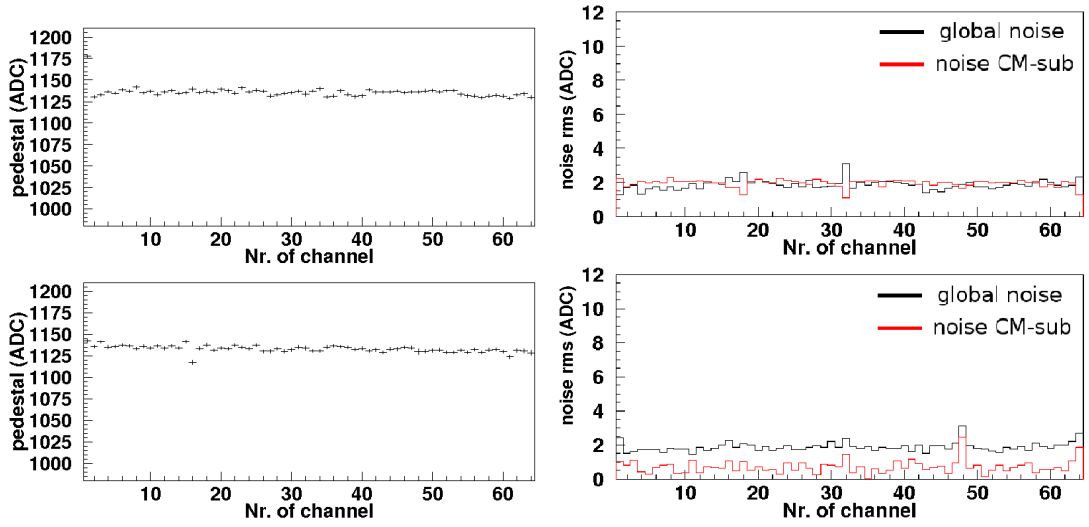


(a) (b)

Figure 4.8: The pedestal (a) and noise rms (b) distributions of the EMR small prototype. The red histograms have been obtained after the common mode subtraction.

of the noise rms has been set: figure 4.9(a) shows an example of the pull distribution of the bar with the maximum signal in the event for one of the EMR layers. This distribution has been used to fix an ADC value (red line in figure 4.9(a)) to distinguish the noise events from the good ones: only the events in which the bar signal was above the value fixed by the red line have been considered as good; a $25\sigma$ pull cut has been chosen.
The pull distribution has also been used to compute the number of bars with a signal over threshold (figure 4.9(b)). Event by event a *counter variable* has been increased of 1 whenever the pull value of a bar was over the chosen threshold: as expected, given the dimension of the T9 beam in each direction ($\sim 3-4$ cm excluding the tales in figure 4.2(a)), this number is tipically 1 or 2; on the other hand the events with only a single bar over threshold were $\sim 4$ times the events with two bars over threshold.
For each event, the method presented above has thus allowed to identify the bar or the group of bars in which the particle releases its energy; the particle position on each EMR layer has been reconstructed considering only the bar with the maximum signal in the event. Given a bar number ($xbar\_max_i$), the hit exact position (in cm) registered by each layer of the EMR small prototype ($xemr_i$) has been obtained with the following transformation:

$$xemr_i = (xbar\_max_i - 1) * width \tag{4.1}$$

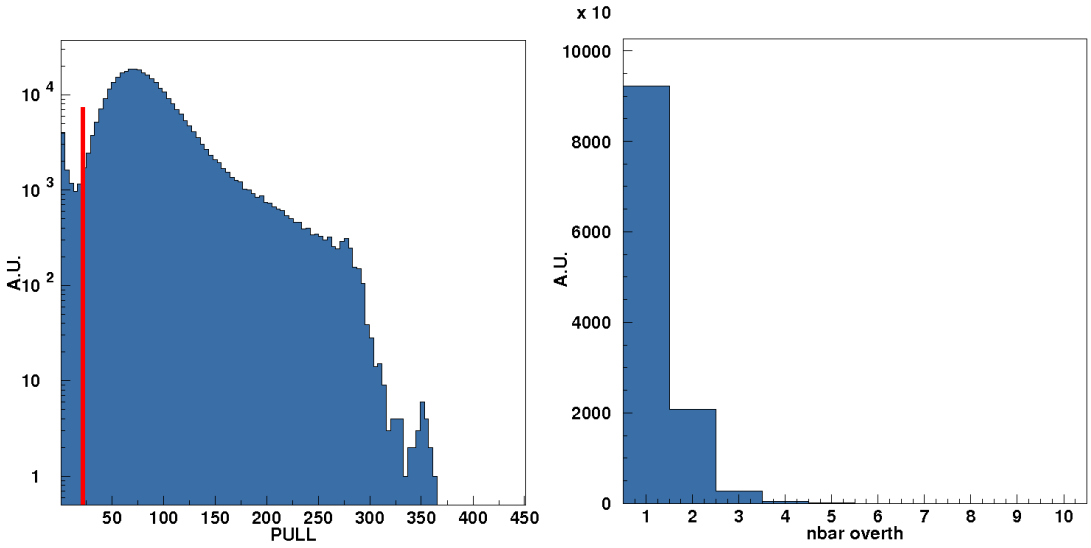


(a) (b)

Figure 4.9: (a) The pull distribution of the bar with the maximum signal in the event of one EMR small prototype layer: the red line shows the set threshold (25σ). (b) The distribution of the number of bars over threshold of one EMR layer (the others behave in the same way).

where the index *i* is the layer number and *width* is the bar dimension along the two directions perpendicular to the beam (that is 1.9 cm). The horizontal beam profiles obtained with the 4 horizontal EMR layers are shown in figure 4.10(a) while the vertical ones are presented in figure 4.10(b): on the left the profiles are shown as a function of the bar number (from 1 to 10 for each layer) while on the right the same profiles have been obtained after the calculation of the effective particle position with equation 4.1.

### 4.3.3 Spatial resolution

The spatial resolution has been computed using the residual method. Referring to figure 4.11:

- the reference detectors (i.e. SiBC 1 and SiBC 2) have been placed before the EMR small prototype at the *zsili*1 and *zsili*2 positions along the beamline and aligned with the method presented in section B.4;

- the trajectory of the particle has been reconstructed by the SiBCs and projected on the surface of each layer of the EMR small prototype with the

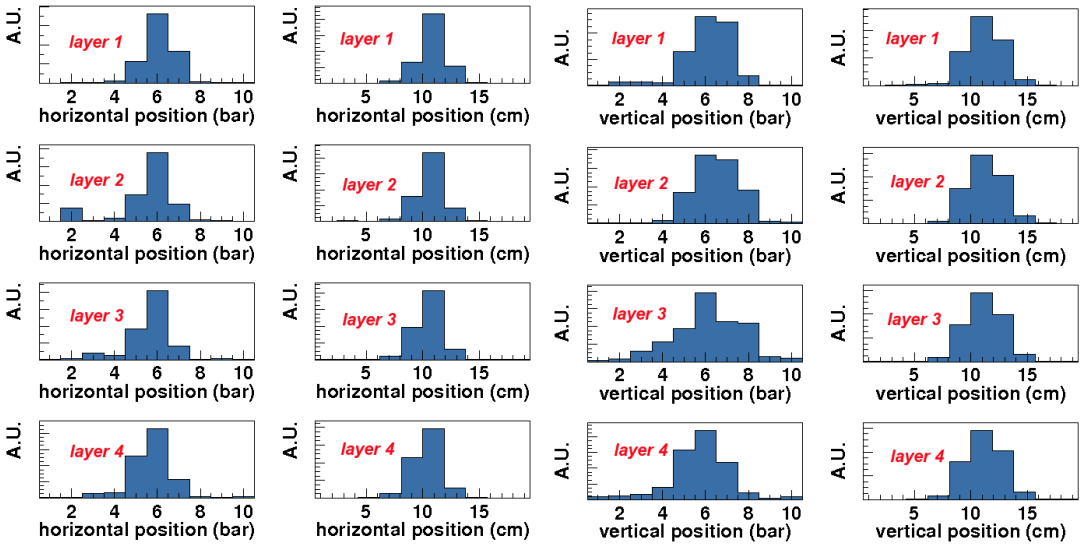


(a) (b)

Figure 4.10: Horizontal (a) and vertical (b) beam profiles obtained with the EMR small prototype layers: the left column of each figure represents the profile as a function of the bar number while the right one is the same as a function of the effective position computed with equation 4.1.

following formulae:

$$\begin{aligned} xproj\_i &= xtan21 * (zemr\_i - zsili1) + xpos1 \\ xtan21 &= \frac{xpos2 - xpos1}{zsili2 - zsili1} \end{aligned} \tag{4.2}$$

where $xtan21$ defines the tangent of the angle between the two silicon detectors;

- the residual is defined as the difference between the position reconstructed with the prototype and the expected one computed with the SiBCs:

$$xres\_i = xproj\_i - xemr\_i \tag{4.3}$$

where $xemr\_i$ is the position measured with each EMR small prototype layer (the formula in equation 4.1 has been used);

- the obtained distributions have been fitted with a Gaussian function (figure 4.12); the sigma value represents the spatial resolution including the Multiple Coulomb scattering contribution. Only the peak region (in the range $\pm 2$ cm) has been considered for the fit since the tails and the lateral

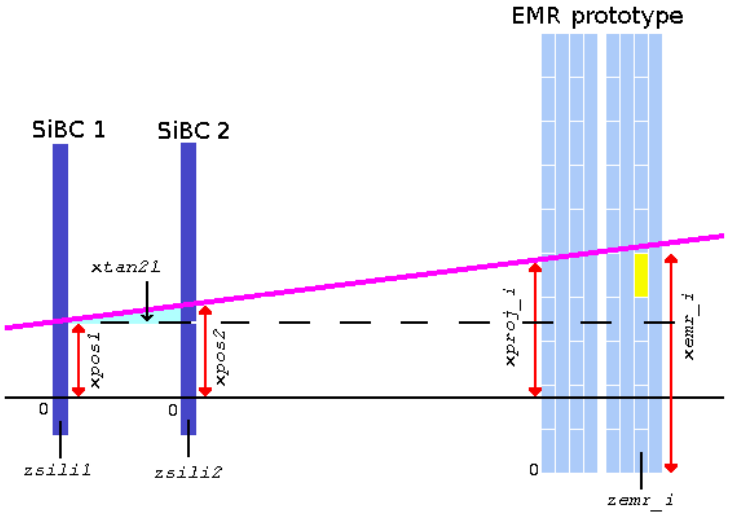


Figure 4.11: Schematic view of the residual method principle: the residual is defined as the difference between the trajectory reconstructed by the SiBCs and the one measured by each EMR small prototype layer.

peaks are due to the cross talk. The resolution values of each layer are listed in table 4.1: an average value of $\sim 6.5$ mm has been obtained for both directions[8].

| layer | res [mm] | layer | res [mm] |
|---|---|---|---|
| 1X | $6.297 \pm 0.008$ | 1Y | $6.396 \pm 0.007$ |
| 2X | $6.405 \pm 0.007$ | 2Y | $6.414 \pm 0.007$ |
| 3X | $6.529 \pm 0.008$ | 3Y | $6.655 \pm 0.008$ |
| 4X | $6.632 \pm 0.008$ | 4Y | $6.651 \pm 0.008$ |
| average | $6.466 \pm 0.158$ | average | $6.529 \pm 0.124$ |

Table 4.1: The spatial resolution of each layer of the EMR small prototype: an average value of $\sim 6.5$ mm has been obtained for both directions.

- the values listed in table 4.1 have been then compared with the theoretical digital one (that is the bar width divided by $\sqrt{12}$) that is $\sim 5.5$ mm. Considering that the measured values include also the Multiple Coulomb scattering contribution and only the bar with the maximum signal has been taken into account to reconstruct the particle position (that means a *digital like* method

[8]The error on the average values has been computed as the standard deviation.

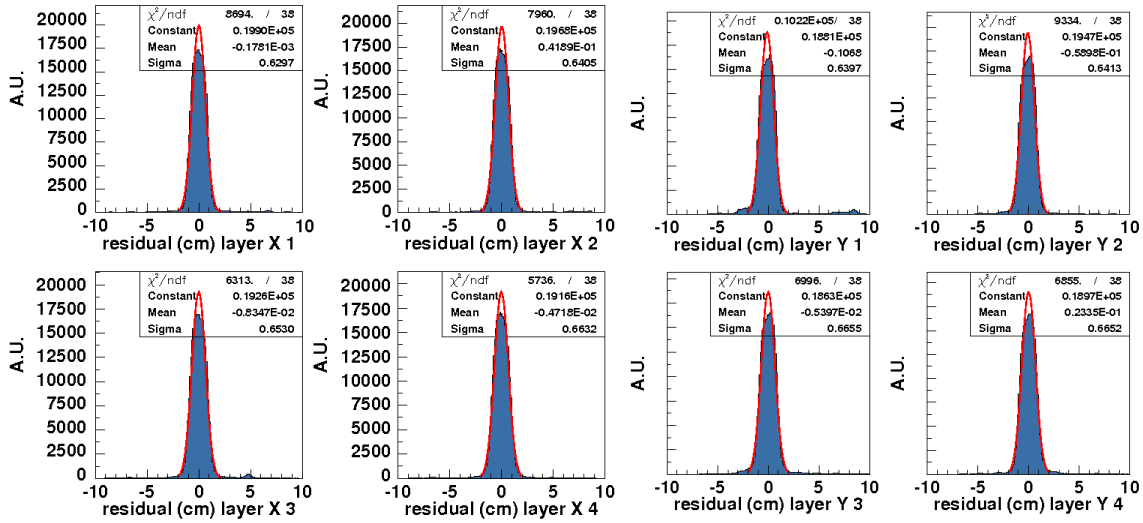


(a) (b)

Figure 4.12: The residual distributions of each EMR small prototype layer: (a) horizontal direction and (b) vertical direction.

has been used), a good agreement has been found for both directions: the average values are $\sim 1$ mm larger than the theoretical one.

### 4.3.4 Efficiency

The efficiency $\xi$ of a detector is defined as the ratio between the number of good events registered by the detector itself ($N_R$) and the total number of good events measured by the reference detectors ($N_{TOT}$), i.e.:

$$\xi = \frac{N_R}{N_{TOT}} \tag{4.4}$$

The efficiency of the EMR small prototype has been evaluated in the following way:

- the beam particles are detected by the SiBCs and the coordinate system of the EMR small prototype has been aligned with the one of the silicon detectors through the residual distributions[9];
- the expected point of interaction on the EMR small prototype has been computed projecting the trajectories reconstructed by the SiBCs on the surface of the different layers;

[9] If the detectors are perfectly aligned, the residual distribution is centered on 0; an offline shift of the EMR small prototype coordinate system has been added to align all the detectors.

- referring to figure 4.13, the reconstructed point of interaction on each EMR small prototype layer (real number in the range $1-19$ cm) has been associated to an expected bar number (integer number in the range $1-10$); the following transformation has been used:

$$xbar\_exp = int\left(\frac{xproj\_i}{width}\right)+1. \tag{4.5}$$

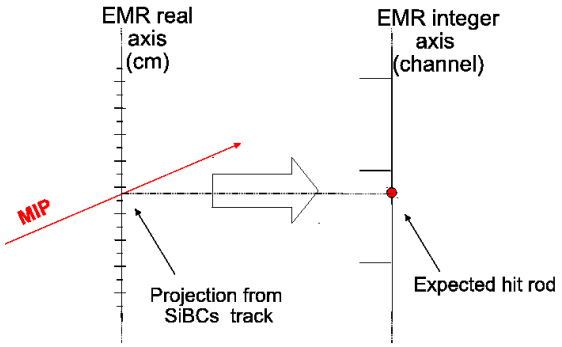


Figure 4.13: Schematic view of the method used to compute the efficiency of the EMR small prototype: the expected point of interaction on the EMR layers reconstructed by the SiBCs is associated to an expected bar number.

- a profile histogram for each layer has been filled with 0 or 1 depending on the pulse height of the expected bar (a threshold to define the passage of the particles has been set as mentioned above considering the pull distribution); the average resulting histogram represents the *raw* efficiency of each EMR layer as a function of the incoming particle position (figure 4.14): only the detector region where the beam impinges (region of interest) has been considered. The regions with a very poor efficiency are due to the efficiency calculation method; in fact, when a particle hits the bar close to the edge, the reconstruction errors are not negligible and the particle could be associated to the wrong bar (figure 4.15);

- the efficiency has thus been computed improving and refining the analysis method of the track reconstruction: it has been evaluated not only considering the expected bar but also taking into account the surrounding ones. A profile histogram of the *effective* efficiency of each layer has been filled with 1 if the pulse height of the expected bar or one of the two neighbouring ones was over the threshold fixed by the pull distribution. In other words, if the particle is expected to pass through bar number 3, the pulse height of bars

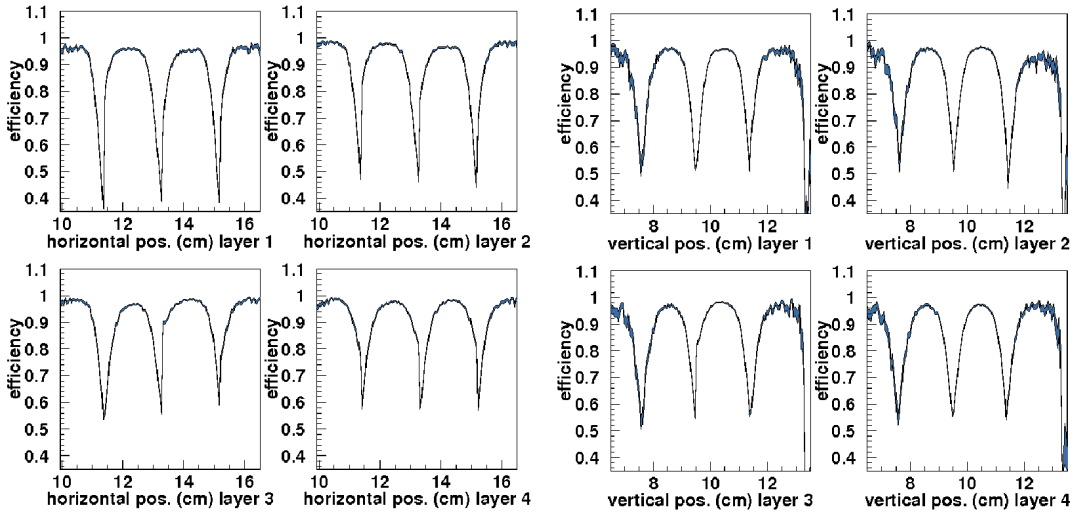


(a) (b)

Figure 4.14: The *raw* efficiency plot obtained for the horizontal (a) and vertical (b) layers of the EMR small prototype: a maximum value of about 97% has been measured in both the directions but deep valleys between following bars are present due to the calculation method.

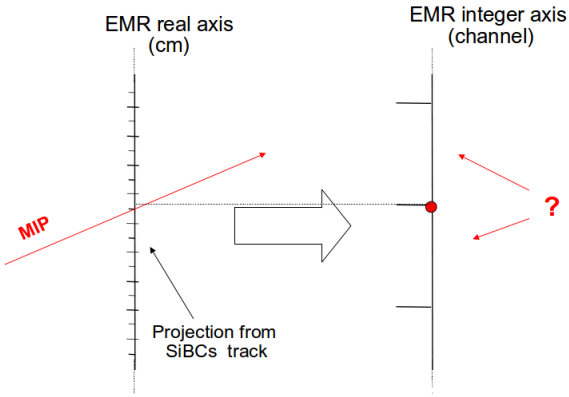


Figure 4.15: When a particle hits the bar close to the edges, the reconstruction errors are not negligible and a wrong bar number could be associated to the incoming particle.

number 2, 3 and 4 has been considered and if at least one of them was over threshold, the particle in the event has been considered as "detected" (that is a 1 has been put into the profile histogram described before). Figure 4.16 shows the effective efficiency measured with the EMR small prototype layers (the spikes at both edges of each figure correspond to the regions with poor statistics): the dead region depth has been reduced and the remaining poor efficiency regions are due to the shape of the bars themselves (the edges are not perfectly regular resulting in a dead region of up to 0.5 mm, figure 4.17(a));

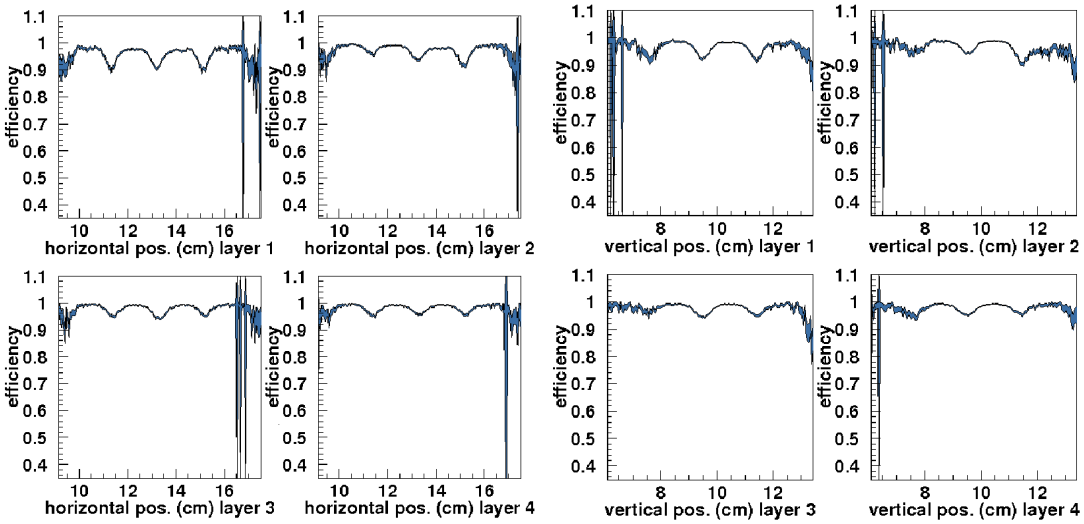


(a) (b)

Figure 4.16: The *effective* efficiency plot obtained for the horizontal (a) and vertical (b) layers of the EMR small prototype (the lateral spikes are the poor statistics regions): the dead regions depth has been reduced and a maximum value of about 99% has been obtained in both the directions.

- the effect of the curved edges has been studied varying the momentum of the incoming particles from 2 to 15 GeV/c (the Multiple Coulomb scattering contribution goes like (energy)$^{-1}$). The efficiency profile in the interesting region has been inverted and offset to 0 in order to fit it with a Gaussian function (figure 4.17(b)):

$$G(x) = P1 \cdot \exp\left[\frac{(x-P2)^2}{2 \cdot P3^2}\right] \tag{4.6}$$

where $P1$ corresponds to the dead regions depth while $P3$ indicates the dead regions width. Figure 4.18 shows the "inverted efficiency" (that is the *in-*

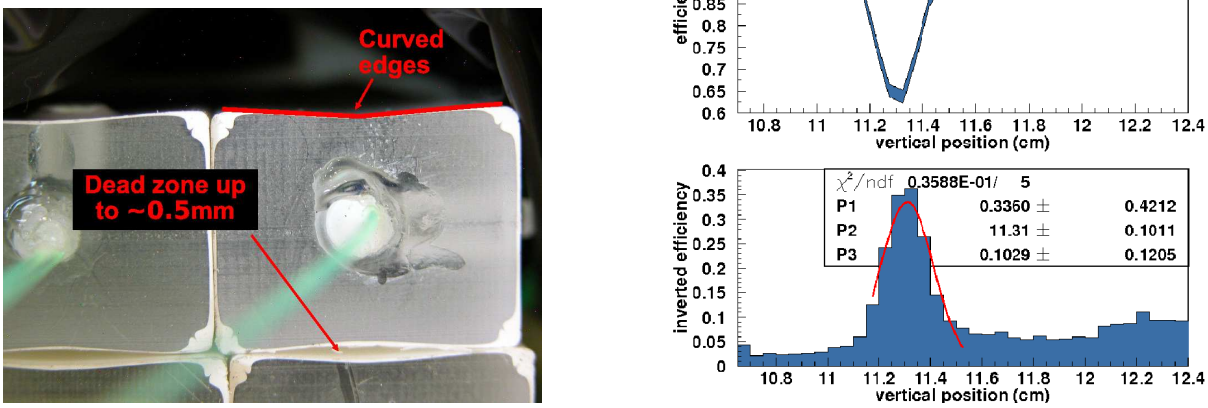


(a) (b)

Figure 4.17: (a) A front view of the rectangular bars: a dead area up to $\sim 0.5$ mm is present. (b) The Gaussian fit of the inefficiency of one vertical layer: the constant and sigma values represent the dead regions width and depth, respectively.

*efficiency*) calculated with one of the vertical EMR small prototype layers at 5 different values of the beam momentum. The greater is the momentum the better is the particle track reconstruction: at 15 GeV/c the dead regions have been reduced to less than 0.5 mm as expected from the bar shape (figure 4.17(a));

- to compute the exact value of the efficiency (both the raw and the effective one), the plots in figures 4.14 and 4.16 have been fitted with a constant. The range of the fit has been chosen by hand in order to exclude the lateral regions of the efficiency plot where the statistics is poor. The results are listed in table 4.2 together with the average over all the four layers of each direction. Given one of the horizontal layers shows an efficiency which is $\sim 6\%$ smaller than the others, the average efficiency has been calculated including (red values in table 4.2) or not that layer. Nevertheless the final effective efficiency values are very close to 99%.

## 4.4 Components test results

The following sections contain the results obtained in the tests with the different components; they have allowed to finalize the design of the final detector readout and to validate the use of the glue and of the triangular shape bars.

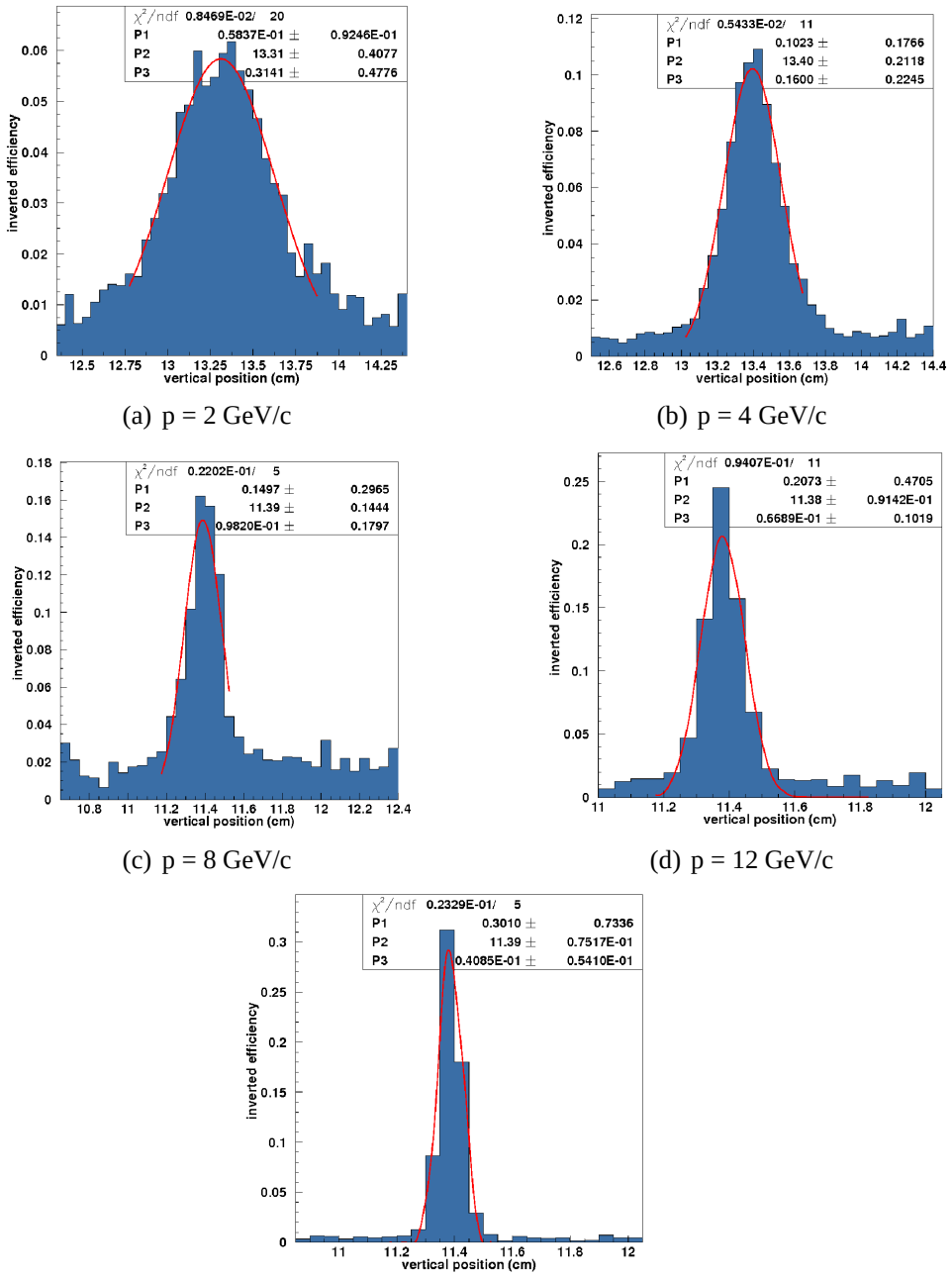


(a) p = 2 GeV/c

(b) p = 4 GeV/c

(c) p = 8 GeV/c

(d) p = 12 GeV/c

(e) p = 15 GeV/c

Figure 4.18: The inefficiency computed with different momentum of the incoming particles. The greater is the energy, the smaller is the Multiple Coulomb scattering contribution: at 15 GeV/c the dead regions have been measured to be $\sim 0.5$ mm.

| layer | *raw* eff [%] | *effective* eff [%] |
|---|---|---|
| 1X | 92.81 | 96.75 |
| 2X | 95.22 | 98.28 |
| 3X | 95.94 | 98.61 |
| 4X | 95.67 | 98.70 |
| average | 94.66 | 98.09 |
| | 95.61 | 98.53 |
| 1Y | 93.66 | 97.78 |
| 2Y | 94.41 | 98.27 |
| 3Y | 95.66 | 98.49 |
| 4Y | 93.68 | 98.54 |
| average | 94.35 | 98.27 |

Table 4.2: The efficiency of each layer of the EMR small prototype: an average value close to 99% has been obtained for the effective efficiency in both directions.

### 4.4.1 Rectangular bars

The four different readout configurations of the rectangular shape bars have been studied in terms of pulse height and pull distributions (figure 4.19). In both cases the configuration with 2 WLS fibers glued in the bar hole (shown with the black lines) is the best one: as expected the use of the glue increases the light collection and thus the signal readout at the end of the bar by the MAPMT is larger. On the other hand also the tail of the noise peak is larger; thus a dedicated cut has been applied to identify correctly the particle events from the noise ones. The configuration with 2 WLS fibers without glue and the one with only one fiber glued in the bar hole (red and green lines, respectively) show a similar behavior: in both cases the pulse height peak is at $\sim$ 85 ADC. The worst case is the one with only one WLS fiber without glue (blue line): the ADC value of the pulse height peak is $\sim$ 2.5 times smaller than the one of the 2 WLS fibers+glue configuration and $\sim$ 1.6 times smaller than the one of the other two cases.
The efficiency of the four long rectangular bars has been measured with the same method presented above for the EMR small prototype and is shown in figure 4.20. On the right side the efficiency of the bars readout with 1 (blue line) or 2 (red line) WLS fibers glued in the hole is presented: in both cases the efficiency values are greater than 90%. On the left side the other two studied configurations are presented: in this case the 2 WLS fiber configuration (green line) shows an efficiency value clearly larger than the 1 WLS fiber one (violet line). The configuration with 2 WLS fibers+glue is thus the best one with a maximum efficiency value of about 98%. In all the four cases the region with poor efficiency corresponds to the bar

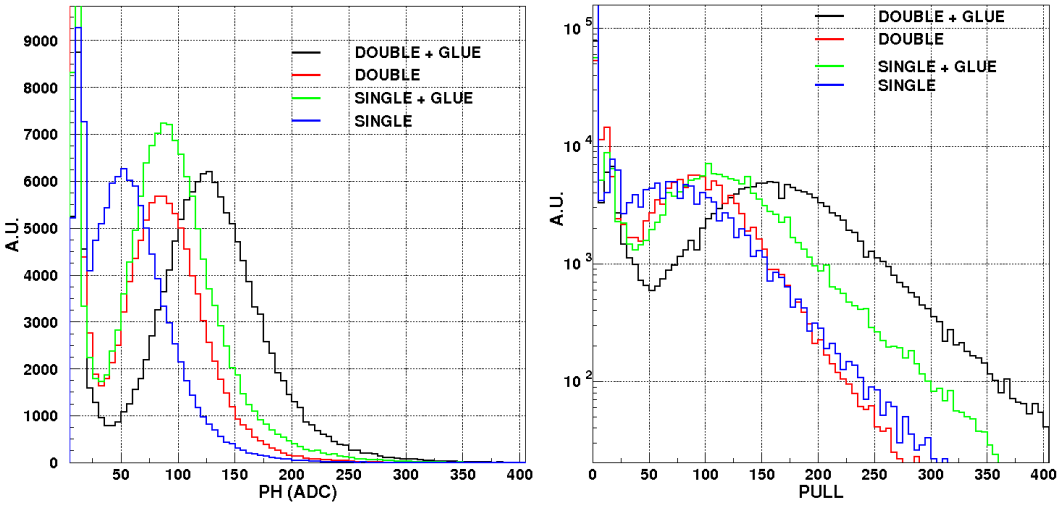


(a) (b)

Figure 4.19: (a) The pulse height and (b) the pull distributions of the four rectangular bars: as expected, given the glue increases the light collection, the best one is the 2 WLS fibers+glue configuration.

hole (about 3.6 mm of diameter).

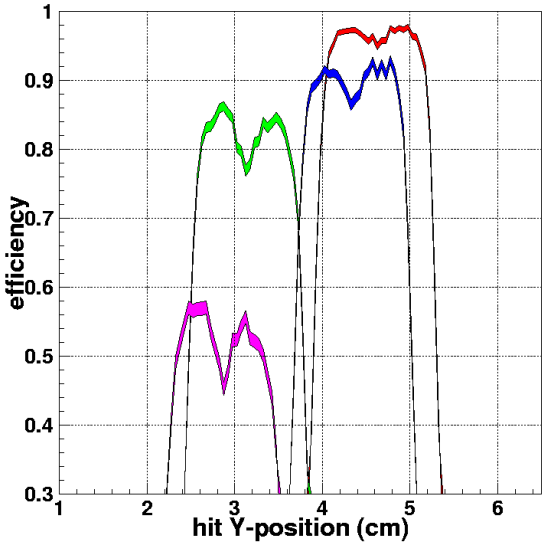


Figure 4.20: The four long rectangular bars efficiency: bars readout by fibers not glued in the hole (left); bars with glued fibers (right). Red and green lines represent the bars readout by 2 WLS fibers while blue and violet lines the bars with 1 WLS fiber.

The long bars have also been tested in terms of pulse height and efficiency as a function of the particle impact position (i.e. the beam position) with respect to the MAPMT. For these tests a 1 mm diameter fiber without glue has been used instead of the 0.8 mm diameter one. Four different positions have been chosen and the results are shown in figure 4.21. The red lines indicate the 2 WLS fibers+glue configuration, the blue ones the 1 WLS fiber+glue case, the green ones the 2 WLS fibers without glue and the violet lines the 1 WLS fiber without glue. As expected considering that the longer the travelled distance the larger the light attenuation, the pulse height values in all four cases fall off with the distance from the MAPMT. In terms of efficiency, the 2 WLS fibers+glue configuration is still the best one: the efficiency value remains quite constant at 98% increasing the distance of the beam with respect to the MAPMT. The 2 WLS fibers without glue and the 1 WLS fiber+glue configurations are in an intermediate position with efficiency values between 80% and 97%. The case of the 1 mm WLS fiber without glue is the worst: the efficiency value falls off drastically (from about 96% to 55%).

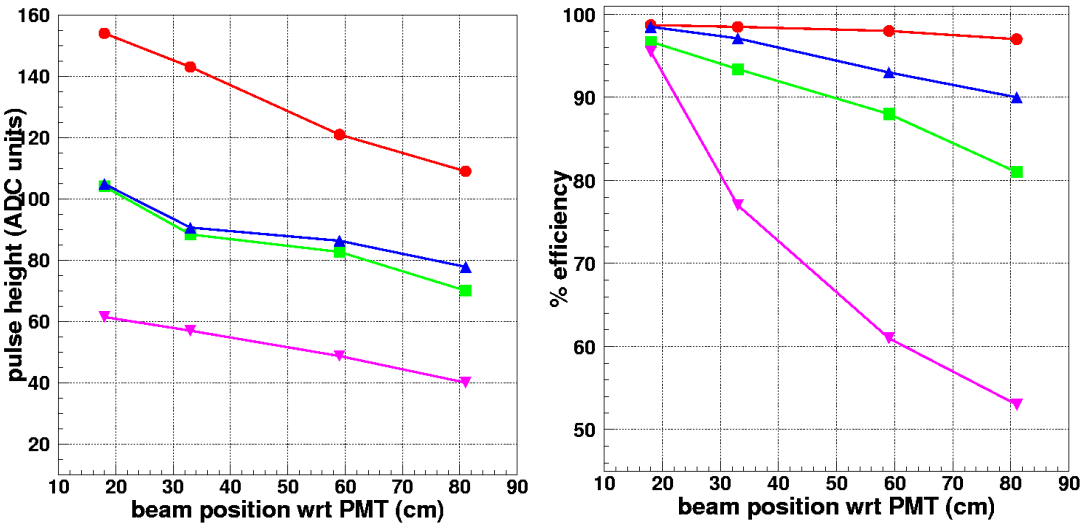


(a) (b)

Figure 4.21: The pulse height peak value (a) and the maximum efficiency (b) as a function of the particle impact position with respect to the MAPMT (see text for the detailed legend). In all the four cases the pulse height value falls off increasing the MAPMT distance while the efficiency shows a smooth decreasing as the distance from the MAPMT increases except for the single 1 mm diameter WLS fiber without glue configuration.

### 4.4.2 Triangular bars

The five triangular shape bars have been tested at the CERN PS T9 beamline with beams in a momentum range between 0.5 and 3.0 GeV/c; the setup was the same used for the test with the EMR small prototype (*type I* scintillator counter + two SiBCs + 5 long bars). Each bar was readout with 2 WLS fibers glued in the bar hole and connected on both sides to a channel of the H7546B MAPMT (see section 3.2.2 for details) readout with the electronics based on the MUSTAP board.

#### 4.4.2.1 Pedestal and noise

The pedestal and noise distributions measured with the five triangular bars are presented in figure 4.22: the average value of the pedestal is of the order of 1900−2000 ADC while the noise rms after the common mode subtraction is in the range 0.5−1.5 ADC[10].

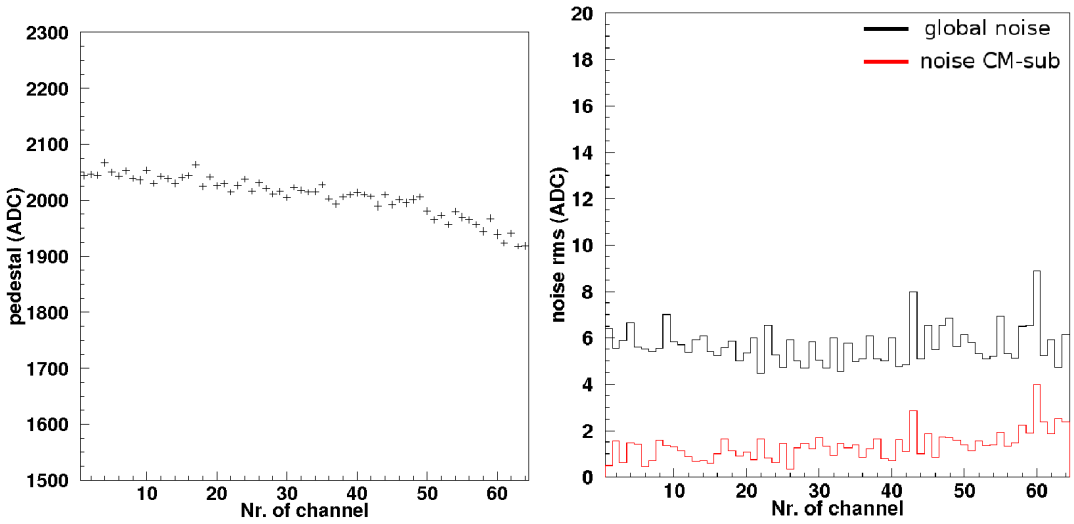


(a) (b)

Figure 4.22: (a) The pedestal distribution (expressed in ADC counts) of the MAPMT connected to the five triangular bars. (b) The noise rms distribution: the black line represents the global noise rms while the red one the common mode subtracted one.

[10]Even if a direct comparison with the FAST electronics is not possible (given the two chains are different), the use of the MUSTAP boards allows to reduce the common mode contribution.

#### 4.4.2.2 Bars behavior

The five triangular bars have been tested in terms of spatial resolution and efficiency using the same particle position identification method used for the EMR small prototype. Figure 4.23(a) presents an example of the pulse height distribution of the bar with the maximum signal in the event: in this case the valley that separates the noise peak from the one of the particle events is not present; this fact could be associated to a non adequate coupling between the MAPMT and the WLS fibers[11]. Also in this case, to fix the right threshold value to distinguish the noise events from the particle ones, the pull distribution of the bar with the maximum signal in the event has been analyzed (figure 4.23(b)): the pull cut has been set at $10\sigma$ and has been checked on a run by run basis, given that the conditions were different (night/day and thus light, MAPMT voltage, beam energy and collimators).

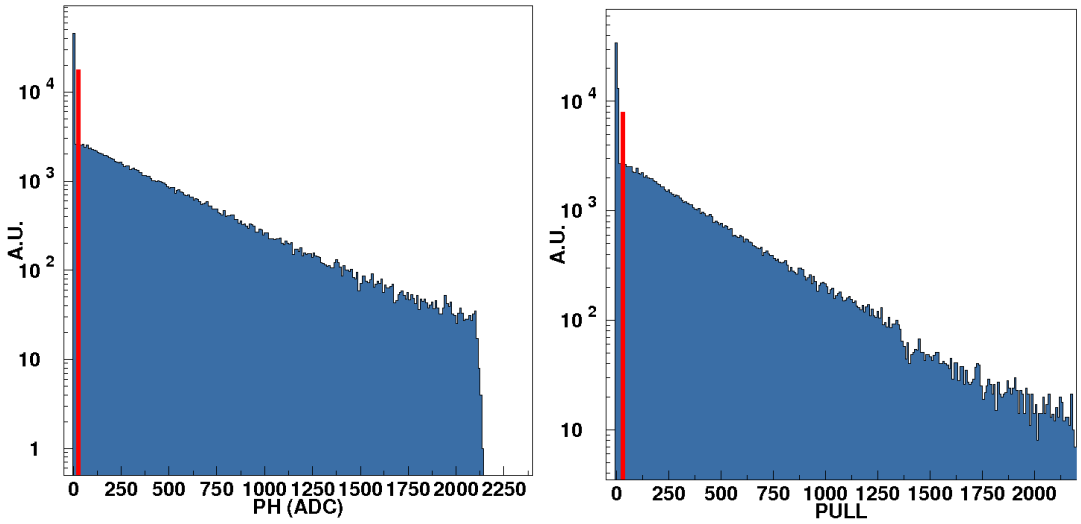


(a) (b)

Figure 4.23: The pulse height (a) and pull (b) distributions of the bar with the maximum signal in the event.

The number of bars over threshold, that means the number of bars with a signal above $10\sigma$ in each event, has been computed exactly in the same way used in the previous tests (figure 4.24): as expected this number is tipically 1 or 2, given the triangular shape of the bars, and no differences between the two readout sides are present.

[11] During the test of the five long bars at the CERN PS T9 beamline, no coupling mask was used and the alignment was not optimal.

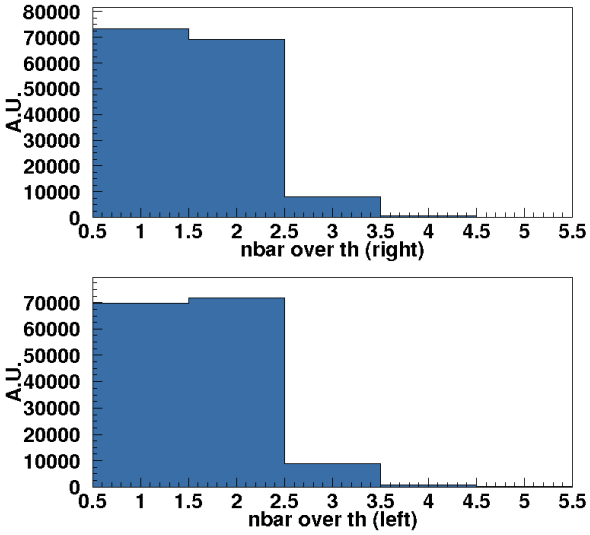


Figure 4.24: The distribution of the number of bars over threshold: right side (top) and left side (bottom).

#### 4.4.2.3 Spatial resolution

The spatial resolution of the five triangular shape bars has been evaluated with the same residual method presented above: the difference between the trajectory reconstructed by the SiBCs and the one measured by the bars themselves has been computed and the result is shown in figure 4.25 (also in this case the bar with the maximum signal in the event has been chosen as the bar crossed by the particle): an average value of $\sim 7$ mm has been obtained. Given the triangular shape of the bar, the theoretical resolution value is in the range $4.8-9.5$ mm (since the readout pitch is between $1.65-3.3$ cm): the measured value is thus satisfactory[12].

#### 4.4.2.4 Efficiency

As mentioned above, the efficiency represents the number of particles effectively registered by the detector under test given a fixed number of good events crossing the detector itself (equation 4.4). A different method from the one used in the previous sections has been adopted to evaluate both the single bar efficiency and the global one (that means the average over all the five bars). The following procedure has been used:

[12] A more rigorous analysis, based on a cluster identification method like the one used for the SiBCs (Appendix B), should be adopted to identify the exact particle position but it will be presented in the next chapter for the analysis of the final detector.

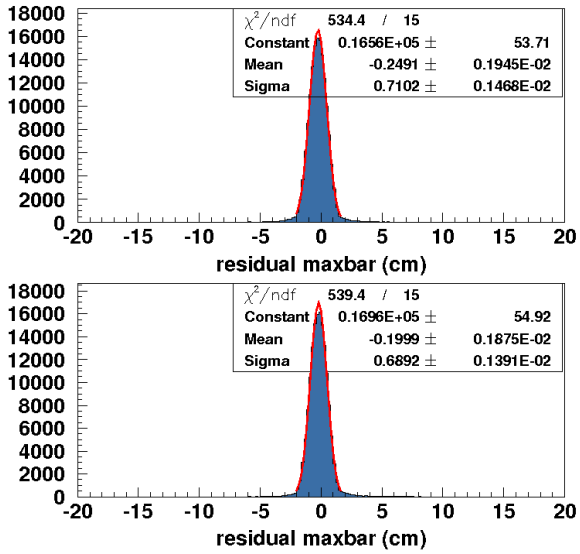


Figure 4.25: The residual distribution of the five triangular bars: right side (top) and left side (bottom). An average value of $\sim$ 7 mm has been obtained.

- the trajectories measured with the silicon detectors have been projected on the surface of the triangular bars and the *projected histogram* (figure 4.26(a)) has been filled with 1 in each event; it thus corresponds to the beam profile at the triangular bar *z* position (where *z* indicates the position along the beam axis) and represents the number of incoming particles (the denominator of equation 4.4);

- the same profile histogram (*shadow histogram*, figure 4.26(b)) for the triangular bars has been filled with 1 depending on the pulse height value. In other words, if the signal of at least one bar in a given event exceeds the threshold fixed by the pull distribution the histogram has been filled with 1; thus the shadow histogram represents the number of good events measured by the triangular bars (the numerator of equation 4.4);

- the *efficiency plot* has been obtained as the ratio of the beam profile reconstructed by the bars (the shadow histogram) and the one measured by the silicon detectors (the projected histogram). The results obtained for the single bar efficiency and the global one are presented in figures 4.27 and 4.28, respectively. The regions with a smaller efficiency in figure 4.27 (green regions) correspond to the edges of the triangular bars (figure 4.29) where the light collection is smaller while the poor efficiency region in the up right corner of figure 4.28 is due to the trigger scintillator area;

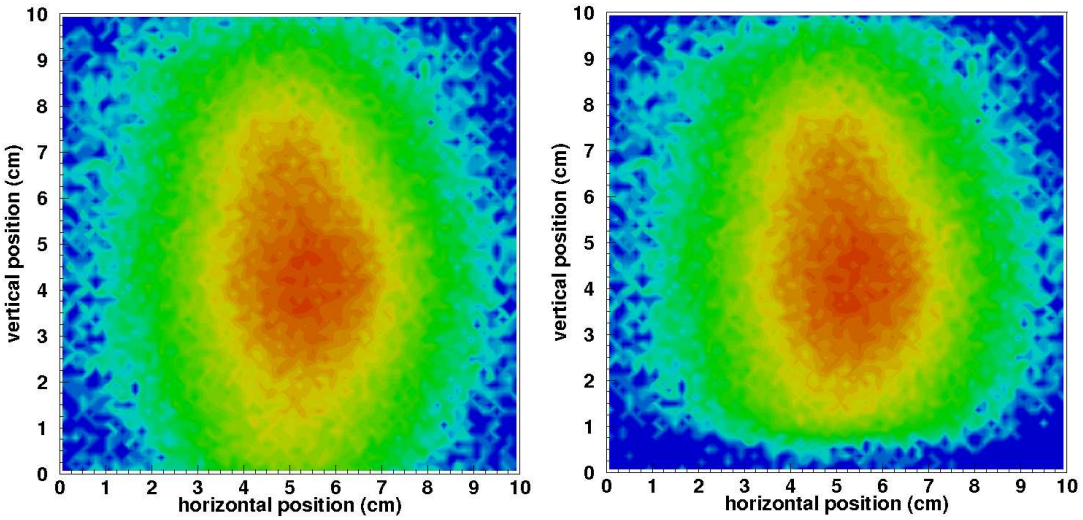


(a) (b)

Figure 4.26: The *projected histogram* (a) and the *shadow histogram* (b) used to evaluate the global and the single bar efficiency (see text for details).

- in order to compute the exact value of the global efficiency, a vertical slice of the efficiency plot has been considered and fitted with a constant (figure 4.30(a)): the arrows correspond to the position of the readout WLS fibers. An efficiency value of about 97% has been obtained in the flat zone for both the readout sides; the shape of the histogram in the range $8.25-10$ cm is due to the edge of the first triangular bar while the poor efficiency region in the range $0-1.65$ cm is given by the fact that the last bar was out of the beam (figure 4.30(b));

- the same slicing method has been used to measure the single bar efficiency[13] and verify that the use of the triangular shape bar can solve the efficiency problem of the EMR small prototype presented in section 4.3.4 (that is the valleys in the efficiency plot). The result is shown in figure 4.31(a): the regions with poor efficiency of one bar overlap with the high efficiency regions of the two neighbouring bars so that the efficiency remains quite constant along the vertical direction (figure 4.31(b)).

[13]Since there were only five bars under test and they were measuring the vertical direction, the exact efficiency value is computed fitting only the vertical slices of the total efficiency plot. As it will be shown in the next section, considering the horizontal slices of the efficiency plot, it is possible to evaluate the uniformity along the length of the bar itself (figure 4.33).

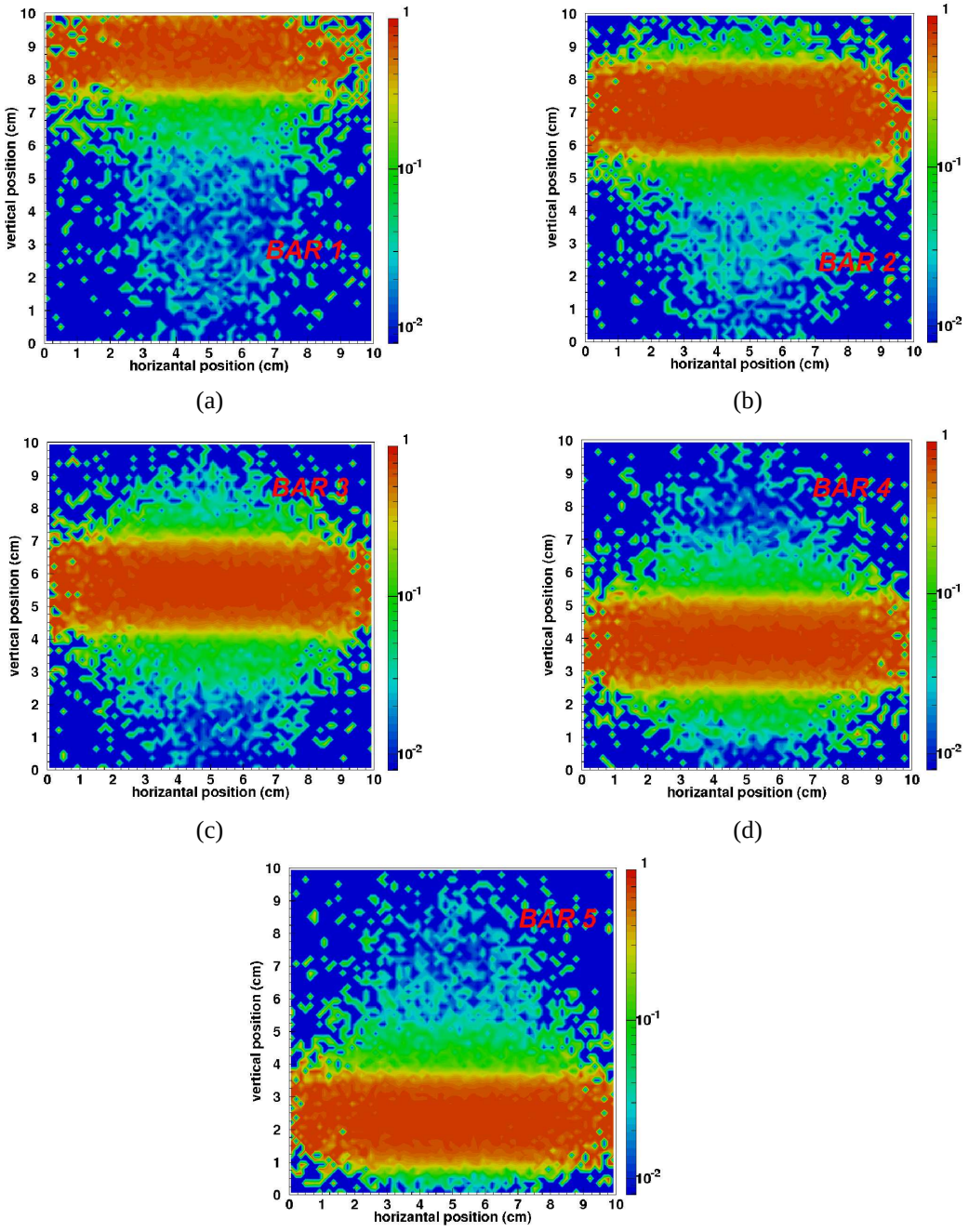


(a) (b) (c) (d) (e)

Figure 4.27: The single bar efficiency.

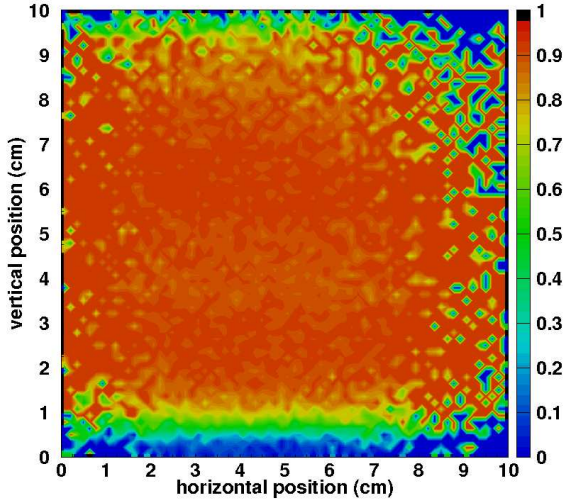


Figure 4.28: The global efficiency measured by all the five triangular bars: the poor efficiency region in the up right corner is due to the trigger scintillator.

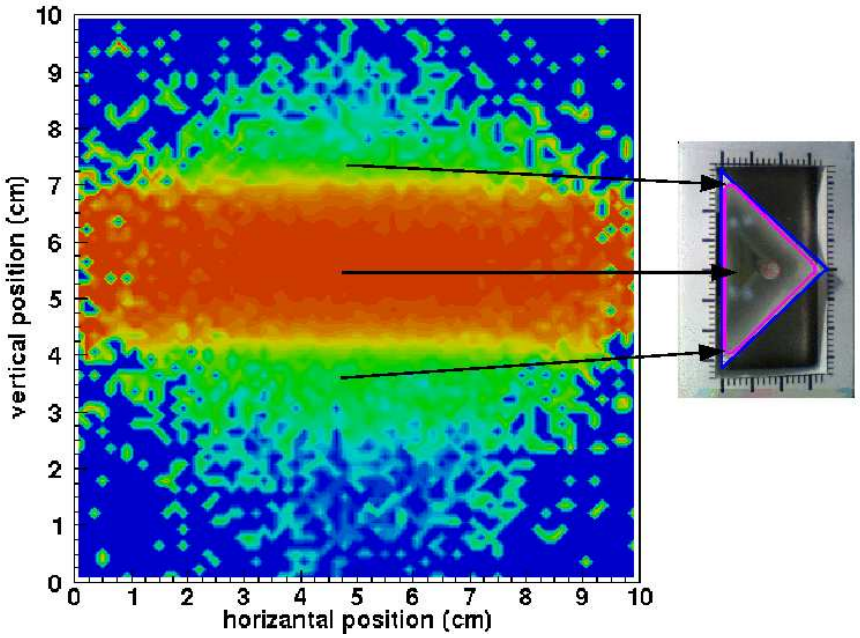


Figure 4.29: Zoom of the single bar efficiency plot: the green regions correspond to the edges of the triangular bar where the ligth collection is smaller.

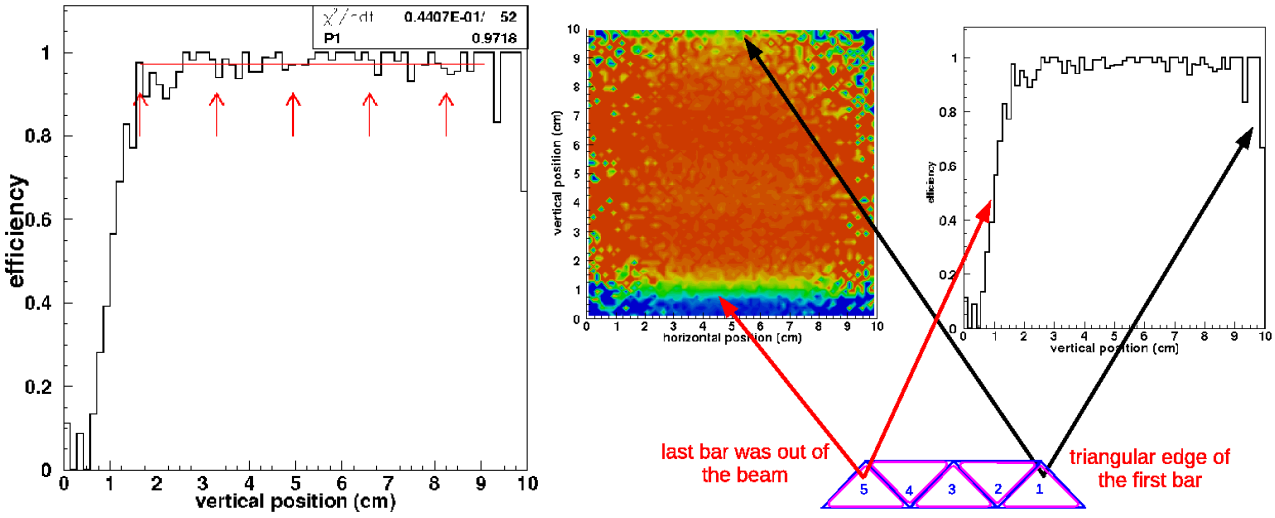


(a) (b)

Figure 4.30: (a) A vertical slice of the global efficiency plot (the arrows indicate the position of the WLS fibers): an efficiency value greater than 97% has been obtained fitting the distribution with a constant. (b) The shape of the histogram in the range 8.25−10 cm is due to the edge of the first bar while the last bar was out of the beam causing a poor efficiency region in the range 0−1.65 cm.

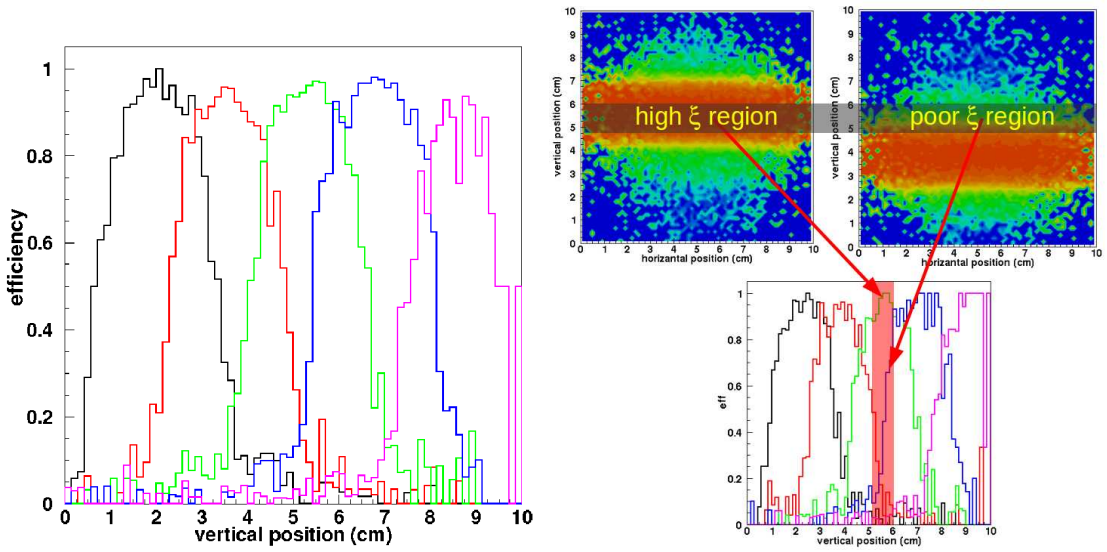


(a) (b)

Figure 4.31: (a) A vertical slice of each single bar efficiency plot. (b) The region with poor efficiency of one bar can be recovered by the region with high efficiency of the neighbouring ones (the grey and red bands indicate the region in which the two bars are overlapped).

#### 4.4.2.5 Efficiency comparison

The behavior of the efficiency along and across the five long bars has been studied for two different runs (that means in two different conditions[14]). The global efficiency plots obtained for the two runs are shown in figure 4.32: the two 2D histograms have been obtained in the same way presented in the previous section. The poor efficiency region in figure 4.32(b) (the yellow one at $\sim$ 3.5 cm in the vertical direction) corresponds to the bar without glue and points out the fact that the use of the glue is thus fundamental to increase the light collection.

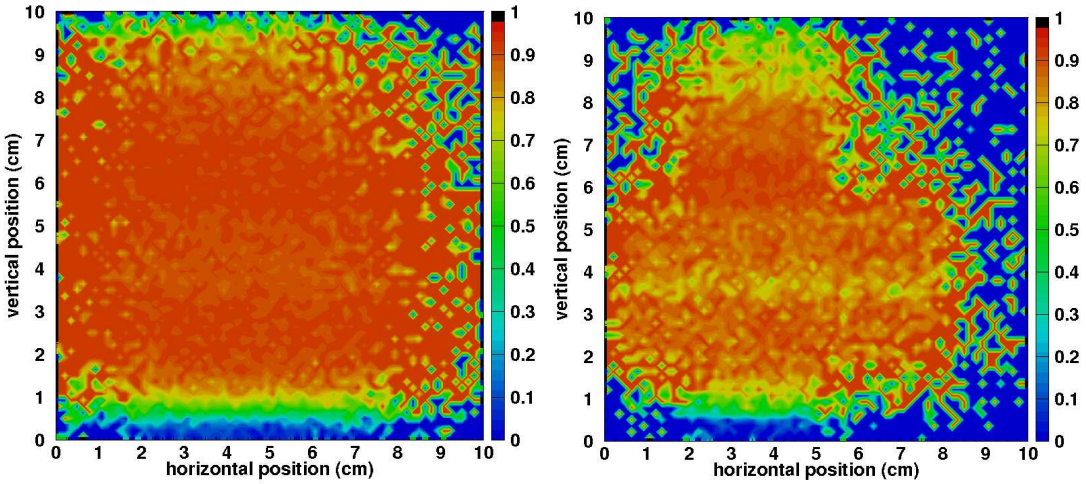


(a) (b)

Figure 4.32: The global efficiency plot measured in two different runs.

The comparison of the efficiency value is again based on the slicing method: horizontal and vertical slices of figure 4.32(a) and 4.32(b) have been fitted with a constant; in total 70 slices of $\sim$ 1.4 mm of width, have been considered for each direction (figure 4.33). In this way both the effective efficiency value across all the bars and an estimation of the bar uniformity along its length can be calculated. Figure 4.34 shows an example of the vertical and horizontal slices fit for the first run: the range of the fit has been chosen by hand in order to fit only the flat zone of each slice excluding the regions with poor statistics (lateral regions in the efficiency plots).
The average of the values obtained from the fit of each slice are listed in table 4.3: a decrease of the measured efficiency has been found and has been associated to a worse light collection due to a movement of the MAPMT.

[14]The beam momentum was changed from 1 GeV/c in the first run to 3 GeV/c in the second one and the distance from the reference detectors (SiBCs) in figure 4.3 was increased.

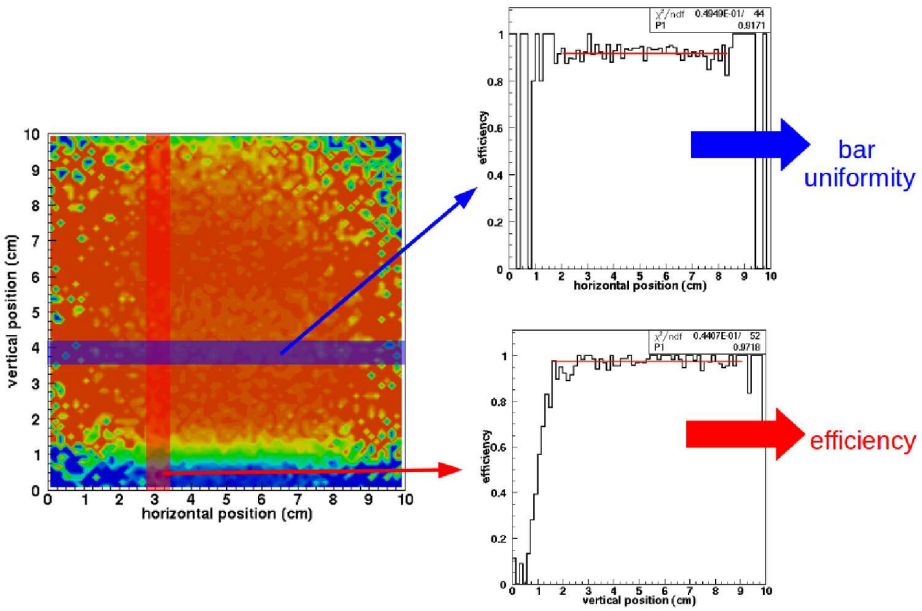


Figure 4.33: The slicing method allows to compute both the value of the efficiency across the bars (vertical slice, red band) and the uniformity along the bar length (horizontal slice, blue band).

| slice | run #1 | run #2 |
|---|---|---|
| horizontal | 97.27 % | 92.25 % |
| | 97.59 % | 92.45 % |
| vertical | 95.86 % | 90.56 % |
| | 95.39 % | 90.78 % |

Table 4.3: Comparison of the efficiency values obtained with the slicing method for the two different runs.

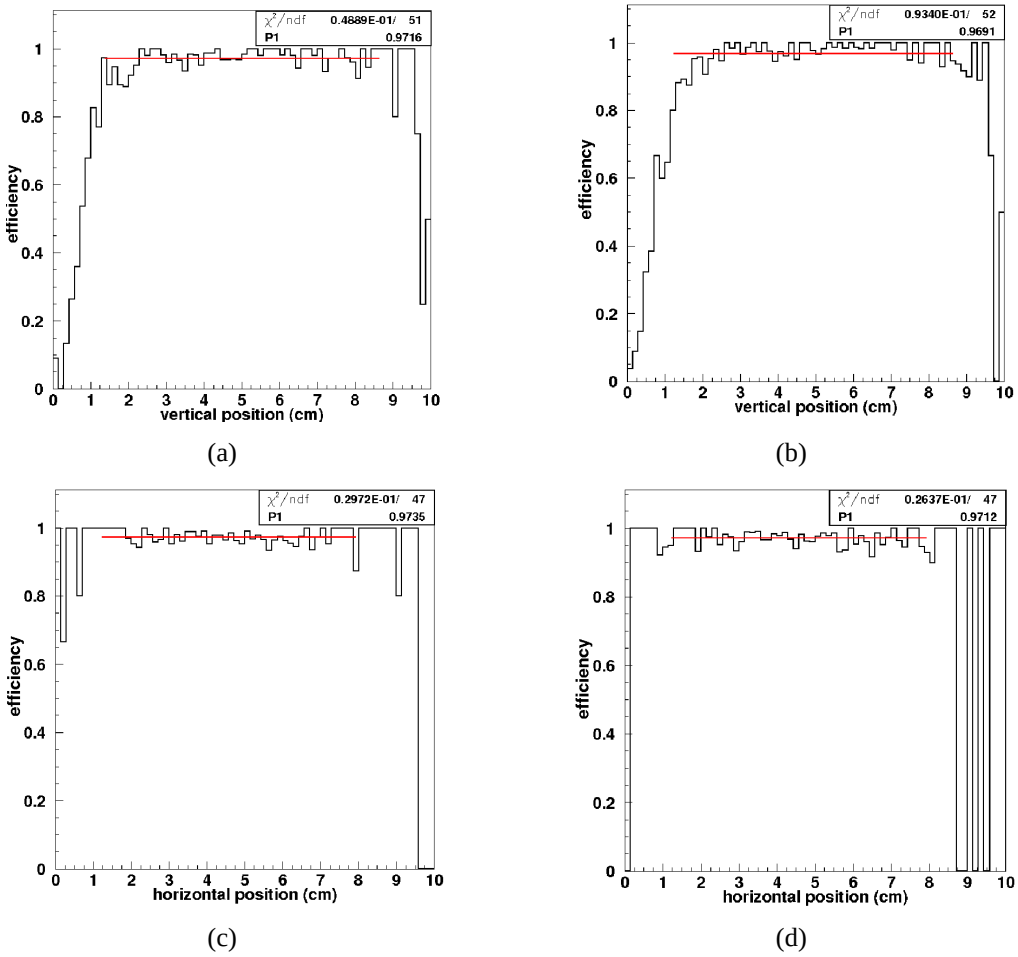


Figure 4.34: Fit with a constant of two vertical (a)−(b) and two horizontal (c)−(d) slices of the global efficiency plot.

To obtain the behavior of the efficiency as a function of the vertical/horizontal position the values of the fit of each slice have been plotted versus the vertical/horizontal position[15]. The results for both runs are shown in figure 4.35: the poor efficiency region at $\sim$ 3.5 cm in the top of figure 4.35(b) corresponds to the bar without glue. As mentioned above, a reduction of the efficiency of $\sim$ 5% has been measured and has been associated to a change in the alignment between the fibers and the MAPMT: given the mechanics used in the beamtest was not optimal (no coupling mask was used), when the bars were moved to increase the distance from the SiBCs, a shift of the MAPMT was caused, that in turn gave a worse light collection.

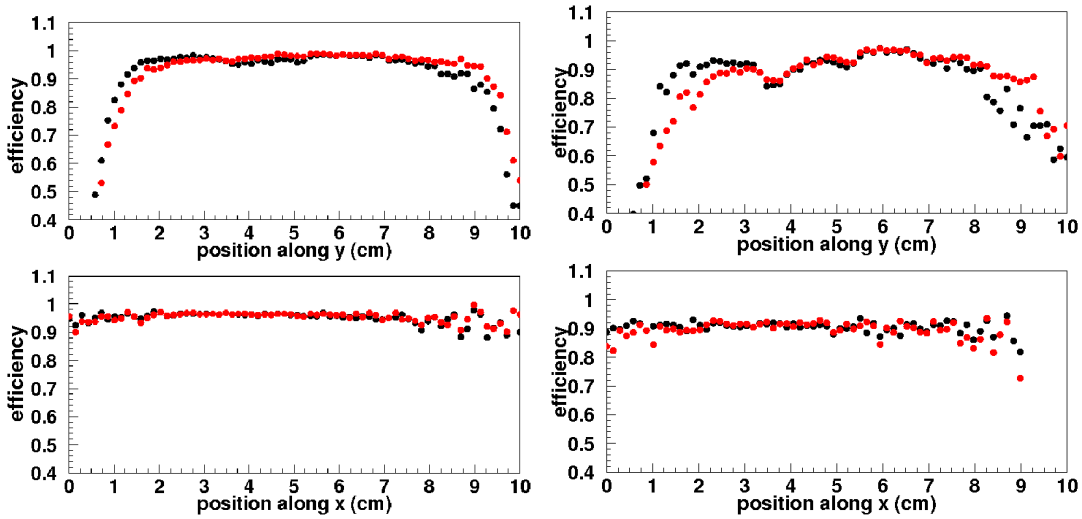


(a) (b)

Figure 4.35: Comparison of the horizontal slices (top) and vertical slices (bottom) of the two runs; in both figures the black dots stand for the right side while the red ones for the left one.

## 4.5 Electronics results

The following sections present some of the results obtained with the EMR small prototype equipped with the MUSTAP board (at the beamtest at the CERN PS T10 beamline) and the FEB prototype board (cosmic rays test at the Insubria University); only the results in terms of noise and pulse height are described given the

[15]For some of the considered slices (especially for the lateral ones of run #2) the statistics was poor; in this case the value of the fit has been set manually to zero.

spatial resolution and the efficiency values are practically the same presented in the previous sections.

### 4.5.1 The CERN PS T10 results

The data taking at the CERN PS T10 beamline has allowed to test the MUSTAP boards connected to the EMR small prototype and study their behavior in terms of noise. The setup was the same used during the T9 beamline test (EMR small prototype + two SiBCs + *type I* scintillator counter).
The pedestal and noise rms distributions are presented in figure 4.36 separately for the horizontal and vertical layers: the up-down position of two following channels in figure 4.36(a) (top plot) is due to the presence of a short in the bondings of the ASIC. The distributions of the global noise (black) and of the common mode subtracted one (red) are similar to the ones measured at the T9 beamline and an average value in the range $2-3$ ADC has been obtained for the common mode subtracted one.

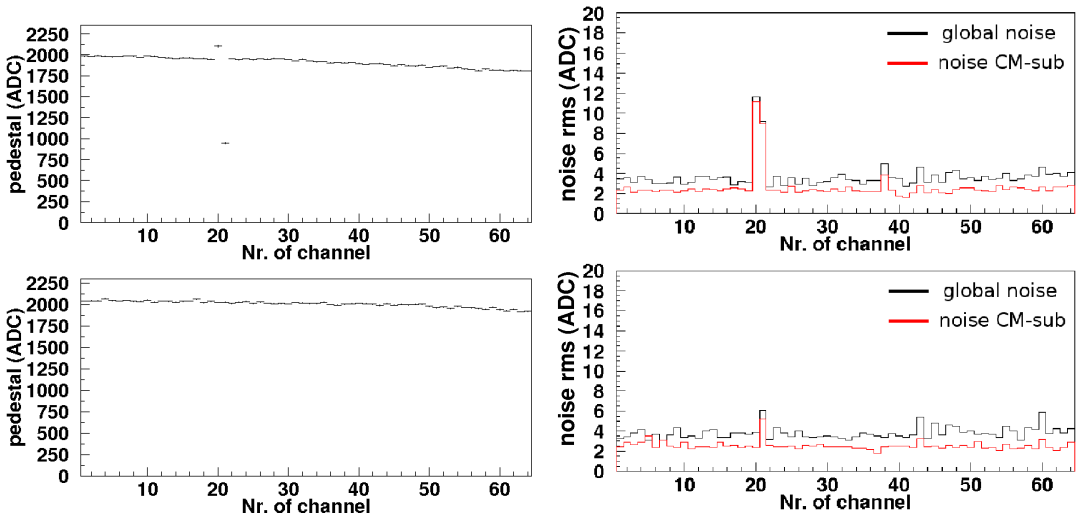


(a) (b)

Figure 4.36: The pedestal (a) and noise rms (b) distributions measured at the CERN PS T10 beamline.

### 4.5.2 The cosmic rays results

Two FEBs equipped with the MAROC-II ASIC and connected with the EMR prototype have been tested at the Insubria University with cosmic rays in order to

check the long term stability of the electronics and understand its performances. The setup consisted of the EMR small prototype, two SiBCs placed on the top of the prototype and the *type III* scintillator counter.
The pedestal and noise rms distributions are presented in figure 4.37: after the common mode subtraction the noise rms value is in the range $4-6$ ADC (the absolute value cannot be compared with the previous one because the electronics chain gain were different); moreover, connecting the board directly to the MAPMT, the noise rms distribution is practically flat and does not present the problem of the spikes due to the cables that behave as antennas shown by the FAST electronics (section 4.3.1).

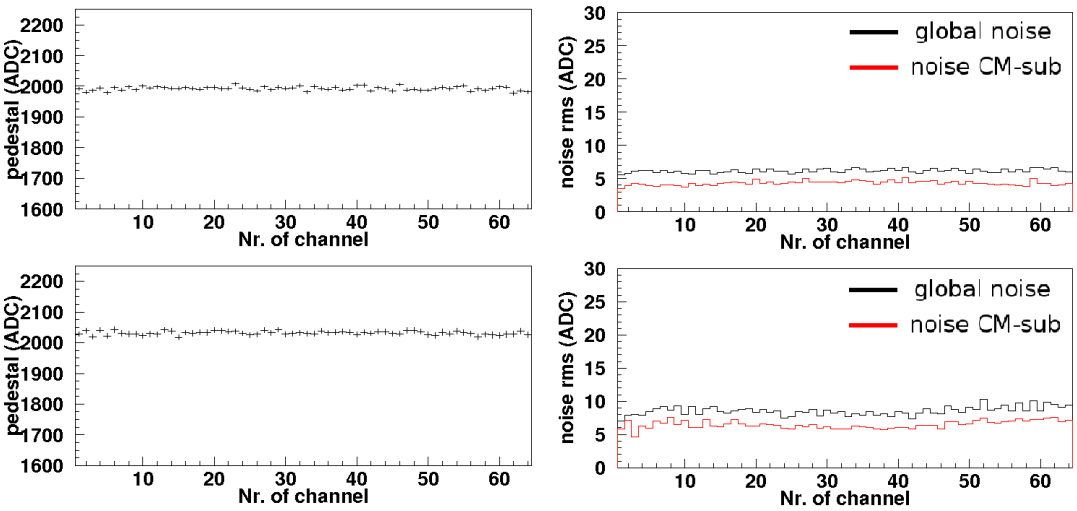


(a) (b)

Figure 4.37: The pedestal (a) and noise rms (b) distributions measured during the cosmic rays test.

Figure 4.38 shows the pulse height and pull distributions of the bar with the maximum signal in the event for one of the layers: also in this case (as in the T9 beamtest) the noise events are well separated from the particle ones.

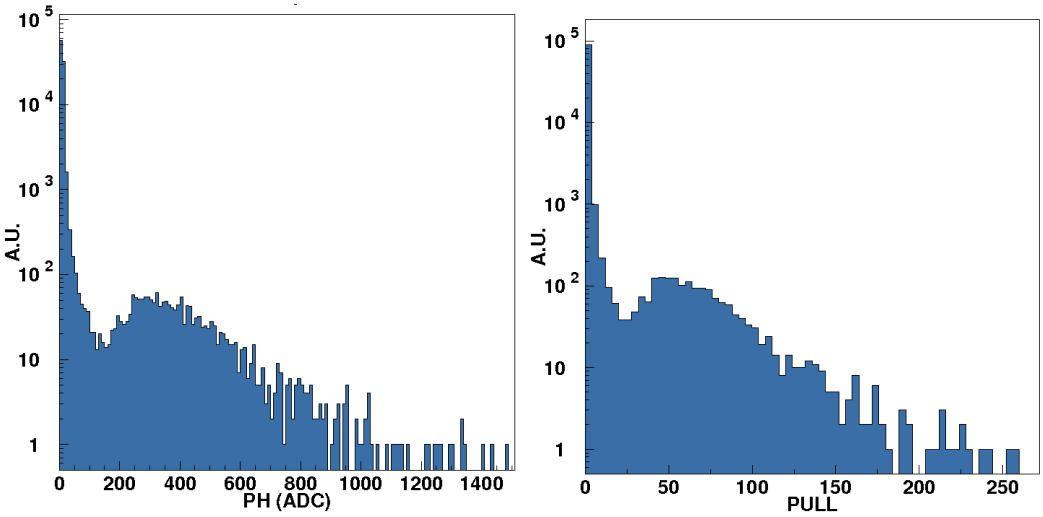


(a) (b)

Figure 4.38: The pulse height (a) and pull (b) distributions measured during the cosmic ray test at the Insubria University: in this case the valley that separates the noise peak from the particle one is clearly visible.

# Chapter 5

# Commissioning at UNIGE

The MICE Electron Muon Ranger (Chapter 3) is under construction at the Département de Physique Nucléaire et Corpusculaire (DPNC) of the Geneva University (UNIGE). A full scale module (that means 1x and 1y layer) has been assembled in January 2010: each layer contains 59 bars as in the final design but is readout with 2 0.8 mm diameter WLS fibers per bar. The module is under test with cosmic rays since the beginning of the year: it has been equipped first with the MUSTAP boards (section 3.2.1.1) and then with a prototype of the FEBs (section 3.1.4.1).
This chapter is dedicated to the results obtained during this commissioning period: the detector behavior in terms of noise, spatial resolution and efficiency is presented; a detailed analysis of the cross talk is also given. The stripping procedure of the raw data is the same used for the test on the prototype (Appendix B).

## 5.1 Setup description

A schematic view of the setup assembled at UNIGE is shown in figure 5.1(a): the module has been placed $\sim$ 1.1 m far from the floor and a wooden box provides the light tightness; it also hosts a patch panel for the cables. A set of two Silicon Beam Chambers (SiBCs) of the same type used for the test phases (section 4.2.2) has been placed on the floor together with a $10\times10$ cm$^2$ scintillator counter (*type II*, section 4.2.1): the SiBCs provide the particle tracking while the scintillator is used for the trigger.
Figure 5.1(b) shows a photo of the module during the assembly of the FEBs (section 3.1.4.1) and equipped with both the single channel PMTs and the MAPMT ones. The single channel signals have been used neither in the trigger nor in the data analysis; nevertheless they have been assembled in order to verify the mechanical constraints of the module and to test their functionality.
The goal of this commissioning period was the characterization of the detector in

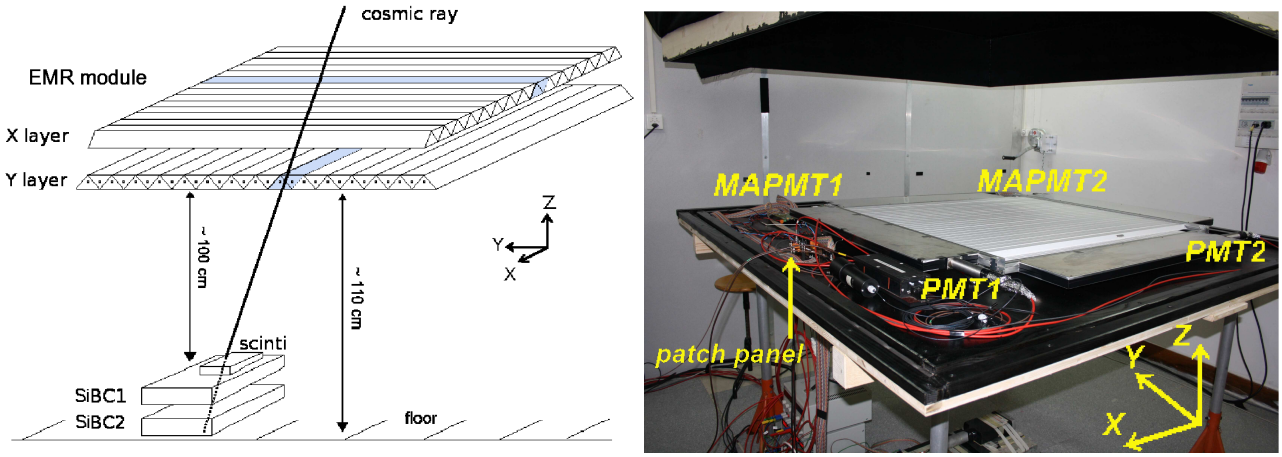


(a) (b)

Figure 5.1: (a) A sketch of the UNIGE setup: on its journey, a cosmic ray hits the EMR module, the plastic scintillator trigger and a couple of SiBCs. (b) A photo of the setup: the electronics patch panel is visible on the left.

terms of spatial resolution and efficiency. The following variations of the experimental setup have been performed:

- *phase I*: the MUSTAP board has directly been connected to each R7600-00-M64 MAPMT (with the H7546B assembly) and the efficiency has been studied varying the bias voltage of the MAPMTs and the hold duration;

- *phase II*: in order to enhance the light collection at the MAPMT level, optical grease has been applied on the surface of the MAPMT connected to the bars measuring the horizontal direction; at the same time, the flexible connector (section 3.1.3) has been installed on the vertical layer and a set of data has been acquired in order to evaluate its behavior, in particular its effect on the common mode;

- *phase III*: the standard MAPMTs have been removed and substituted with two green enhanced ones, the same that will be used in the final detector design;

- *phase IV*: the module has been equipped with a prototype of the final electronics (two FEBs with the MAROC-II ASIC) working in analog mode.

The behavior of the full scale EMR module has been studied with the following figures of merit:

- the *noise*: it has been studied considering the pedestal runs acquired during the different phases; in particular the common mode noise contribution has been estimated for each MAPMT-fiber interface;

- the *spatial resolution*: the residual method presented in section 4.3.3 has been used;

- the detector *efficiency*: the same slicing method used for the efficiency calculation of the five triangular bars tested at the CERN PS T9 beamline has been adopted;

- the *cross talk*: when the light enters in one channel of the MAPMT, it happens that, if the fiber mask and the MAPMT window are not perfectly aligned, the light is spread also in the neighbouring channels; this means a signal in a wrong channel is present causing a wrong reconstruction of the particle trajectory. This effect has been studied in detail in order to obtain the effective value of the EMR spatial resolution.

### 5.1.1 The DAQ

A schematic view of the DAQ used during the commissioning test at UNIGE is presented in figure 5.2: a SBS Bit3 board is responsible of the interface with a PC running the Linux operating system and of the data transmission while an Input/Output (I/O) board controls both the silicon chamber ADC boards and the EMR FEBs. The I/O is organized in two piggy back boards: the *master* one (shown in red) handles the FEBs signals, the configuration (input) and the readout (output) signals while the *slave* board (shown in blue) manages the silicon chamber ADC boards. The input signals (light blue filled lines) are brought from the VME crate to the detectors through standard 34 line twisted cables in a daisy chain way while the outputs (red dashed lines) from the detector to the VME are sent on parallel differential lines. The master board also handles the scintillator signal to provide the readout trigger to the other boards.
The DAQ software has been developed in C with a user interface written in Tcl/Tk (figure 5.3); the output data are stored in binary files (PAW ntuples) and processed offline to obtain ASCII DST output files (see Appendix B for details); the analysis software is written in FORTRAN.
The DAQ main window (figure 5.3(a)) allows the user to select the configuration window or the acquisition one. The configuration window (*TRIGGER VA64*, figure 5.3(b) left) is used to load the trigger mask of each ASIC housed in the FEBs and enable/disable the self-triggering capability[1]. The acquisition window (*MUS*

[1]The self-trigger capability of the VA64TAP2.1 has not been used in the UNIGE setup.

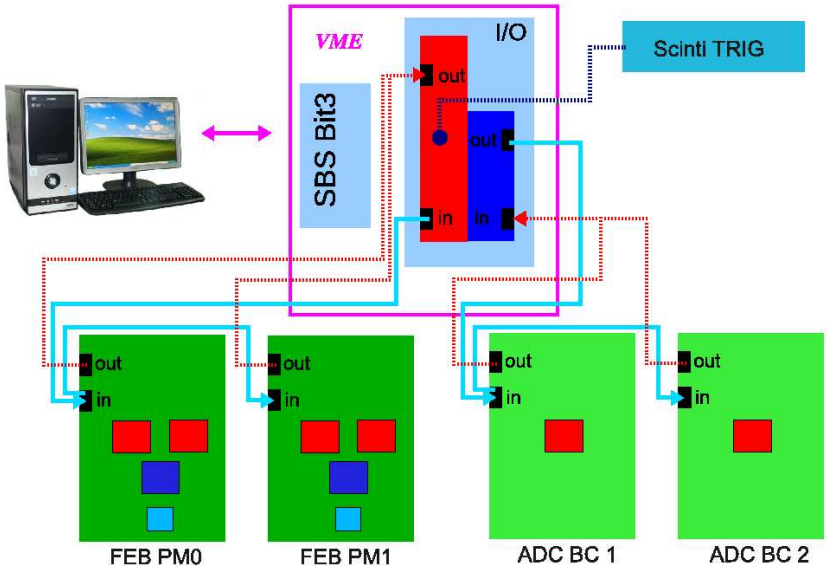


Figure 5.2: The overall DAQ scheme for the commissioning tests at UNIGE. The VME crate hosts two boards: the SBS Bit3 for the interface with the PC and an Input/Output one for the control of both the silicon chamber ADC boards and the EMR module FEBs; all the connections are based on standard twisted cables.

*ADC TEST*, figure 5.3(b) right) allows to select the run type (pedestal or data run), the number of events and the hold value for both the FEB ASICs and the silicon chambers.

## 5.2 MUSTAP board results

In the following sections the results obtained in the first three phases are described; in particular the noise behavior with the different experimental setups is presented.

### 5.2.1 Noise behavior

The pedestal runs acquired during the first three phases have been analyzed in order to study the variation of the noise rms[2]. Figure 5.4 presents the behavior of the noise rms before (black) and after (red) the subtraction of the common mode contribution: the spikes show that on some of the channels there is a noise problem. Both in *phase II* and in *phase III* the global noise rms is larger than the one in *phase I* while the common mode subtracted noise rms is small enough and

[2]The pedestal distributions are not presented here given they were practically the same obtained in the beamtest with the EMR small prototype at the CERN PS T10 beamline (section 4.5.1).

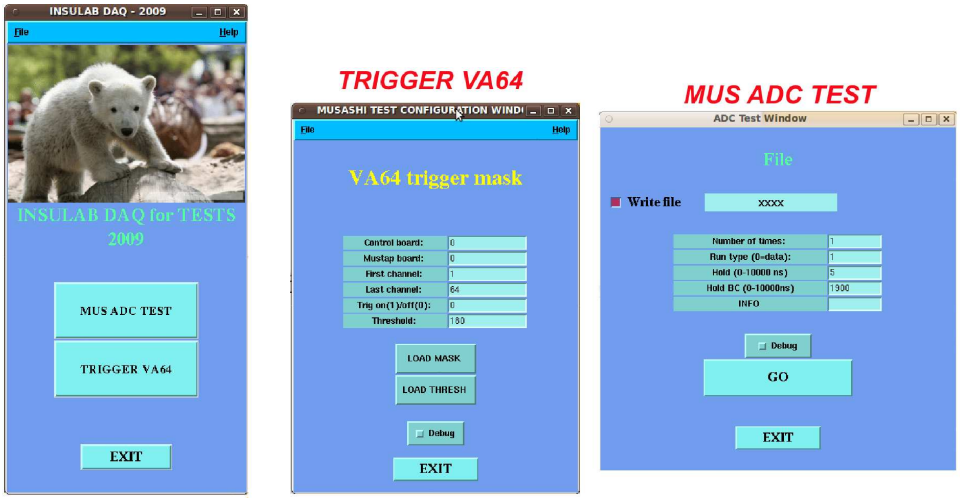


(a) (b)

Figure 5.3: The DAQ user interface: (a) the main window and (b) the configuration and acquisition ones.

quite constant in all the three cases.
The values of the global noise rms, of the common mode contribution and of the noise rms after its subtraction are listed in table 5.1: even if the use of the flexible connector and of the green enhanced MAPMTs caused an increase of the common mode contribution (and thus of the global noise) after its subtraction an average value for the global noise rms in the range $4-6$ ADC has been obtained, that is $\sim 2-3$ ADC larger than the configuration without the flexible. Nevertheless, in case of a digital readout (as in the final detector at RAL) given the output signals are sampled only if over threshold, the overall global noise has to be kept under control not to either increase the number of sampled channels or to lose channels with an effective signal.

### 5.2.2 Bars behavior

The same particle position identification method adopted during the test phases has been applied in the analysis of the module at UNIGE[3]. The global distributions of the pulse height, that is the pulse height value of all the bars of each layer, has been considered (figure 5.5(a)) to study the behavior of the module: the peak at $\sim$ 8000 ADC corresponds to the events in which the electronics chain is saturated. Given the length of the cables was not optimal (that is the cables could

[3]In the following only the results from a run of *phase III* are shown as an example of the obtained distributions.

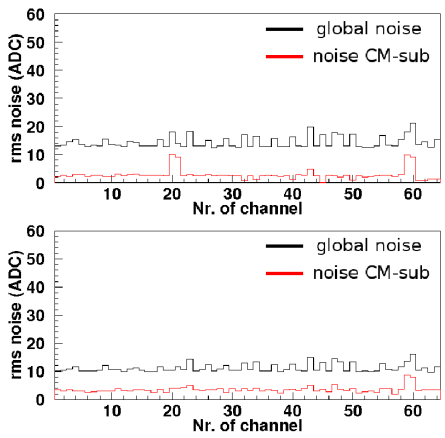


(a) *phase I*

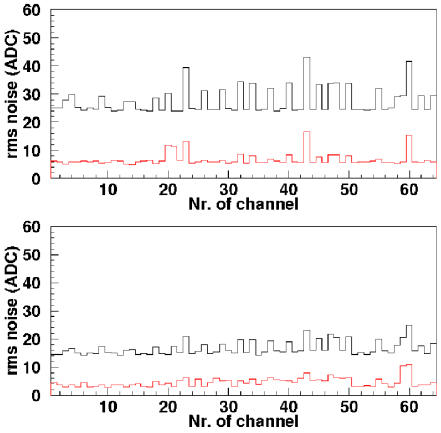


(b) *phase II*

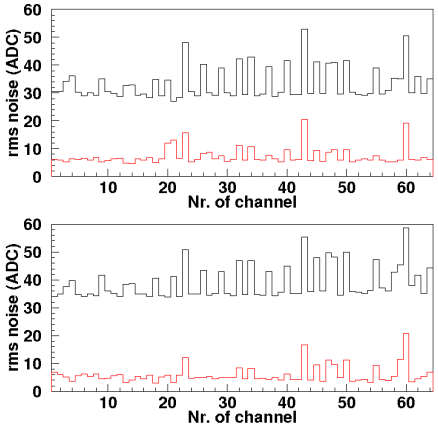


(c) *phase III*

Figure 5.4: The noise rms distributions measured during the first three phases: even if the global noise is larger adding the flexible connector and the optical grease, the common mode subtracted one remains in the range 4−6 ADC.

| *phase* | layer | global noise rms [ADC] | CM noise [ADC] | CM-sub noise rms [ADC] |
|---|---|---|---|---|
| *I* | Y | 13.43 | 8.19 | 2.34 |
| | X | 10.44 | 8.92 | 3.28 |
| *II* | Y | 25.07 | 12.90 | 5.97 |
| | X | 15.36 | 8.73 | 3.47 |
| *III* | Y | 19.15 | 14.93 | 5.98 |
| | X | 14.37 | 12.04 | 3.37 |

Table 5.1: The noise rms behavior as a function of the different MAPMT-fiber interfaces: an average value in the range $2-6$ ADC has been obtained for the global noise rms after the common mode subtraction.

not be as short as needed), both negative and positive signals are present in the distributions: this means the signal may be sampled on the undershoot (at least for some channels).
For this reason a scan on the hold value has been performed in order to optimize the readout (figure 5.5(b)), trying both to minimize the saturated signals and to sample all the channels in the same way (that is all positive or all negative). A hold value of 60 ns has been chosen corresponding to a sampling on the undershoot in most cases. In the analysis, the absolute value of the pulse height has been used: figure 5.6 shows an example of the pulse height and pull distributions obtained for the bar with the maximum signal in the event. The threshold (red lines) is set considering both the pulse height and the pull and excluding the regions corresponding to the noise (high peaks near 0).
The pull distribution has also been used to compute the number of bars over threshold (figure 5.7); the threshold has been set on a run by run basis given the different setups: the typical range for the pulse height cut and the pull one was $80-100$ ADC and $25-35\sigma$, respectively. The same method used in the test phases has been adopted: event by event a counter variable has been increased of 1 whenever the pulse height value was over the threshold cut. As expected, given the geometry of the setup, the number of bars over threshold is typically 2.

### 5.2.3 Particle position identification method

To reconstruct the exact position on each EMR layer a *cluster-finding algorithm* has been adopted: a cluster has been defined as a group of contiguous bars with a signal over the threshold set with the pulse height and pull cuts (figure 5.8(a) top). The identification of the cluster has been performed using the following procedure based on the same center of gravity method used for the SiBCs (Appendix B):

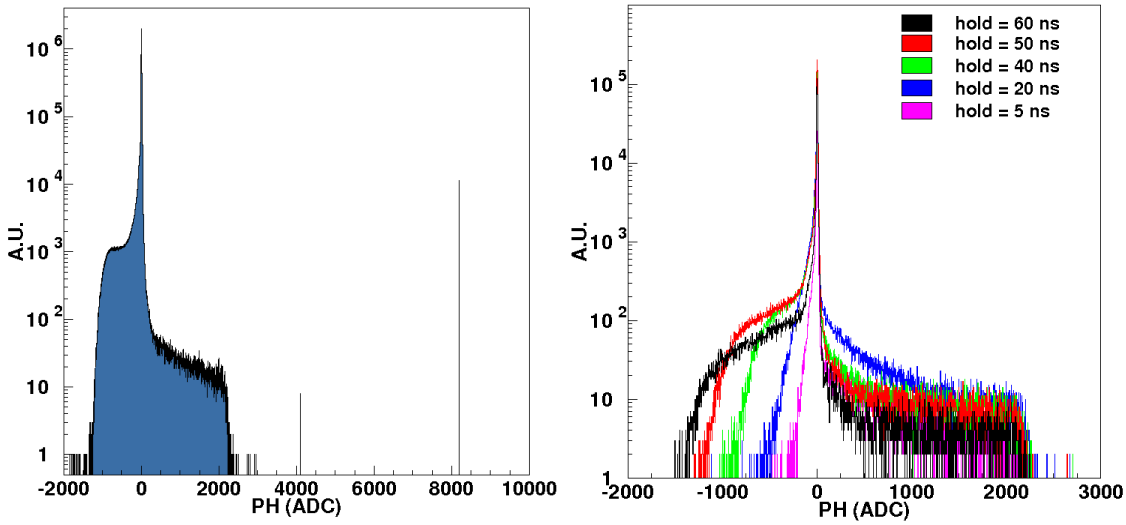


(a) (b)

Figure 5.5: (a) The global pulse height distribution of one EMR layer (the other behaves in the same way): both positive and negative signals are present given the cable length. (b) The pulse height distribution for different values of the hold signal: the best choice for the module readout is the black one (hold=60 ns).

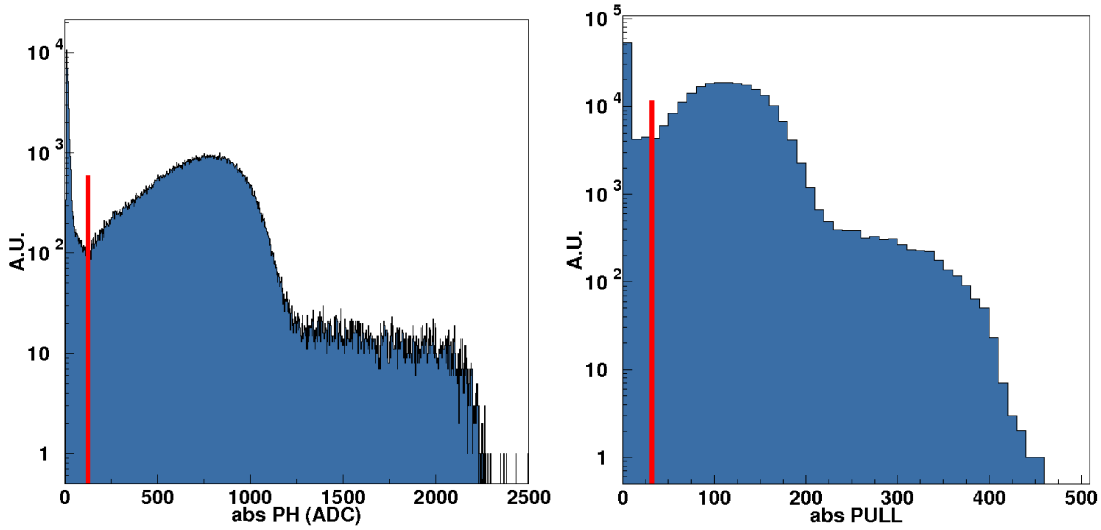


(a) (b)

Figure 5.6: The global distribution of the absolute value of the pulse height (a) and pull (b) of the bar with the maximum signal in the event.

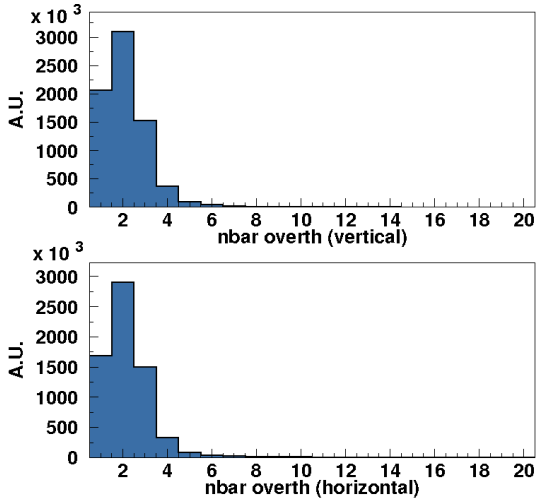


Figure 5.7: The distribution of the number of bars over threshold for both layers: typically 2 bars were crossed by a particle in each event.

- the pulse height of all the bars of each layer has been compared with the threshold: if the signal of a bar overcomes the cut, the bar has been considered as the one crossed (*fired*) by a particle and its number has been identified (figure 5.8(b) gives an example of the used procedure);

- the difference *diff* between each couple of "fired" bars has been computed in order to evaluate the number of clusters in each layer and the number of bars composing each cluster:

  · two clusters are considered as separated (figure 5.8(a) bottom) if the difference *diff* is greater than 2; the distributions obtained for each of the EMR layers are shown in figure 5.9(a): the single cluster events are $\sim 5$ times the multicluster ones in both layers;

  · if the difference *diff* is smaller than 2 a counter variable defining the number of bars in each cluster has been increased of 1; the obtained distributions are shown in figure 5.9(b): as expected, given the geometry of the setup, in most of the events the cluster is composed of $1-3$ bars. A number of bars per cluster greater than 2 has been associated to the cross talk effect; in particular in the vertical layer the worse interface with the MAPMT caused a larger number of bars per cluster;

- for each cluster in the layer the position of the particle has been defined as:

$$xweig\_emr = \frac{\Sigma_i \left(\mathrm{BAR_i} * width * \mathrm{PH_i}\right)}{\Sigma_i \, \mathrm{PH_i}} \tag{5.1}$$

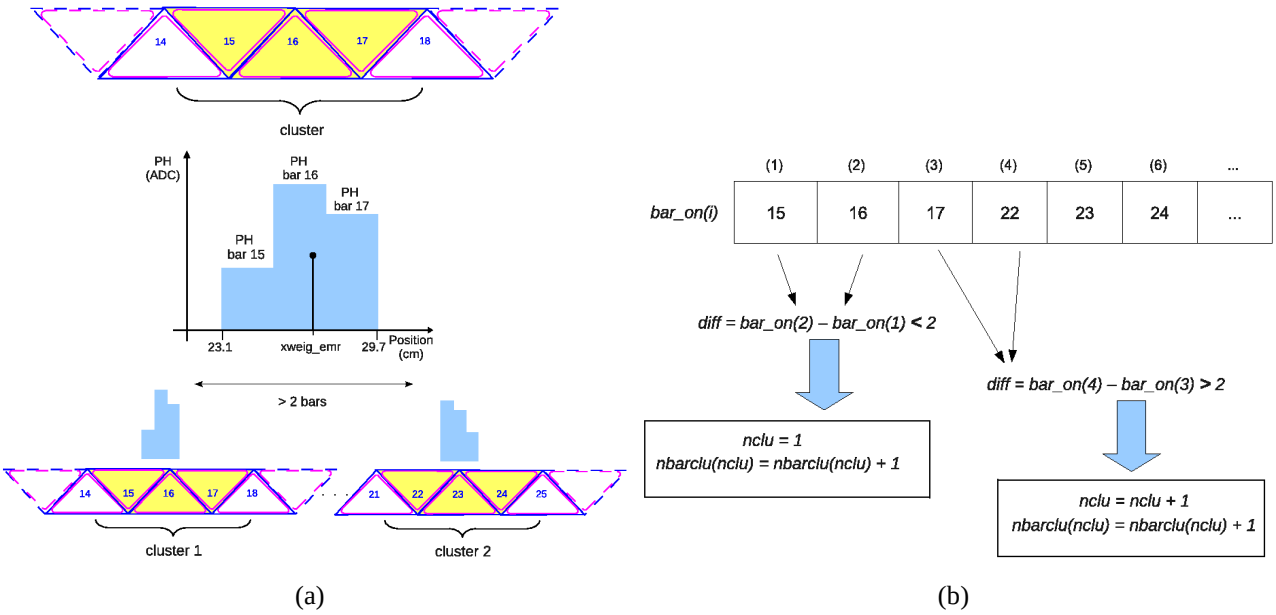


(a) (b)

Figure 5.8: (a) Schematic view of the cluster-finding algorithm: the position on each EMR layer has been computed with equation 5.1. (b) Scheme of the method used to compute the number of clusters in each layer and the number of bars per cluster.

where the *i* index runs over the number of bars composing the cluster, PH is the corresponding pulse height and *width* is the transversal dimension of the bar (that is 3.3 cm) used to convert the position in cm (figure 5.8(a) top).

Once the particle position has been identified, the profile histograms for both the directions have been considered (figure 5.10): as expected both the distributions are quite flat given the cosmic flux is constant in the azimuthal direction.

### 5.2.4 Spatial resolution

The spatial resolution of both the EMR layers has been evaluated with the same residual method presented in section 4.3.3 for the test phases: the residual distribution (that is the distribution of the difference between the position reconstructed by the SiBCs and the one measured by the layers themselves) has been computed and the result is shown in figure 5.11. Both the single cluster events and the multicluster ones have been considered: the distributions have been fitted with a Gaussian function and the ranges of the fit have been chosen by hand in order to exclude the tail regions that are affected by the cross talk effect. This effect is clearly visible in the top of figure 5.11(b) in which two additional peaks are

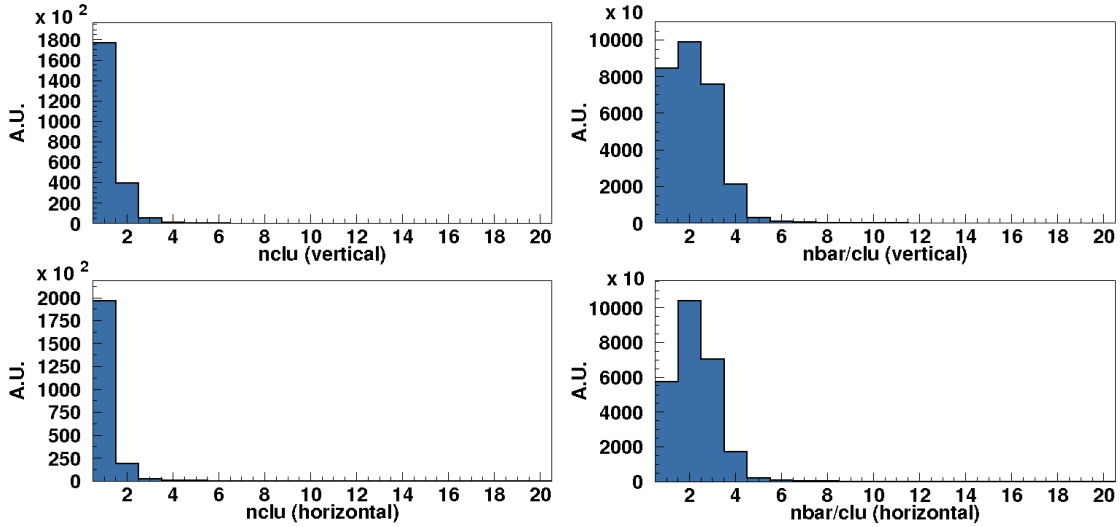


(a) (b)

Figure 5.9: (a) The distribution of the number of clusters: typically each layer has a single cluster per event. (b) The distribution of the number of bars per cluster: in most cases the cluster is composed of $1-3$ bars (including the cross talk contribution).

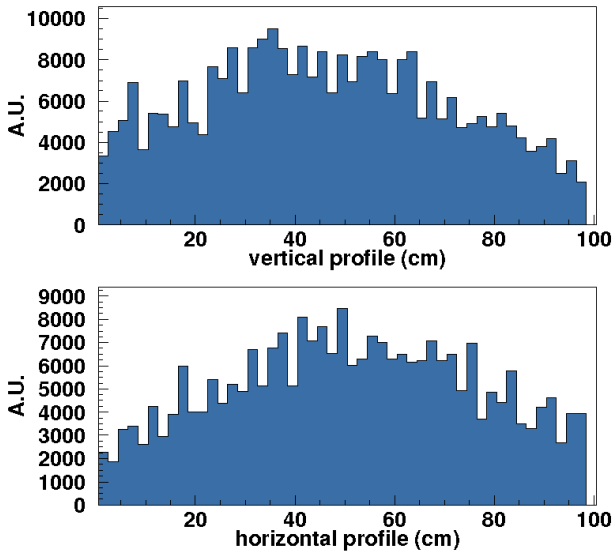


Figure 5.10: The cosmic rays profile measured with the EMR module: vertical (top) and horizontal (bottom) direction.

present at $\pm$ 25 cm reflecting again the fact that in the vertical layer the MAPMT-fiber mask interface is worse.
An average value of $\sim$ 7.4 mm has been obtained considering the single cluster events while the spatial resolution value grows up to $\sim$ 8 mm for the multicluster events: nevertheless, both the results are satisfactory and the agreement with the theoretical value is good enough, considering that the Multiple Coulomb scattering contribution has not been excluded in the residual calculation.

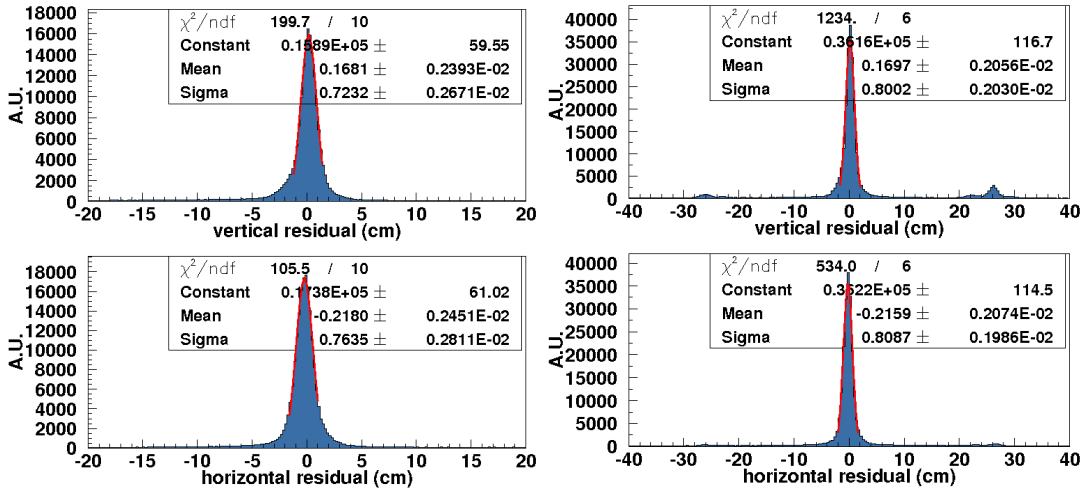


(a) (b)

Figure 5.11: The spatial resolution measured with the EMR module; both the single cluster events (a) and the multicluster ones (b) have been considered: an average value of $\sim$ 7.4 mm and $\sim$ 8 mm has been obtained, respectively.

### 5.2.5 Efficiency

A slicing method similar to the one used for the test phases (section 4.4.2.4) has been adopted to compute the efficiency of the EMR module at UNIGE; the following procedure has been used[4]:

- the trajectories measured with the silicon detectors have been projected on the surface of each of the EMR layers. The *projected histogram* (that is the beam profile at the EMR *z* position) has been used to define a fiducial area (red square in figure 5.12) with a statistics large enough for the computation of the efficiency value; this means that only the particles with a trajectory between $-20$ cm and $+40$ cm in both directions have been considered;

[4]The same nomenclature used in section 4.4.2.4 is used here.

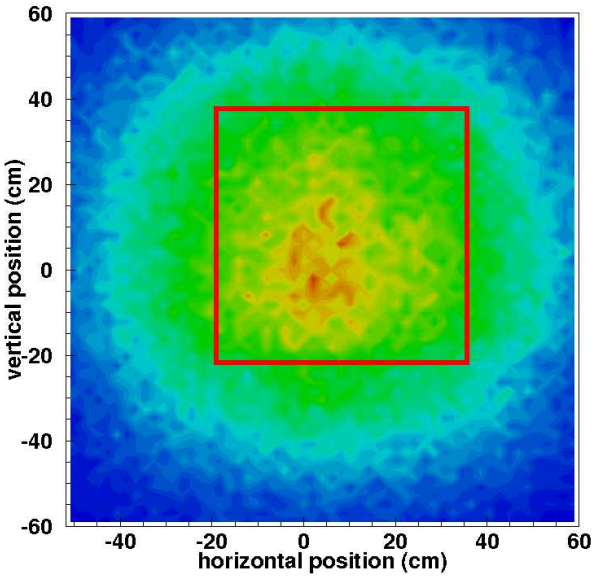


Figure 5.12: The projected histogram measured with the SiBCs has been used to identify a fiducial area with a statistics large enough (red square) for the efficiency calculation.

- for all the single cluster events in the fiducial area, the residual of each layer has been computed: an event is considered good if the cluster has a residual value in the range $\pm 5.5$ cm, that is only the particles which have a residual value in the central peak of figure 5.11 have been taken into account. Figure 5.13 shows an example of good and bad events measured by the vertical EMR layer;

- the *shadow histogram* for each of the EMR layers has been filled with 1 whenever a good event has been reconstructed by the layers themselves;

- the *efficiency plot* (figure 5.14) has been obtained as the ratio of the beam profile reconstructed by the EMR layers with the correct residual (the shadow histogram) and the one measured by the silicon detectors in the fiducial area (the projected histogram);

- to compute the exact value of the efficiency both along and across the bars, the horizontal and vertical slices of figure 5.14(a) and 5.14(b) have been fitted with a constant; in total 59 slices, $\sim 18.6$ mm wide (that is one slice for each bar), have been considered for each direction. The values obtained in the fit have been then plotted as a function of the vertical/horizontal position (figure 5.15). To extract the final value of the efficiency, a fit with a constant

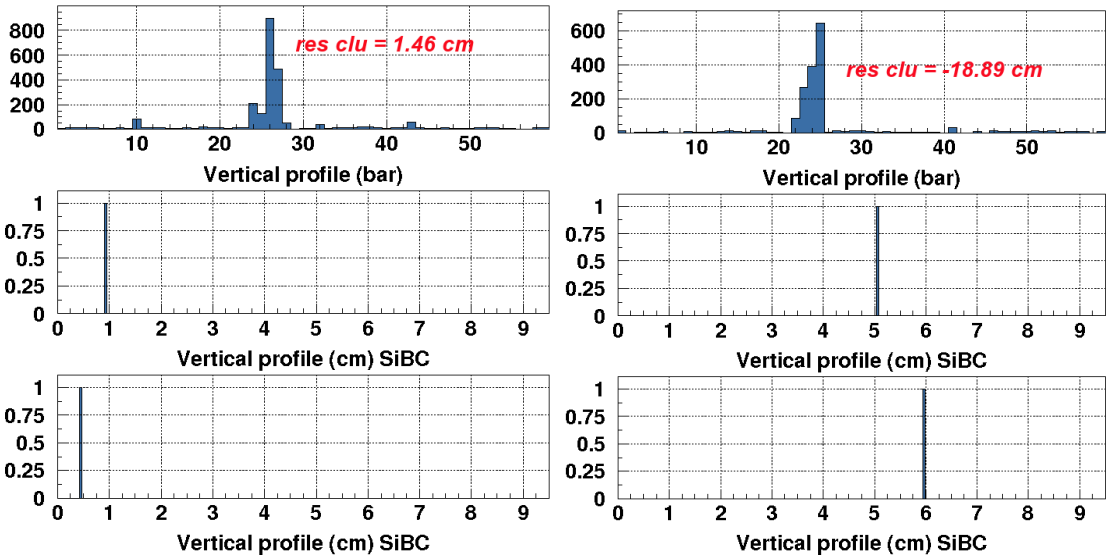


(a) (b)

Figure 5.13: Example of good (a) and bad (b) events measured by the EMR vertical layer: an event is considered good if the particle trajectory is in the range defined by the red square in figure 5.12 and the residual is in the range $\pm 5.5$ cm.

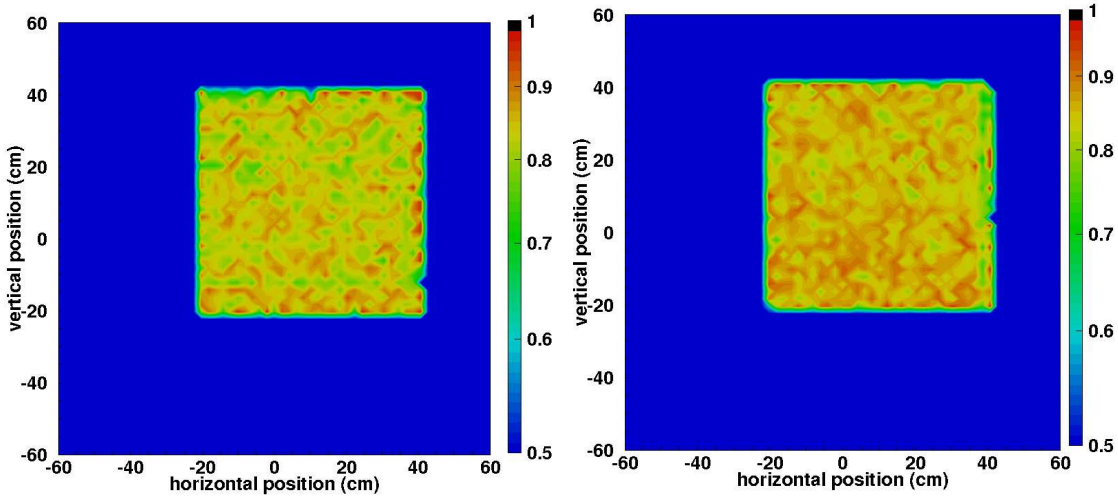


(a) (b)

Figure 5.14: The efficiency plot measured with the vertical (a) and horizontal (b) layer of the EMR module.

function has been performed: an efficiency value of about 91% has been obtained both for the efficiency across and along the bars;

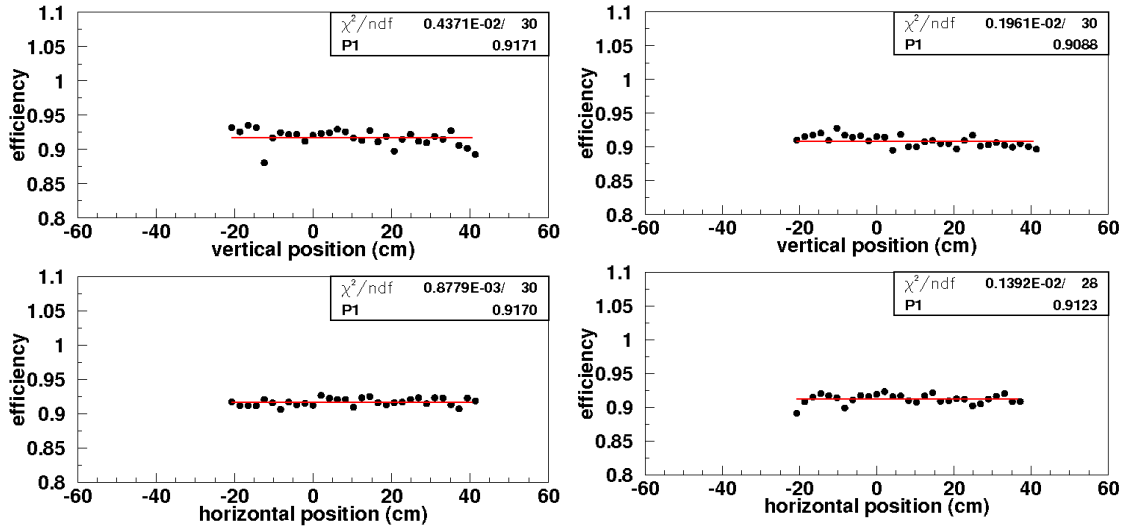


(a) (b)

Figure 5.15: Comparison of the horizontal and vertical slices of the two EMR layers: vertical (a) and horizontal (b) layer. An efficiency value of $\sim$ 91% has been measured for both layers.

- given the values obtained for the efficiency were not satisfactory, a more detailed analysis has been performed to refine the good event selection. In particular the contribution of the so-called *muon decay events* has been studied. When the muon interacts with the EMR module, in fact, there is a non zero probability that the muon decays inside the triangular bars (or travelling between the module and the SiBCs) and the produced electron is detected underneath by the silicon chambers (figure 5.16). Also the possibility of having two tracks coming from air showers, given the size of the EMR module, is not negligible. This means that, even if the reconstructed trajectory is inside the fiducial area defined in figure 5.12, this event must be excluded in the calculation of the efficiency[5];

- the computation of the muon decay event contribution and the exclusion of such events in the efficiency calculation have been performed considering again the residual distribution. Taking as an example the vertical layer:

[5]In particular, referring to the efficiency definition (equation 4.4), the muon decay events must be excluded in the computation of the denominator.

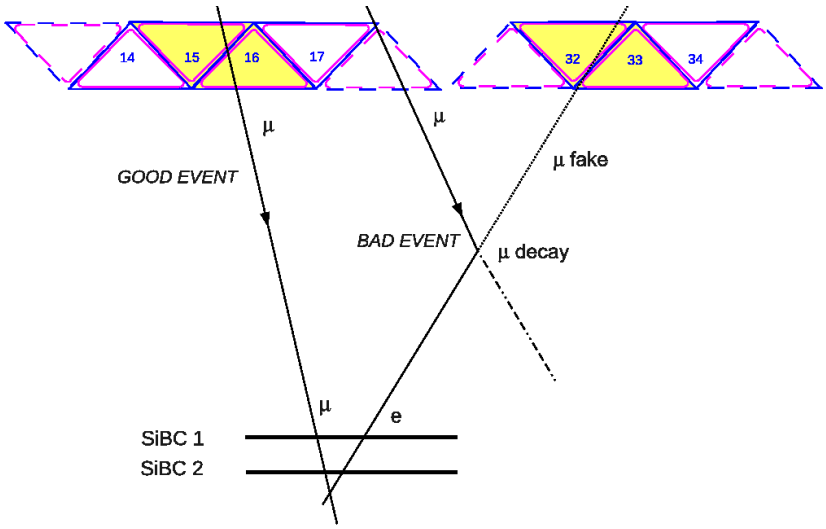


Figure 5.16: Schematic view of a muon decay event in the EMR module: in $\sim$ 6.5% of the cases the muon interacting with the EMR module decays inside it or after the bar layers and the produced electron is detected by the SiBCs underneath giving a single track event in the chambers. These events must be excluded in the efficiency computation.

- whenever the cluster residual *yres* was in the range $\pm$5.5 cm, the event has been considered good;
- whenever the cluster residual *yres* was larger than $\pm$5.5 cm, also the cluster residual in the horizontal layer (*xres*) has been computed and the event has been considered good only if *xres* was smaller than $\pm$5.5 cm: these cases correspond to an inefficiency of the vertical layer;
- the cases in which both *yres* and *xres* were larger than $\pm$5.5 cm correspond to the muon decay events.

In this way $\sim$ 6.5% of the total events in the fiducial area have been identified as muon decay events and have been excluded from the efficiency calculation;

- the new 2D efficiency plots filled with the correct number of events are shown in figure 5.17;
- the same slicing method presented above has been used to compute the efficiency trend and the results are presented in figure 5.18: the measured efficiency is of the order of $\sim$ 98% for both the EMR layers and the uniformity along the bars themselves has been confirmed.

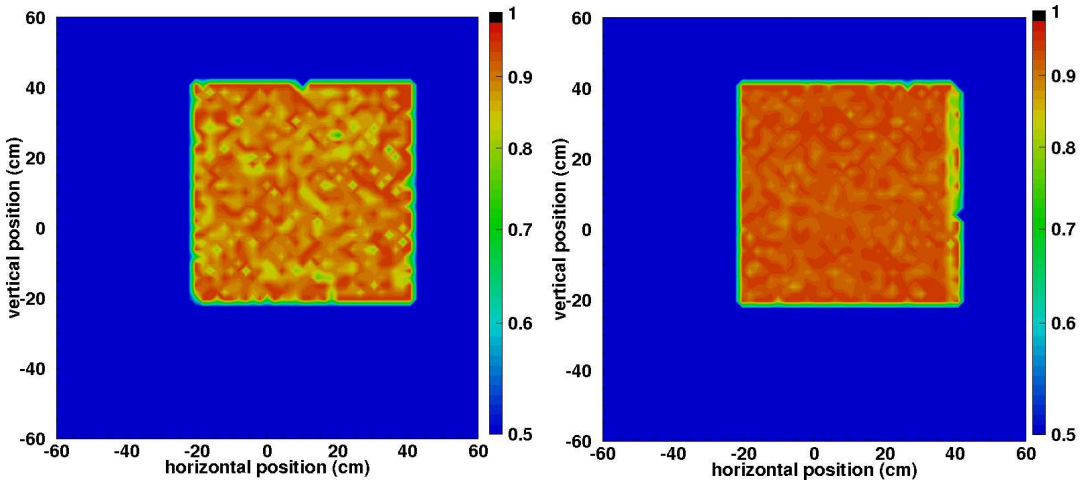


(a) (b)

Figure 5.17: The efficiency plot measured after the exclusion of the muon decay events: vertical (a) and horizontal (b) layer.

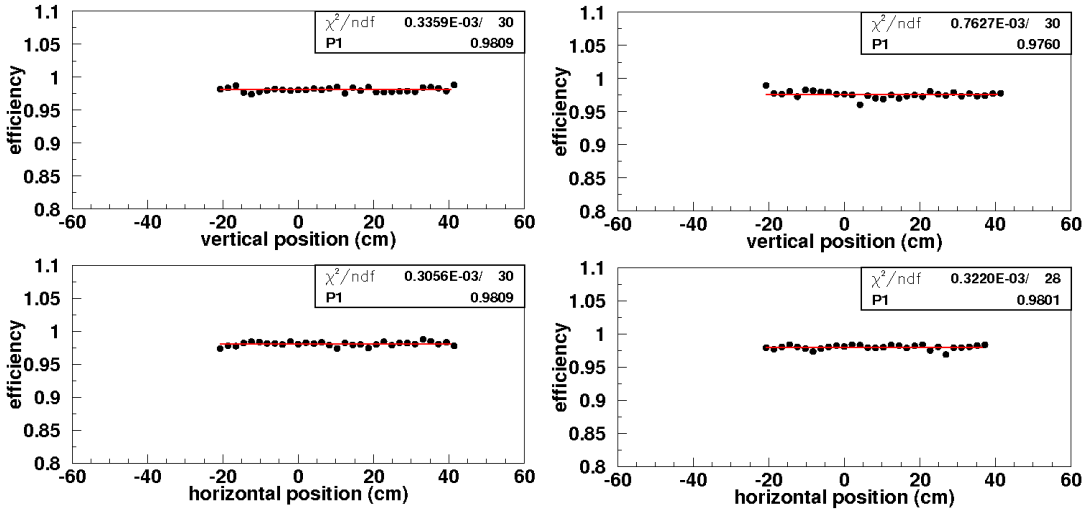


(a) (b)

Figure 5.18: Comparison of the horizontal and vertical slices after the exclusion of the muon decay events: vertical (a) and horizontal (b) layer. An efficiency value of $\sim$ 98% has been measured for both layers.

### 5.2.6 Cross talk

As mentioned above, a non adequate alignment between the MAPMT window and the plastic fiber mask causes the light entering in one of the MAPMT channels to spread also in the neighbouring ones. This effect is known as *optical cross talk*[6] and leads to a wrong reconstruction of the particle position. In particular, this means that the spatial resolution value is affected by this effect and the results presented in the previous sections are not the effective ones.
Figure 5.19 shows an example of event display as measured by the vertical layer (*module view*, top) and as seen at the MAPMT window level (*MAPMT view*, bottom): the red squares indicate the bars over threshold. In this way it is possible to distinguish the bars that are over threshold given the cross talk effect (blue circle and arrows) from the good ones that effectively identify the particle position (red ellipse and arrows). Given the geometry of the setup, a number of bars per cluster larger than 2 is due to the cross talk effect; the maximum angular range to have a trajectory in all the three detectors (SiBC1 + SiBC2 + EMR layer) is in fact smaller than the maximum angular range to hit more than two bars in the EMR layers (figure 5.20(a)). Moreover, given the fiber ordering at the MAPMT window level (figure 5.20(b)), the gap between bar # 24 and # 26 in figure 5.19 reflects the fact that a number of bars per cluster larger than 2 is effectively caused by cross talk and not because the particle crosses more than two bars.
The cross talk effect has been investigated in detail with the following procedure:

- only the single cluster events with a good residual value (that is in the range $\pm 5.5$ cm) have been taken into account;

- for each group of hits (that is for each cluster) the center of the cluster, that is the bar with the maximum signal (or, equivalently, the MAPMT pad with the maximum signal), has been identified;

- a 3 by 3 grid around it has been considered (figure 5.21(a)); each cell of the grid has been filled with 1 whenever the corresponding channel is over threshold;

- the resulting lego plot for each of the EMR layers (figures 5.21(b) and 5.21(c)) gives the percentage of the different cases in which the light is diffused among the MAPMT pads; the corresponding values (expressed in %) are listed in table 5.2. In a cross talk event, in fact, the light can be spread in the up/down pads or both (that is, referring to figure 5.21(a), cell # 4 and # 6), in the rigth/left ones or both (cell # 2 and # 8) or in the diagonal ones (cell # 1, # 3, # 7 and # 9) with respect to the central pad;

[6] For a detailed description of the processes that lead to the cross talk effect see [97].

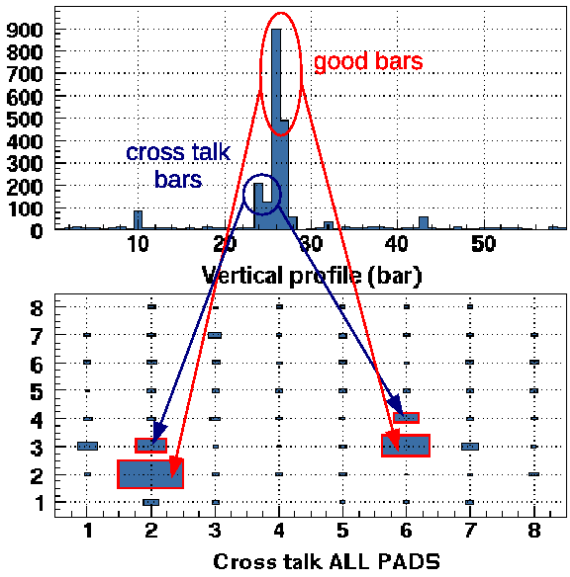


Figure 5.19: EMR event display: both the *module view* (top) and the *MAPMT view* (bottom) are shown. The red squares indicate the bars over threshold: given the cross talk effect, two additional bars are over threshold (blue arrows).

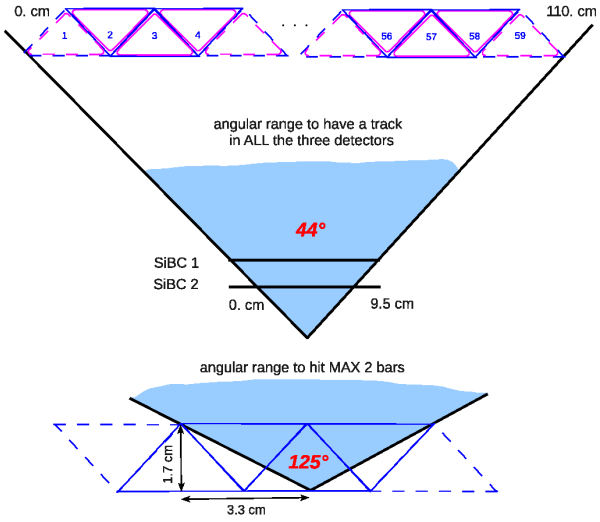


(a)

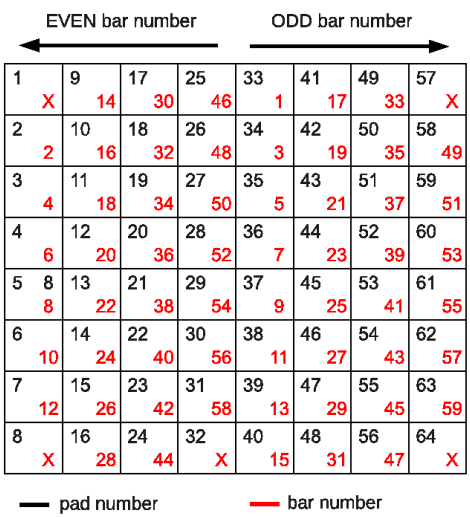


| | | | | | | | |
|---|---|---|---|---|---|---|---|
| 1 X | 9 14 | 17 30 | 25 46 | 33 1 | 41 17 | 49 33 | 57 X |
| 2 2 | 10 16 | 18 32 | 26 48 | 34 3 | 42 19 | 50 35 | 58 49 |
| 3 4 | 11 18 | 19 34 | 27 50 | 35 5 | 43 21 | 51 37 | 59 51 |
| 4 6 | 12 20 | 20 36 | 28 52 | 36 7 | 44 23 | 52 39 | 60 53 |
| 5 8 8 | 13 22 | 21 38 | 29 54 | 37 9 | 45 25 | 53 41 | 61 55 |
| 6 10 | 14 24 | 22 40 | 30 56 | 38 11 | 46 27 | 54 43 | 62 57 |
| 7 12 | 15 26 | 23 42 | 31 58 | 39 13 | 47 29 | 55 45 | 63 59 |
| 8 X | 16 28 | 24 44 | 32 X | 40 15 | 48 31 | 56 47 | 64 X |

(b)

Figure 5.20: (a) The angular range to have a trajectory in all the three detectors is smaller than the one to hit more than two bars in the EMR layers: a number of bars per cluster larger than 2 can thus be associated to the cross talk effect. (b) Bars ordering at the MAPMT window level: the black numbers indicate the MAPMT pad number while the red ones the corresponding bar number.


(a)

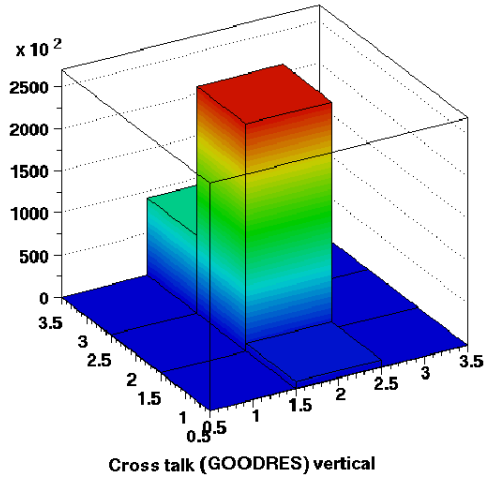


(b)

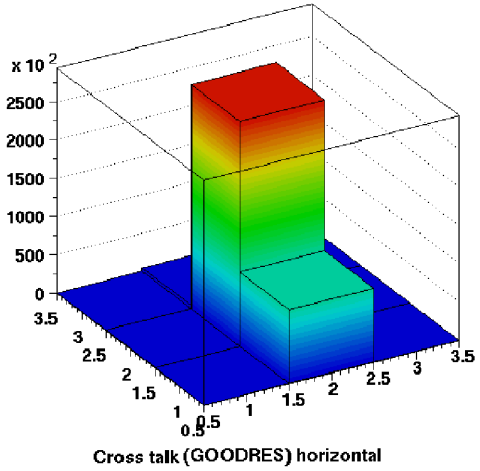


(c)

Figure 5.21: Pad numbering for the cross talk percentage computation (a). Lego plot for the vertical (b) and horizontal (c) EMR layer: an up/down shift of the MAPMT with respect to the fiber mask is present in both layers.

| type | 1 | 2 | 3 | 4 | 5 | 6 | 7 | 8 | 9 |
|---|---|---|---|---|---|---|---|---|---|
| vertical layer | 0. | 0. | 0. | 34.1 | 100.0 | 3.1 | 0. | 0. | 0. |
| horizontal layer | 0. | 0. | 0. | 1.5 | 100.0 | 32.8 | 0. | 0. | 0. |

Table 5.2: The cross talk percentage (expressed in %) measured with the EMR module (the pad numbering is the same shown in figure 5.21(a)).

- an up/down shift of the MAPMT with respect to the fiber mask is present in both layers as expected given the fiber ordering at the MAPMT level.

Once the cross talk has been taken into account the residual distribution has been recomputed to extract the final value for the detector spatial resolution; in this case only the result obtained taking into account the single cluster events is shown in figure 5.22: as expected, smaller values (of the order of 6 mm) have been obtained excluding the cross talk events.

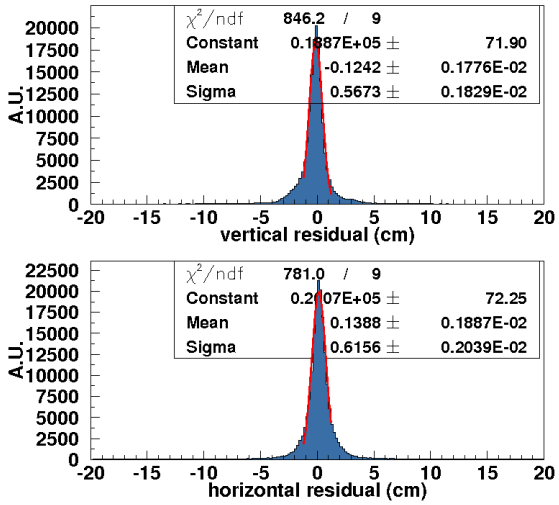


Figure 5.22: The spatial resolution measured after the cross talk correction considering the single cluster events: an average value of $\sim$ 6 mm has been obtained.

## 5.3 FEB results

In the following sections the preliminary results obtained in the last phase (that is with a prototype of the MAROC-II FEB) are presented.

### 5.3.1 Pedestal and noise

Figure 5.23 presents the behavior of the noise rms before (black) and after (red) the subtraction of the common mode contribution measured with the final FEB: the global noise rms distribution of the first MAPMT (the one with the flexible connector which measures the vertical direction) is shown on the top while the distribution for the second layer is presented in the bottom. Given the noise of the

first MAPMT was very low, its distribution has an irregular shape. After the common mode subtraction the noise rms value is quite constant over all the channels and is in the range 2−4 ADC for both the MAPMTs.

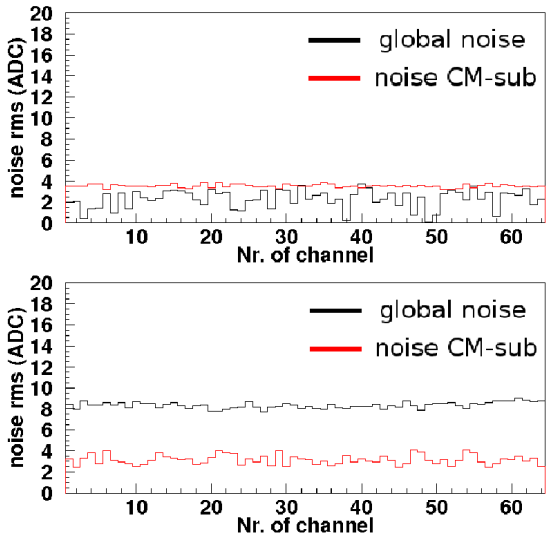


Figure 5.23: The noise rms distributions measured with the MAROC-II FEB (*phase IV*): once the common mode contribution has been subtracted the noise rms has a value in the range 2−4 ADC.

### 5.3.2 Bars behavior

Figure 5.24 shows the global distributions of the pulse height and of the pull of the bar with the maximum signal in the event measured during *phase IV*: also in this case the valley that separates the particle events from the noise ones is clearly visible. The threshold (red lines) is thus set excluding the high peaks near 0: whenever the pull of a bar is larger than $15\sigma$ the event is considered as good and the particle position has been computed using the method presented in section 5.2.3.
The cluster-finding algorithm has also been used to calculate the number of clusters in each layer and the number of bars composing each cluster (figure 5.25): in this case a better alignment between the MAPMT window and the fiber mask has allowed to reduce the cross talk effect and consequently the single cluster events are $\sim$ 10 times the multicluster ones while the number of bars per cluster has a value of 1−2 in most cases.

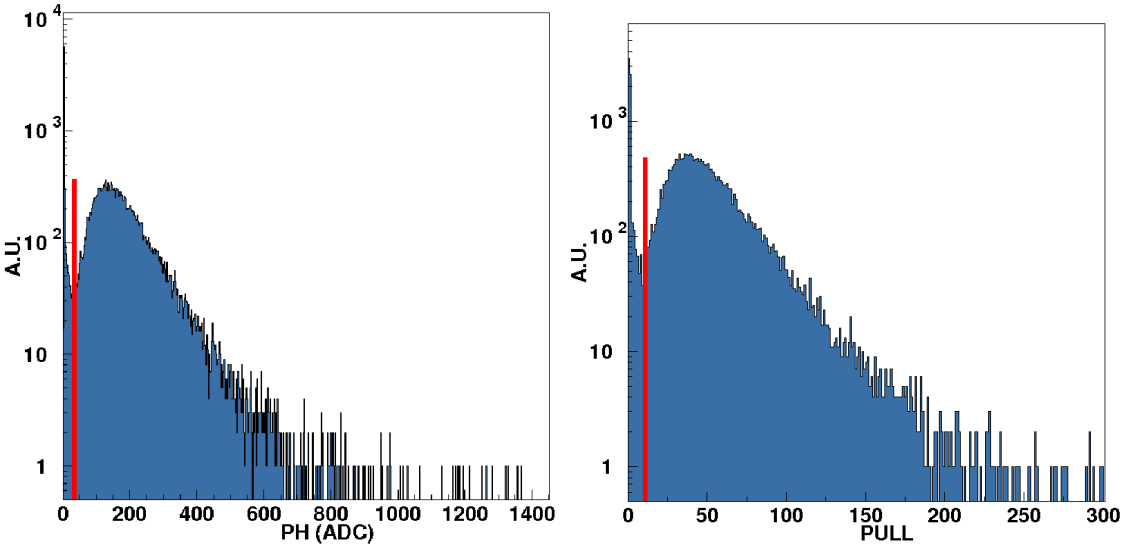


(a) (b)

Figure 5.24: The pulse height (a) and pull (b) distributions of the bar with the maximum signal in the event measured with the MAROC-II board (*phase IV*): the valley between the noise peak and the particle one is well defined and a threshold value of $\sim 15\sigma$ has been chosen.

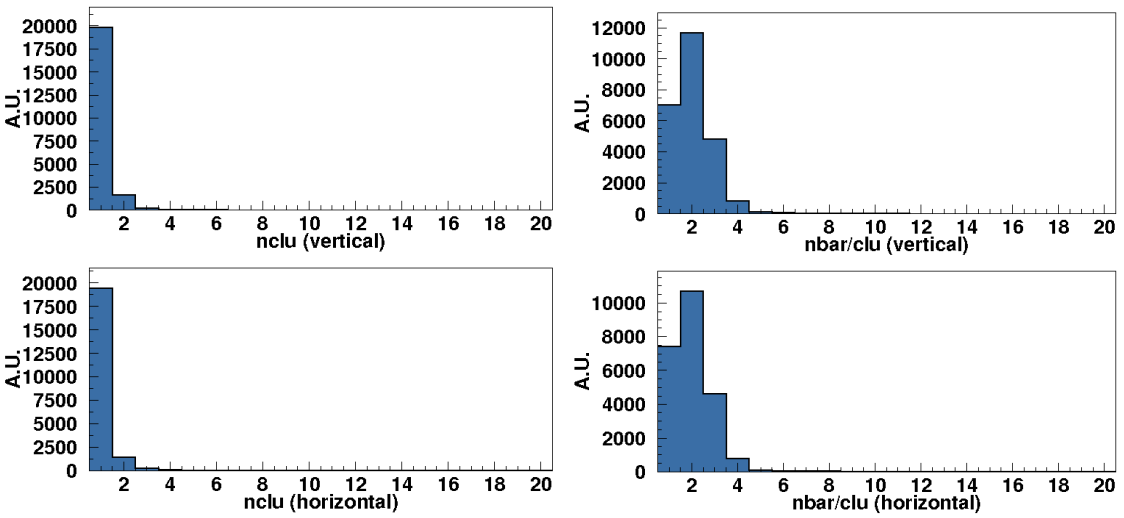


(a) (b)

Figure 5.25: (a) The distribution of the number of clusters: also in this case the events are typically single cluster events. (b) The distribution of the number of bars per cluster: in most cases the cluster is composed of $1-2$ bars (given the better alignment of the MAPMT with the fiber mask).

### 5.3.3 Spatial resolution

The residual distribution (see section 4.3.3 for details) measured by the two EMR layers during the last phase of the commissioning is presented in figure 5.26; the single cluster events have been considered and the obtained distribution has been fitted with a Gaussian function. In this case the distribution shown in figure 5.26 is the one computed after the subtraction of the cross talk: the better MAPMT-fiber mask alignment in *phase IV*, in fact, allows to reduce the cross talk contribution. Also in this case a preliminary average value of $\sim$ 6.8 mm has been obtained and is in good agreement with the theoretical one.

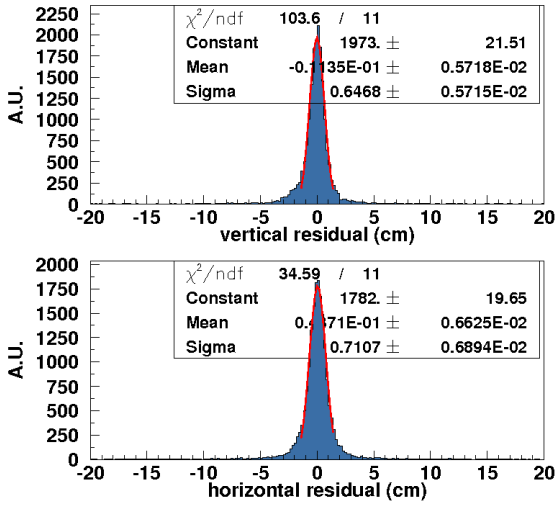


Figure 5.26: The spatial resolution measured considering the single cluster (a) and the multicluster (b) events: as expected, a spatial resolution value similar to the one measured with the MUSTAP boards has been found.

### 5.3.4 Efficiency

The same slicing method presented above (section 5.2.5) has been adopted to compute the efficiency during *phase IV*; in figure 5.27 the comparison of the vertical and horizontal slices is presented: even if the statistics is not large enough, also in this case a preliminary value of $\sim$ 98% for the efficiency has been measured.

### 5.3.5 Cross talk

The same procedure presented in section 5.2.6 has been used to evaluate the cross talk contribution in the last phase (figure 5.28).
As mentioned above, the better alignment between the MAPMT window and the

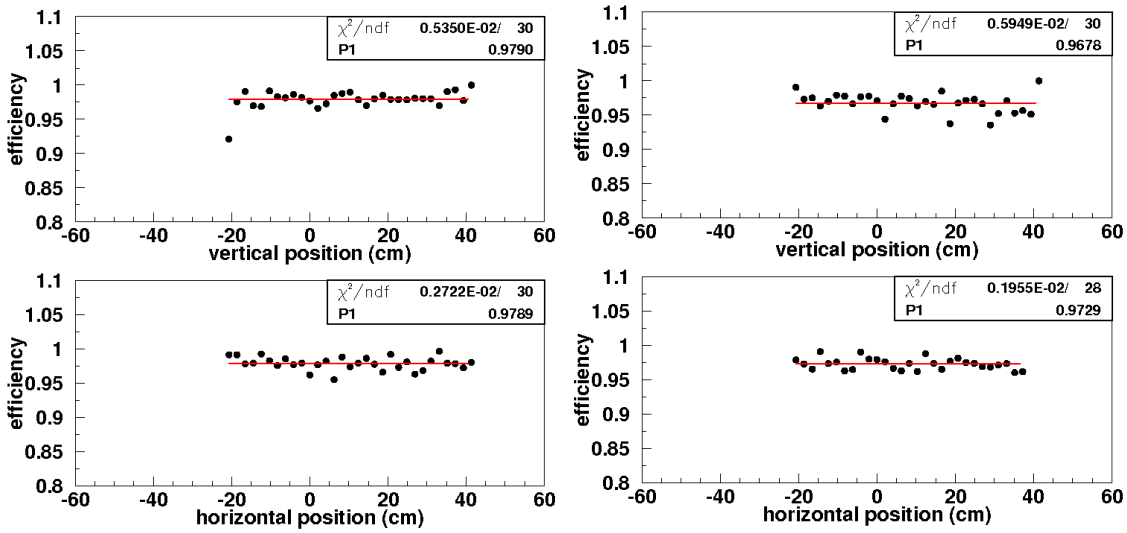


(a) (b)

Figure 5.27: Comparison of the horizontal and vertical slices measured during the *phase IV*: an efficiency value very close to 98% has been obtained for both the layers.

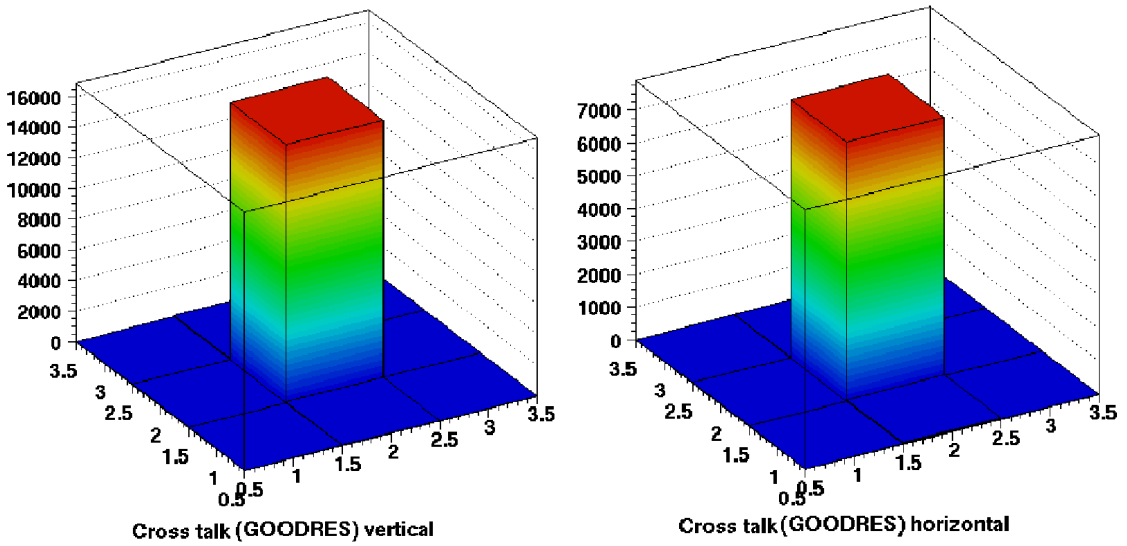


(a) (b)

Figure 5.28: Lego plot of the vertical (a) and horizontal (b) layer: in this case the better alignment between the MAPMT and fiber interface guarantees a lower cross talk among the MAPMT pads.

fiber mask leads to a reduction of the cross talk effect that in *phase IV* is practically absent (see also the values listed in table 5.3).

| type | 1 | 2 | 3 | 4 | 5 | 6 | 7 | 8 | 9 |
|---|---|---|---|---|---|---|---|---|---|
| vertical layer | 0. | 0. | 0. | 0.5 | 100.0 | 0.2 | 0. | 0. | 0. |
| horizontal layer | 0. | 0. | 0. | 0.2 | 100.0 | 0.4 | 0. | 0. | 0. |

Table 5.3: The cross talk percentage (expressed in %) measured with the EMR module (the pad numbering is the same shown in figure 5.21(a)): in this case the cross talk between the MAPMT pads is greatly reduced given the better alignment with the fiber mask.

# Chapter 6

# Conclusions & Outlooks

Since the '30s, when Pauli first solved the anomaly observed in the β decay, neutrino physics has played an important role in the field of modern physics; nevertheless some aspects still need to be studied and could represent the first steps beyond the Standard Model. For this reason, the development of new facilities and new techniques (that should provide neutrino beams with the desired intensity, purity and collimation to deeply investigate the neutrino nature) represents a fundamental step for the future of particle physics. The Muon Ionization Cooling Experiment, together with the Neutrino Factory and Muon Collider Collaboration, works in this direction and in particular aims at developing and testing a cooling section to experimentally demonstrate the ionization cooling technique of a muon beam (which in turn produces neutrinos).
This thesis work has been performed in the framework of the MICE experiment and in particular has focused on the design, the construction, the tests and the commissioning of the Electron Muon Ranger (EMR). EMR will be placed at the end of the MICE cooling section and will provide the muon/electron separation needed for the emittance measurement.
EMR consists of 48 layers of extruded scintillator bars with a triangular cross section readout by a single Wave Length Shifter (WLS) fiber glued in the bar hole and connected on both sides to single channel (PMT) and multianode (MAPMT) photomultipliers. The PMT signals are sampled and digitized by a Wave Form Digitizer (WDF) while the conditioning of the MAPMT signals is performed with a dedicated board (the *FrontEnd Board*) based on the MAROC ASIC and tested in this thesis work.
The construction of EMR has required several characterization tests to define the final design and, in particular, the use of triangular shape bars, the number of WLS fibers per bar and the use of the glue inside the bar hole. For this reason, a small scale prototype of EMR (with only 8 layers and shorter bars with a rectangular cross section) has been built to define the assembly procedure and to use it as a

test bench for the optimization of the final electronics. The prototype has been tested with extracted particle beams at the CERN Proton Synchrotron with two different electronics chains (the *FAST electronics* and the *MUSTAP board* both based on the VA64TAP2.1+LS64_2 ASICs) obtaining good results in terms of spatial resolution ($\sim$ 6.5 mm) and efficiency ($\sim$ 99%). Together with the prototype, dedicated setups have been developed to understand the improvement in efficiency moving from a rectangular to a triangular shape bar and for the study of the cross talk at the MAPMT level.
A third electronics chain (that is the final one based on the MAROC ASIC) has been tested with cosmic rays with the small scale prototype at the Insubria University and with the first two EMR layers assembled at the University of Geneva (where EMR is under construction). The spatial resolution (by means of a couple of high spatial resolution silicon detectors) has been measured to be $\sim$ 6.5 mm after the subtraction of the cross talk contribution. The efficiency is of the order of $\sim$ 98% and the uniformity across and along the bars themselves has been verified.
As far as the next future is concerned, the last version of the electronics has to be implemented. Given the MICE beam structure (one good event every 5 $\mu$s in a 1 ms spill every second) a digital readout of the MAPMT signals must be considered. The analog readout, being multiplexed, lasts $\sim$ 12.8 $\mu$s and is incompatible with the experimental duty cycle. For this reason the commissioning and tests of the final FEB working in digital mode are needed. The EMR detector installation at RAL is foreseen in spring 2011.
The MICE and the Neutrino Factory and Muon Collider Collaborations are also involved in long term projects. As mentioned in Chapter 1, the physics potential of a Neutrino Factory will guarantee unprecedent precision on the measurement of the neutrino oscillation parameters and will offer the possibility to study both the QCD and the slow muon physics. Nevertheless, there are two other main technologies to produce neutrino beams of large intensity and purity:

- the so-called *Super Beams (SBs)* [50] in which the proton beam is produced with an unprecedent power (up to 4 MW) and the associated detectors have a very large fiducial mass. In particular, the so-called *Off-Axis Beam (OAB)* method [48] will be used to achieve very low contamination in the beam and to produce $\nu$s with an energy independent from the one of the parent beam (figure 6.1(a));

- the so-called *Beta Beams ($\beta$Bs)* which are based on the concept (first proposed by Zucchelli [50]) of creating a high purity, well collimated, well defined and intense $\nu_e$ and $\bar{\nu}_e$ beams from the $\beta$-decay of radioactive ionized ions (typically Ne and He nuclides); figure 6.1(b) shows a possible future scenario for a Beta Beam complex at CERN [24, 50].

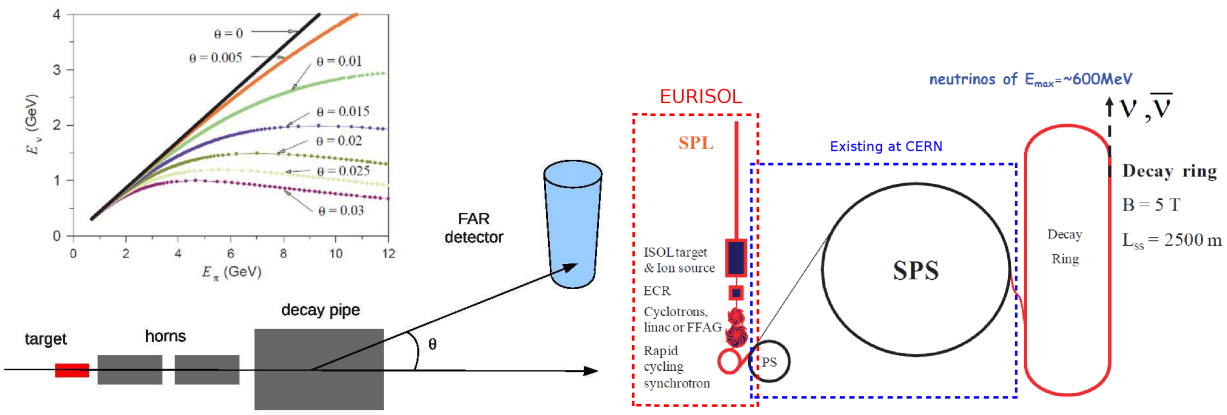


(a) (b)

Figure 6.1: (a) Schematic principle of the Super Beam production and correlation between the $\nu$ and $\pi$ energy. (b) Schematic layout of a possible Beta Beam at CERN [24].

Even if these technologies (and the one presented in Chapter 1 for a Neutrino Factory) are based on different methods, they share some common aspects: the most important and intriguing is the R&D of the near and far detectors. In particular, several detector types have been foreseen [53]:

- the Magnetized Iron Neutrino Detectors (**MINDs**, figure 6.2(a)); they are very large mass sampling calorimeters (typically made of iron/steel and scintillator) immersed in a magnetic field able to provide matter/antimatter distinction and to increase the neutrino interaction probability (thanks to their very large mass); they represent the baseline option for near and far detectors of a future Neutrino Factory complex and will be optimized for the detection of the *golden channel* (that is the appearance channel $\nu_e \rightarrow \nu_\mu$);

- the Liquid Argon detectors (**LAr TPCs**, figure 6.2(b)); they consist in Time Projection Chambers (TPCs) made of massive (up to 100 kton) dense material that provide high uniform and accurate imaging; they will be used in a Neutrino Factory, together with the MINDs, to detect the so-called *platinum channel* ($\nu_\mu \rightarrow \nu_e$);

- the Totally Active Scintillating Detectors (**TASDs**) in which a large mass of scintillator (up to 35 kton) is segmented in both directions (providing the particle position identification) and immersed in a 0.5 T magnetic field. The most popular design is an extrapolation of the MINER$\nu$A experiment [95] and consists of triangular shape bars with the same cross section of the ones used in EMR but with a length up to 15 m (figure 6.3); they represent the

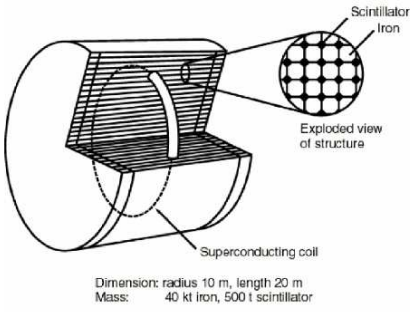


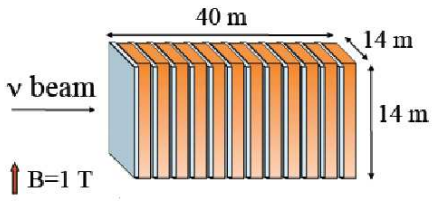


(a)

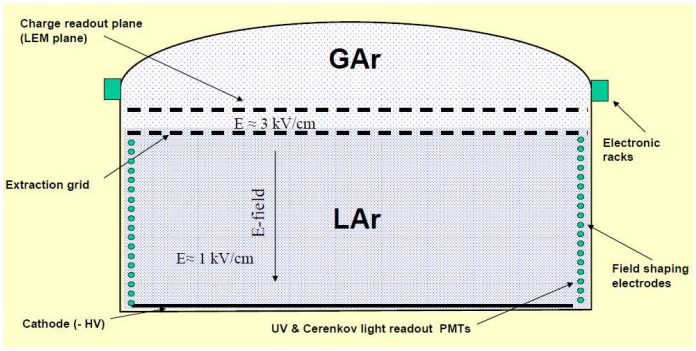


(b)

Figure 6.2: (a) Two examples of the MIND design. (b) Layout of a Liquid Argon detector.

most versatile detector type and could be used both in SB and βB facilities to provide electron/muon/pion separation with high efficiency.

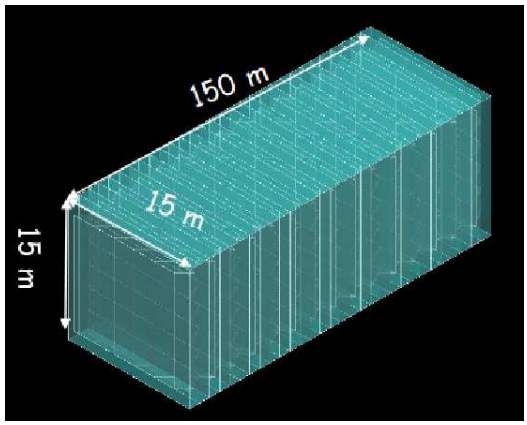


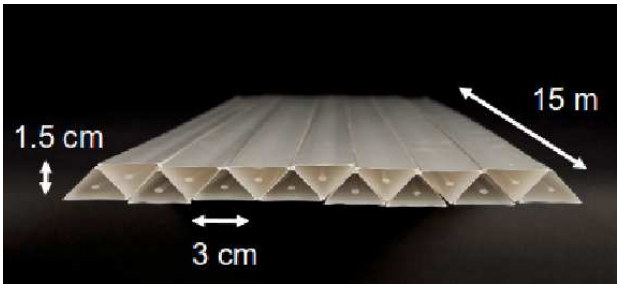


(a) (b)

Figure 6.3: (a) Schematic view of a TASD: the typical dimensions are $15\times15\times150$ m$^3$. (b) The triangular shape bars have a $3.3\times1.7$ cm$^2$ cross section and a length of 15 m.

As mentioned above, these detector types represent the new frontiers in the detector technology and open the way towards an intense R&D program both from the instrumentation and the physics points of view. In particular, dedicated studies on the way to produce such detectors, their electronics and all the problems related to the mechanical constraints and the assembly will be needed. As far as the TASD is concerned, the development of EMR could represent a first step towards its construction. In particular, different aspects in the design and engineering of a TASD, that is the production of scintillator bars with a considerable length (and thus the uniformity along the bar itself), the development of the associated electronics (that must be fast enough and able to operate in magnetic fields), the design of the mechanical support for several tons of material and all the problems related to the fiber glueing, are still open questions and will become crucial in case of such a large mass detector. The knowledge acquired in this thesis work and, in particular, during the tests with the prototype (that is the need of glue to increase the light collection and the choice of the exact number of fibers per bar) and during the construction of the final detector (in terms of mechanics and assembly procedure) are thus fundamental steps. Moreover, EMR could be used as a test bench for the development and the optimization of a different electronics chain based on Silicon PhotoMultipliers (SiPMs).

# Appendix A

# Tests on the FEB prototype

Several characterization tests have been performed on the prototype of the FrontEnd Board (FEB) in order to verify both the functionality of the FEB and the capabilities of the ASIC. The schematics of a single channel of the MAROC-II ASIC assembled on the FEB is given in figure A.1. It has 64 channels, each one consisting of a preamplifier (blue rectangle in figure A.1) feeding three different paths (red rectangles in figure A.1)[1].

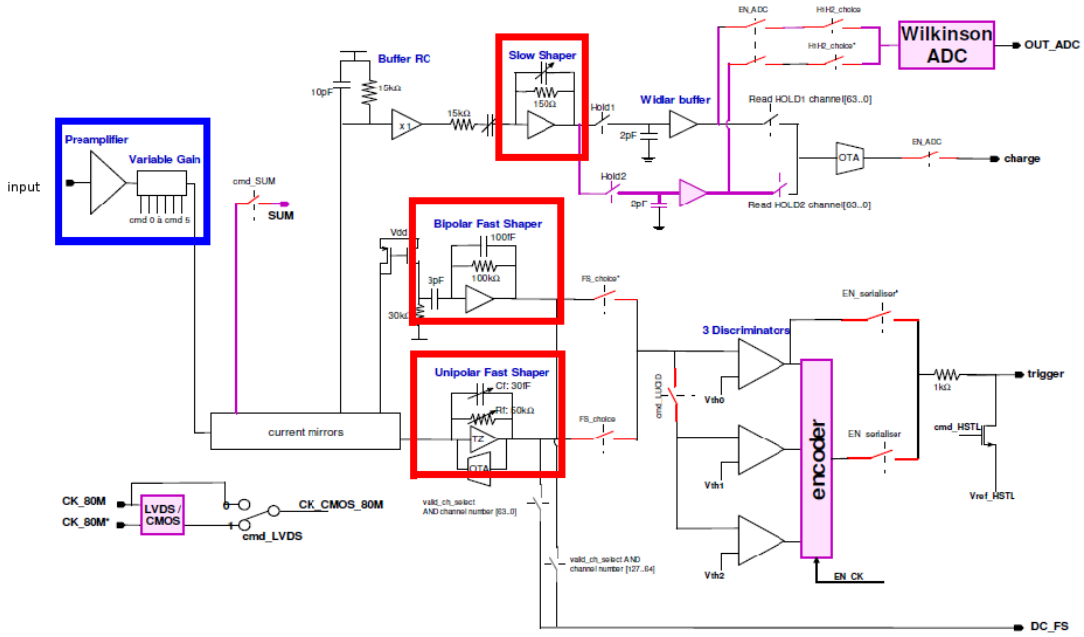


Figure A.1: Architecture of a single channel of the MAROC-II ASIC.

[1]For a complete description see section 3.1.4.1.

A scheme of the test setup is given in figure A.2. It consists of:

- the FEB prototype under test (see section 3.1.4.1 for a complete description);
- an oscilloscope to see the input/ouput signals (the FEB houses two LEMO connectors for the hold[2] and trigger outputs);
- a multimeter to control and measure the DAC threshold values;
- a pulse generator that provides the input signal;
- a VME crate that hosts the VME MAROC control board and a SBS Bit3 for the data transfer;
- a PC with the Linux operating system with both the DAQ software and the analysis routines.

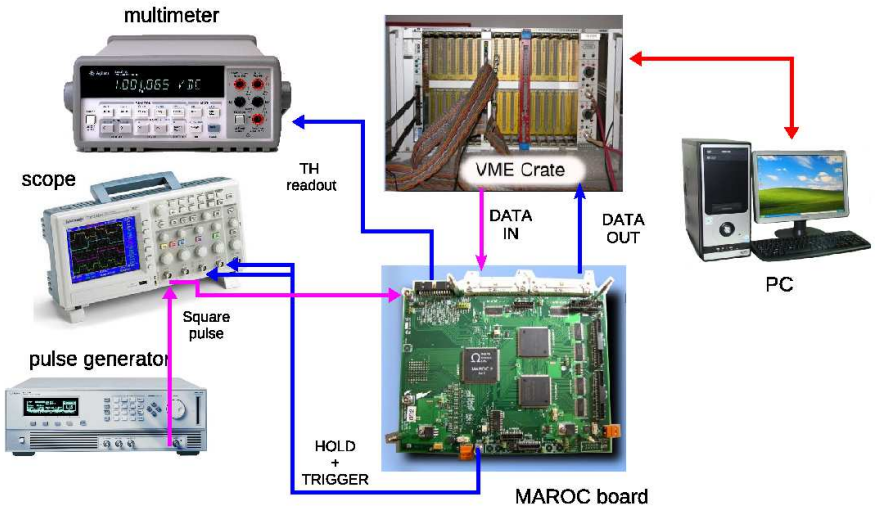


Figure A.2: Scheme of the test setup for the FEB prototype tests. It consists of the board under test, an oscilloscope, a multimeter, a pulse generator, a VME crate and a Linux PC.

[2]The *hold* signal represents the time between the trigger and the moment the signal itself is sampled and held. Its value can be set by the DAQ software.

## A.1 Test procedure & results

The MAROC-II analog output has been studied as a function of different tunable parameters; the following procedure has been applied:

- the so-called *pedestal* and *noise rms* distributions[3] have been acquired in order to evaluate the behavior of each ASIC channel in case of no signal. The obtained results are shown in figure A.3(a): the red histogram in the bottom figure corresponds to the noise rms after the *common mode* subtraction (see Appendix B for details);

- a 1 V square pulse with a frequency of 10 kHz (the so-called *calibration signal*) has been sent to a capacitor connected to each channel. The global response, that means the average over all the 64 channels, has been computed; figure A.3(b) gives an example of the obtained distribution: it has been fitted with a Gaussian function to determine the peak position and the obtained values have been used in the following analysis.

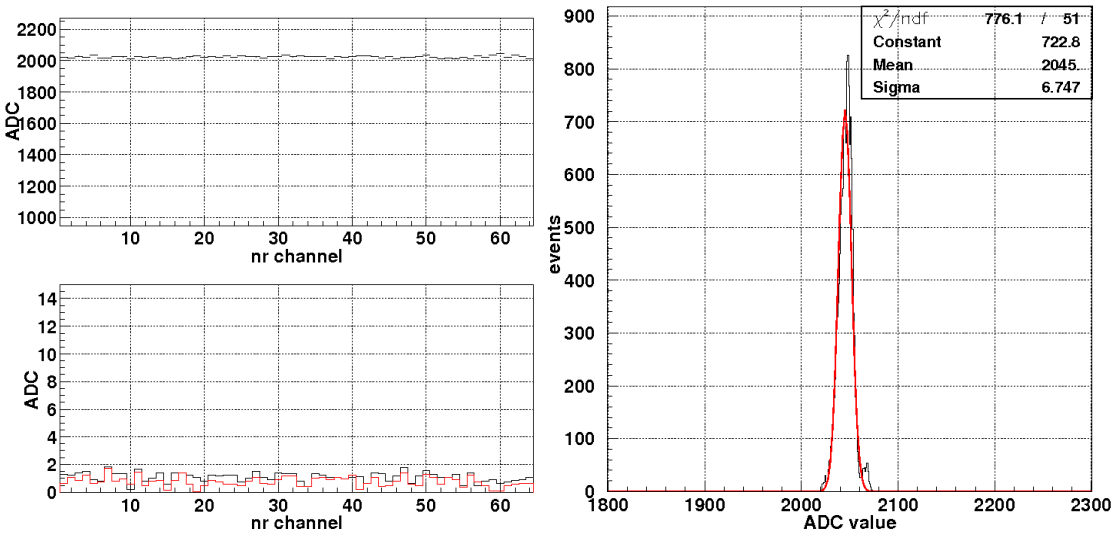


(a) (b)

Figure A.3: (a) Pedestal and noise rms distributions: the red histogram represents the common mode subtracted noise rms. (b) Example of the Gaussian fit to measure the mean value of the response of all the channels to a square pulse input.

The tests performed on the FEB prototype board were the following:

[3]They indicate, respectively, the baseline and the noise rms of the complete electronics chain (see Appendix B for details).

- a **hold scan** for a fixed value of the preamplifier gain has been performed to reconstruct the shape of the signal and measure the hold value that corresponds to the signal maximum. The output signal amplitude has been measured for different hold values in the range $0-250$ ns as mentioned above: the peak mean positions obtained with the Gaussian fit have been plotted as a function of the hold values. The results for three tested boards are shown in figure A.4: in all the cases the hold peak is at $\sim 70$ ns;

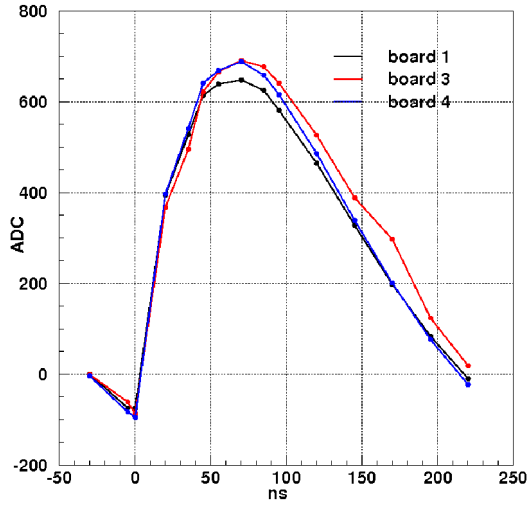


Figure A.4: Hold scan of 3 boards: the shape of the signal has been reconstructed and the peaking time corresponds to a hold value of $\sim 70$ ns.

- with a fixed hold value of 70 ns (that means at the signal peak), a **scan on the input voltage amplitude** has been performed to test the linearity of the ASIC. The input voltage has been varied in the range $0.1-6$ V while 4 values for the preamplifier gain have been chosen ($4-8-16-32$; 16 corresponds to the unity gain that is the preamplifier input is equal to the output). The mean values corresponding to the peak positions have been plotted as a function of the input voltage: the results for all the four gain configurations, together with a linear fit (violet lines), are given in figure A.5. For all the studied gain configurations the linearity has been verified up to an input signal of 1 V while the flat regions for gain values of 16 and 32 correspond to a saturation of the MAROC-II ASIC;

- the **signal shape and its duration** have been studied varying the slow shaper parameters; a schematic of the slow shaper architecture is presented in figure A.6(a): there are 3 feedback capacitors, common to all the channels, that can be switched on and off independently.

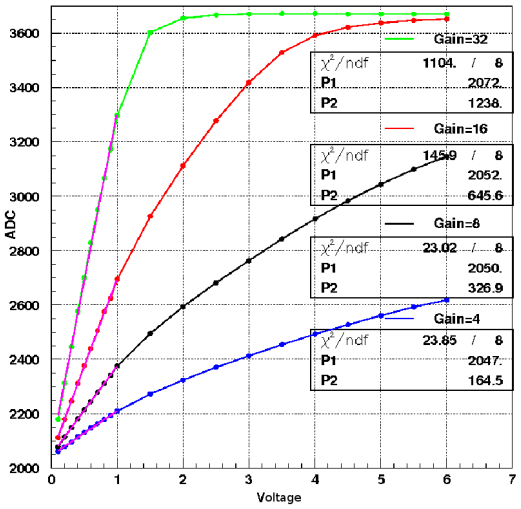


Figure A.5: Linearity of the slow shaper for 4 different gain values.

The channel response to the calibration signal (with a fixed value of the preamplifier gain of 16) has been recorded and fitted with a Gaussian function in the hold range $0-250$ ns. All the 9 possible configurations have been investigated and the result is shown in figure A.6(b). As expected, changing the three capacitors the shape of the signal has been modified. The best choice for the EMR MAPMTs readout is the one with all the three capacitors enabled that corresponds to the slower output signal (black solid line in figure A.6(b));

- a test of the **linearity** of the DAC has been performed. Figure A.7(a) shows the DAC schematics; it is divided in two parts:

  · one 16 bit thermometer DAC made of 16 switched identical current sources ($i_{ref} = 20$ $\mu$A) for coarse tuning;

  · one 8 bit switched scaled current source DAC for fine tuning. Therefore $3*(16+8)$ bits must be sent serially to load the whole DAC mask.

  The DAC linearity was checked by scanning the thermometer DAC (the coarse one) and keeping the fine tuning bits all disabled. The amplitude of the threshold output signal has been measured (with the multimeter) enabling 1 by 1 each bit of the DAC: the result is presented in figure A.7(b) where the linearity is verified up to 12 enabled current sources;

- the **behavior of the FAST shaper** has been studied. The schematics of the two fast shapers is shown in figure A.8: bipolar (left) and unipolar (right).

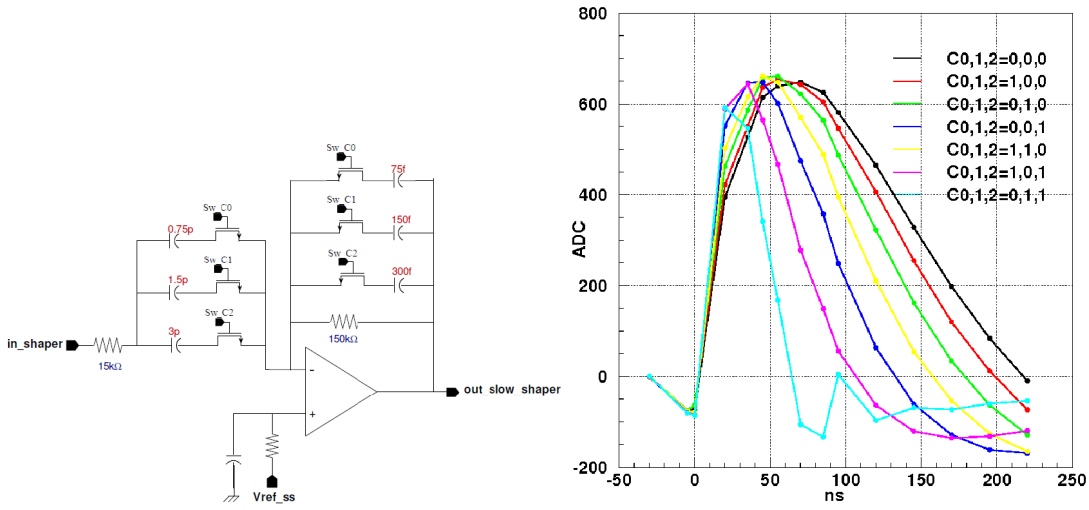


(a) (b)

Figure A.6: (a) Slow shaper architecture: the three tunable feedback capacitors are indicated as $C_0$=75 fF, $C_1$=150 fF and $C_2$=300 fF. (b) Slow shaper analog output as a function of the feedback capacitors setting.

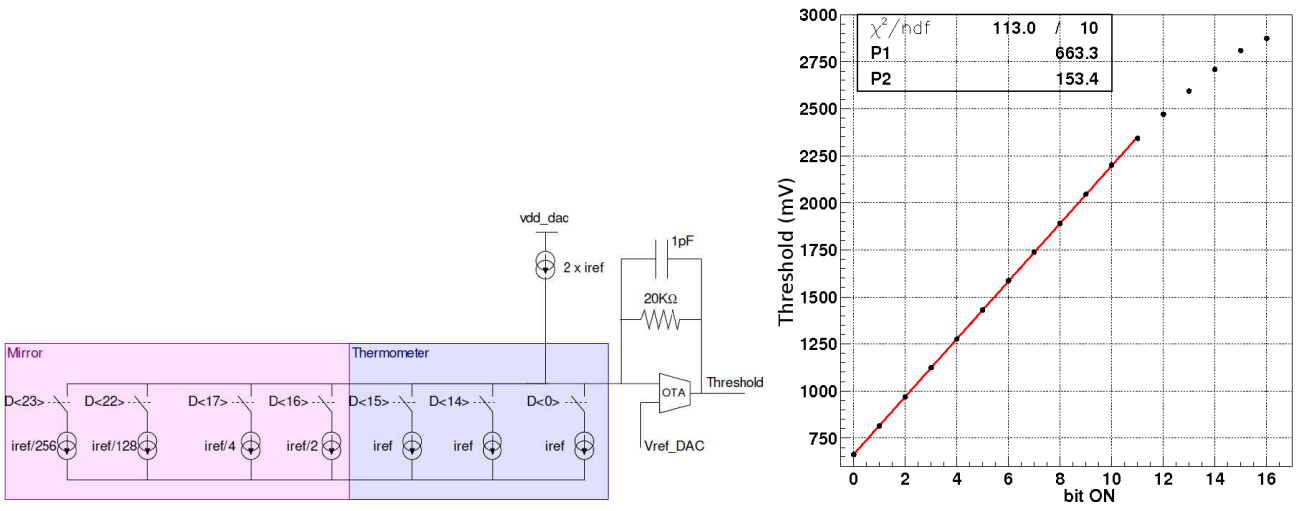


(a) (b)

Figure A.7: (a) DAC schematics. (b) Linear fit of the DAC output (only the coarse tuning has been tested): the linearity is well verified up to 12 enabled current sources.

Given the output of the unipolar shaper is faster than the one of the bipolar, only the bipolar fast shaper has been tested.

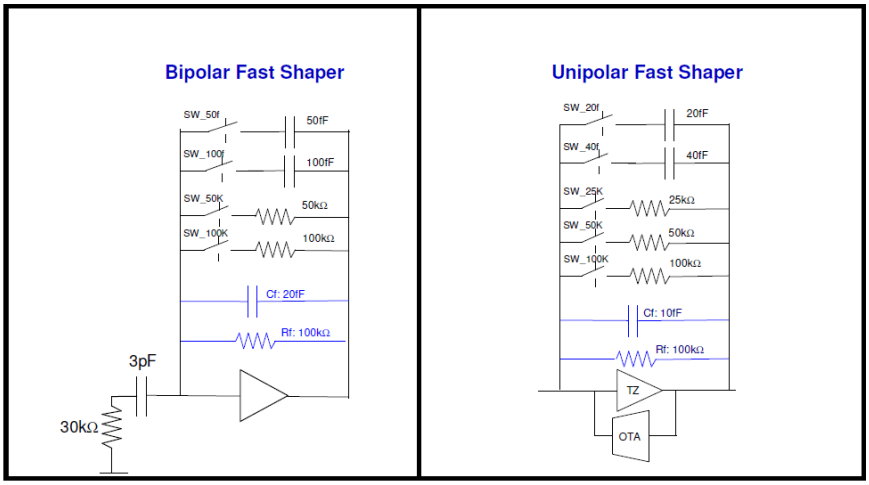


Figure A.8: Schematic view of the two fast shapers: bipolar (left) and unipolar (right).

All the 16 possible configurations changing the two resistors and the two capacitors in figure A.8 have been investigated (only 16 channels of the ASIC have been tested). A train of square pulses with a frequency of 10 kHz and variable amplitude has been sent to each channel. The number of counts, that is the number of times that the input signal overcomes the threshold, has been acquired for each channel with a VME scaler varying the threshold.
Figure A.9(a) gives a representation of an event while figure A.9(b) shows the corresponding threshold scan:

- when the threshold value is very small the system is always triggered (that means the output signal of the shaper is always higher than the one of the discriminator): the registered counts value is 0;
- increasing the threshold, the ASIC counts twice the number of pulses; this is due to the undershoot (that becomes an overshoot) of the other edge of the square pulse (this situation corresponds to the red line in figure A.9(a));
- when the threshold reaches the value indicated by the blue line in figure A.9(a), the ASIC counts the effective number of pulses;
- finally when the threshold is too high, the shaper signal never crosses the threshold and the system does not count.

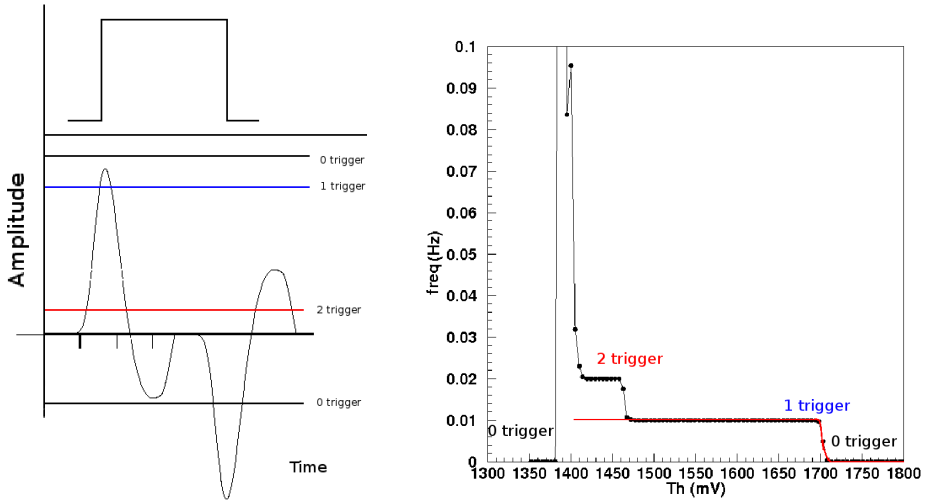


(a) (b)

Figure A.9: (a) Schematic view of the threshold scan principle. (b) Fit of the frequency (defined as the the ratio between the number of counts and the acquisition time) as a function of the threshold.

For each of the 16 channels, the number of counts registered by the channel as a function of the threshold has been fit with a step function:

$$f(x) = a * \mathrm{erf}((-(x\text{-}b)) * c) + d \tag{A.1}$$

where erf is the error function

$$\mathrm{erf(x)} = \frac{2}{\sqrt{\pi}} \int_0^{\mathrm{x}} \exp[-\mathrm{t}^2]\mathrm{dt} \tag{A.2}$$

The two parameters of interest are $b$ and $c$ in equation A.1 that represent respectively the threshold value corresponding to the mean value of the signal (inflection point in the curve) and to its spread. Fitting the parameter $b$, and taking $c$ as its error, as a function of the pulse amplitude, it is possible to test the linearity of each single channel.
The result for one of the studied configurations is given in figure A.10(a): typically each channel is linear up to a 200 mV input signal (that corresponds to $\sim$ 9 MIPs with a preamplifier gain of 16) for all the studied configurations.
The slope of the linear fit corresponds to the gain of each channel while the constant term is the channel offset (that is the 0 of the discriminator). Figure A.10(b) shows the gain spread and the offset one for the 16 channels; the data obtained fitting with a Gaussian function the gain and offset distributions for all the configurations are listed in table A.1;

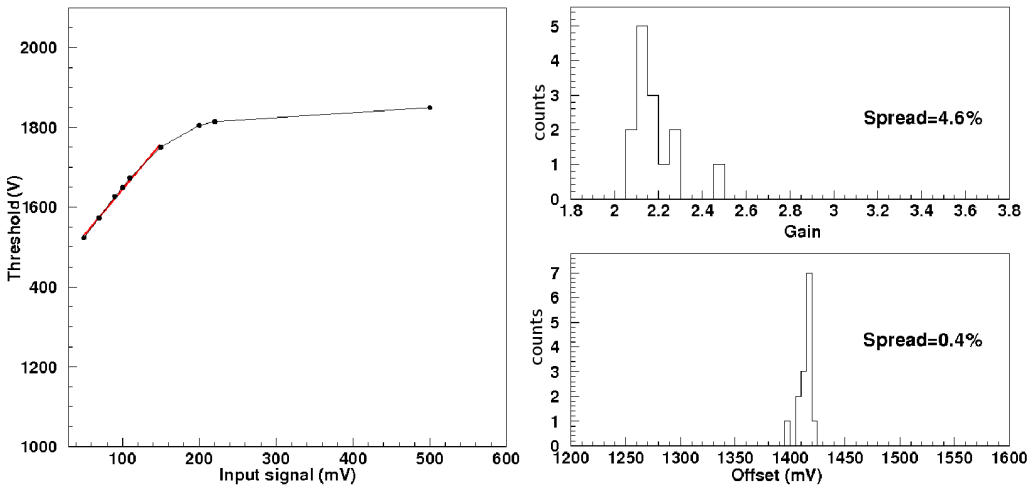


(a) (b)

Figure A.10: (a) Linearity of one channel in one of the studied configurations. (b) Gain and offset obtained repeating the linear fit in figure A.10(a) for all the channels. The spread has been evalutated as the ratio of the rms and mean of the histogram.

| R 50 kΩ | R 100 kΩ | C 50 fF | C 100 fF | gain | offset |
|---|---|---|---|---|---|
| 0 | 0 | 0 | 0 | $0.736 \pm 0.0167$ | $1810.5 \pm 1.2$ |
| 0 | 0 | 0 | 1 | $3.853 \pm 0.449$ | $1434.9 \pm 5.3$ |
| 0 | 0 | 1 | 0 | $4.596 \pm 0.334$ | $1470.4 \pm 19.1$ |
| 0 | 0 | 1 | 1 | $3.371 \pm 0.082$ | $1427.5 \pm 5.1$ |
| 0 | 1 | 0 | 0 | $3.649 \pm 0.204$ | $1465.4 \pm 7.3$ |
| 0 | 1 | 0 | 1 | $3.091 \pm 0.031$ | $1407.9 \pm 2.7$ |
| 0 | 1 | 1 | 0 | $3.516 \pm 0.061$ | $1413.9 \pm 2.3$ |
| 0 | 1 | 1 | 1 | $2.687 \pm 0.047$ | $1398.8 \pm 2.1$ |
| 1 | 0 | 0 | 0 | $2.921 \pm 0.023$ | $1415.6 \pm 1.6$ |
| 1 | 0 | 0 | 1 | $2.183 \pm 0.023$ | $1421.9 \pm 2.5$ |
| 1 | 0 | 1 | 0 | $2.321 \pm 0.044$ | $1426.8 \pm 2.2$ |
| 1 | 0 | 1 | 1 | $1.885 \pm 0.014$ | $1415.0 \pm 1.0$ |
| 1 | 1 | 0 | 0 | $2.016 \pm 0.045$ | $1427.5 \pm 6.9$ |
| 1 | 1 | 0 | 1 | $1.656 \pm 0.022$ | $1423.6 \pm 1.0$ |
| 1 | 1 | 1 | 0 | $1.821 \pm 0.027$ | $1422.0 \pm 2.1$ |
| 1 | 1 | 1 | 1 | $1.587 \pm 0.153$ | $1402.7 \pm 2.2$ |

Table A.1: Gain and offset values for all the 16 studied configurations (1 means disabled while 0 means enabled).

- one of the MAROC-II features is that the discriminated signal duration is correlated to the pulse height of the shaper output; this means a readout based on the Time Over Threshold (TOT) principle can be implemented. It is presented in figure A.11(a): the red signal stays above the threshold for a time interval T2 while the blue signal does the same for a time interval T1. If it were possible to find a relationship between the time the signal stays over the threshold and its amplitude, an “analog” info would be extracted.

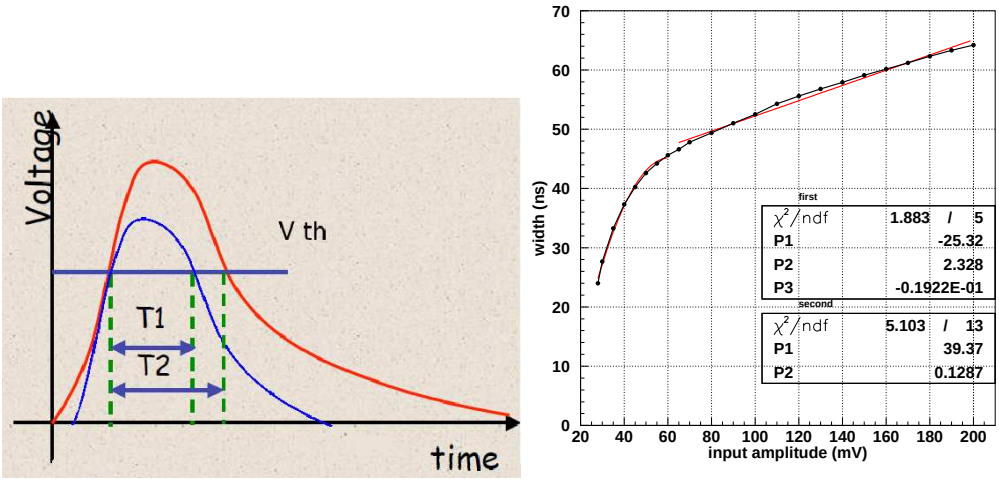


(a) (b)

Figure A.11: (a) Time Over Threshold principle. (b) Fit of the Time Over Threshold: the first part of the curve (up to 45 ns) has been fitted with a quadratic function while the second one has been fitted with a linear function.

The **TOT measurements** have thus been performed varying the input signal amplitude and keeping the threshold value fixed (at a preamplifier gain of 16); the time width has been measured with an oscilloscope. The result is shown in figure A.11(b); two fits have been performed: up to 45 ns the relationship between the time width and the signal amplitude is well described by a quadratic function, then the correspondence becomes linear.

# Appendix B

# Analysis procedure

A *stripping procedure* has been applied to all the data collected in the data taking periods presented in Chapters 4 and 5 in order to select a set of *good events*[1]. The event selection has been performed considering the Silicon Beam Chambers (SiBCs) data in order to use only the single track events, i.e. one single particle crossing all the detectors.
The data taking/analysis procedure has been divided in three different steps:

- acquisition and analysis of the so-called *pedestal run* (section B.1); the electronics baseline, its noise and common mode have been studied to evaluate a threshold for each silicon strip (bar) to identify the strips (bars) in which the particle has deposited its energy. This threshold value has also been used in the ADCs to perform the so-called *zero suppression*;

- data acquisition and selection of the good events (section B.2); for each event, particles can hit one or more silicon strips; a *cluster-finding algorithm* has been applied to identify the exact position of the particle in the detector using a center of gravity method;

- data storage (section B.3); the stripping program generates as an output an ASCII DST (Data Summary Tape) file, containing the relevant information of all the detectors: the event time, the hit position in the Silicon Beam Chambers and the pulse height of each EMR channel.

[1]The stripping procedure was the same for all the data taking periods; the examples presented in these sections are taken from the data analysis of the five triangular shape bars (see section 3.2.2 for details).

## B.1 Pedestal analysis

A particle crossing a detector deposits a charge which is then amplified, sampled and sent to the ADC for the digitization[2].
When no signal is present, the baseline level digitized by the ADCs (due to the complete detector+electronics chain) is called *pedestal*.
A pedestal run is obtained acquiring data with a random trigger in order to evaluate the electronics baseline and the *noise* of each channel: 200 triggers are randomly generated and the mean value of each channel of the ASICs represents the pedestal while the rms corresponds to the noise.
Figure B.1 presents an example of the pedestal distribution of one silicon detector and of the MAPMT connected to the five triangular bars; the three different regions in figure B.1(a) correspond to the three readout ASICs (see [103] for details). Figure B.2 presents the global noise rms (black lines) and the noise rms after the common mode subtraction (red lines).

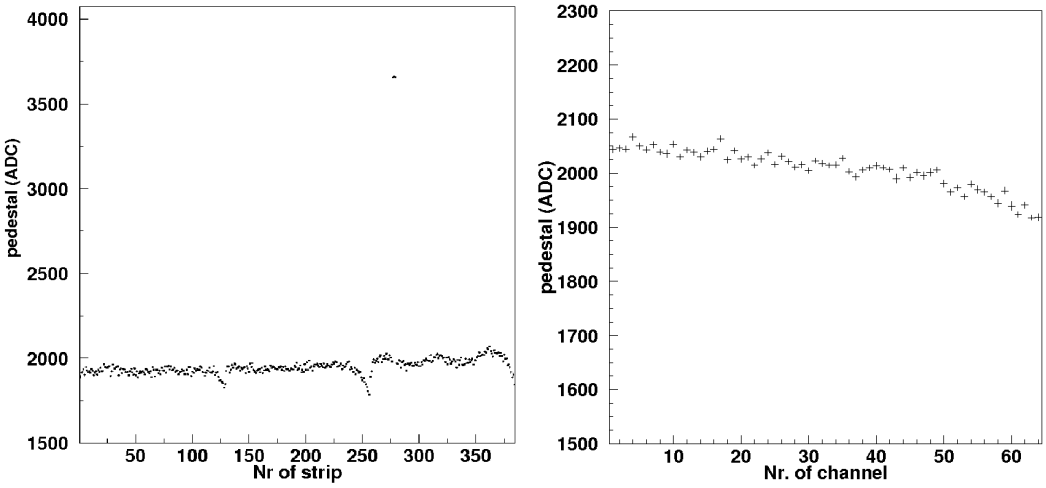


(a) (b)

Figure B.1: (a) The pedestal distribution (expressed in ADC counts) of one tile of one silicon detector: the three different regions correspond to the three readout ASICs. (b) The pedestal distribution of the MAPMT connected to the five triangular bars.

The *common mode noise* is defined as the noise contribution due to the external noise on the detector bias line (for example the electromagnetic noise). In other

[2]In the case of the silicon detectors this procedure is performed by the ADC board while for EMR a dedicated frontend board, the FEB, is used (see Chapter 3 for details).

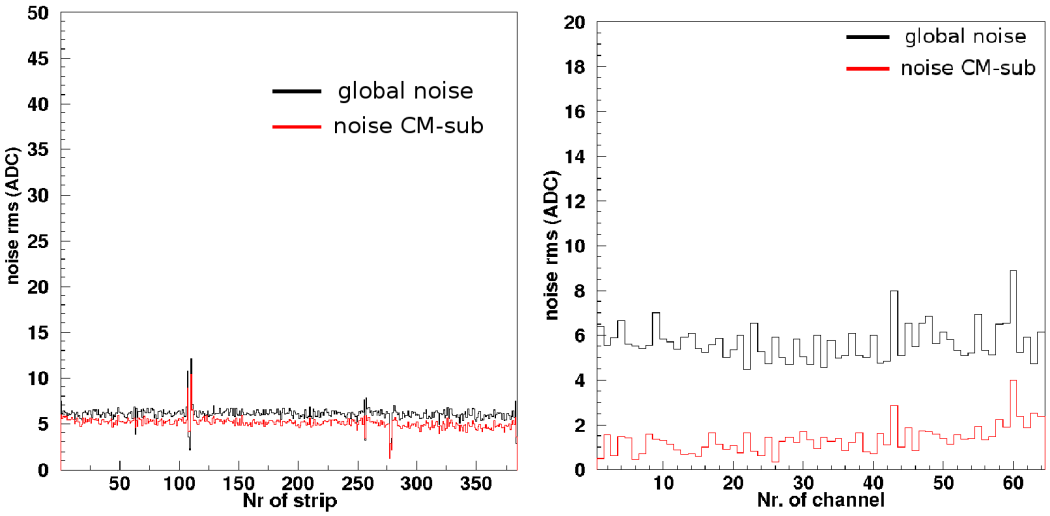


(a) (b)

Figure B.2: (a) The noise rms distribution of one Silicon Beam Chamber and (b) of the MAPMT connected to the five triangular bars. The black lines represent the global noise rms while the red ones the noise rms after the common mode subtraction.

words, the common mode noise corresponds to a common variation of the baseline of all the channels on an event by event basis. The following procedure has been performed in order to compute the pedestal and the intrinsic noise rms (that is without the common mode contribution):

- calculation of the pedestal and noise rms values of each strip;
- calculation of the common mode:

$$
\begin{aligned}
&CM_j = \frac{\Sigma_i^N (raw_i - pede_i)}{N} \\
&j \rightarrow \text{ number of ASIC} \quad \text{i} \rightarrow \text{ number of channel} \\
&j = 1,2,3 \quad \text{and} \quad \text{i} = 1,..,128 \quad (\text{SiBCs}) \\
&j = 1 \quad \text{and} \quad \text{i} = 1,..,64 \quad (\text{bars})
\end{aligned}
\tag{B.1}
$$

  event by event, the pedestal value of each channel ($pede_i$) has been subtracted from the raw data ($raw_i$) and the mean value ($CM_j$) has been computed ASIC by ASIC excluding the dead or noisy channels ($N$ indicates the number of *good* channels); the rms value associated to this number (i.e. the rms of $CM_j$) represents the common mode noise of a single ASIC;

- subtraction of the mean value of the common mode on an event by event basis from the raw data;

- re-calculation of the pedestal and noise rms distributions.

Figure B.3(a) shows an example of the common mode distribution of one silicon chamber ASIC: the mean value is $\sim 0$ while the rms is $\sim 3.3$ ADC. Figure B.3(b) shows the correlation of the common mode distribution of two different ASICs connected to the same silicon detector: the correlation demonstrates that the common mode noise is a detector feature.

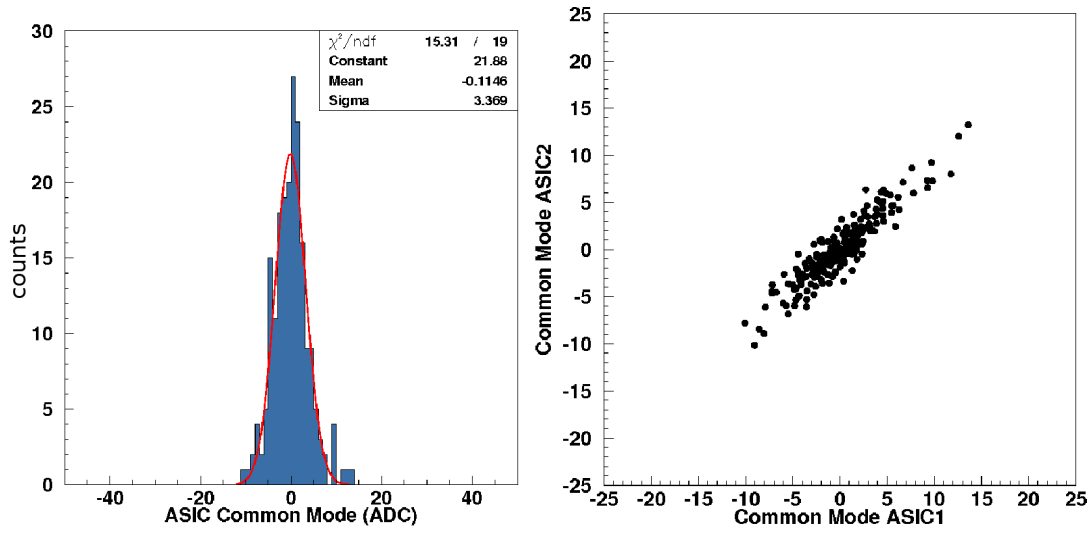


(a) (b)

Figure B.3: (a) The common mode noise distribution of one SiBC ASIC. (b) The common mode correlation of two readout ASICs of the same silicon chamber side.

The value of the common mode for the SiBCs (figure B.2(a)) is clearly negligible with respect to the intrinsic noise. This means the ADCs can work in a *zero suppression* mode. In fact if the common mode noise is high the threshold should be increased reducing the detector efficiency. On the other hand, high noise and standard threshold means a larger number of strips to read per module (since they are over threshold) and thus a smaller DAQ rate.
The threshold was set to 5 times the overall noise rms (that means to $\sim 25-30$ ADC referring to figure B.2(a)).

## B.2 Single track events selection

To identify the number of the strip, and thus the position, in which the particles release their energy, the *pull* distribution has been considered. It is defined as the ratio between the pulse height (that means the signal) of the channel with the

maximum signal in the event and its corresponding noise rms event by event: in practice the signal is expressed in terms of its noise rms.
The pull distribution of one silicon detector is shown in figure B.4(a): the shape of the distribution is due to the fact that the detector has one floating strip (see section 4.2.2 for details). When the particle crosses the center of the floating strip, each of the two neighbouring readout strips collects 38% of the total charge and the pulse height is lower [103]. This case corresponds to the first peak, named *A* in figure B.4(a), while the higher one, named *B*, is the one due to the particle crossing a readout strip (see [103] for details). The lower peak near 0 (*C* in figure B.4(a)) corresponds to the noise events that means the events without signal.

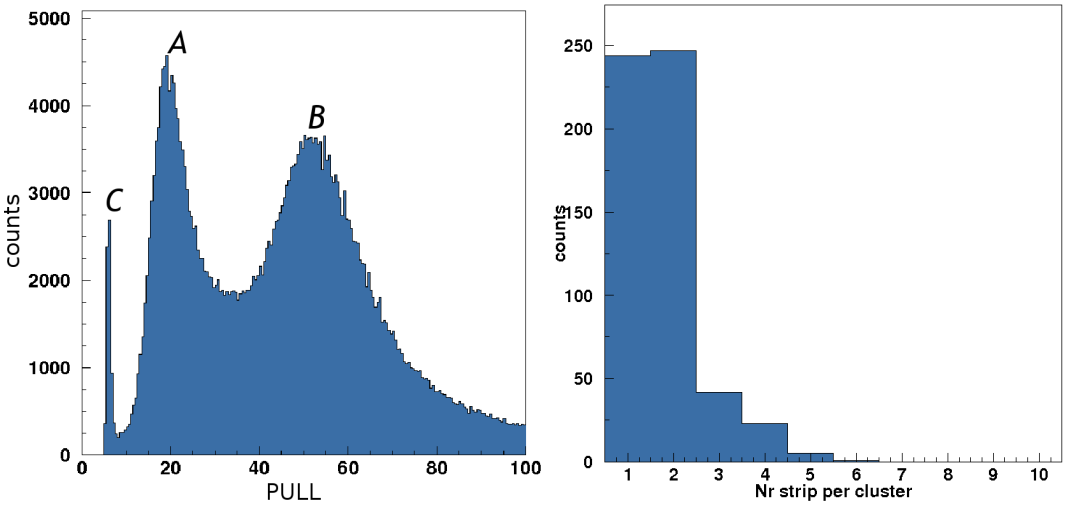


(a) (b)

Figure B.4: (a) The pull distribution of one silicon detector: the high peak near 0 corresponds to the noise events while the other two peaks represent the fact that a floating strip method is exploited to readout the silicon detector [103]. (b) The distribution of the number of strips per cluster.

Considering the pull distribution it is possible to fix a threshold in terms of noise rms in order to identify the strip with the maximum signal. Channel by channel, the pedestal has been subtracted from the raw data of each strip and the obtained value compared with the threshold (typically the chosen threshold was $10\sigma$). The strip with the maximum is the one whose signal overcomes both the threshold and the signal of all the other channels.
Given the capacitive coupling and the fact that the tracks incidence angle is not $90^\circ$ with respect to the strip, the charge is readout by several neighbouring strips: this group of contiguous strips is called *cluster*. Thus a *cluster-finding algorithm* has been applied to identify the exact position of the particle in the detector using

a center of gravity method. The identification of the cluster has been performed considering the strips that surround the one with the maximum and choosing a lower threshold for the signals of these strips (typically the chosen threshold was $5\sigma$). The position of the particle is defined as:

$$\text{xpos} = \frac{\Sigma_i \ (\text{STRIP}_i * \text{PH}_i)}{\Sigma_i \ \text{PH}_i} \tag{B.2}$$

where the *i* index runs over the number of strips composing the cluster and PH is the pulse height. The distribution of the number of strips per cluster is shown in figure B.4(b): as expected each cluster is composed of $1-2$ strips.
The single track events have thus been defined as the ones in which only one cluster is present in every silicon detector tile.

## B.3 DST file

The set of good events obtained using the stripping method described in the previous sections has been organized in a DST file for each run; it contains:

- a first row with the noise rms of all the channels connected to the fibers (80 for the EMR small prototype + 4 for the rectangular shape bar tests, 10 for the triangular bar data taking and 128 for the EMR module commissioning at UNIGE);
- a row for each event with: the event number, the absolute time in seconds, the position measured by the silicon chambers (x1, y1, x2, y2), the pulse height of each MAPMT channel.

## B.4 Silicon detector alignment

Given the silicon detectors have not been installed with absolute precision (both in the beamtest setups and in the commissioning phase ones), an offline detector alignment procedure is needed for a correct analysis.
The procedure was based on the translation of the coordinate system of one of the two SiBCs (figure B.5(a)), that is:

- the distribution of the difference of the particle position reconstructed by the first SiBC and the one measured by the second SiBC has been computed for each direction:

$$\begin{aligned} x_2 - x_1 &= a \\ y_2 - y_1 &= b \end{aligned} \tag{B.3}$$

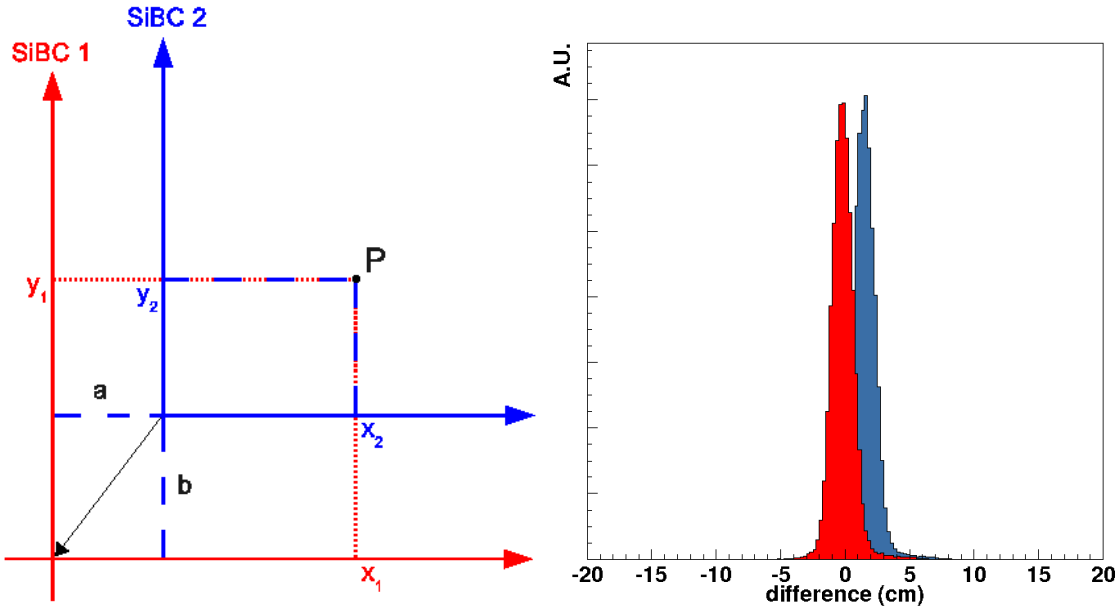


(a) (b)

Figure B.5: The Silicon Beam Chambers alignment procedure: (a) a translation of the coordinate system of the second SiBC has been performed; (b) the distributions of the difference of the particle position reconstructed by each SiBC: the one calculated after the alignment is shown in red.

- if the detectors are perfectly aligned, the distribution is centered on 0 (red histogram in figure B.5(b));
- if the detectors are misaligned (blue histogram in figure B.5(b)) the values computed with equation B.3 are used to translate the axes of the second SiBC to obtain the red histogram.

# List of acronyms

| | |
|---|---|
| **0ββ** | Neutrinoless Double Beta decay |
| **ADC** | Analog to Digital Converter, also stands for Analog to Digital Converter unit |
| **AFC** | Absorber and Focusing Coil |
| **AFE IIt** | Analogue Front End with Timing board |
| **AGILE** | Astro-rivelatore Gamma a Immagini LEggero |
| **AMS** | Austria Mikro Systeme International AG (Austria) |
| **ASACUSA** | Atomic Spectroscopy And Collisions Using Slow Antiproton |
| **ASCII** | American Standard Code for Information Interchange |
| **ASIC** | Application Specific Integrated Circuit |
| **ATLAS** | A Toroidal LHC ApparatuS |
| **BB** | Buffer Board |
| **βB** | Beta Beam |
| **CC** | Charged Current |
| **CERN** | Conseil Europeen pour la Recherche Nucleaire - European Organization for Nuclear Research |
| **CFT** | Central Fiber Tracker |
| **CKM** | Cabibbo - Kobayashi - Maskawa |
| **CKOV** | CherenKOV detector |
| **CνB** | Cosmic ν (neutrino) Background |
| **CMOS** | Complementary Metal Oxide Semiconductor |
| **CP** | Charge - Parity |
| **CPT** | Charge - Parity - Time |
| **D∅** | Particle experiment at Fermilab |
| **DAC** | Digital to Analog Converter |
| **DAΦNE** | Double Annular Φ factory for Nice Experiments |
| **DAQ** | Data AcQuisition |

**DIS** Deep Inelastic Scattering
**DONuT** Direct Observation of the Nu Tau
**DPNC** Departement de Physique Nucleaire et Corpusculaire
**DST** Data Summary Tape

**EMcal** Electron Muon calorimeter
**EMR** Electron Muon Ranger
**EOB** EMR Outer Box
**ERNI** ERNI Electronics Inc. (USA)
**ES** Elastic Scattering

**FADC** Flash Analog to Digital Converter
**FAST** Fiber Antiproton Scintillating Tracker
**FEB** FrontEnd Board
**FNAL** Fermi National Accelerator Laboratory
**FODO** FOcus DefOcus solenoid lattice
**FOFO** FOcus FOcus solenoid lattice
**FORTRAN** FORmula TRANslation
**FPGA** Field Programmable Gate Array

**G4MICE** GEANT 4 for MICE
**GALLEX** GALLium EXperiment at Gran Sasso
**GNO** Gallium Neutrino Observatory
**GUT** Grand Unified Theory

**HARP** HAdRoProduction experiment
**HCC** Helical Cooling Channel
**HOMESTAKE** Solar neutrino experiment in the HOMESTAKE Gold Mine in South Dakota

**IDS** International Design Study
**INFN** Istituto Nazionale di Fisica Nucleare
**INFN TS** INFN Sezione di Trieste

**JPARC** Japan Proton Accelerator Research Complex
**JPARC-HK** JPARC to HyperKamiokande
**JPARC-SK** JPARC to SuperKamiokande

**KAMIOKANDE** KAMIOKA Nucleon Decay Experiments
**KAMLAND** KAMioka Liquid scintillator AntiNeutrino Detector
**KL** KLOE-Light

**KLOE** K LOng Experiment

**LAL** Laboratoire de L'Acelerateur Lineaire
**LAr TPC** Liquid Argon Time Projection Chamber
**LBL** Long BaseLine
**LNF** Laboratori Nazionali di Frascati

**MANX** Muon collider And Neutrino factory eXperiment
**MAPMT** MultiAnode PhotoMultiplier Tube
**MAROC** Multi-Anode ReadOut Chip
**MERIT** MERcury Intense Target
**MICE** Muon Ionization Cooling Experiment
**MINERνA** Main INjector ExpeRiment for ν-A
**MIND** Magnetized Iron Neutrino Detector
**MINOS** Main Injector Neutrino Oscillation Search
**MIP** Minimun Ionizing Particle
**MSW** Mikheyev - Smirnov - Wolfenstein
**MUSASHI** Monoenergetic Ultra-Slow Antiproton Source for High precision Investigation
**MUSTAP** MUSashi vaTAP

**NC** Neutral Current
**NF-MCC** Neutrino Factory and Muon Collider Collaboration
**NOνA** NuMI Off-axis $\nu_e$ Appearance experiment
**NuMI** Neutrinos at the Main Injector
**NuFact** Neutrino Factory
**NuTeV** Neutrinos at the TeVatron

**OAB** Off-Axis Beam
**OPERA** Oscillation Project with Emulsion tRacking Apparatus

**PAW** Physics Analysis Workstation
**PC** Personal Computer
**PCB** Printed Circuit Board
**PH** Pulse Height
**PID** Particle IDentification
**PMT** PhotoMultiplier Tube
**PS** Proton Synchrotron
**PSI** Paul Scherrer Institute
**PVC** PolyVinyl Chloride

**QCD** Quantum Chromo Dynamics
**QDC** Charge to Digital Converter

**R&D** Research & Development
**RAL** Rutherford Appleton Laboratory
**RF** Radio Frequency
**RFCC** Radio Frequency cavity and Coupling Coil station
**RFOFO** Reverse FOcus FOcus solenoid lattice
**RLA** Recirculating Linear Accelerator

**SAGE** Soviet-American Gallium Experiment
**SB** Super Beam
**SBL** Short BaseLine
**SiBC** Silicon Beam Chamber
**SiPM** Silicon PhotoMultiplier
**SM** Standard Model
**SK** Super KAMIOKANDE
**SNP** Solar Neutrino Puzzle
**SNO** Sudbury Neutrino Observatory
**SSM** See Saw Mechanism
**SW** SandWich

**TASD** Totally Active Scintillator Detector
**Tcl/Tk** Tool Command Language/Toolkit
**TDC** Time to Digital Converter
**TOF** Time Of Flight
**TOT** Time Over Threshold
**TPC** Time Projection Chamber

**UNIGE** University of Geneva

**VLPC** Visible Light Photon Counter
**VLSI** Very Large Scale Integration
**VME** Versa Module Eurocard

**WFD** Wave Form Digitizer
**WLS** Wave Length Shifter

# List of Figures

# List of Tables

# Bibliography


[1] H. R. Crane. *The Energy and Momentum Relations in the Beta-Decay, and the Search of the Neutrino*. Rev. of Mod. Phys. 20, 1: 278–295, 1948.

[2] C. P. Enz. *50 years ago Pauli invented the neutrino*. Helvetica Physica Acta 54: 411–418, 1981.

[3] W. Pauli. *Letter to a physicist's gathering at Tubingen, December 4, 1930*. Reprinted in Wolfgang Pauli, Collected Scientific Papers vol. 2, ed. R. Kronig and V. Weisskopf: 1313, 1964.

[4] F. Reines and C. L. Cowan. *Detection of the Free Neutrino*. Phys. Rev. 92: 830–831, 1953.

[5] F. Reines *et al. Detection of the Free Antineutrino*. Phys. Rev. 117: 59–173, 1960.

[6] J. N. Bahcall *et al. Present Status of the Theoretical Predictions for the* $^{36}$*Cl Solar-Neutrino Experiment.* Phys. Rev. Lett. 20: 1209–1212, 1968.

[7] R. M. Bionta *et al. Observation of a neutrino burst in coincidence with Supernova 1987A in the Large Magellanic Cloud*. Phys. Rev. Lett. 58: 1494–1496, 1987.

[8] Y. Fukuda *et al. Evidence for Oscillation of Atmospheric Neutrinos*. Phys. Rev. Lett. 81: 1562–1567, 1998.

[9] The SNO Collaboration. *Measurements of the rate of* $\nu_e + d \rightarrow p + p + e^-$ *interactions produced by* $^8$*B solar neutrinos at the Sudbury Neutrino Observatory*. Phys. Rev. Lett. 87: 071301, 2001.

[10] K. Eguchi *et al. First results from KAMLAND: evidence for reactor antineutrino disappearance*. Phys. Rev. Lett. 90, 2: 021802, 2003.

[11] H. Pessardl *et al. Observation of a first* $\nu_\tau$ *candidate in the OPERA experiment in the CNGS beam.* Phys. Lett. B 691: 138–145, 2010.

[12] M. C. Gonzalez-Garcia and M. Maltoni. *Phenomenology with Massive Neutrinos.* Phys. Rept. 460: 1–129, 2007.

[13] D. G. Koshkarev. *Proposal for a decay ring to produce intense secondary particle beams at the SPS.* CERN ISR-DI-74-62, 1974.

[14] D. Neuffer. *Principles and Application of Muon Cooling.* Particle Accelerators 14, 1983.

[15] R. B. Palmer *et al. Muon Collider Design.* SLAC-PUB-9921: acc–phys/9604001, 1995.

[16] N. Holtkamp. *A feasibility study of a neutrino source based on a muon storage ring.* SLAC-REPRINT-2000-054, 2000.

[17] C. Albright *et al. Physics at a Neutrino Factory.* Fermilab-FN-692, 2000.

[18] V. M. Lobashev *et al. Direct Search for the Mass of Neutrino and Anomaly in the Tritium Beta-Spectrum: Status of 'Troitsk Neutrino Mass' Experiment.* Nucl. Instr. and Meth. in Phys. Res. B (Proc. Suppl.) 91:280–286, 2001.

[19] R. Davis. *Nobel Lecture: A half-century with solar neutrinos.* Review of Modern Physics 75: 985–994, 2003.

[20] B. Eberle. *Big Bang Relic Neutrinos and Their Detection.* PhD Thesis, University of Hamburg, 2005. http://www-library.desy.de/preparch/desy/thesis/desy-thesis-05-024.pdf.

[21] M. C. Gonzalez-Garcia and Y. Nir. *Neutrino masses and mixing: evidence and implications.* Review of Modern Physics 75: 345–402, 2003.

[22] T. Araki *et al. Experimental investigation of geologically produced antineutrinos with KAMLAND.* Nature 436: 499–503, 2005.

[23] C. Bemporad *et al. Reactor-based neutrino oscillation experiments.* Review of Modern Physics 74: 297–328, 2002.

[24] A. R. Sandström. *Background and Instrumentations in MICE.* PhD Thesis, University of Geneva, 2007.

[25] J. Chadwick. *Possible Existence of a Neutron.* Nature 129: 312, 1932.

[26] E. Fermi. *Tentativo di una teoria dei raggi* $\beta$. Il Nuovo Cimento 11: 1–19, 1934.

[27] M. Goldhaber *et al. Helicity of neutrino*. Phys. Rev. 109: 1015–1017, 1958.

[28] G. Danby *et al. Observation of high-energy neutrino reactions and the existence of two kinds of neutrinos*. Phys. Rev. Lett. 9: 36–44, 1962.

[29] K. Kodama *et al. Observation of tau-neutrino interactions*. Phys. Lett. B 504: 218–224, 2001.

[30] B. Pontecorvo. J.Exptl. Theoret. Phys. 33: 549, 1957.

[31] S. M. Bilenky. *Early years of neutrino oscillations*. arXiv:hep-ph/9908335v2, 1999.

[32] Z. Maki *et al. Remarks on the Unified Model of Elementary Particles*. Prog. Theor. Phys. 28: 870–880, 1962.

[33] PDG Collaboration. *Particle Data Group*. 2008. URL http://pdg.lbl.gov.

[34] B. T. Cleveland *et al. Measurement of the solar electron neutrino flux with the Homestake chlorine detector*. Astrophys. Journal 496: 505–526, 1998.

[35] SAGE Collaboration. *Measurement of the solar neutrino capture rate with gallium metal*. Phys. Rev. C 60: 055801, 1999.

[36] W. Hampel *et al. GALLEX solar neutrino observations: results for GALLEX IV*. Phys. Lett. B 447: 127–133, 1999.

[37] K. Anderson *et al. White Paper Report on Using Nuclear Reactors to Search for a value of* $\theta_{13}$. arXiv:hep-ex/0402041v1, 2004.

[38] M. Maltoni and T. Schwetz. *Three-flavour neutrino oscillation update and comments on possible hints for a non-zero* $\theta_{13}$. Proceedings of Science: 113011, 2008.

[39] T. D. Lee and C. N. Yang. *Parity Non conservation and a Two-Component Theory of the Neutrino*. Phys. Rev. 105: 1671–1675, 1957.

[40] M. Giunti and T. Kim. *Fundamental of neutrino physics and astrphysics*. Oxford University Press, 2007. ISBN:978-0-198-50871-7.

[41] R. N. Mohapatra and G. Senjanovic. *Neutrino masses and mixings in gauge models with spontaneous parity violation*. Phys. Rev. Lett. D 23: 165–180, 1981.

[42] C. H. Albright. *Overview of grand unified models and their predictions for neutrino oscillations*. Nucl. Instr. and Meth. in Phys. Res. A 472: 359–363, 2001.

[43] A. Faessler and F. Simkovic. *Double beta decay*. Journal of Physics G 24: 2139–2178, 1998.

[44] B. Kayser. *Neutrino Physics*. FERMILAB-PUB-05-236-T, 2005.

[45] W. M. Yao. *Review of Particle Physics*. Journal of Physics G 33: 1, 2006.

[46] MICE Collaboration. *An International Muon Ionization Cooling Experiment (MICE)*. Proposal to the Rutherford Appleton Laboratory, 2003.

[47] H. J. Lipkin. *What is coherent in neutrino oscillations*. Phys. Lett. B 579: 355–360, 2004.

[48] The NO$\nu$A Collaboration. *NuMI Off-Axis* $\nu_e$ *Appearance Experiment Proposal*. 2005. Fermilab-Proposal-0929.

[49] R. Saakyan. *Status and Prospects of the MINOS Experiment*. Physics of Atomic Nuclei 67: 1084–1091, 2004.

[50] A. Blondel *et al.* *Future neutrino oscillation facilities*. Acta Physica Polonica B 37, 2006.

[51] R. G. H. Robertson. *Direct Determination of Neutrino Mass*. Journal of Physics: Conference Series 173, 2009.

[52] E. Roulet. *Mikheyev-Smirnov-Wolfenstein effect with flavor-changing neutrino interactions*. Phys. Rev. D 44: 935–938, 1991.

[53] IDS-NF Collaboration. *International Design Study for the Neutrino Factory - First progress report*. IDS-NF-017, 2010.

[54] A. Blondel *et al. ECFA/CERN studies of a European neutrino factory complex*. CERN-2004-002, 2004.

[55] Muon Collider Collaboration. *Status of muon collider research and development and future plans*. Phys. Rev. ST Accel. Beams 2: 081001, 1999.

[56] The $\mu^+$ $\mu^-$ Collaboration. *Muon Muon Collider: a feasibility study*. BNL 52503, 1997.

[57] C. R. Prior. *The Neutrino Factory and Related Accelerator R&D*. Journal of Physics: Conference Series 110, 2008.

[58] MERIT Collaboration. *Studies of a Target System for a 4 MW, 24 GeV Proton Beam*. CERN-INTC-2004-016 INTC-P-186, 2004.

[59] S. Ozaki *et al. Feasibility Study II of a muon-based Neutrino source*. 2001. BNL-52623.

[60] R. Raja *et al. The Program in Muon and Neutrino Physics: Super Beams, Cold Muon Beams, Neutrino Factory and the Muon Collider*. FNAL-CONF-01/226-E, 2001.

[61] M. Lindner. *The Physics Potential of Future Long Baseline Neutrino Oscillation Experiments*. Springer Tracts Mod. Phys. 190: 209–242, 2003.

[62] P. Huber *et al. Synergies between the first-generation JHF-SK and NuMI superbeam experiments*. Nucl. Phys. B 654: 3–29, 2003.

[63] Y. Itow *et al. The JHF-Kamioka neutrino project*. KEK report 2001-4: ICRR–report–477–2001–7, 2001.

[64] J. Hylen *et al. Conceptual Design for the Technical Components of the Neutrino Beam for the Main Injector (NuMI)*. Fermilab-TM-2018, 1997.

[65] V. Antonelli *et al. Tests of the Standard Model with Low-Energy Neutrino Beams*. Nucl. Phys. B (Proc. Suppl.) 168: 192–194, 2007.

[66] A. N. Skrinskii and V. V. Parkhomchuk. *Method of cooling beams of charged particles*. Sov. J. Part. Nucl. 12(3): 223–247, 1981.

[67] W. R. Leo. *Techniques for Nuclear and Particle Physics Experiments*. Springer-Verlag, 1994. ISBN: 978-3-540-57280-0.

[68] R. P. Johnson. *Ionization Cooling and Muon Colliders*. Proceedings of EPAC08, Genova, Italy, 2008.

[69] E. Courant and H. Snyder. *Theory of the Alternating-Gradient Synchrotron*. Annals of Physics 281, 1: 360–408, 2000.

[70] T. Hart. *MICE: the international Muon Ionization Cooling Experiment. Phase space cooling measurements*. Proceedings of EPAC08, Genova, Italy, 2008.

[71] A. Blondel. *An International Muon Ionization Cooling Experiment: goals and preliminary design*. MICE Note 4, 2001.

[72] D. M. Kaplan. *MANX: A 6D Ionization Cooling Experiment*. AIP Conf. Proc. 981: 296–298, 2008.

[73] J. S. Berg *et al.* *RFOFO Ring Cooler*. http://www.hep.ph.ic.ac.uk/NuFact02/Scientific-programme/files/Wednesday/proceedings/Palmer/palmer.pdf.

[74] D. M. Kaplan. *Progress in Muon Cooling Research and Development.* Proc. 4th Workshop on Neutrino Factories based on Muon Storage Rings (NuFact02), 2002.

[75] D. E. Baynham *et al.* *A Liquid Cryogen Absorber for MICE*. MICE Note 128, 2005.

[76] K. A. Walaron. *Neutrino Factory Targets and the MICE Beam.* PhD Thesis, University of Glasgow, 2007. http://ppewww.physics.gla.ac.uk/theses/thesis_walaron_k_a-2007.pdf.

[77] A. Alekou. *MICE Status.* MICE Note 297, 2010.

[78] M. Apollonio *et al.* *The MICE diffuser system.* Proceedings of EPAC08, Genova, Italy, 2008.

[79] D. Li *et al.* *A 201-MHz normal conductig RF cavity for the International MICE Experiment.* Proceedings of EPAC08, Genova, Italy, 2008.

[80] M. Bonesini *et al.* *The design and commissioning of the MICE upstream Time-Of-Flight system*. Nucl. Instr. and Meth. in Phys. Res. A 615: 14–26, 2010.

[81] Y. Karadzhov *et al.* *TOF Detectors Time Calibration*. MICE Note 251, 2009.

[82] D. Orestano. *The detector system of the MICE experiment*. Nucl. Instr. and Meth. in Phys. Res. A 617: 45–47, 2010.

[83] L. Cremaldi *et al.* *A Cherenkov Radiation Detector with High Density Aerogels.* IEEE Transactions on Nuclear Science 56: 1475–1478, 2009.

[84] G. Grègoire. *Geometry and construction of mirrors for CKOV1*. MICE Note 148, 2006.

[85] M. G. Catanesi *et al.* *The HARP detector at the CERN PS.* Nucl. Instr. and Meth. in Phys. Res. A 571: 527–561, 2007.

[86] M. Bonesini and M. Rayner. *The MICE PID Detector System.* MICE Note 304, 2010.

[87] M. Ellis *et al. The design, construction and performance of the MICE scintillating fibre trackers*. MICE Note 254, 2010.

[88] A. Bross *et al. Characterization and Performance of Visible Light Photon Counters (VLPCS) for the Upgraded DØ Detector at the FERMILAB Tevatron*. Nucl. Instr. and Meth. in Phys. Res. A 47: 172–178, 2002.

[89] J. Lee-Franzini *et al. The KLOE electromagnetic calorimeter*. Nucl. Instr. and Meth. in Phys. Res. A 360: 201–205, 1995.

[90] D. Lietti *et al. The prototype of the MICE Electron Muon Ranger: design, construction and test*. Nucl. Instr. and Meth. in Phys. Res. A 604: 314–318, 2009.

[91] A. Pla-Dalmau *et al. Low-cost extruded plastic scintillator*. Nucl. Instr. and Meth. in Phys. Res. A 466: 482–491, 2001.

[92] V. Mascagna. *A scintillating bar tracking detector for the ASACUSA - "trap group" experiment at the CERN AD*. Proceedings of the 11th ICATPP Conference on Astroparticle, Particle, Space Physics, Detectors and Medical Physics Applications Como, Italy, 2009.

[93] ATLAS Collaboration. *Forward Detectors for Measurements of Elastic Scattering and Luminosity Determination*. Technical Design Report CERN/LHC/2007, 2007.

[94] A. Pla-Dalmau *et al. Extruded plastic scintillator for MINERνA*. FERMILAB-CONF-05-506-E, 2005.

[95] B. A. Wolthuis. *Development of Scintillation Counters for the MINERνA Neutrino Detector*. Bachelor Thesis, The College of William and Mary in Virginia, 2007. http://web.wm.edu/physics /SeniorThesis2007/Wolthuis.pdf.

[96] V. Mascagna. *Design and performance of FAST, a tracker for antiproton physics*. Master Thesis, Università dell'Insubria, 2007. http://cdsweb.cern.ch/record/1063076/files/thesis-2007-070.pdf.

[97] A. Mozzanica. *FAST: a scintillating tracker for antiproton cross section measurements*. PhD Thesis, Università degli Studi di Milano, 2007. http://cdsweb.cern.ch/record/1077510/files/thesis-2007-083.pdf.

[98] V. Mascagna *et al. Operation and performance of the FAST detector at the AD machine*. Nucl. Phys. B Proc. Suppl. 572: 299–301, 2007.

[99] L. Stoppani. *Il tracciatore a barre scintillanti dell'esperimento ASACUSA (CUSP-TRAP).* Bachelor Thesis, Università dell'Insubria, 2009. http://insulab.dfm.uninsubria.it/images/download_files/thesis_stoppani_triennale.pdf.

[100] D. Lietti *et al. Performance of the readout electronics chain of the MICE Electron Muon Ranger*. Proceedings of the 11th ICATPP Conference on Astroparticle, Particle, Space Physics, Detectors and Medical Physics Applications Como, Italy, 2009.

[101] L. Durieu *et al. The CERN PS East area in the LHC era.* CERN CH-1211 Geneva 23, 1997.

[102] A. Berra. *MICRO: un mini osservatorio per raggi cosmici*. Bachelor Thesis, Università dell'Insubria, 2005. http://insulab.dfm.uninsubria.it/images/download_files/tesi_triennale_berra.pdf.

[103] M. Prest *et al. The AGILE silicon tracker: an innovative γ-ray instrument for space*. Nucl. Instr. and Meth. in Phys. Res. A, 501: 280–287, 2003.

# Acknowledgement

I would like to acknowledge the institutions and the people whose work led to the described research. First of all the MICE Collaboration and in particular its sposksman Prof. Alain Blondel for the opportunities he gave me. Really thanks to the University of Insubria and the INFN Sections of Milano Bicocca and Trieste and in particular to Prof. Gianrossano Giannini. I would also like to thank the PS staff at CERN, in particular Emmanuelle Perez and Lau Gatignon, for the support during the data taking and Alan Bross and Anna Pla-dalmau (from FNAL) that have provided the long bars.
Many thanks to the Insulab group: Valerio, Said, Alessandro, Federica, Sara, Greta, Laura and Elena. A special thank to Andrea and Alberto whose support and friendship have been so important during the writing of this thesis. Also thanks to the Astrophysical group, expecially to Max!
Thanks to my Co-Tutors, Davide and Erik, for the support and the help. Really thanks to my Tutor, Michela: thanks for the opportunities in these two years, thanks for the help in the analysis, thanks for all the corrections and suggestions for the thesis...in other words thanks for everything!
Thanks to my whole family: thanks to my mother and father, my sisters and brother, my “brothers in law” Davide and Matteo. Thanks to all my friends, in particular to Camilla. A special thank to my boyfriend Paolo: your love, your help and your support have been fundamental in these years.
My last words are for you, Vally, for always being in my heart.